

COLLIDER PHENOMENOLOGY OF HEAVY CHARGED GAUGE BOSONS

By

Jiang-Hao Yu

A DISSERTATION

Submitted to
Michigan State University
in partial fulfillment of the requirements
for the degree of

DOCTOR OF PHILOSOPHY

Physics and Astronomy

2012

ABSTRACT

COLLIDER PHENOMENOLOGY OF HEAVY CHARGED GAUGE BOSONS

By

Jiang-Hao Yu

New vector resonances, such as heavy W' and Z' gauge bosons, may be one of the cleanest and most important signals of new physics that can be discovered in the early data from the CERN Large Hadron Collider (LHC). Such new heavy gauge bosons arise in numerous gauge extensions of the Standard Model (SM) of particle interactions. Their discovery would help to elucidate the nature of the spontaneous symmetry breaking at the weak scale. In this thesis, we focus on extended gauge models with these novel electroweak gauge bosons in the framework of an effective theory. Based on breaking patterns and fermion assignments, we classify a number of models with $SU(2)_1 \times SU(2)_2 \times U(1)_X$ gauge symmetry (the so-called $G(221)$ models) and write down the general Lagrangian and Feynman rules in a linearized effective field theory.

The current constraints on $G(221)$ models are studied in detail. This is done by combining the indirect constraints from the precision electroweak tests (EWPT) at the Large Electron Positron (LEP) collider with other low energy observables. Moreover, direct search constraints from the Fermilab TeVatron and the LHC are also included. Our results indicate that, although the light W' and Z' bosons are allowed by EWPTs, direct constraints require the masses of the W' and Z' bosons in $G(221)$ models to be at the TeV scales.

In this thesis, we also consider the prospect for discovering these bosons in the coming data from the LHC. We focus on searches for heavy resonances in final states with a lepton plus large amounts of missing energy. Having a lepton and large missing energy in the final

state ensures the experimental collaborations can readily identify these potential signatures of new physics. We explore the potential for discovering the heavy charged gauge bosons in the $G(221)$ models in the coming data, as well as the ability to place limits on their masses and couplings. It is shown that in some models it is more efficient to use the W' leptonic decay channel for discovery or exclusion than the Z' leptonic decay channel. Also, we note, for various $G(221)$ phobic models, observing a Z' alone cannot rule out the possibility of a non-abelian gauge extension of new physics.

To help unravel the nature of the new gauge bosons, it is necessary to study the properties of the charge gauge bosons in the top quark channels. We show that it is possible to probe the chiral structure of the charged gauge bosons using top quark polarization with the upcoming data from the LHC. Furthermore, a flavor-violating W' model might explain the anomalously large forward-backward asymmetry of the top pairs. An anomalously large forward-backward asymmetry was observed at both the CDF and DØ experiments at the TeVatron. Finally, we explore the searches for a top-philic W' in the top quark pair plus a hard b-jet final states at the LHC. This provides a sensitive test for exotically charged gauged bosons.

Copyright by
JIANG-HAO YU
2012

Dedicate to my parents and Nan.

ACKNOWLEDGMENTS

First, I would like to thank my advisors, Prof. C.-P. Yuan and Prof. Carl Schmidt for their inspiration and support during my years at Michigan State University. I am deeply indebted to Prof. Yuan, who opened the door for me to enjoy the beauty and simplicity of particle physics. I have benefited continuously from sharing many of his ideas and intuitions with me, which helped me grow as a physicist. I owe my deep appreciation to Prof. Schmidt, who taught me how to do research as a physicist, and how to see the simplicity behind the complex. Both of them gave me free times, supported my interests, and allowed me to collaborate with others.

I am also grateful to Prof. R. Sekhar Chivukula and Prof. Elizabeth H. Simmons for their invaluable advise and suggestions. I am indebted to Prof. Edmond Berger at Argonne National Lab, who offered me the chance to work at Argonne, and he has also provided invaluable guidance on my research. I thank Prof. Wayne Repko for his advise and suggestions, and Prof. Reinhard Schwienhorst for his endless patience to answer my questions on experimental techniques. I have further benefited from the following professors, Raymond Brock, Wad Fisher, Joey Huston and James Linnemann, who have given me important advice and suggestions. I also want to thank my committee members Prof. Bhanu Mahanti and Prof. Scott Pratt for their guidance.

My appreciation also goes to current and former post-docs: Anupama Atre, Neil Christensen, Roshan Foadi, Ken Hsieh, Zhao Li, for many illuminating discussions and collaborations. I especially thank to Prof. Yuan's former students, Qing-Hong Cao and Chuan-Ren Chen, who gave me lots of help when I started to learn the techniques of calculation and numerical codes. I also thank Devin Walker for his patience to polish the English in my

thesis. Thanks to Baradhvaj Coleppa, Stefano DiChiara, Arsham Farzinnia, Mohammad Hussein, Pawin Ittisamai, Jing Ren, and Kai Schmitz for the discussions in our office. Thank my friends, He Huang, Liyuan Jia, Xu Lu, Bai Nie, Chen Sun, Zhensheng Tao, Ding Wang, Hui Wang, Kaijie Xu and He Zhang for the great times during my years at Michigan State University.

I am sincerely grateful to Debbie Simmons and Brenda Wenzlick and all of my friends who gave me lots of help during my year at Michigan State University. Finally, my sincere gratitude goes to my parents and my wife, who bring joy to each day of my life.

TABLE OF CONTENTS

List of Tables	xi
List of Figures	xiii
Chapter 1 INTRODUCTION	1
1.1 Charged Gauge Bosons in the Standard Model	1
1.1.1 Fermi Theory of Weak Interaction and Unitarity Violation	2
1.1.2 Intermediate Charged Weak Boson Model	4
1.1.3 The Standard Model and Moose Diagram	6
1.2 New Physics and Heavy Charged Gauge Bosons	15
1.2.1 Motivation for New Physics	15
1.2.2 Phenomenology of New Charged Gauge Bosons	18
 Chapter 2 MODELS OF HEAVY CHARGED GAUGE BOSONS	 21
2.1 Introduction	21
2.2 Model Classification by Moose Diagrams	23
2.3 $G(221)$ Lagrangian in the Gauge Basis and Physical Basis	28
2.3.1 Lagrangian in the Gauge Basis	28
2.3.1.1 The Scalar Sector	28
2.3.1.1.1 Scalar Multiplets in the Breaking Pattern I	28
2.3.1.1.2 Scalar Multiplets in the Breaking Pattern II	30
2.3.1.2 The Gauge Boson Sector	31
2.3.1.3 The Fermion Sector	31
2.3.1.4 The Yukawa Sector	34
2.3.2 Symmetry Breaking and Mass Eigenstates	37
2.3.2.1 Higgs Potential and VEV	37
2.3.2.2 Gauge Boson Mass Mixing in Breaking Pattern I	42
2.3.2.3 Gauge Boson Mass Mixing in Breaking Pattern II	44
2.3.3 Lagrangian in the Physical Basis	47
2.3.3.1 Gauge couplings of fermions	47
2.3.3.2 Couplings of Gauge Bosons and Higgs Boson	52
2.4 Model Parameters and Mass Spectrum	52
2.4.1 Input Parameters	53

2.4.1.1	Electric Charge	55
2.4.1.2	The Fermi Constant	55
2.4.1.3	Z -Mass	59
2.4.2	Mass Spectra	61
2.4.2.1	Breaking Pattern I with Doublet Higgs	61
2.4.2.2	Breaking Pattern I with Triplet Higgs	62
2.4.2.3	Breaking Pattern II	63
2.5	Indirect and Direct Constraints on Parameter Spaces	64
2.5.1	Indirect Constraints from Electroweak Precision Tests	65
2.5.1.1	Precision Measurements at the Z -Pole	68
2.5.1.2	The Tau Lifetime	69
2.5.1.3	νN Deep Inelastic Scattering	70
2.5.1.4	νe Scattering	71
2.5.1.5	Parity Violation Experiments	72
2.5.2	Direct Searches at the Tevatron and LHC	74
2.5.3	Parameter constraints	75
2.6	Summary	95
Chapter 3 DISCOVERY OF HEAVY CHARGED GAUGE BOSONS		96
3.1	Introduction	96
3.2	Drell-Yan Production and Decay at Next-to-Leading Order	98
3.2.1	Drell-Yan Production at the NLO	99
3.2.2	V' Decay	102
3.3	Event Simulation and Search Limits	109
3.3.1	Signal and Backgrounds	109
3.3.2	Object Reconstructions and Event Selections at the LHC	115
3.3.3	Upper Limits on W' masses at the LHC	118
3.4	Discovery Potential and Significance	119
3.5	Summary	152
Chapter 4 PROPERTIES OF HEAVY CHARGED GAUGE BOSONS		155
4.1	Introduction	155
4.2	s -channel Production of W' : Resonances in Single Top Channel	157
4.2.1	New Physics Models	157
4.2.2	Cross Section and Event Simulation	159
4.2.3	Lepton Angular Distribution and Chiral Structure	169
4.3	t -channel Production of W' : Top Quark Forward-backward Asymmetry	170
4.3.1	Forward-backward Asymmetry of Top Quark	170
4.3.2	Kinematics	172
4.3.3	A_{FB}^t and A_{FB}^ℓ	180
4.3.4	Flavor-changing W' Model	184
4.3.5	Correlations on A_{FB}^ℓ and A_{FB}^t	187
4.4	Summary	189

Chapter 5	EXOTIC HEAVY CHARGED GAUGE BOSONS	191
5.1	Introduction	191
5.2	The model	192
5.3	Collider phenomenology	196
5.3.1	Selection cuts	198
5.3.2	χ^2 -template and extra-jet tagging	203
5.3.3	Mass window ΔM cut	207
5.3.4	Discovery potential	210
5.4	W' - t - b coupling and t -polarization	213
5.5	Summary	216
Chapter 6	CONCLUSION	217
Appendix A	Statistics for Upper limit and Significance	223
A.1	Upper Limit	224
A.1.1	Bayesian Approach	224
A.1.2	Frequentist Approach	228
A.2	Discovery Significance	236
A.2.1	Bayesian Approach	236
A.2.2	Frequentist Approach	237
Bibliography	241

LIST OF TABLES

Table 2.1	These tables display the model-specific Higgs representations and VEVs that achieve the symmetry breaking of $G(221)$ models. . . .	27
Table 2.2	Assignment of SM fermions under the $G(221)$ symmetry: $(T_L, T_R)_X$ in breaking pattern I while $(T_l, T_h)_Y$ in breaking pattern II. Unless otherwise specified, the fermion doublet represents three generations of SM fermions. LRD (LRT) denotes the left-right doublet (triplet) model, where the $G(221)$ model is broken by a scalar doublet (triplet). Similarly, LPD (LPT) denotes the lepto-phobic doublet (triplet) model, HPD (HPT) the hadro-phobic doublet (triplet) model, FPD (FPT) the fermio-phobic doublet (triplet) model, SQD the sequential doublet model, TFD the top-flavor doublet model, and UUD the un-unified doublet model.	33
Table 2.3	The left-handed fermion couplings of the heavy gauge boson in Breaking Pattern I and II. For the fermion couplings, the quantum numbers (T_L, T_R) in BP-I and (T_l, T_h) in BP-II are implied in Tab. 2.2. In BP-II, the fermion notation f means the fermions listed in the column $SU(2)_1$, while F means the fermions listed in the column $SU(2)_2$ in Tab. 2.2.	48
Table 2.4	The right-handed fermion couplings of the heavy gauge boson in Breaking Pattern I and II. For the fermion couplings, the quantum numbers (T_L, T_R) in BP-I and (T_l, T_h) in BP-II are implied in Tab. 2.2. In BP-II, the fermion notation f means the fermions listed in the column $SU(2)_1$, while F means the fermions listed in the column $SU(2)_2$ in Tab. 2.2.	49
Table 2.5	The triple boson couplings of the heavy gauge boson in Breaking Pattern I.	50
Table 2.6	The triple boson couplings of the heavy gauge boson in Breaking Pattern II.	51

Table 3.1	Expected and observed numbers of events in 1.04 fb^{-1} in ref. [54] from the various background sources in each decay channel for $M_T > 891 \text{ GeV}$, the region used to search for a W' with a mass of 1500 GeV . In the table, the signal selection efficiency, ϵ_{sig} , and the prediction for the number of signal events, N_{sig} , obtained with this efficiency. The last two columns are the expected number of background events, N_{bg} , and the number of events observed in data, N_{obs} . The uncertainties are statistical.	117
Table 3.2	The current lowest limits and discovery reaches at the LHC14 with 100 fb^{-1} luminosity on W' masses.	153
Table 3.3	The current lowest limits and discovery reaches at the LHC14 with 100 fb^{-1} luminosity on W' and Z' masses.	153
Table 4.1	Cross sections for the signal and various background processes at the 7 TeV LHC in different cut levels are listed.	169
Table 5.1	The numbers of signal and background events at 14 TeV with an integrated luminosity of 100 fb^{-1} before and after cuts, with $f_L = 1$, for seven values of $m_{W'}$ (GeV). The top quark decay branching ratio $2/27$ is included in the “no cut” column, and the b tagging efficiency is included in the fifth column. The cut acceptances ϵ_{cut} are also listed.	197
Table 5.2	The efficiency for extra jet reconstruction with the χ^2 -template method. The net b -tagging efficiencies ($\epsilon_{extra-j-tag}$), calculated with Eqs. (5.17) and (5.19), are shown in the last column.	208

LIST OF FIGURES

Figure 1.1	The Moose diagram for the standard model. For interpretation of the references to color in this and all other figures, the reader is referred to the electronic version of this thesis.	11
Figure 1.2	Scattering cross sections for $W_L^+ W_L^- \rightarrow W_L^+ W_L^-$ versus $\sqrt{s_{WW}}$. Various values of δ are shown, where δ denotes the size of the Higgs amplitude relative to the SM one. An angular cut of $ \cos \theta_{WW} < 0.8$ is applied and the light Higgs boson mass $m_h = 200$ GeV is assumed. Figure taken from [10].	14
Figure 1.3	The scale Λ at which the two-loop RGEs drive the quartic SM Higgs coupling non-perturbative (upper curves), and the scale Λ at which the RGEs create an instability in the electroweak vacuum (lower curves). Figure taken from [9].	17
Figure 2.1	The Moose diagram for the breaking pattern I (Left-Right Model).	25
Figure 2.2	The Moose diagram for the breaking pattern II (Sequential Model).	26
Figure 2.3	The Moose diagram for the breaking pattern I (Lepton-phobic Model with vector-like fermions).	36
Figure 2.4	The Moose diagram for the breaking pattern II (Top-Flavor model with vector-like fermions).	37
Figure 2.5	Allowed parameter space of the LRD and LRT models at 95% CL in the $M_{W'} - M_{Z'}$ plane after including indirect and direct constraints: EWPTs (green), Tevatron (red) and LHC7 (blue).	77
Figure 2.6	Allowed parameter space of the LPD and LPT models at 95% CL in the $M_{W'} - M_{Z'}$ plane after including indirect and direct constraints: EWPTs (green), Tevatron (red) and LHC7 (blue).	78

Figure 2.7	Allowed parameter space of the HPD and HPT models at 95% CL in the $M_{W'} - M_{Z'}$ plane after including indirect and direct constraints: EWPTs (green), Tevatron (red) and LHC7 (blue).	79
Figure 2.8	Allowed parameter space of the FPD and FPT models at 95% CL in the $M_{W'} - M_{Z'}$ plane after including indirect and direct constraints: EWPTs (green), Tevatron (red) and LHC7 (blue).	80
Figure 2.9	Allowed parameter space of the SQD and MSQ models at 95% CL in the $M_{W'} - M_{Z'}$ plane after including indirect and direct constraints: EWPTs (green), Tevatron (red) and LHC7 (blue).	81
Figure 2.10	Allowed parameter space of the TFD and UUQ models at 95% CL in the $M_{W'} - M_{Z'}$ plane after including indirect and direct constraints: EWPTs (green), Tevatron (red) and LHC7 (blue).	82
Figure 2.11	Allowed parameter space of the LRD and LRT models at 95% CL in the $M_{W'} - c_\phi$ plane after including indirect and direct constraints: EWPTs (green), Tevatron (red) and LHC7 (blue). The dashed black lines in LRD represent MLR models.	83
Figure 2.12	Allowed parameter space of the LPD and LPT models at 95% CL in the $M_{W'} - c_\phi$ plane after including indirect and direct constraints: EWPTs (green), Tevatron (red) and LHC7 (blue).	84
Figure 2.13	Allowed parameter space of the HPD and HPT models at 95% CL in the $M_{W'} - c_\phi$ plane after including indirect and direct constraints: EWPTs (green), Tevatron (red) and LHC7 (blue).	85
Figure 2.14	Allowed parameter space of the FPD and FPT models at 95% CL in the $M_{W'} - c_\phi$ plane after including indirect and direct constraints: EWPTs (green), Tevatron (red) and LHC7 (blue).	86
Figure 2.15	Allowed parameter space of the SQD models at 95% CL in the $M_{W'} - c_\phi$ plane after including indirect and direct constraints: EWPTs (green), Tevatron (red) and LHC7 (blue). The dashed black lines represent MSQ models.	87
Figure 2.16	Allowed parameter space of the TFD and UUQ models at 95% CL in the $M_{W'} - c_\phi$ plane after including indirect and direct constraints: EWPTs (green), Tevatron (red) and LHC7 (blue).	88

Figure 2.17	Allowed parameter space of the LRD and LRT models at 95% CL in the $M_{Z'} - c_\phi$ plane after including indirect and direct constraints: EWPTs (green), Tevatron (red) and LHC7 (blue). The dashed black lines in LRD represent MLR models.	89
Figure 2.18	Allowed parameter space of the LPD and LPT models at 95% CL in the $M_{Z'} - c_\phi$ plane after including indirect and direct constraints: EWPTs (green), Tevatron (red) and LHC7 (blue).	90
Figure 2.19	Allowed parameter space of the HPD and HPT models at 95% CL in the $M_{Z'} - c_\phi$ plane after including indirect and direct constraints: EWPTs (green), Tevatron (red) and LHC7 (blue).	91
Figure 2.20	Allowed parameter space of the FPD and FPT models at 95% CL in the $M_{Z'} - c_\phi$ plane after including indirect and direct constraints: EWPTs (green), Tevatron (red) and LHC7 (blue).	92
Figure 2.21	Allowed parameter space of the SQD models at 95% CL in the $M_{Z'} - c_\phi$ plane after including indirect and direct constraints: EWPTs (green), Tevatron (red) and LHC7 (blue). The dashed black lines represent MSQ models.	93
Figure 2.22	Allowed parameter space of the TFD and UUQ models at 95% CL in the $M_{Z'} - c_\phi$ plane after including indirect and direct constraints: EWPTs (green), Tevatron (red) and LHC7 (blue).	94
Figure 3.1	Upper panel: the LO and NLO cross sections of $pp \rightarrow W'$ process with a SM like coupling as a function of new heavy gauge boson mass ($m_{W'}$) in hadron collisions. Lower panel: the K -factor as a function of $m_{W'}$	103
Figure 3.2	Upper panel: the LO and NLO cross sections of $pp \rightarrow Z'$ process with a SM like coupling as a function of new heavy gauge boson mass ($m_{Z'}$) in hadron collisions. Lower panel: the K -factor as a function of $m_{Z'}$	104
Figure 3.3	Upper panel: the LO and NLO cross sections of $pp \rightarrow Z'$ process with a SM-like couplings as a function of $m_{Z'}$ in hadron collision: induced by up-type quark initial state Lower panel: the K -factor as a function of $m_{Z'}$	105

Figure 3.4	Upper panel: the LO and NLO cross sections of $pp \rightarrow Z'$ process with a SM-like couplings as a function of $m_{Z'}$ in hadron collision: induced by down-type quark initial state. Lower panel: the K -factor as a function of $m_{Z'}$	106
Figure 3.5	The p_T^ℓ distribution for 1500 GeV W' in the charged lepton and missing transverse energy final states.	112
Figure 3.6	The E_T^{miss} distribution for 1500 GeV W' in the charged lepton and missing transverse energy final states.	113
Figure 3.7	The M_T distribution for 1500 GeV W' in the charged lepton and missing transverse energy final states is shown.	114
Figure 3.8	5σ Discovery potential (fb^{-1}) in the LRD and LRT models for different luminosity at LHC7 via W' leptonic decay channel. The current combined constraints are within solid black contour. The dashed black lines in LRD represent MLR models.	125
Figure 3.9	5σ Discovery potential (fb^{-1}) in the LPD and LPT models for different luminosity at LHC7 via W' leptonic decay channel. The current combined constraints are within solid black contour.	126
Figure 3.10	5σ Discovery potential (fb^{-1}) in the HPD and HPT models for different luminosity at LHC7 via W' leptonic decay channel. The current combined constraints are within solid black contour.	127
Figure 3.11	5σ Discovery potential (fb^{-1}) in the FPD and FPT models for different luminosity at LHC7 via W' leptonic decay channel. The current combined constraints are within solid black contour.	128
Figure 3.12	5σ Discovery potential (fb^{-1}) in the SQD models for different luminosity at LHC7 via W' leptonic decay channel. The current combined constraints are within solid black contour. The dashed black lines in SQD represent MSQ models.	129
Figure 3.13	5σ Discovery potential (fb^{-1}) in the TFD and UUD models for different luminosity at LHC7 via W' leptonic decay channel. The current combined constraints are within solid black contour.	130

Figure 3.14	5σ Discovery potential (fb^{-1}) in the LRD and LRT models for different luminosity at LHC7 via Z' leptonic decay channel. The current combined constraints are within solid black contour. The dashed black lines in LRD represent MLR models.	132
Figure 3.15	5σ Discovery potential (fb^{-1}) in the LPD and LPT models for different luminosity at LHC7 via Z' leptonic decay channel. The current combined constraints are within solid black contour.	133
Figure 3.16	5σ Discovery potential (fb^{-1}) in the HPD and HPT models for different luminosity at LHC7 via Z' leptonic decay channel. The current combined constraints are within solid black contour.	134
Figure 3.17	5σ Discovery potential (fb^{-1}) in the FPD and FPT models for different luminosity at LHC7 via Z' leptonic decay channel. The current combined constraints are within solid black contour.	135
Figure 3.18	5σ Discovery potential (fb^{-1}) in the SQD models for different luminosity at LHC7 via Z' leptonic decay channel. The current combined constraints are within solid black contour. The dashed black lines in SQD represent MSQ models.	136
Figure 3.19	5σ Discovery potential (fb^{-1}) in the TFD and UUD models for different luminosity at LHC7 via Z' leptonic decay channel. The current combined constraints are within solid black contour.	137
Figure 3.20	5σ Discovery potential (fb^{-1}) in the LRD and LRT models for different luminosity at LHC14 via W' leptonic decay channel. The current combined constraints are within solid black contour. The dashed black lines in LRD represent MLR models.	138
Figure 3.21	5σ Discovery potential (fb^{-1}) in the LPD and LPT models for different luminosity at LHC14 via W' leptonic decay channel. The current combined constraints are within solid black contour.	139
Figure 3.22	5σ Discovery potential (fb^{-1}) in the HPD and HPT models for different luminosity at LHC14 via W' leptonic decay channel. The current combined constraints are within solid black contour.	140
Figure 3.23	5σ Discovery potential (fb^{-1}) in the FPD and FPT models for different luminosity at LHC14 via W' leptonic decay channel. The current combined constraints are within solid black contour.	141

Figure 3.24	5σ Discovery potential (fb^{-1}) in the SQD models for different luminosity at LHC14 via W' leptonic decay channel. The current combined constraints are within solid black contour. The dashed black lines in SQD represent MSQ models.	142
Figure 3.25	5σ Discovery potential (fb^{-1}) in the TFD and UUD models for different luminosity at LHC14 via W' leptonic decay channel. The current combined constraints are within solid black contour.	143
Figure 3.26	5σ Discovery potential (fb^{-1}) in the LRD and LRT models for different luminosity at LHC14 via Z' leptonic decay channel. The current combined constraints are within solid black contour. The dashed black lines in LRD represent MLR models.	145
Figure 3.27	5σ Discovery potential (fb^{-1}) in the LPD and LPT models for different luminosity at LHC14 via Z' leptonic decay channel. The current combined constraints are within solid black contour.	146
Figure 3.28	5σ Discovery potential (fb^{-1}) in the HPD and HPT models for different luminosity at LHC14 via Z' leptonic decay channel. The current combined constraints are within solid black contour.	147
Figure 3.29	5σ Discovery potential (fb^{-1}) in the FPD and FPT models for different luminosity at LHC14 via Z' leptonic decay channel. The current combined constraints are within solid black contour.	148
Figure 3.30	5σ Discovery potential (fb^{-1}) in the SQD models for different luminosity at LHC14 via Z' leptonic decay channel. The current combined constraints are within solid black contour. The dashed black lines in SQD represent MSQ models.	149
Figure 3.31	5σ Discovery potential (fb^{-1}) in the TFD and UUD models for different luminosity at LHC14 via Z' leptonic decay channel. The current combined constraints are within solid black contour.	150
Figure 4.1	Feynman diagrams of the s -channel and t -channel single top production with exchanging a W'	159
Figure 4.2	Total cross section of W' for $f_L = 1$, $f_R = 0$ at the LHC.	160
Figure 4.3	The normalized P_T distributions of the leading jet for signal and backgrounds.	163

Figure 4.4	The normalized P_T distributions of the subleading jet for signal and backgrounds.	164
Figure 4.5	The normalized H_T distributions of the system for signal and backgrounds.	165
Figure 4.6	After all the cuts, the reconstructed invariant mass distributions of the system for W' signal and backgrounds.	167
Figure 4.7	Before and after basic cuts, the $\cos\theta$ angular distributions of the final state leptons for left-handed W' and right-handed W'	168
Figure 4.8	(a) $\cos\theta_{\text{hel}}$ distribution in the top quark rest frame for both t_L and t_R . (b) $\cos\theta_{t\ell}$ distribution in the boosted frame for a top quark with $E_t = 200$ GeV.	173
Figure 4.9	The ratio R_F as a function of y_t for a top quark with fixed energy: (a) $E_t = 200$ GeV and (b) $E_t = 600$ GeV.	176
Figure 4.10	The ratio of the charged lepton in the forward and backward region as a function of the top quark rapidity for top quarks with fixed transverse momentum $p_T = 10, 50$ GeV.	178
Figure 4.11	The ratio of the charged lepton in the forward and backward region as a function of the top quark rapidity for top quarks with fixed transverse momentum $p_T = 100, 300$ GeV.	179
Figure 4.12	Correlation between A_{FB}^ℓ and A_{FB}^t in the W' models. The point corresponding to the D0 data is also shown. The numbers within the parentheses label the lower and upper limits of the mass of the W'	185
Figure 4.13	The statistics for the ratio of predicted A_{FB}^ℓ to A_{FB}^t in the W' models.	186
Figure 5.1	Feynman diagrams for the associated production of a W' and a top quark: (a, b) W'^-t , and (c, d) $W'^+\bar{t}$	194
Figure 5.2	The inclusive cross section of the tW'^- and $\bar{t}W'^+$ associated production at a 14 TeV LHC with $f_L = 1$ and $f_R = 0$	195

Figure 5.3	Normalized p_T distribution of (a) the leading jet, (b) the second leading jet distributions. The black-solid curves represent the signal ($m_{W'} = 1$ TeV), the red-dashed curves the $t\bar{t}b$ background, while the blue-dotted curves the $t\bar{t}j$ background.	200
Figure 5.4	Normalized p_T distribution of (a) the third leading jet, as well as (b) the normalized H_T distribution. The black-solid curves represent the signal ($m_{W'} = 1$ TeV), the red-dashed curves the $t\bar{t}b$ background, while the blue-dotted curves the $t\bar{t}j$ background.	201
Figure 5.5	(a) Reconstructed invariant mass distribution of the leptonic decaying top and extra jet; (b) reconstructed hadronic decaying top and extra jet invariant mass distribution.	209
Figure 5.6	The discovery potential for the top-philic W' 14 TeV with an integrated luminosity of 100 fb^{-1}	212
Figure 5.7	The angular distributions of the final lepton $\cos\theta_l$ for the left-handed and the right-handed W'	214
Figure 5.8	The angular distributions of the final lepton $\cos\theta_l$ for the SM background.	215

Chapter 1

INTRODUCTION

1.1 Charged Gauge Bosons in the Standard Model

The standard model (SM) provides a very successful description of the properties and interactions of the existing particles without serious discrepancy with almost all existing data. The discovery of the charged gauge bosons W^\pm and the neutral massive gauge boson Z with expected masses is a great triumph of the model. During the development of the SM, the charged gauge bosons W^\pm played an important role in the discovery of the electroweak gauge symmetry $SU(2)_L \times U(1)_Y$, in which the electromagnetic and weak interaction are unified into a renormalizable field theory. Here we briefly review the history of charged gauge bosons in the standard model, and refer to refs. [1, 2, 3] for details.

1.1.1 Fermi Theory of Weak Interaction and Unitarity Violation

The weak interaction among elementary particles was first discovered in the β -decay of neutron

$$n \rightarrow p + e^{-} + \bar{\nu}. \quad (1.1)$$

The theory of weak interactions was originally formulated by Fermi through the charged current-current interactions in quantum field theory

$$H_{\text{weak}} = G_F [\bar{\psi}_p \gamma_\mu \psi_n] [\bar{\psi}_e \gamma^\mu \psi_\nu], \quad (1.2)$$

where G_F is the weak coupling constant which has a much smaller value than the electromagnetic coupling constant e . After discovery of parity violation in the weak interaction, the weak interaction Hamiltonian was reformulated to a more general form

$$H_{\text{weak}} = \sum_i G_{Fi} [\bar{\psi}_p \mathcal{O}_i \psi_n] [\bar{\psi}_e \mathcal{O}_i (1 + c_i \gamma_5) \psi_\nu], \quad (1.3)$$

where c_i is taken to be -1 since the parity violation is maximum and the neutrino is left-handed, and the index i represents the type of the Lorentz structure \mathcal{O} with

$$\mathcal{O}_S = 1 \quad (\text{scalar}),$$

$$\mathcal{O}_V = \gamma_\mu \quad (\text{vector}),$$

$$\mathcal{O}_P = \gamma_5 \quad (\text{axial-scalar}),$$

$$\mathcal{O}_A = \gamma_\mu \gamma_5 \quad (\text{axial-vector}),$$

$$\mathcal{O}_T = \sigma_{\mu\nu} \quad (\text{tensor}).$$

Later experimental evidence on the $V - A$ Lorentz structure and universality of the fermi constant G_F in various weak processes, suggested that the Hamiltonian of the weak interaction was described by the $V - A$ current-current interactions

$$H_{\text{weak}} = \frac{G_F}{\sqrt{2}} [\bar{\psi}_p \gamma_\mu (1 - g_A \gamma_5) \psi_n] [\bar{\psi}_e \gamma^\mu (1 - \gamma_5) \psi_\nu], \quad (1.4)$$

where the Fermi constant is $G_F = 1.166364 \times 10^{-5} \text{ GeV}^{-2}$, and $g_A \simeq 1.26$.

Although the Fermi theory described the low energy weak interaction processes successfully, it encountered difficulty in explaining theory-motivated problems, *i.e.*, unitarity violation in the weak scattering process, and non-renormalizability beyond the lowest-order approximation. Consider the neutrino-electron scattering process

$$\nu_e + e^- \rightarrow \nu_e + e^-, \quad (1.5)$$

where the Hamiltonian is given by

$$H_{\text{weak}} = \frac{G_F}{\sqrt{2}} [\bar{\psi}_{\nu_e} \gamma_\mu (1 - \gamma_5) \psi_e] [\bar{\psi}_e \gamma^\mu (1 - \gamma_5) \psi_{\nu_e}]. \quad (1.6)$$

The differential cross section for this process is

$$\frac{d\sigma}{d\Omega} = \frac{G_F^2}{4\pi^2} s, \quad (1.7)$$

where s is the center of mass energy squared of the system. On the other hand, the differential

cross section can be decomposed into partial wave amplitudes

$$\frac{d\sigma}{d\Omega} = \left| \frac{1}{2\sqrt{s}} \sum_{\ell=0}^{\infty} (2\ell+1) a_{\ell} P_{\ell}(\cos\theta) \right|^2, \quad (1.8)$$

where a_{ℓ} is the partial wave amplitude for angular momentum ℓ . In the case of Fermi interaction, only a_0 contributes to the differential cross section

$$\frac{d\sigma}{d\Omega} = \frac{1}{s} |a_0|^2 \leq \frac{1}{s}, \quad (1.9)$$

where $|a_0| < 1$ from the unitarity property in quantum mechanics. From the upper bound of the cross section, one find that the Fermi theory violates unitarity at an energy above

$$E = \frac{\sqrt{s}}{2} \geq \sqrt{\frac{\pi}{2G_F}} \simeq 370 \text{ GeV}. \quad (1.10)$$

1.1.2 Intermediate Charged Weak Boson Model

The difficulty of unitarity violation can be avoided if the analogy with the electromagnetic interaction is extended to include a virtual intermediate charged weak boson as the mediator of the weak processes. This is a successful phenomenological model to describe the charged weak processes even at the high energy scale. Consider again the process $\nu_e + e^- \rightarrow \nu_e + e^-$ as an example. Assuming the charged gauge boson exchange between two charged currents, the matrix element describing this process is

$$\mathcal{M} = \left[\frac{g_W}{\sqrt{2}} \bar{u}_e \gamma_{\mu} \frac{1-\gamma_5}{2} u_{\nu_e} \right] \frac{-g^{\mu\nu} + \frac{q^{\mu} q^{\nu}}{M_W^2}}{q^2 - M_W^2} \left[\frac{g_W}{\sqrt{2}} \bar{u}_{\nu_e} \gamma_{\nu} \frac{1-\gamma_5}{2} u_e \right], \quad (1.11)$$

where M_W is the mass of the charged gauge bosons W , q is the four-momentum of the W -boson, and g_W is the dimensionless weak coupling constant. At low energy where q^2 is far smaller than the gauge boson mass M_W , the propagator term reduces to

$$\frac{-g^{\mu\nu} + \frac{q^\mu q^\nu}{M_W^2}}{q^2 - M_W^2} \rightarrow \frac{g^{\mu\nu}}{M_W^2}, \quad (1.12)$$

and the above matrix element reduces to the Fermi Hamiltonian of Eq. 1.6, with

$$\frac{G_F}{\sqrt{2}} = \frac{g^2}{8M_W^2}. \quad (1.13)$$

Because the range of the weak interaction is very small, this indicates the mass of the intermediate gauge bosons is large, and can be estimated to be of the order of $\mathcal{O}(100 \text{ GeV})$. In this model, the unitarity problem in the scattering process $\nu_e + e^- \rightarrow \nu_e + e^-$ is solved, because of the existence of the weak boson mediator.

Although this immediate charged weak boson model cures the unitarity violation problem in this particular channel, it still has problems of non-renormalizability. Loop calculation involving in the charge gauge boson can not be renormalized to get the finite results in this model. Furthermore, the unitarity violation still occurs in other scattering processes like $\nu + \bar{\nu} \rightarrow W^+ + W^-$. Writing down the matrix element in this process, one can calculate the differential cross section

$$\frac{d\sigma}{d\Omega} = \frac{G_F^2 \sin^2 \theta}{3\pi^2} s, \quad (1.14)$$

where s and θ are the center of mass energy squared of the system and the polar angle in the center of mass frame. Notice that the cross section increases with s and hence violates

the unitarity bound at some high energy.

1.1.3 The Standard Model and Moose Diagram

Although the intermediate charged boson model describes the phenomenology relevant to the charged-current processes successfully, it is still an effective theory, due to the non-renormalizability and unitarity violation. A beautiful renormalizable theory was finally formulated based on the unification of the electromagnetic and weak interactions, which is the so-called electroweak standard model. Let us review the essential elements of the electroweak theory following the ref. [4].

The essential ingredient of the SM is the non-abelian gauge group with $SU(2)_L \times U(1)_Y$ symmetry, where the subscript L represents the weak isospin for the left-handed fermion fields, and Y denotes the weak hyper-charge. The electroweak gauge group, $SU(2)_L \times U(1)_Y$, implies two sets of gauge fields: a weak isovector \mathcal{W}_μ , including two charged components W_μ^\pm and one neutral component W_μ^3 , with coupling constant g , and a weak isoscalar B_μ , with coupling constant g' . Corresponding to these gauge fields are the field-strength tensors

$$F_{\mu\nu}^a = \partial_\nu \mathcal{W}_\mu^a - \partial_\mu \mathcal{W}_\nu^a + g\varepsilon_{abc} \mathcal{W}_\mu^b \mathcal{W}_\nu^c, \quad (1.15)$$

for the weak-isospin symmetry, and

$$B_{\mu\nu} = \partial_\nu B_\mu - \partial_\mu B_\nu, \quad (1.16)$$

for the weak-hypercharge symmetry. From the non-abelian gauge theory, the kinematic term

in the gauge boson sector can be written as

$$\mathcal{L}_{\text{gauge}} = -\frac{1}{4}F_{\mu\nu}^a F^{a\mu\nu} - \frac{1}{4}B_{\mu\nu}B^{\mu\nu}. \quad (1.17)$$

For the fermion sector, the electroweak theory takes the crucial clues from experiment: the existence of left-handed weak-isospin doublets and massless neutrinos. To conserve the electromagnetic interaction in the gauge group, the quantum numbers satisfy the relation between the weak hypercharge Y and weak isospin, $Q = I_3 + \frac{1}{2}Y$. The fermions are specified based on the quantum numbers: a left-handed weak isospin doublet

$$\begin{array}{rcccl} & I_3 & Q & Y = 2(Q - I_3) & \\ \mathbb{L}_l = \begin{pmatrix} \nu \\ e \end{pmatrix}_L & \frac{1}{2} & +0 & -1, & (1.18) \\ & -\frac{1}{2} & -1 & & \end{array}$$

and right-handed weak isospin singlets

$$\begin{array}{rcccl} & I_3 & Q & Y = 2(Q - I_3) & \\ \mathbb{R}_\nu = \nu_R & 0 & +0 & +0 & (1.19) \\ & & & & , \\ \mathbb{R}_e = e_R & 0 & -1 & -2 & \end{array}$$

where we have induced the possibility of a right-handed neutrino. To extend our theory to include the electroweak interactions of quarks, we observe that each generation consists of a

left-handed doublet

$$\begin{array}{rcc}
 & I_3 & Q & Y = 2(Q - I_3) \\
 \mathbf{L}_q = \begin{pmatrix} u \\ d \end{pmatrix}_L & \begin{matrix} 1 \\ -\frac{1}{2} \end{matrix} & \begin{matrix} 2 \\ -\frac{1}{3} \end{matrix} & \begin{matrix} 1 \\ -\frac{1}{3} \end{matrix}
 \end{array} \tag{1.20}$$

and two right-handed singlets,

$$\begin{array}{rcc}
 & I_3 & Q & Y = 2(Q - I_3) \\
 \mathbf{R}_u = u_R & 0 & \begin{matrix} 2 \\ +\frac{2}{3} \end{matrix} & \begin{matrix} 4 \\ +\frac{4}{3} \end{matrix} \\
 \mathbf{R}_d = d_R & 0 & \begin{matrix} 1 \\ -\frac{1}{3} \end{matrix} & \begin{matrix} 2 \\ -\frac{2}{3} \end{matrix}
 \end{array} , \tag{1.21}$$

The fermion Lagrangian can be written as

$$\begin{aligned}
 \mathcal{L}_{\text{fermions}} &= \bar{\mathbf{R}} i\gamma^\mu \left(\partial_\mu + i\frac{g'}{2} \mathcal{A}_\mu Y \right) \mathbf{R} \\
 &+ \bar{\mathbf{L}} i\gamma^\mu \left(\partial_\mu + i\frac{g'}{2} \mathcal{A}_\mu Y + i\frac{g}{2} \vec{\tau} \cdot \vec{b}_\mu \right) \mathbf{L}.
 \end{aligned} \tag{1.22}$$

The $SU(2)_L \times U(1)_Y$ gauge symmetry forbids a mass term for the fermions. Moreover, the theory we have described contains four massless electroweak gauge bosons, namely B_μ , W_μ^1 , W_μ^2 , and W_μ^3 , whereas nature has but one: the photon. To give masses to the gauge bosons and constituent fermions, we must hide the electroweak symmetry. The Higgs mechanism can give masses to the gauge bosons and fermions through the spontaneous breakdown of the gauge symmetry. Since nature has one massless photon, the following breaking pattern

is taken

$$SU(2)_L \times U(1)_Y \rightarrow U(1)_{\text{em}}. \quad (1.23)$$

To fulfill this symmetry breaking, we introduce a complex doublet of scalar fields

$$\phi \equiv \begin{pmatrix} \phi^+ \\ \phi^0 \end{pmatrix} \quad (1.24)$$

with weak hyper-charge $Y_\phi = +1$. The gauge-invariant Lagrangian for the interaction and propagation of the scalars is given by,

$$\mathcal{L}_{\text{scalar}} = (\mathcal{D}^\mu \phi)^\dagger (\mathcal{D}_\mu \phi) - V(\phi^\dagger \phi), \quad (1.25)$$

where the gauge-covariant derivative is

$$\mathcal{D}_\mu = \partial_\mu + i\frac{g}{2}\vec{\tau} \cdot \mathcal{A}_\mu + i\frac{g'}{2}B_\mu, \quad (1.26)$$

and the potential interaction has the form

$$V(\phi^\dagger \phi) = \mu^2(\phi^\dagger \phi) + |\lambda|(\phi^\dagger \phi)^2, \quad (1.27)$$

where μ and λ are real constant parameters. To give masses to the fermions, it is necessary to add a Yukawa interaction between the scalar fields and the fermions,

$$\mathcal{L}_{\text{Yukawa}} = - \left[\bar{\mathbf{R}}(Y^\star \phi^\dagger \mathbf{L}) + (\bar{\mathbf{L}} Y \phi) \mathbf{R} \right], \quad (1.28)$$

where Y are called Yukawa coupling matrices, and cannot be predicted within the model.

To summarize the above, the full Lagrangian in the electroweak standard model can be given by

$$\begin{aligned} \mathcal{L} = & -\frac{1}{4}\mathbf{F}_{\mu\nu}^a\mathbf{F}^{a\mu\nu} + i\bar{\psi}\not{D}\psi + h.c. \\ & + \bar{\psi}_i y_{ij} \psi_j \phi + h.c. + |D_\mu\phi|^2 - V(\phi) , \end{aligned}$$

where we have summed over the different fermions and gauge bosons. However, the above simple Lagrangian does not contain the information on the quantum numbers of the gauge bosons, fermions and scalars. The Moose notation [5] is introduced to summarize the SM Lagrangian with full information diagrammatically. In Fig. 1.1, we plot the Moose diagram for the standard model. Each circle represents a gauge group, and the links between circles are the Higgs doublet which is charged under two symmetry groups. The dashed lines emerging downward and upward from the circles represent the left-handed and right-handed leptons, respectively, and the solid lines emerging downward and the upward represent the left-handed and right-handed quarks, respectively. The diagonal dashed green lines represent the Yukawa couplings through the Higgs doublet.

The electroweak symmetry is spontaneously broken if the parameter $\mu^2 < 0$. The minimum energy, or vacuum state, may then be chosen to correspond to the vacuum expectation value

$$\langle\phi\rangle = \begin{pmatrix} 0 \\ v/\sqrt{2} \end{pmatrix}, \tag{1.29}$$

where $v = \sqrt{-\mu^2/|\lambda|}$. In the unitary gauge, the Lagrangian for the scalars and gauge boson

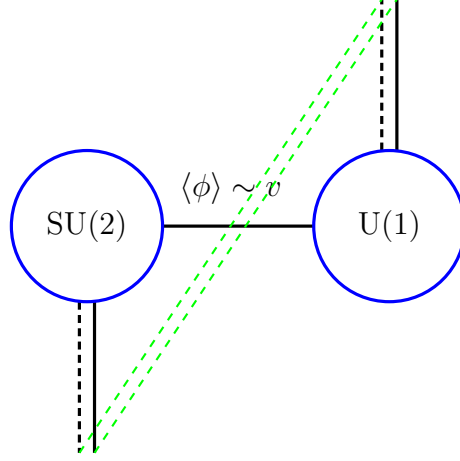


Figure 1.1: The Moose diagram for the standard model. For interpretation of the references to color in this and all other figures, the reader is referred to the electronic version of this thesis.

masses becomes,

$$\begin{aligned}
\mathcal{L}_{\text{scalar}} &= \frac{1}{2} \partial_\mu H \partial^\mu H - \frac{1}{2} M_H^2 H^2 - \lambda v H^3 - \frac{\lambda}{4} H^4 \\
&+ \frac{g^2}{8} (H^2 + 2Hv) \left[\frac{1}{\cos^2 \theta_W} Z_\mu Z^\mu + 2W_\mu^+ W^{-\mu} \right] \\
&+ M_W^2 W_\mu^+ W^{-\mu} + \frac{1}{2} M_Z^2 Z_\mu Z^\mu,
\end{aligned} \tag{1.30}$$

where the new gauge bosons Z and A are admixtures of the gauge bosons W^3 and B as follows

$$Z = \cos \theta_W W^3 - \sin \theta_W B, \tag{1.31}$$

$$A = \cos \theta_W B + \sin \theta_W W^3, \tag{1.32}$$

and the masses of the W -boson and Z -boson are

$$M_W^2 = \frac{v^2}{4} \frac{e^2}{\sin^2 \theta_W}, \quad (1.33)$$

$$M_Z^2 = \frac{v^2}{4} \frac{e^2}{\sin^2 \theta_W \cos^2 \theta_W}. \quad (1.34)$$

With the wave-function mixing, the charged current and neutral current are

$$\mathcal{L}_{\text{CC}} = \frac{g}{\sqrt{2}}(J_\mu^- W^{-\mu} + J_\mu^+ W^{+\mu}), \quad (1.35)$$

$$\begin{aligned} \mathcal{L}_{\text{NC}} &= g J_\mu^3 W^{3\mu} + g' \frac{J_\mu^Y}{2} B^\mu \\ &= (g \sin \theta_W J_\mu^3 + g' \cos \theta_W \frac{J_\mu^Y}{2}) A^\mu \\ &+ (g \cos \theta_W J_\mu^3 - g' \sin \theta_W \frac{J_\mu^Y}{2}) Z^\mu, \end{aligned} \quad (1.36)$$

where the currents are

$$J_\mu^a = \bar{L} \gamma_\mu \frac{\tau^a}{2} L, \quad (1.37)$$

$$J_\mu^Y = \bar{L} \gamma_\mu Y L + \bar{R} \gamma_\mu Y R. \quad (1.38)$$

In the standard model, the unitarity violation is recovered even at high energy scales. Consider the charged gauge boson scattering process $W_L^+ W_L^- \rightarrow W_L^+ W_L^-$ [6], in which the Feynman diagrams are the t - and s -channels of γ and Z exchanges, the 4-point vertex, and the s - and t -channels of Higgs exchanges. At high energies, the longitudinal polarization of the W boson can be expressed as $\epsilon_L^\mu(p) = p^\mu/m_W + v^\mu(p)$, which is used in the equivalent theorem [7]. Because the longitudinal polarization of the charged gauge boson dominates in

the scattering process, the high energy behavior of individual Feynman diagram grows with the center of mass energy squared s like

$$\mathcal{M}(s, t) = A \left(\frac{\sqrt{s}}{M_W} \right)^4 + B \left(\frac{\sqrt{s}}{M_W} \right)^2 + C, \quad (1.39)$$

where the coefficients A , B and C are functions of the polar angle θ in the CMS frame and the coupling constant g . On summing over diagrams except the Higgs exchange, the coefficient A cancels, but B has contributions

$$B = -\frac{g^2}{8M_W^2} (1 + \cos\theta). \quad (1.40)$$

Including in the Higgs contribution, there is full cancellation of the B term. Thus, the bad energy-growing term is delicately canceled between the gauge diagrams and the Higgs diagrams. On summing over all diagrams, the final result is

$$\mathcal{M}(s, t) = -\frac{g^2 M_H^2}{4M_W^2} \left[\frac{s}{s - M_H^2} + \frac{t}{t - M_H^2} \right]. \quad (1.41)$$

Performing the partial wave analysis, we obtain that the dominate S-wave amplitude is

$$\begin{aligned} |a_0|^2 &= \frac{1}{64\pi} \int_{-1}^1 d\cos\theta \mathcal{M} \left(W_L^+ W_L^+ \rightarrow W_L^+ W_L^+ \right) \\ &= -\frac{G_F M_H^2}{8\sqrt{2}\pi} \left[2 + \frac{M_H^2}{s - M_H^2} - \frac{M_H^2}{s} \ln\left(1 + \frac{s}{M_H^2}\right) \right]. \end{aligned} \quad (1.42)$$

If the Higgs mass is smaller than $\frac{4\sqrt{2}\pi}{G_F} \simeq 1$ TeV, the unitarity violation is avoided. However, if the Higgs couplings to the charged gauge boson deviate from the standard model couplings

to a fraction $\sqrt{\delta}$ of the SM value, the unitarity cancellation is only partial. In the high energy limit, the total amplitude becomes

$$i\mathcal{M}^{\text{gauge}} + i\mathcal{M}^{\text{Higgs}} \simeq i \frac{g^2}{4m_W^2} (u+t) (1-\delta). \quad (1.43)$$

One can then obtain [10] the cross section of WW scattering as a function of δ , as shown in Fig.1.2.

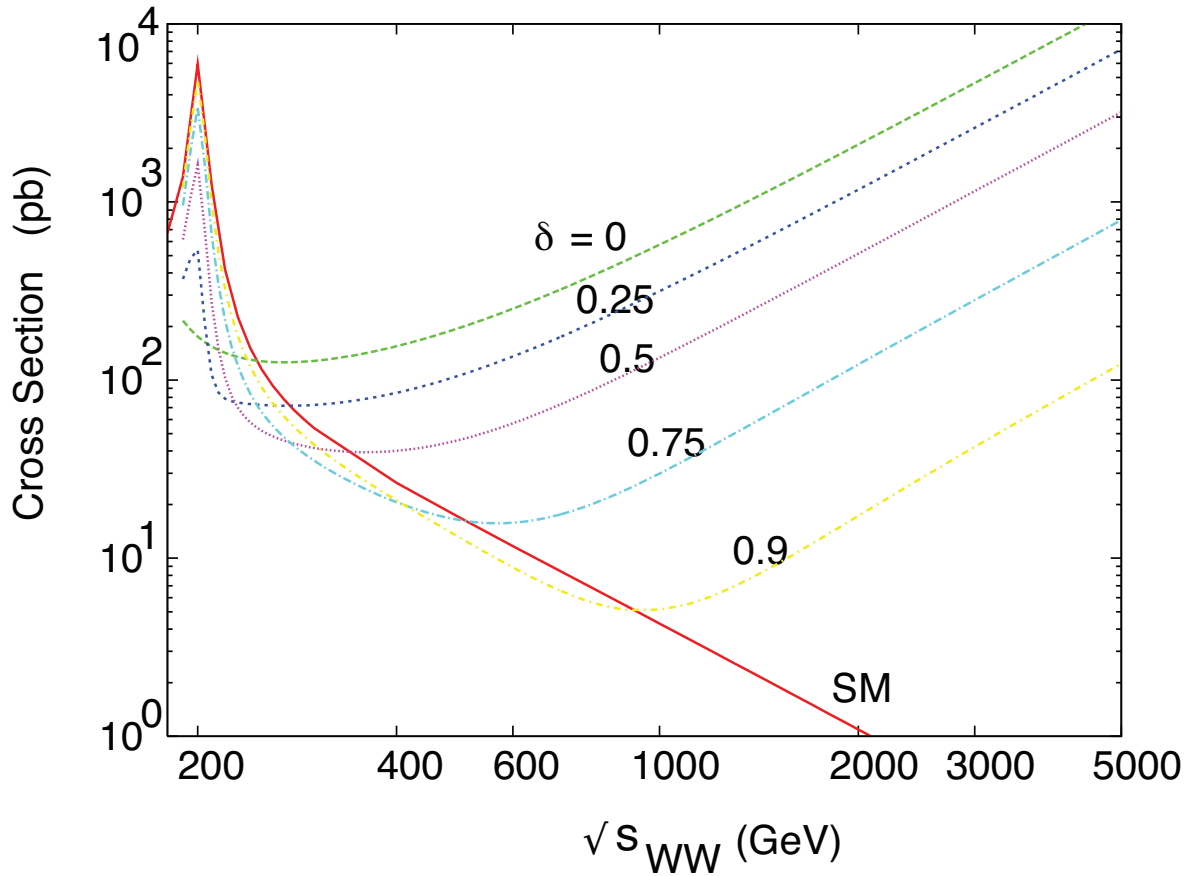


Figure 1.2: Scattering cross sections for $W_L^+ W_L^- \rightarrow W_L^+ W_L^-$ versus $\sqrt{s_{WW}}$. Various values of δ are shown, where δ denotes the size of the Higgs amplitude relative to the SM one. An angular cut of $|\cos\theta_{WW}| < 0.8$ is applied and the light Higgs boson mass $m_h = 200$ GeV is assumed. Figure taken from [10].

1.2 New Physics and Heavy Charged Gauge Bosons

1.2.1 Motivation for New Physics

With the start of the CERN Large Hadron Collider (LHC), a new era of discovery has just begun. It will revolutionize particle physics by opening the TeV energy region to direct experimental exploration. One of the primary motivations for LHC experiments is searching for the Higgs boson, and understanding its role in the origin of electroweak symmetry breaking. Recently, the ATLAS and CMS Collaborations have reported their updated searches for the SM Higgs boson: they find a local 3σ level excess in $\gamma\gamma$ final states at 125 GeV, and a small excess in ZZ final states.

Although the 3σ evidence of a 125 GeV Higgs boson indicates another success of the SM, it also guides us towards the physics beyond the standard model. If it is a non-SM Higgs boson, which means the Higgs couplings to gauge bosons deviate from the SM value, we showed that unitarity violation will happen in the WW scattering process at some high energy scale. New particles are needed to remedy this problem. On the other hand, if it is the SM Higgs, there are still some theoretic issues in the SM: the hierarchy problem and vacuum stability.

Let us consider the hierarchy problem first, following ref. [4]. Beyond the classical approximation, gauge boson, fermion and scalar mass parameters receive quantum corrections from loops that contain particles of spins $J = 0, \frac{1}{2},$ and 1. Because of gauge symmetry and chiral symmetry, the loop corrections of the gauge boson and fermion mass parameters are proportional to $\ln\Lambda$, where Λ defines a reference scale where the SM is still valid. However, there is no symmetry to protect the Higgs mass parameters in the loop calculation.

Symbolically we write down the loop corrections to the Higgs mass parameters

$$M_H^2(p^2) = M_H^2(\Lambda^2) + \text{[dashed loop]} + \text{[fermion loop]} + \text{[wavy loop]},$$

where the dashed lines represent the Higgs boson, solid lines represent fermions and anti-fermions, and wavy lines represent gauge bosons. The quantum corrections can be written, with the divergence Λ included, as follows,

$$\begin{aligned} M_H^2 &= M_H^2(\Lambda^2) + \mathcal{C}g^2 \int_0^{\Lambda^2} dk^2 + \dots \\ &= M_H^2(\Lambda^2) + \frac{G_F \Lambda^2}{4\pi^2 \sqrt{2}} (6M_W^2 + 3M_Z^2 + M_H^2 - 12m_t^2), \end{aligned} \quad (1.44)$$

where \mathcal{C} is a finite coefficient. The loop integrals are quadratically divergent, $\propto \Lambda^2$. In the absence of new physics, a natural reference scale Λ is the Planck mass, $\Lambda \sim M_{\text{Planck}} = (\hbar c/G_{\text{Newton}})^{1/2} \approx 1.2 \times 10^{19}$ GeV. The challenge of preserving a modest value of the Higgs mass M_H^2 at about the electroweak scale through the fine-tuning cancellation between the huge loop corrections and $M_H^2(\Lambda^2)$ is known as the hierarchy problem. Some new physics, a new symmetry or new dynamics, should reduce the loop correction from the quadratic divergence to a reasonable value.

Another inconsistency comes from the vacuum stability [8]. Shown in Fig. 1.3, for a light Higgs with about 125 GeV mass, there is a band below which the present electroweak vacuum becomes unstable against decay into a vacuum with $\langle |\phi| \rangle \sim 10^{10}$ GeV. This instability is due to the negative renormalization of λ by the top quark, which overcomes the positive renormalization due to λ itself, and drives $\lambda < 0$. One could avoid this vacuum instability by introducing some new physics at an energy scale $< \Lambda$ to overcome the negative effects of

renormalization of λ .

Although there are several existing theoretical problems with the SM, the experimental measurements at the LEP, Tevatron and LHC are very consistent with the SM. Since there are no obvious hints of new physics beyond SM, many possible theories of new physics have been proposed to solve the hierarchy problem and to explain the electroweak symmetry breaking mechanism, such as supersymmetry, extra dimensions, strong dynamics, and so on.

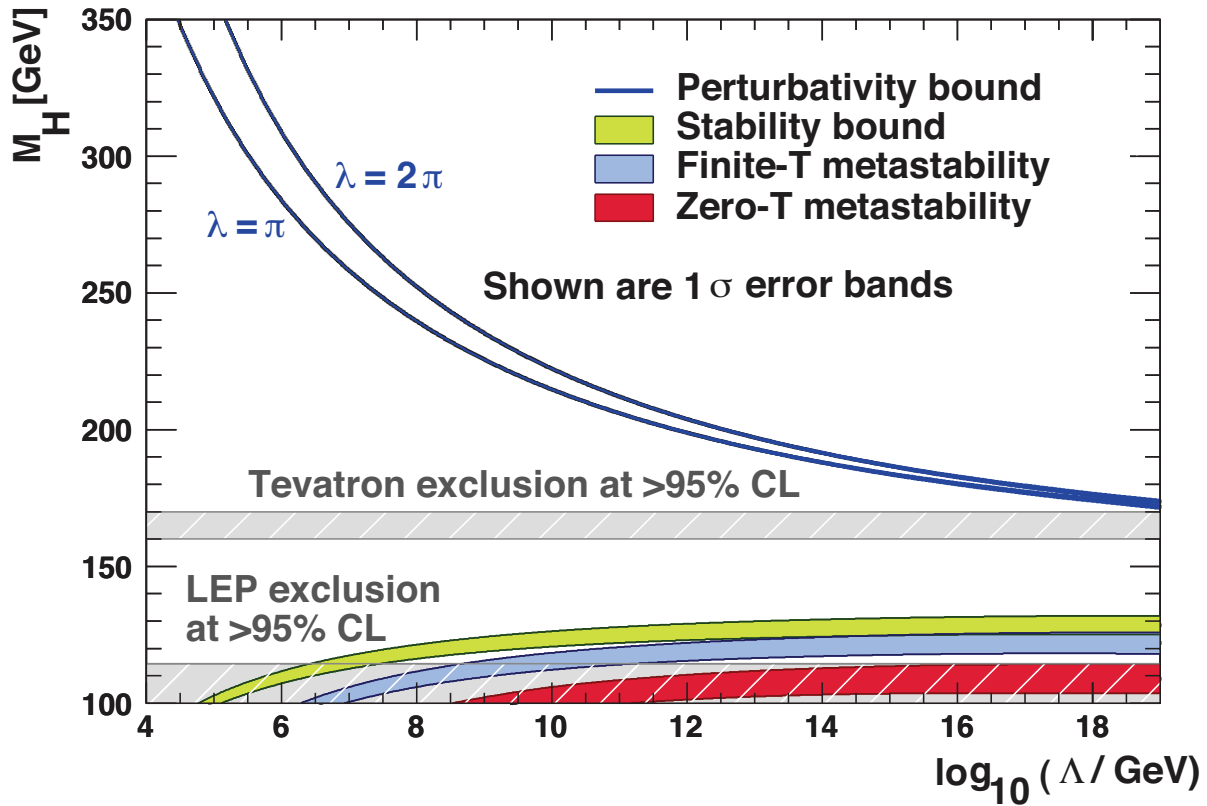


Figure 1.3: The scale Λ at which the two-loop RGEs drive the quartic SM Higgs coupling non-perturbative (upper curves), and the scale Λ at which the RGEs create an instability in the electroweak vacuum (lower curves). Figure taken from [9].

1.2.2 Phenomenology of New Charged Gauge Bosons

There are two approaches to the theoretical exploration of new physics: top-down model building and bottom-up effective theory. The effective theory approach offers us a way to explore the unknown physics before it is finally formulated. Like the intermediate gauge boson model of the weak interactions, we would like to study phenomenology of new particles, such as new gauge bosons, new fermions, new scalars, and the graviton, in the framework of an effective field theory.

As remnants of electroweak symmetry breaking, extra gauge bosons exist in many new physics (NP) models beyond the standard model of particle physics. Importantly, their discovery would help to elucidate the nature of the spontaneous symmetry breaking at the weak scale. According to their electromagnetic charges, extra gauge bosons are usually separated into two categories: charged gauge bosons W' and neutral gauge bosons Z' . While a Z' boson could originate from an additional abelian $U(1)$ group, the W' bosons are often associated with an extra non-abelian group.

Such new heavy gauge bosons arise in numerous gauge extensions of the standard model of particle interactions. The simplest gauge extension involves an additional $U(1)_X$ gauge symmetry (and thus an extra gauge boson Z'). One of the next-simplest extensions is the model with a $SU(2)_1 \times SU(2)_2 \times U(1)_X$ gauge group, obtained by adding an additional $SU(2)$ group to the SM. The left-right model [11, 12, 13] is perhaps the most widely-studied example of such a model. Motivated from the unification of gauge couplings, grand unified models are proposed by extending the gauge symmetry to the $SU(5)$ or $SO(10)$ group [14]. However, the above extensions of the gauge symmetry can not solve the hierarchy problem. To resolve the hierarchy problem, new symmetries or new dynamics are needed in addition

to the extended gauge groups. An example of a class of extended gauge models with new global symmetries is the little Higgs scenario[15][16][17], in which the Higgs is a pseudo-Goldstone boson. Another scenario is the extra-dimensional models with Kaluza-Klein W' bosons [18], such as Higgsless models [19][20], and Gauge-Higgs models [21][22]. However, we will not address the hierarchy problem in the extended gauge models, but only focus on the phenomenological consequences of the heavy charged gauge bosons.

In this thesis, we focus on the collider phenomenology of heavy charged gauge bosons. The minimal extension of the standard model, which consists of heavy charge gauge bosons, exhibits a gauge structure of $SU(2) \times SU(2) \times U(1)$, named the $G(221)$ in ref. [24]. Searches for the heavy charged gauge bosons in the lepton final states, may yield one of the cleanest and most important signals of new physics that can be discovered in the early data from the LHC. On the other hand, investigating these new gauge bosons in the top quark final states, and determining their quantum numbers would shed light on the gauge structure of new physics.

This thesis is organized as follows. Chapter 2 introduces the $G(221)$ models within the framework of an effective field theory with the gauge symmetries $SU(2)_1 \times SU(2)_2 \times U(1)_X$ models. We discuss the Lagrangians, the particle spectrum, and the experimental observables in these $G(221)$ models. The combined constraints from the electroweak precision data, and direct searches at the Tevatron and LHC are discussed.

Chapter 3 presents the Drell-Yan production of the heavy charged gauge bosons in $G(221)$ models and its decay channels. We perform the next-to-leading order calculation of the Drell-Yan production of the heavy gauge bosons. Then we analyze the signal and backgrounds in the lepton plus missing transverse energy final states at the LHC. We show how to calculate

the upper limits using Bayesian statistics. Finally, we discuss the discovery reach of the heavy gauge bosons at the LHC.

Chapter 4 describes the study of the heavy charged gauge bosons in the top quark final states. A Monte-Carlo simulation is performed on the signal and backgrounds. We show that it is possible to probe the chiral structure of the charged gauge bosons using the top quark polarization. We also investigate the possible origin of the forward-backward asymmetry in the top pair final states in the flavor-violating W' model.

Chapter 5 discusses the discovery and identification of a possible exotic W' , in which W' only couples to the third generation quarks, in the top pair plus bottom jet final states. We also study the chiral structure of the W' -bosons using the final state lepton angular distribution of the top quark.

In appendix A, we list the complete sets of Feynman rules of the $G(221)$ models. In appendix B, we discuss the statistics for the upper limit and significance in the Bayesian and frequentist approaches.

Chapter 2

MODELS OF HEAVY CHARGED GAUGE BOSONS

2.1 Introduction

Although the Standard Model has tremendous success in describing a wide range of physical phenomena, there are still open questions that are unanswered and motivate further model-building. Since the electroweak gauge group $SU(2)_L \times U(1)_Y$ is the cornerstone of this model, one of the most common model-building tools is to extend the gauge structure of the Standard Model. The simplest extension involves an additional $U(1)_X$ gauge symmetry (and thus an extra gauge boson Z'). One of the next-simplest extensions is the model with $SU(2)_1 \times SU(2)_2 \times U(1)_X$ gauge group by adding an additional $SU(2)$ group. The left-right model [11, 12, 13] is perhaps the most widely-studied case of such models. On the other hand, given the extended gauge group $SU(2)_1 \times SU(2)_2 \times U(1)_X$ in the electroweak sector, there are many other kinds of models besides the left-right model which can be constructed, and

which may have very different collider phenomenology. Motivated by the unification of gauge couplings, grand unified models are proposed by extending the gauge symmetry to $SU(5)$ or $SO(10)$ group. To incorporate a global symmetry in which the Higgs is a pseudo-Goldstone boson, there are various Little Higgs models with extended gauge groups. In the case that $SU(2)_1 \times SU(2)_2 \times U(1)_X$ symmetry is the sub-group of the new physics models, one can establish an effective theory with $SU(2)_1 \times SU(2)_2 \times U(1)_X$ symmetry by integrating out the heavy particles in the higher scale.

Based on the effective theory framework, we present a unified, systematic study of many such models, which are commonly called $G(221)$ models in the literature. In this section we briefly review the $G(221)$ model and the masses and couplings of W' and Z' bosons. In particular we consider various $G(221)$ models categorized as follows: left-right (LR) [11, 12, 13], lepto-phobic (LP), hadro-phobic (HP), fermio-phobic (FP) [27, 25, 26], un-unified (UU) [28, 29], and Top-flavor (TF) [31, 30, 32]. We also considered a widely-used reference model in the experimental searches: the sequential W' model (SQ). In the LR model and SQ models, if the gauge couplings are assigned to be the same for the two $SU(2)$ gauge groups, the models are considered as the manifest left-right model (MLR), and manifest sequential model (MSQ). In the MSQ, the W' couplings to fermions are the same as the standard model W couplings to fermions, which served as the reference model in the experimental searches. We focus our attention on the full Lagrangian of the extra gauge bosons in the $G(221)$ model.

2.2 Model Classification by Moose Diagrams

We focus on the so-called $G(221)$ models having a $SU(2)_1 \times SU(2)_2 \times U(1)_X$ gauge structure that ultimately breaks to $U(1)_{\text{em}}$. Relative to the Standard Model, these models have three additional massive gauge bosons, and their phenomenology depends on the specific patterns of symmetry breaking as well as the charge assignments of the SM fermions.

The $SU(2)_1 \times SU(2)_2 \times U(1)_X$ gauge symmetry can be broken through mass mixing or/and kinetic mixing of the gauge bosons. In this note, we would like to discuss the models with mass mixing only, which can be categorized by three patterns of symmetry breaking:

- Breaking pattern I (BP-I):

We identify $SU(2)_1$ as $SU(2)_L$ of the SM. The first stage of symmetry breaking then is $SU(2)_2 \times U(1)_X \rightarrow U(1)_Y$, giving rise to three heavy gauge bosons W'^{\pm} and Z' at the TeV-scale. The second stage is $SU(2)_L \times U(1)_Y \rightarrow U(1)_{\text{em}}$ at the electroweak scale.

- Breaking pattern II (BP-II):

We identify $U(1)_X$ as $U(1)_Y$ of the SM. The first stage of symmetry breaking is $SU(2)_1 \times SU(2)_2 \rightarrow SU(2)_L$. The second stage is $SU(2)_L \times U(1)_Y \rightarrow U(1)_{\text{em}}$ at the electroweak scale.

- Breaking pattern III (BP-III):

We assume there is a hidden $SU(2)$ gauge symmetry, which comes from dynamical symmetry breaking sector. There is only one stage of symmetry breaking $SU(2)_L \times SU(2)_{\text{hidden}} \times U(1)_Y \rightarrow U(1)_{\text{em}}$ at the electroweak scale.

The symmetry breaking is assumed to be induced by fundamental scalar fields, except in the

breaking pattern III, in which the model has no Higgs, called the Higgs-less model [27]. The quantum number of the scalar fields under the $G(221)$ gauge group depends on the breaking pattern. It is possible to choose several kinds of Higgs multiplets in first or second breaking stages, as shown in Table 2.1. In the BPI, the symmetry breaking of $SU(2)_2 \otimes U(1)_X \rightarrow U(1)_Y$ at the TeV scale could be induced by a scalar doublet field $\Phi \sim (1, 2)_{1/2}$, or a triplet scalar field $(1, 3)_1$ with a vacuum expectation value (VEV) u , and the subsequent symmetry breaking of $SU(2)_1 \otimes U(1)_Y \rightarrow U(1)_Q$ at the electroweak scale could be via another scalar field $H \sim (2, \bar{2})_0$ with two VEVs v_1 and v_2 , which can be redefined as a VEV $v = \sqrt{v_1^2 + v_2^2}$ and a mixing angle $\beta = \arctan(v_1/v_2)$. In the BPII, the symmetry breaking of $SU(2)_1 \otimes SU(2)_2 \rightarrow SU(2)_L$ at the TeV scale is owing to a Higgs bi-doublet $\Phi \sim (2, \bar{2})_0$ with only one VEV u , and the subsequent breaking of $SU(2)_L \otimes U(1)_Y \rightarrow U(1)_Q$ at the electroweak scale is generated by a Higgs doublet $H \sim (1, 2)_{1/2}$ with the VEV v . Since the precision data constraints (including those from CERN LEP and SLAC SLC experimental data) pushed the TeV symmetry breaking higher than 1 TeV, we shall approximate the predictions of physical observables by taking a Taylor expansion in $1/x$ with $x = u^2/v^2$. We will only focus on models with physical Higgs multiplet. Thus, the Higgsless model is not discussed.

The $G(221)$ models can be further classified based on the charge assignments of the SM fermions. In the breaking patterns I and II, the SM fermions can be assigned to be the electroweak doublets under $SU(2)_1$ and/or $SU(2)_2$ symmetry, such as the left-right model (LR) in BP-I and the sequential model (SQ) in BP-II. If the SM fermions with different flavors or generations belong to doublets in different $SU(2)$ gauge symmetries, it is called a flavor or generation non-universal model, such as the lepto-phobic (LP), hadro-phobic (HP),

and fermio-phobic (FP) model in BP-I, and the top-flavor (TF), and un-unified (UU) model. We display the moose diagrams for BP-I models and BP-II models, in Figs. 2.1 and 2.2. In Figs. 2.1 and 2.2 Each circle represents a gauge group, and the links between circles are the Higgs multiplets which is charged under two symmetry groups. The dashed lines emerging downward and upward from the circles represent the left-handed and right-handed leptons, respectively, and the solid lines emerging downward and the upward represent the left-handed and right-handed quarks, respectively. The diagonal dashed green lines represent the Yukawa couplings through the Higgs doublet. For LP, remove the dashed line in the middle $SU(2)$, and attach to $U(1)$. For HP, remove the black line in the middle $SU(2)$, and attach to $U(1)$. For FP, remove both the black line and dashed line in the middle $SU(2)$, and attach to $U(1)$. In Table 2.2, we list the possible assignments for Ψ_L and Ψ_R .

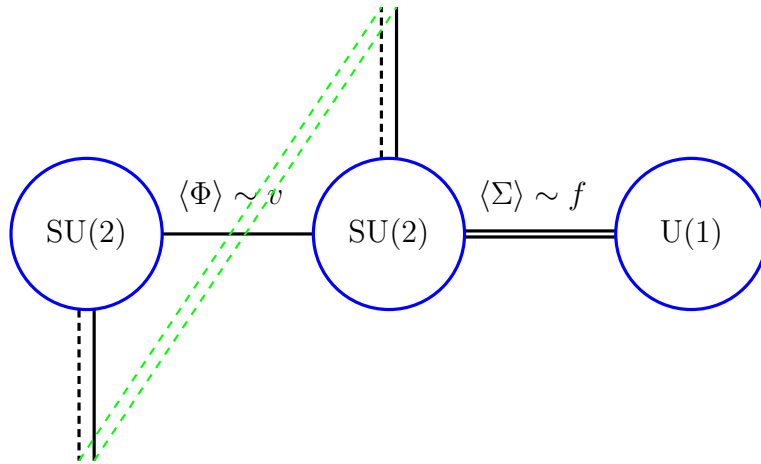


Figure 2.1: The Moose diagram for the breaking pattern I (Left-Right Model).

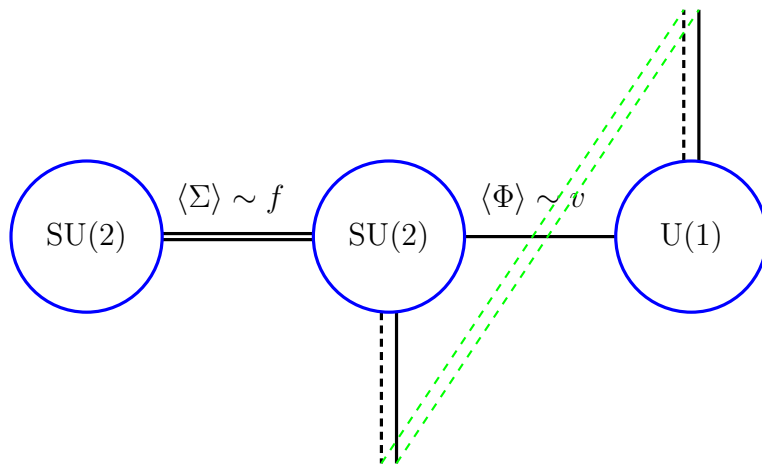


Figure 2.2: The Moose diagram for the breaking pattern II (Sequential Model).

First stage breaking		
	Rep.	Multiplet and VEV
LR-D, LP-D HP-D, FP-D	$\Sigma \sim (1, 2, \frac{1}{2})$	$\Sigma = \begin{pmatrix} \phi^+ \\ \phi^0 \end{pmatrix}, \langle \Sigma \rangle = \frac{1}{\sqrt{2}} \begin{pmatrix} 0 \\ u_D \end{pmatrix}$
LR-T, LP-T HP-T, FP-T	$\Sigma \sim (1, 3, 1)$	$\Sigma = \frac{1}{\sqrt{2}} \begin{pmatrix} \delta^+ & \sqrt{2}\delta^{++} \\ \sqrt{2}\delta^0 & -\delta^+ \end{pmatrix}, \langle \Sigma \rangle = \frac{1}{\sqrt{2}} \begin{pmatrix} 0 & 0 \\ u_T & 0 \end{pmatrix}$
SQ, TF, UU	$\Sigma \sim (2, \bar{2}, 0)$	$\Sigma = \begin{pmatrix} \sigma^0 + \pi^0 & \sqrt{2}\pi^+ \\ \sqrt{2}\pi^- & \sigma^0 - \pi^0 \end{pmatrix}, \langle \Sigma \rangle = \frac{1}{\sqrt{2}} \begin{pmatrix} \tilde{u} & 0 \\ 0 & \tilde{u} \end{pmatrix}$

Second stage breaking		
	Rep.	Multiplet and VEV
LR-D, LP-D HP-D, FP-D	$\Phi \sim (2, \bar{2}, 0)$	$\Phi = \begin{pmatrix} \phi_1^0 & \phi_1^+ \\ \phi_2^- & \phi_2^0 \end{pmatrix}, \langle \Phi \rangle = \frac{\tilde{v}}{\sqrt{2}} \begin{pmatrix} c_\beta & 0 \\ 0 & s_\beta \end{pmatrix}$
LR-T, LP-T HP-T, FP-T	$\Phi \sim (2, \bar{2}, 0)$	$\Phi = \begin{pmatrix} \phi_1^0 & \phi_1^+ \\ \phi_2^- & \phi_2^0 \end{pmatrix}, \langle \Phi \rangle = \frac{\tilde{v}}{\sqrt{2}} \begin{pmatrix} c_\beta & 0 \\ 0 & s_\beta \end{pmatrix}$
SQ, TF, UU	$\Phi \sim (1, 2, \frac{1}{2})$	$\Phi = \begin{pmatrix} \phi^+ \\ \phi^0 \end{pmatrix}, \langle \Phi \rangle = \frac{\tilde{v}}{\sqrt{2}} \begin{pmatrix} 0 \\ 1 \end{pmatrix}$

Table 2.1: These tables display the model-specific Higgs representations and VEVs that achieve the symmetry breaking of $G(221)$ models.

2.3 $G(221)$ Lagrangian in the Gauge Basis and Physical Basis

2.3.1 Lagrangian in the Gauge Basis

The classical gauge invariant $G(221)$ Lagrangian can be decomposed as

$$\mathcal{L} = \mathcal{L}_{\text{Higgs}} + \mathcal{L}_{\text{Gauge}} + \mathcal{L}_{\text{Fermion}} + \mathcal{L}_{\text{Yukawa}}, \quad (2.1)$$

where the terms on the right hand side are identified as the Higgs scalar part, the gauge boson part, the fermion part and the Yukawa part respectively.

2.3.1.1 The Scalar Sector

The Lagrangian for the scalar fields are written as

$$\mathcal{L}_{\text{Higgs}} = \text{Tr} \left[(D_\mu \Sigma)^\dagger (D^\mu \Sigma) \right] + \text{Tr} \left[(D_\mu \Phi)^\dagger (D^\mu \Phi) \right] - V(\Sigma, \Phi), \quad (2.2)$$

where Σ is the scalar multiplet in the TeV symmetry breaking stage, and Φ is the Higgs multiplet in the electroweak symmetry breaking stage. In the Moose diagram notation, two link fields connect the three gauge groups. One link field with double lines represents Σ in the first stage, while another link field with single line represents Φ in the second stage. The Higgs potential $V(\Sigma, \Phi)$ is introduced to break the TeV and electroweak symmetries.

2.3.1.1.1 Scalar Multiplets in the Breaking Pattern I At the TeV breaking stage, there are two kinds of typical scalar multiplet Σ , doublet and triplet, to generate masses for

heavy gauge bosons W' and Z' . In the doublet case, we assign the Higgs doublet Σ as

$$\Sigma = \begin{pmatrix} \phi^+ \\ \phi^0 \end{pmatrix} \equiv \begin{pmatrix} (\phi_3 + i\phi_4)/\sqrt{2} \\ (\phi_1 + i\phi_2)/\sqrt{2} \end{pmatrix}. \quad (2.3)$$

The covariant derivative in the Eq. 2.2 is defined as follows

$$D_\mu \Sigma = \partial^\mu \Sigma + ig_R W_R^{a\mu} T_R^a \Sigma + ig_X B^\mu X \Sigma. \quad (2.4)$$

To generate the neutrino mass, it is popular to assign a scalar triplet,

$$\Sigma = \begin{pmatrix} \delta_R^+/\sqrt{2} & \delta_R^{++} \\ \delta_R^0 & -\delta_R^+/\sqrt{2} \end{pmatrix}, \quad (2.5)$$

where $\delta = \frac{\delta_r + i\delta_i}{\sqrt{2}}$. The covariant derivative in the Eq. 2.2 is defined as follows

$$D_\mu \Sigma = \partial_\mu \Sigma + ig_R \left[\frac{\vec{\tau}}{2} \vec{W}_{R\mu}, \Sigma \right] + ig_X X B_\mu \Sigma, \quad (2.6)$$

where the quantum number X is 1.

In order to generate the masses for the W and Z bosons and SM fermion at the second breaking stage, one introduces the bi-doublet

$$\Phi = \begin{pmatrix} \phi_1^0 & \phi_1^+ \\ \phi_2^- & \phi_2^0 \end{pmatrix} : (2, 2, 0), \quad (2.7)$$

with

$$\tilde{\Phi} = \tau_2 \Phi^* \tau_2 = \begin{pmatrix} \phi_2^{0*} & -\phi_2^+ \\ -\phi_1^- & \phi_1^{0*} \end{pmatrix} \quad (2.8)$$

where $\phi_i = \frac{1}{\sqrt{2}}(\phi_{ia} + i\phi_{ib})$. The covariant derivative in Eq. 2.2 can be written as

$$D^\mu \Phi = \partial^\mu \Phi + ig_L W_L^{b\mu} T_L^b \Phi - ig_R W_R^{b\mu} \Phi T_R^b. \quad (2.9)$$

2.3.1.1.2 Scalar Multiplets in the Breaking Pattern II To generate masses for the heavy gauge bosons W' and Z' at the TeV symmetry breaking stage, one introduces the Higgs bi-doublet with the quantum number $(2, 2)_0$

$$\Sigma = \sigma + i\frac{\tau}{2} \cdot \pi = \frac{1}{\sqrt{2}} \begin{pmatrix} \frac{\sigma + i\pi^3}{\sqrt{2}} & \frac{\pi^1 + i\pi^2}{\sqrt{2}} \\ -\frac{\pi^1 - i\pi^2}{\sqrt{2}} & \frac{\sigma - i\pi^3}{\sqrt{2}} \end{pmatrix}, \quad (2.10)$$

where the coefficient $\frac{1}{\sqrt{2}}$ comes from the normalization of the kinetic term in Eq. 2.2. The covariant derivative in Eq. 2.2 is defined as follows

$$D^\mu \Sigma = \partial^\mu \Sigma + ig_L W_L^{\mu a} T^a \Sigma - ig_R W_R^{\mu a} \Sigma T^a. \quad (2.11)$$

At the electroweak breaking stage, we use the Higgs doublet

$$\Phi = \begin{pmatrix} \phi^+ \\ \phi^0 \end{pmatrix}. \quad (2.12)$$

The covariant derivative is written as

$$D_\mu \Phi = \partial^\mu \Phi + ig_L W_L^{a\mu} T^a \Phi + ig_X B^\mu X \Phi. \quad (2.13)$$

2.3.1.2 The Gauge Boson Sector

We define W_1^μ , W_2^μ , and B^μ as the $SU(2)_1$, $SU(2)_2$, and $U(1)_X$ gauge fields, respectively.

The Lagrangian of the gauge bosons with $SU(2)_1 \times SU(2)_2 \times U(1)_X$ gauge invariance is given as

$$\mathcal{L} = -\frac{1}{4} W_1^{a\mu\nu} W_{1\mu\nu}^a - \frac{1}{4} W_2^{a\mu\nu} W_{2\mu\nu}^a - \frac{1}{4} B^{\mu\nu} B_{\mu\nu}, \quad (2.14)$$

where

$$W_1^{a\mu\nu} = \partial^\mu W_1^\nu - \partial^\nu W_1^\mu + f^{abc} g_1 (W_1^{b\mu} W_1^{c\nu} - W_1^{c\mu} W_1^{b\nu}), \quad (2.15)$$

$$W_2^{a\mu\nu} = \partial^\mu W_2^\nu - \partial^\nu W_2^\mu + f^{abc} g_2 (W_2^{b\mu} W_2^{c\nu} - W_2^{c\mu} W_2^{b\nu}), \quad (2.16)$$

$$B^{\mu\nu} = \partial^\mu B^\nu - \partial^\nu B^\mu. \quad (2.17)$$

Notice that the gauge bosons are still massless at this stage to ensure a gauge invariant Lagrangian.

2.3.1.3 The Fermion Sector

The generic fermion terms can be written as

$$\mathcal{L} = \sum_{\Psi_L} \bar{\Psi}_L i\gamma^\mu D_\mu \Psi_L + \sum_{\psi_R} \bar{\psi}_R i\gamma^\mu D_\mu \psi_R. \quad (2.18)$$

In Table 2.2, we list the possible assignments for Ψ_L and Ψ_R .

In the breaking pattern I, the covariant derivatives are

$$D_\mu \Psi_L = \left(\partial_\mu + ig_1 T_L^a W_{1\mu}^a + ig_X X B_\mu \right) \Psi_L, \quad (2.19)$$

$$D_\mu \psi_R = \left(\partial_\mu + ig_2 T_R^a W_{1\mu}^a + ig_X X B_\mu \right) \psi_R. \quad (2.20)$$

where Ψ_L can be

$$Q_L = \begin{pmatrix} u \\ d \end{pmatrix}_L \sim (2, 1)_{\frac{1}{6}}, \quad L_L = \begin{pmatrix} \nu \\ e \end{pmatrix}_L \sim (2, 1)_{-\frac{1}{2}}; \quad (2.21)$$

and ψ_R are different in different models in breaking pattern I. If the ψ_R is the right-handed doublet Q_R , or L_R , one will obtain

$$Q_R = \begin{pmatrix} u \\ d \end{pmatrix}_R \sim (1, 2)_{\frac{1}{6}}, \quad L_R = \begin{pmatrix} \nu \\ e \end{pmatrix}_R \sim (1, 2)_{-\frac{1}{2}}. \quad (2.22)$$

One the other hand, if ψ_R is the right-handed singlet, the possible ψ_R would be

$$u_R \sim (1, 1)_{\frac{2}{3}}, \quad d_R \sim (1, 1)_{-\frac{1}{3}}, \quad e_R \sim (1, 1)_{-\frac{1}{2}}, \quad \nu_R \sim (1, 1)_0. \quad (2.23)$$

In the breaking pattern II, the covariant derivatives are

$$D_\mu \Psi_L = \left(\partial_\mu + ig_1 T_l^a W_{1\mu}^a + ig_2 T_h^a W_{2\mu}^a + ig_X X B_\mu \right) \Psi_L, \quad (2.24)$$

$$D_\mu \psi_R = \left(\partial_\mu + ig_X X B_\mu \right) \psi_R. \quad (2.25)$$

Models	$SU(2)_1 (T_L, T_l)$	$SU(2)_2 (T_R, T_h)$	$U(1)_X (X, Y)$
LRD LRT	$\begin{pmatrix} u_L \\ d_L \end{pmatrix}, \begin{pmatrix} \nu_L \\ e_L \end{pmatrix}$	$\begin{pmatrix} u_R \\ d_R \end{pmatrix}, \begin{pmatrix} \nu_R \\ e_R \end{pmatrix}$	$X_q = 1/6$ $X_l = -1/2$
LPD LPT	$\begin{pmatrix} u_L \\ d_L \end{pmatrix}, \begin{pmatrix} \nu_L \\ e_L \end{pmatrix}$	$\begin{pmatrix} u_R \\ d_R \end{pmatrix}$	$X_q = 1/6$ $X_l = Y_{\text{SM}}$
HPD HPT	$\begin{pmatrix} u_L \\ d_L \end{pmatrix}, \begin{pmatrix} \nu_L \\ e_L \end{pmatrix}$	$\begin{pmatrix} \nu_R \\ e_R \end{pmatrix}$	$X_q = Y_{\text{SM}}$ $X_l = -1/2$
FPD FPT	$\begin{pmatrix} u_L \\ d_L \end{pmatrix}, \begin{pmatrix} \nu_L \\ e_L \end{pmatrix}$		$X_f = Y_{\text{SM}}$
SQD	$\begin{pmatrix} u_L \\ d_L \end{pmatrix}, \begin{pmatrix} \nu_L \\ e_L \end{pmatrix}$		$X_f = Y_{\text{SM}}$
TFD	$\begin{pmatrix} u_L \\ d_L \end{pmatrix}_{1st,2nd}, \begin{pmatrix} \nu_L \\ e_L \end{pmatrix}_{1st,2nd}$	$\begin{pmatrix} u_L \\ d_L \end{pmatrix}_{3rd}, \begin{pmatrix} \nu_L \\ e_L \end{pmatrix}_{3rd}$	$X_f = Y_{\text{SM}}$
UUD	$\begin{pmatrix} u_L \\ d_L \end{pmatrix}$	$\begin{pmatrix} \nu_L \\ e_L \end{pmatrix}$	$X_f = Y_{\text{SM}}$

Table 2.2: Assignment of SM fermions under the $G(221)$ symmetry: $(T_L, T_R)_X$ in breaking pattern I while $(T_l, T_h)_Y$ in breaking pattern II. Unless otherwise specified, the fermion doublet represents three generations of SM fermions. LRD (LRT) denotes the left-right doublet (triplet) model, where the $G(221)$ model is broken by a scalar doublet (triplet). Similarly, LPD (LPT) denotes the lepto-phobic doublet (triplet) model, HPD (HPT) the hadro-phobic doublet (triplet) model, FPD (FPT) the fermio-phobic doublet (triplet) model, SQD the sequential doublet model, TFD the top-flavor doublet model, and UUD the un-unified doublet model.

where Ψ_L can be

$$Q_L = \begin{pmatrix} u \\ d \end{pmatrix}_L \sim (2, 1)_{\frac{1}{6}}, \quad L_L = \begin{pmatrix} \nu \\ e \end{pmatrix}_L \sim (2, 1)_{-\frac{1}{2}}; \quad (2.26)$$

and ψ_R are the right-handed singlets, given by

$$u_R \sim (1, 1)_{\frac{2}{3}}, \quad d_R \sim (1, 1)_{-\frac{1}{3}}, \quad e_R \sim (1, 1)_{-\frac{1}{2}}, \quad \nu_R \sim (1, 1)_0. \quad (2.27)$$

2.3.1.4 The Yukawa Sector

To generate the SM fermion masses, we introduce the Yukawa Lagrangian

$$\mathcal{L} = - \sum_{ij} \bar{L}_{iL} \left(\mathcal{Y}_{ij}^l \Phi + \mathcal{Y}_{ij}^{*l} \tilde{\Phi} \right) L_{jR} - \sum_{ij} \bar{Q}_{iL} \left(\mathcal{Y}_{ij}^q \Phi + \mathcal{Y}_{ij}^{*q} \tilde{\Phi} \right) Q_{jR}, \quad (2.28)$$

where $\tilde{\Phi} = \sigma_2 \Phi^* \sigma_2$ in the breaking pattern I, and $\tilde{\Phi} = \sigma_2 \Phi^*$ in the breaking pattern II.

In the flavor universal models, the dashed lines in the Moose diagrams correspond to the Yukawa terms in above.

Notice that in the breaking pattern I, \mathcal{Y}_{ij}^l and \mathcal{Y}_{ij}^q are defined as the matrix form

$$\mathcal{Y}_{ij}^l = Y_{ij}^l \begin{pmatrix} 1 & 0 \\ 0 & 1 \end{pmatrix}, \quad \mathcal{Y}_{ij}^q = Y_{ij}^q \begin{pmatrix} 1 & 0 \\ 0 & 1 \end{pmatrix}, \quad (2.29)$$

where the Yukawa couplings Y_{ij}^l and Y_{ij}^q are the same for the up- and down-type fermions.

In this case, after symmetry breaking the mass splitting of the up- and down-type fermions comes from the different VEVs of the Φ for the up- and down-type fermions. while in the

breaking pattern II, \mathcal{Y}_{ij}^l and \mathcal{Y}_{ij}^q are defined as the matrix form

$$\mathcal{Y}_{ij}^l = \begin{pmatrix} Y_{ij}^\nu & 0 \\ 0 & Y_{ij}^e \end{pmatrix}, \quad \mathcal{Y}_{ij}^q = \begin{pmatrix} Y_{ij}^u & 0 \\ 0 & Y_{ij}^d \end{pmatrix}, \quad (2.30)$$

where the Yukawa couplings are different for the up- and down-type fermions.

In the flavor non-universal models, such as the LP and HP models in breaking pattern I, and the TF and UU models in breaking pattern II, one Φ field is not enough to give masses to all the SM fermions. There are two simple ways to solve this problem by adding new particle content to the Lagrangian.

Usually, we can add heavy vector-like fermions to generate the SM fermion masses through the see-saw mechanism, as displayed in Figs. 2.3, and 2.4. For example, in the LP model, the Yukawa terms can be re-written as

$$\mathcal{L} = -\sum_{ij} \bar{Q}_{iL} \left(\mathcal{Y}_{ij}^q \Phi + \mathcal{Y}_{ij}^{*q} \tilde{\Phi} \right) Q_{jR} - \sum_{ij} \bar{L}_{iL} \left(\mathcal{Y}_{ij}^l \Phi + \mathcal{Y}_{ij}^{*l} \tilde{\Phi} \right) \mathcal{L}_{jR} \quad (2.31)$$

$$- \sum_{ij} \bar{\mathcal{L}}_{iL} \mathcal{M}_{ij} \mathcal{L}_{jR} - \sum_{ij} \bar{\mathcal{L}}_{iL} \left(\mathcal{Y}_{ij}^l \Sigma + \mathcal{Y}_{ij}^{*l} \tilde{\Sigma} \right) L_{jR}, \quad (2.32)$$

where \mathcal{L} is a vector-like doublet

$$\mathcal{L}_{L,R} = \begin{pmatrix} N \\ E \end{pmatrix}_{L,R}, \quad (2.33)$$

with mass matrix \mathcal{M} and the Yukawa couplings are

$$\mathcal{Y}_{ij}^l = \begin{pmatrix} Y_{ij}^\nu & 0 \\ 0 & Y_{ij}^e \end{pmatrix}, \quad \mathcal{Y}_{ij}^q = Y_{ij}^q \begin{pmatrix} 1 & 0 \\ 0 & 1 \end{pmatrix}. \quad (2.34)$$

Similarly, one can write the Yukawa Lagrangian for UU and TF models in the second breaking pattern. If the vector-like fermions are heavy enough, they will decouple at the low energy scale.

Alternatively, one can add another Higgs multiplet ϕ to generate the SM fermion masses. In this case, the Higgs scalar Lagrangian will be modified, and the mass spectrum of gauge bosons will be affected. In our current study, we don't consider this case in detail.

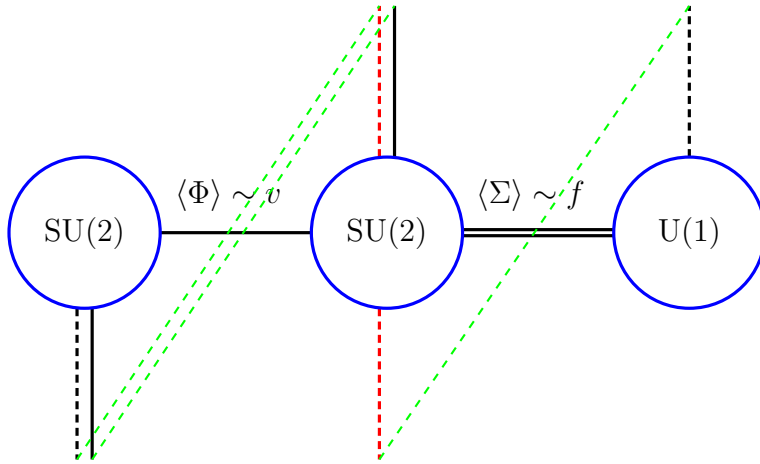


Figure 2.3: The Moose diagram for the breaking pattern I (Lepton-phobic Model with vector-like fermions).

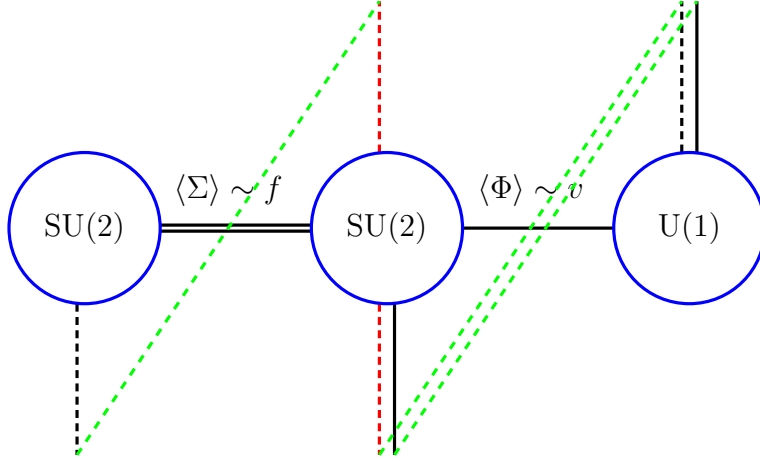


Figure 2.4: The Moose diagram for the breaking pattern II (Top-Flavor model with vector-like fermions).

2.3.2 Symmetry Breaking and Mass Eigenstates

2.3.2.1 Higgs Potential and VEV

In the first breaking pattern, at the scale u , there are two kinds of Higgs multiplets. The Higgs doublet gets the VEV

$$\langle \Sigma \rangle = \begin{pmatrix} 0 \\ u \\ \frac{u}{\sqrt{2}} \end{pmatrix}. \quad (2.35)$$

Another possibility is the Higgs triplet which gets the VEV

$$\langle \Sigma \rangle = \begin{pmatrix} 0 & 0 \\ u & 0 \\ \frac{u}{\sqrt{2}} & 0 \end{pmatrix}. \quad (2.36)$$

At the scale v , the Higgs bi-doublet gets the VEV

$$\langle \Phi \rangle = \begin{pmatrix} \kappa_1/\sqrt{2} & 0 \\ 0 & \kappa_2/\sqrt{2} \end{pmatrix}. \quad (2.37)$$

To relate these VEV parameters κ_1, κ_2 to the conventional parameter v , we define

$$v^2 = \kappa_1^2 + \kappa_2^2, \quad (2.38)$$

$$\tan \beta = \frac{\kappa_2}{\kappa_1}. \quad (2.39)$$

In the breaking pattern II, at the scale u , the Higgs bi-doublet gets the VEV

$$\langle \Sigma \rangle = \frac{1}{2} \begin{pmatrix} u & 0 \\ 0 & u \end{pmatrix}. \quad (2.40)$$

At the scale v , the Higgs doublet gets the VEV

$$\langle \Phi \rangle = \begin{pmatrix} 0 \\ v \\ \frac{v}{\sqrt{2}} \end{pmatrix}. \quad (2.41)$$

The Higgs potential can be decomposed into three parts, V_Φ , V_Σ and $V_{(\Phi, \Sigma)}$. If no CP violation originates from the Higgs potential, all the coefficients in the Higgs potential will be real. In this study, we only consider Φ and Σ as doublet, bi-doublet, or triplet scalars. The general Higgs potential V_Φ and V_Σ are given by

$$V_\Phi = \mathcal{V}(\Phi), \quad V_\Sigma = \mathcal{V}(\Sigma), \quad (2.42)$$

where \mathcal{V} has the form as follows

$$\begin{aligned}
\mathcal{V}(\phi) &= -\mu_1^2 \text{Tr}(\phi^\dagger \phi) - \mu_2^2 \left[\text{Tr}(\tilde{\phi} \phi^\dagger) + \text{Tr}(\tilde{\phi}^\dagger \phi) \right] \\
&+ \lambda_1 \left[\text{Tr}(\phi^\dagger \phi) \right]^2 + \lambda_2 \left\{ \left[\text{Tr}(\tilde{\phi} \phi^\dagger) \right]^2 + \left[\text{Tr}(\tilde{\phi}^\dagger \phi) \right]^2 \right\} \\
&+ \lambda_3 \text{Tr}(\tilde{\phi} \phi^\dagger) \text{Tr}(\tilde{\phi}^\dagger \phi) + \lambda_4 \text{Tr}(\phi^\dagger \phi) \left[\text{Tr}(\tilde{\phi} \phi^\dagger) + \text{Tr}(\tilde{\phi}^\dagger \phi) \right].
\end{aligned} \tag{2.43}$$

If ϕ is a scalar doublet, one can reduce \mathcal{V} by

$$\text{Tr}(\phi^\dagger \phi) = \text{Tr}(\tilde{\phi} \phi^\dagger) = \text{Tr}(\tilde{\phi}^\dagger \phi) \tag{2.44}$$

to obtain

$$\mathcal{V}(\phi) = -\mu^2 \text{Tr}(\phi^\dagger \phi) + \lambda \left[\text{Tr}(\phi^\dagger \phi) \right]^2 \tag{2.45}$$

with $\mu^2 = \mu_1^2 + \mu_2^2$ and $\lambda = \lambda_1 + 2\lambda_2 + \lambda_3 + 2\lambda_4$.

The Higgs potential $V_{(\Phi, \Sigma)}$ has the following typical form

$$\begin{aligned}
\mathcal{V}(\phi, \Delta) &= \alpha_1 \text{Tr}(\phi^\dagger \phi) \text{Tr}(\Delta \Delta^\dagger) + \alpha_2 \left[\text{Tr}(\tilde{\phi}^\dagger \phi) \text{Tr}(\Delta \Delta^\dagger) + \text{Tr}(\tilde{\phi} \phi^\dagger) \text{Tr}(\Delta \Delta^\dagger) \right] \\
&+ \alpha_3 \text{Tr}(\phi^\dagger \phi \Delta \Delta^\dagger).
\end{aligned} \tag{2.46}$$

In the breaking pattern I, the Higgs potential $V_{(\Phi, \Sigma)}$ is defined as

$$V_{(\Phi, \Sigma)} = \mathcal{V}(\Phi, \Sigma). \tag{2.47}$$

While in the breaking pattern II, the Higgs potential $V_{(\Phi, \Sigma)}$ is defined as

$$V_{(\Phi, \Sigma)} = \mathcal{V}(\Sigma, \Phi). \quad (2.48)$$

After spontaneous symmetry breaking, a full analysis of the Higgs mass spectrum can be performed in detail. However, we would like to do a simple analysis focusing on the Higgs potential in which only the Higgs scalar Φ is included, through replacing the scalar Σ with its VEV u in the Higgs potential. The reason is in the following. We know the scalar Σ is mainly giving masses to the W' and Z' bosons, but not giving masses to the SM gauge bosons and fermions. So the scalar Σ mainly couples to W' and Z' , and the couplings to the SM gauge bosons are suppressed by the order of $\mathcal{O}(v^2/u^2)$. When the VEV u is much larger than the VEV v , the scalar Σ becomes heavy and almost decouple from the Higgs scalar Φ .

In the breaking pattern I, the Higgs potential, only involving the bi-doublet scalar Φ and VEV u , is

$$\begin{aligned} \mathcal{V}_{\Phi} &= -\mu_1^2 \text{Tr}(\Phi^\dagger \Phi) - \mu_2^2 \left[\text{Tr}(\tilde{\phi} \phi^\dagger) + \text{Tr}(\tilde{\phi}^\dagger \phi) \right] \\ &+ \lambda_1 \left[\text{Tr}(\phi^\dagger \phi) \right]^2 + \lambda_2 \left\{ \left[\text{Tr}(\tilde{\phi} \phi^\dagger) \right]^2 + \left[\text{Tr}(\tilde{\phi}^\dagger \phi) \right]^2 \right\} \\ &+ \lambda_3 \text{Tr}(\tilde{\phi} \phi^\dagger) \text{Tr}(\tilde{\phi}^\dagger \phi) + \lambda_4 \text{Tr}(\phi^\dagger \phi) \left[\text{Tr}(\tilde{\phi} \phi^\dagger) + \text{Tr}(\tilde{\phi}^\dagger \phi) \right] + \mathcal{V}\left(\Phi, \frac{u}{\sqrt{2}}\right). \end{aligned} \quad (2.49)$$

After electroweak symmetry breaking, the charged fields $\phi_{1,2}^\pm$ form the Goldstone bosons of W^\pm and two charged Higgses. The Goldstone bosons are given by

$$G^\pm = c_\beta \phi_1^\pm - s_\beta \phi_2^\pm. \quad (2.50)$$

The physical charged Higgs states are the linear combinations

$$H^\pm = s_\beta \phi_1^\pm + c_\beta \phi_2^\pm. \quad (2.51)$$

The mass of the lightest charged Higgs is given to a very good approximation by

$$M_{H^\pm} = \frac{\alpha_3 u^2}{c_\beta^2 - s_\beta^2}. \quad (2.52)$$

The neutral Goldstone boson is

$$G^0 = c_\beta \Im \phi_1^0 - s_\beta \Im \phi_2^0. \quad (2.53)$$

In addition there are three neutral Higgs fields in the spectrum, given by

$$h^0 = c_\beta \Re \phi_1^0 + s_\beta \Re(\phi_2^0) \quad (2.54)$$

$$H_1^0 = -s_\beta \Re \phi_1^0 + c_\beta \Re(\phi_2^0) \quad (2.55)$$

$$H_2^0 = s_\beta \Im \phi_1^0 + c_\beta \Im(\phi_2^0), \quad (2.56)$$

where h_0 can be identified as the light Higgs with a mass of $\mathcal{O}(v)$, while H_1^0 and H_2^0 are two new neutral Higgses with masses $\mathcal{O}(u)$. To leading order their masses are equal to each other

$$M_H^2 \equiv M_{H_1^0}^2 = M_{H_2^0}^2 = \frac{\alpha_3 u^2}{c_\beta^2 - s_\beta^2}. \quad (2.57)$$

In the breaking pattern II, there is only one Higgs doublet. So after electroweak symmetry breaking, only one light Higgs is left with three Goldstone bosons eaten by the W and Z

gauge bosons.

2.3.2.2 Gauge Boson Mass Mixing in Breaking Pattern I

In this breaking pattern, the gauge couplings are related to the $U(1)_{em}$ gauge coupling by the relation

$$\frac{1}{e^2} = \frac{1}{g_L^2} + \frac{1}{g_R^2} + \frac{1}{g_X^2}, \quad (2.58)$$

with

$$g_L = \frac{e}{\sin \theta}, \quad g_R = \frac{e}{\cos \theta \sin \phi}, \quad g_X = \frac{e}{\cos \theta \cos \phi}, \quad (2.59)$$

where θ is the usual weak mixing angle, and ϕ is the new mixing angle between W_R^3 and B in this model.

To get the gauge boson mass eigenstates, there are two steps. For the charged gauge bosons, there is no rotation. The mass matrix is

$$M_W^2 = M_0^2 \begin{pmatrix} 1 & -\frac{\tan \theta}{\sin \phi} \sin 2\beta \\ -\frac{\tan \theta}{\sin \phi} \sin 2\beta & \frac{\tan^2 \theta}{\sin^2 \phi} (1+x) \end{pmatrix}, \quad (2.60)$$

where

$$M_0^2 = \frac{1}{4} g_L^2 v^2 = \frac{v^2}{4} \frac{e^2}{\sin^2 \theta}, \quad (2.61)$$

and $x = \frac{u^2}{v^2}$ for Higgs doublet, and $x = \frac{2u^2}{v^2}$ for Higgs triplet.

For the neutral gauge bosons W_L^3, W_R^3, B , one rotates the gauge fields by the angle ϕ and re-parametrize them by θ :

$$W_H^3 = \cos \phi W_R^3 - \sin \phi B, \quad (2.62)$$

$$W_Z^3 = \cos \theta W_L^3 - \sin \theta (\sin \phi W_R^3 + \cos \phi B) \quad (2.63)$$

$$A = \sin \theta W_L^3 + \cos \theta (\sin \phi W_R^3 + \cos \phi B) \quad (2.64)$$

The mixing mass matrix in the (A, W_Z^3, W_H^3) basis reduces to

$$M_Z^2 = \frac{M_0^2}{\cos^2 \theta} \begin{pmatrix} 0 & 0 & 0 \\ 0 & 1 & -\frac{\sin \theta}{\tan \phi} \\ 0 & -\frac{\sin \theta}{\tan \phi} & \frac{\sin^2 \theta}{\sin^2 \phi \cos^2 \phi} (x + \cos^4 \phi) \end{pmatrix}, \quad (2.65)$$

where $x = \frac{u^2}{v^2}$ for Higgs doublet, and $x = \frac{4u^2}{v^2}$ for Higgs triplet.

To get the mass eigenstates, one can further diagonalize the mass matrices M_W^2 and M_Z^2 . Here we focus on the region $x \ll 1$. (one can impose further constraints on g_R and g_X , of course.) Up to the leading order of x , the wave-function mixing is given by the ratio of the non-diagonal term and the diagonal term. To order $1/x$ the eigenstates of the charged gauge bosons are

$$W_\mu^\pm = W_{L\mu}^\pm + \frac{\sin \phi \sin 2\beta}{x \tan \theta} W_{R\mu}^\pm, \quad (2.66)$$

$$W'_{\mu}{}^\pm = -\frac{\sin \phi \sin 2\beta}{x \tan \theta} W_{L\mu}^\pm + W_{R\mu}^\pm, \quad (2.67)$$

while for the neutral gauge bosons

$$Z_\mu = W_{Z\mu}^3 + \frac{\sin\phi \cos^3\phi}{x \sin\theta} W_{H\mu}^3, \quad (2.68)$$

$$Z'_\mu = -\frac{\sin\phi \cos^3\phi}{x \sin\theta} W_{Z\mu}^3 + W_{H\mu}^3. \quad (2.69)$$

To the same order, the gauge boson masses are

$$M_{W^\pm}^2 = M_0^2 \left(1 - \frac{\sin^2 2\beta}{x}\right), \quad (2.70)$$

$$M_{W'^\pm}^2 = M_0^2 \left(\frac{x \tan^2\theta}{\sin^2\phi} + \frac{\tan^2\theta}{\sin^2\phi} \right), \quad (2.71)$$

and

$$M_Z^2 = \frac{M_0^2}{\cos^2\theta} \left(1 - \frac{\cos^4\phi}{x}\right), \quad (2.72)$$

$$M_{Z'}^2 = \frac{M_0^2}{\cos^2\phi} \left(\frac{x \tan^2\theta}{\sin^2\phi} + \frac{\tan^2\theta \cos^4\phi}{\sin^2\phi} \right). \quad (2.73)$$

2.3.2.3 Gauge Boson Mass Mixing in Breaking Pattern II

In this breaking pattern, the gauge coupling relation is

$$g_l = \frac{e}{\sin\theta \cos\phi}, \quad g_h = \frac{e}{\sin\theta \sin\phi}, \quad g_X = \frac{e}{\cos\theta}, \quad (2.74)$$

with the relation

$$\frac{1}{e^2} = \frac{1}{g_l^2} + \frac{1}{g_h^2} + \frac{1}{g_Y^2}, \quad (2.75)$$

where θ is the usual weak mixing angle, and ϕ is the new mixing angle between W_l^μ and W_h^μ in this model. If ϕ is small, the couplings of the third generation will become large.

There are two steps to get the gauge boson mass eigenstates: For the charged gauge bosons, one can rotate the gauge fields by ϕ :

$$W_H^\pm = -\sin\phi W_l^\pm + \cos\phi W_h^\pm, \quad (2.76)$$

$$W_L^\pm = \cos\phi W_l^\pm + \sin\phi W_h^\pm. \quad (2.77)$$

The mass matrix reduces to

$$M_W^2 = M_0^2 \begin{pmatrix} 1 & -\tan\phi \\ -\tan\phi & \frac{x}{\sin^2\phi \cos^2\phi} + \tan^2\phi \end{pmatrix}, \quad (2.78)$$

where

$$M_0^2 = \frac{v^2}{4} \frac{e^2}{\sin^2\theta} = \frac{1}{4} g_L^2 v^2. \quad (2.79)$$

For the neutral gauge bosons W_L^3, W_R^3, B , one rotates the gauge fields by the angle ϕ and re-parametrize them by θ :

$$W_H^3 = -\sin\phi W_l^3 + \cos\phi W_h^3, \quad (2.80)$$

$$W_L^3 = \cos\theta(\cos\phi W_l^3 + \sin\phi W_h^3) - \sin\theta B \quad (2.81)$$

$$A = \cos\theta B + \sin\theta(\cos\phi W_l^3 + \sin\phi W_h^3) \quad (2.82)$$

The mixing mass matrix in the (A, W_Z^3, W_H^3) basis reduces to

$$M_Z^2 = \frac{M_0^2}{\cos^2 \theta} \begin{pmatrix} 0 & 0 & 0 \\ 0 & 1 & -\cos \theta \tan \phi \\ 0 & -\cos \theta \tan \phi & \cos^2 \theta \left(\frac{x}{\sin^2 \phi \cos^2 \phi} + \tan^2 \phi \right) \end{pmatrix}. \quad (2.83)$$

To get the mass eigenstates, one can further diagonalize the mass matrices M_W^2 and M_Z^2 . Here we focus on the region $x \ll 1$. Up to the leading order of x , the wave-function mixing is given by the ratio of the non-diagonal term and the diagonal term. To order $1/x$ the eigenstates of the charged gauge bosons are

$$W_\mu^\pm = W_{L\mu}^\pm + \frac{\cos \phi \sin^3 \phi}{x} W_{H\mu}^\pm, \quad (2.84)$$

$$W'_{\mu}{}^\pm = -\frac{\cos \phi \sin^3 \phi}{x} W_{L\mu}^\pm + W_{H\mu}^\pm, \quad (2.85)$$

while for the neutral gauge bosons

$$Z_\mu = W_{L\mu}^3 + \frac{\cos \phi \sin^3 \phi}{x \cos \theta} W_{H\mu}^3, \quad (2.86)$$

$$Z'_\mu = -\frac{\cos \phi \sin^3 \phi}{x \cos \theta} W_{L\mu}^3 + W_{H\mu}^3. \quad (2.87)$$

To the same order, the gauge boson masses are

$$M_{W^\pm}^2 = M_0^2 \left(1 - \frac{\sin^4 \phi}{x} \right), \quad (2.88)$$

$$M_{W'_{\mu}{}^\pm}^2 = \frac{M_0^2}{\cos^2 \phi} \left(\frac{x}{\sin^2 \phi} + \sin^2 \phi \right), \quad (2.89)$$

and

$$M_Z^2 = \frac{M_0^2}{\cos^2 \theta} \left(1 - \frac{\sin^4 \phi}{x}\right), \quad (2.90)$$

$$M_{Z'}^2 = \frac{M_0^2}{\cos^2 \phi} \left(\frac{x}{\sin^2 \phi} + \sin^2 \phi\right). \quad (2.91)$$

2.3.3 Lagrangian in the Physical Basis

After the symmetry breaking and mass mixing, one can obtain the Lagrangian involving the physical fields. Here we listed the Feynman rules of the Lagrangian in the physical basis in all the models. In the Feynman rules, all particles are assumed to be outgoing, and we adopt the conventional Feynman rule, $i\mathcal{L}$.

2.3.3.1 Gauge couplings of fermions

The most general interaction of the Z and W to SM fermions is

$$\mathcal{L}_f = g_2 Z_\mu \bar{f} \gamma^\mu (g_L P_L + g_R P_R) f + g_2 W_\mu \bar{f} \gamma^\mu (g'_L P_L + g'_R P_R) f' + h.c., \quad (2.92)$$

where $g_2 = e/\sin \theta$ is the weak coupling strength and $P_{L,R} = (1 \mp \gamma_5)/2$ are the usual chirality projectors. On the other hand, the most general interaction of the Z' and W' to SM fermions is

$$\mathcal{L}_f = g_2 Z'_\mu \bar{f} \gamma^\mu (g_L P_L + g_R P_R) f + g_2 W'_\mu \bar{f} \gamma^\mu (g'_L P_L + g'_R P_R) f' + h.c., \quad (2.93)$$

For simplicity, we use g_L and g_R for both Z' and W' bosons from now on. Detailed expressions of g_L and g_R for each individual NP model are listed in Tables 2.3.3.1 and 2.3.3.1.

Couplings	g_L
$W'^{+\mu} \bar{f} f'$ (BPI)	$-\frac{e_m}{\sqrt{2}c_W s_\phi} \gamma_\rho T_L^+ \frac{c_W^2 s^2 \beta s_\phi^2}{x s_W^2}$
$Z' \bar{f} f$ (BPI)	$\frac{e_m}{c_W c_\phi s_\phi} \gamma_\rho \left[(T_{3L} - Q) s_\phi^2 - \frac{c_\phi^4 s_\phi^2 (T_{3L} - Q s_W^2)}{x s_W^2} \right]$
$W'^{\pm\mu} \bar{f} f'$ (BPII)	$-\frac{e_m s_\phi}{\sqrt{2} s_W c_\phi} \gamma^\mu T_l^\pm \left(1 + \frac{s_\phi^2 c_\phi^2}{x} \right)$
$W'^{\pm\mu} \bar{F} F'$ (BPII)	$\frac{e_m c_\phi}{\sqrt{2} s_W s_\phi} \gamma^\mu T_h^\pm \left(1 - \frac{s_\phi^4}{x} \right)$
$Z' \bar{f} f$ (BPII)	$-\frac{e_m}{s_W} \gamma^\mu \left[\frac{s_\phi}{c_\phi} T_{3l} \left(1 + \frac{s_\phi^2 c_\phi^2}{x c_W^2} \right) - \frac{s_\phi s_\phi^2 c_\phi^2}{c_\phi x c_W^2} s_W^2 Q \right]$
$Z' \bar{F} F$ (BPII)	$\frac{e_m}{s_W} \gamma^\mu \left[\frac{c_\phi}{s_\phi} T_{3h} \left(1 - \frac{s_\phi^4}{x c_W^2} \right) + \frac{c_\phi s_\phi^4}{s_\phi x c_W^2} s_W^2 Q \right]$

Table 2.3: The left-handed fermion couplings of the heavy gauge boson in Breaking Pattern I and II. For the fermion couplings, the quantum numbers (T_L, T_R) in BP-I and (T_l, T_h) in BP-II are implied in Tab. 2.2. In BP-II, the fermion notation f means the fermions listed in the column $SU(2)_1$, while F means the fermions listed in the column $SU(2)_2$ in Tab. 2.2.

Couplings	g_R
$W'^{+\mu} \bar{f} f'$ (BPI)	$\frac{em}{\sqrt{2}c_W s_\phi} \gamma_\rho T_R^+$
$Z' \bar{f} f$ (BPI)	$\frac{em}{c_W c_\phi s_\phi} \gamma_\rho \left[(T_{3R} - Q s_\phi^2) + Q \frac{c_\phi^4 s_\phi^2}{x} \right]$
$W'^{\pm\mu} \bar{f} f'$ (BPII)	0
$W'^{\pm\mu} \bar{F} F'$ (BPII)	0
$Z' \bar{f} f$ (BPII)	$\frac{em}{s_W} \gamma^\mu \left(\frac{s_\phi}{c_\phi} \frac{s_\phi^2 c_\phi^2}{x c_W^2} s_W^2 Q \right)$
$Z' \bar{F} F$ (BPII)	$\frac{em}{s_W} \gamma^\mu \left(\frac{c_\phi}{s_\phi} \frac{s_\phi^4}{x c_W^2} s_W^2 Q \right)$

Table 2.4: The right-handed fermion couplings of the heavy gauge boson in Breaking Pattern I and II. For the fermion couplings, the quantum numbers (T_L, T_R) in BP-I and (T_l, T_h) in BP-II are implied in Tab. 2.2. In BP-II, the fermion notation f means the fermions listed in the column $SU(2)_1$, while F means the fermions listed in the column $SU(2)_2$ in Tab. 2.2.

Couplings	BPI
$H W_\nu^+ W_\rho^-$	$\frac{i e_m^2}{2 s_W^2} v g_{\nu\rho} \left(1 - \frac{2s_{2\beta}^2}{x} \right)$
$H W_\nu W'_\rho$	$-\frac{i e_m^2 s_{2\beta}}{2 c_W s_W s_\phi} v g_{\nu\rho} \left[1 + \frac{(c_W^2 s_\phi^2 - s_W^2)}{x s_W^2} \right]$
$H Z_\nu Z_\rho$	$\frac{i e_m^2}{2 s_W^2 c_W^2} v g_{\nu\rho} \left(1 - \frac{2c_\phi^4}{x} \right)$
$H Z_\nu Z'_\rho$	$-\frac{i e_m^2 c_\phi}{2 c_W^2 s_W s_\phi} v g_{\nu\rho} \left[1 - \frac{c_\phi^2 (c_\phi^2 s_W^2 - s_\phi^2)}{x s_W^2} \right]$
$W_\mu^+ W_\nu^- Z_\rho$	$\frac{c_W e m}{s_W}$
$W_\mu^+ W_\nu'^- Z_\rho$	$i \frac{e m s_{2\beta} s_\phi}{x s_W^2}$
$W_\mu^+ W_\nu^- Z'_\rho$	$i \frac{e m c_W s_\phi c_\phi^3}{x s_W^2}$

Table 2.5: The triple boson couplings of the heavy gauge boson in Breaking Pattern I.

Couplings	BP II
$H W_\nu^+ W_\rho^-$	$\frac{i e_m^2}{2 s_W^2} v g_{\nu\rho} \left(1 - \frac{2s_\phi^4}{x} \right)$
$H W_\nu W'_\rho$	$-\frac{i e_m^2 s_\phi}{2 s_W^2 c_\phi} v g_{\nu\rho} \left[1 + \frac{s_\phi^2 (c_\phi^2 - s_\phi^2)}{x} \right]$
$H Z_\nu Z_\rho$	$\frac{i e_m^2}{2 s_W^2 c_W^2} v g_{\nu\rho} \left(1 - \frac{2s_\phi^4}{x} \right)$
$H Z_\nu Z'_\rho$	$-\frac{i e_m^2 s_\phi}{2 c_W s_W^2 c_\phi} v g_{\nu\rho} \left[1 - \frac{s_\phi^2 (s_\phi^2 c_W^2 - c_\phi^2)}{x c_W^2} \right]$
$W_\mu^+ W_\nu^- Z_\rho$	$\frac{c_W e m}{s_W}$
$W_\mu^+ W_\nu'^- Z_\rho$	$i \frac{e m c_\phi s_\phi^3}{x s_W c_W}$
$W_\mu^+ W_\nu^- Z'_\rho$	$i \frac{e m c_\phi s_\phi^3}{x s_W}$

Table 2.6: The triple boson couplings of the heavy gauge boson in Breaking Pattern II.

2.3.3.2 Couplings of Gauge Bosons and Higgs Boson

For the bosonic sector, we are only interested in the triple gauge boson couplings and gauge boson - gauge boson -Higgs couplings. So we write down the most general Lagrangian involving in triple couplings of gauge bosons and Higgs, as follows,

$$\mathcal{L} = -g_{VVV}f^{abc}(\partial_\mu V_\nu^a)V^{b\mu}V^{c\nu} + g_{VVH}g^{\mu\nu}HV_{a\mu}V_{a\nu}, \quad (2.94)$$

where the coefficients g_{VVV} and g_{VVH} are listed in the Table. For the triple gauge boson couplings, the Lorentz index in the Feynman rules $[g^{\mu\nu}(k_1 - k_2)^\rho + g^{\nu\rho}(k_2 - k_3)^\mu + g^{\rho\mu}(k_3 - k_1)^\nu]$ is implied. For the gauge boson - gauge boson -Higgs couplings, the Lorentz index in the Feynman rules $g^{\mu\nu}$ is implied. Feynman rules of the triple gauge boson couplings and gauge boson - gauge boson -Higgs couplings are shown in Tabs. 2.3.3.1 and 2.3.3.1.

2.4 Model Parameters and Mass Spectrum

From Tables 2.1, 2.3.3.1 and 2.3.3.1, we see that the $G(221)$ models contain six (five) parameters for the first (second) breaking pattern: three (two) VEV's $\{u_{D,T}, v \sin \beta, v \cos \beta\}$ in Table 2.1 and three gauge couplings $\{g_1, g_2, g_X\}$ in Table IV. (For breaking pattern II, there are only two VEV's $\{u, v\}$.) Compared to the gauge sector of the SM, which contains only three parameters (two gauge couplings and one VEV; g_L, g_Y and v), there are three (two) additional parameters. We would like to find a useful parameterization of these three additional parameters, so as to parameterize the effects of *new physics*. We discuss these in detail in turn.

2.4.1 Input Parameters

As stated above, the $G(221)$ models contain six (five) parameters in the gauge sector:

$$\{g_1, g_2, g_X, u_D(u_T, \text{ or } u), v^2, s_\beta\}, \quad (2.95)$$

where the parameter β only exists in models with breaking pattern I. An equivalent set of parameters is

$$\{\alpha_e, \sin \theta, \cos \phi, x, v^2, s_{2\beta}\}, \quad (2.96)$$

where θ is the weak mixing angle, ϕ is the new mixing angle, and x is defined as

$$x \equiv \begin{cases} u_D^2/v^2 & (\text{for LRD, LPD, HPD, FPD}) \\ u_T^2/v^2 & (\text{for LRT, LPT, HPT, FPT}) \\ u^2/v^2 & (\text{for SQ, TF, UU}). \end{cases} \quad (2.97)$$

As we expect x to be large ($x \gtrsim 100$), we work to leading order in x^{-1} .

In addition to these parameters, the loop-level predictions will require the values of the masses of the top quark (m_t) and the Higgs boson (M_H). The bar ($\bar{}$) over m_t indicates that we will use the top quark mass as defined in the $\overline{\text{MS}}$ -scheme.

We take as reference observables the experimental measurements of

- the fine structure constant ($\alpha_e^{-1}(M_Z^{\text{SM}}) = 127.918$ at the scale M_Z).
- the Fermi constant ($G_F^{\text{SM}} = 1.16637 \times 10^{-5} \text{ GeV}^{-2}$), determined from the lifetime of

the muon,

- the mass of the Z boson ($M_Z^{\text{SM}} = 91.1876 \text{ GeV}$), determined from the Z -line shape at LEP-I.

Our task then is to express the model parameters, cf Eq. 2.96

$$\{\alpha_e, \sin \theta, v^2, x, \cos \phi, s_{2\beta}, \bar{m}_t, M_H\},$$

in terms of the reference and fit parameters

$$\{\alpha_e^{\text{SM}}, M_Z^{\text{SM}}, G_F^{\text{SM}}, x, \cos \phi, s_{2\beta}, \bar{m}_t, M_H\}. \quad (2.98)$$

That is, we want the relationships

$$\underbrace{\{\alpha_e, \sin \theta, v^2, x, \cos \phi, s_{2\beta}, \bar{m}_t, M_H\}}_{\text{model parameters}} \Leftrightarrow \underbrace{\{\alpha_e^{\text{SM}}, M_Z^{\text{SM}}, G_F^{\text{SM}}\}}_{\text{reference parameters}} \underbrace{\{x, \cos \phi, s_{2\beta}, \bar{m}_t, M_H\}}_{\text{fit parameters}} \quad (2.99)$$

Since $\{x, \cos \phi, s_{2\beta}, \bar{m}_t, M_H\}$ appear in both the model and fit parameters (by construction), we only have to solve for $\{\alpha_e, \sin \theta, v^2\}$ in terms of the reference and fit parameters. This can be done by analyzing how the reference parameters are related to the model parameters.

2.4.1.1 Electric Charge

The electric charge in the $G(221)$ models is the gauge coupling of the unbroken $U(1)_{\text{em}}$ group, which we have parameterized as e defined as

$$\frac{1}{e^2} = \frac{1}{g_1^2} + \frac{1}{g_2^2} + \frac{1}{g_X^2}, \quad (2.100)$$

and $\alpha_e \equiv e^2/4\pi$. There are no tree-level modifications to the wavefunction renormalization of the photon, so we then simply have the relationship

$$\alpha_e = \alpha_e^{\text{SM}}. \quad (2.101)$$

2.4.1.2 The Fermi Constant

The Fermi constant, G_F , is experimentally determined from the muon lifetime as [39]

$$\tau_\mu^{-1} = \frac{G_F^2 m_\mu^5}{192\pi^3} \left[1 + \mathcal{O}\left(\frac{m_e^2}{m_\mu^2}\right) \right] \left[1 + \mathcal{O}\left(\frac{m_\mu^2}{M_W^2}\right) \right] \left[1 + \mathcal{O}\left(\frac{1}{16\pi^2}\right) \right], \quad (2.102)$$

where the precise forms of the higher-order corrections are given in Ref. [39]. Neglecting these higher-order corrections, the SM contribution to the muon lifetime is

$$\tau_\mu^{-1} = \frac{g_L^4}{192 \cdot 32\pi^3 M_W^4} m_\mu^5, \quad (2.103)$$

and, using the SM relation $4M_W^2 = g_L^2 v^2$, we obtain

$$G_F^{\text{SM}} = \frac{1}{\sqrt{2}v_{\text{SM}}^2}. \quad (2.104)$$

In the standard model, the effective four fermion Lagrangian gives us

$$\mathcal{L}_{\text{SM}} = \left(\frac{e_{\text{SM}}}{\sqrt{2} \sin(\theta_{\text{SM}})} \right)^2 \frac{1}{M_{W \text{ SM}}^2} J_L^+ J_L^- = \frac{2}{v_{\text{SM}}^2} J_L^+ J_L^- = 2\sqrt{2} G_F J_L^+ J_L^-. \quad (2.105)$$

In the $G(221)$ models, we have extra contributions to the four-fermion charged-current effective theory below the electroweak scale. The effective four fermion Lagrangian is

$$\mathcal{L}_{\text{eff}} = c_{LL} J_L^+ J_L^- + c_{LR} J_L^+ J_R^- + c_{RL} J_R^+ J_L^- + c_{RR} J_R^+ J_R^- \quad (2.106)$$

where the charged currents are

$$J_{L,R}^{-\mu} = \bar{\nu}_{L,R} \gamma^\mu l_{L,R}, \quad J^+ = (J^-)^\dagger \quad (2.107)$$

and the coefficients are

$$c_{LL} = \frac{g_{WL}^2}{M_W^2} + \frac{g_{WPL}^2}{M_{W'}^2}, \quad (2.108)$$

$$c_{LR} = c_{RL} = \frac{g_{WL} g_{WR}}{M_W^2} + \frac{g_{WPL} g_{WPR}}{M_{W'}^2}, \quad (2.109)$$

$$c_{RR} = \frac{g_{WR}^2}{M_W^2} + \frac{g_{WPR}^2}{M_{W'}^2}. \quad (2.110)$$

These contributions will modify the SM relation in Eq. 2.104. In principle, the fermionic contributions can have both left- and right-handed components and differ among the different generations. However, for the $G(221)$ models we consider here, the charged currents couples universally to the first two generations. Furthermore, the charged current is either purely right-handed (the LR, HP, LP, FP models) or purely left-handed (the UU and TF models).

We therefore focus on these special cases instead of performing the general analysis.

In the BP-I, the contributions to the amplitude do not interfere with one another in the limit of neglecting the masses of electrons and neutrinos. From the lifetime to the $\frac{1}{x^2}$ order we can obtain

$$\begin{aligned} 8G_F^2 &= c_{LL}^2 + 2c_{LR}^2 + c_{RR}^2 \\ &= \frac{4}{v^4} \left(1 + \frac{\sin^2(2\beta)}{x}\right)^2 + 2\frac{4}{v^4} \left(\frac{\sin 2\beta}{x}\right)^2 + \frac{4}{v^4} \left(\frac{1}{x}\right)^2 + \mathcal{O}\left(\frac{1}{x^3}\right), \end{aligned} \quad (2.111)$$

in BP-I with doublet Higgs, and

$$G_F = \frac{1}{\sqrt{2}v^2} \left(1 + \frac{\sin^2 2\beta}{2x}\right), \quad (2.112)$$

in BP-I with triplet Higgs. Though the left-right and right-right current operators do not contribute to the total muon decay rate at the order $\mathcal{O}(\tilde{x}^{-1})$, they do contribute at leading order to the Michel parameters (for a detailed discussion of the Michel parameters, see the Muon Decay Parameters article in the Particle Data Group (PDG) [39]). The expression of G_F , which depends on the details of the Higgs representation, is written in terms of model parameters as

$$G_F = \begin{cases} \frac{1}{\sqrt{2}v^2} \left(1 + \frac{\sin^2 2\beta}{x}\right), & \text{(for LRD, LPD, HPD, FPD)} \\ \frac{1}{\sqrt{2}v^2} \left(1 + \frac{\sin^2 2\beta}{2x}\right), & \text{(for LRT, LPT, HPT, FPT)} \end{cases} \quad (2.113)$$

In the BP-II, the expression of the charged-current operators is

$$c_{LL} = \frac{g_{WL}^2}{M_W^2} + \frac{g_{WPL}^2}{M_{W'}^2}, \quad (2.114)$$

$$c_{LR} = c_{RL} = 0, \quad (2.115)$$

$$c_{RR} = 0. \quad (2.116)$$

From the lifetime, we can obtain, to the $\frac{1}{x^2}$ order

$$\begin{aligned} 8G_F^2 &= c_{LL}^2 + 2c_{LR}^2 + c_{RR}^2 \\ &= \frac{4}{v^4} + \mathcal{O}\left(\frac{1}{x^3}\right). \end{aligned} \quad (2.117)$$

So we are simply left with

$$G_F = \frac{1}{\sqrt{2}\tilde{v}^2} \quad (\text{for SQ, TF, UU}). \quad (2.118)$$

We can rewrite our results in a more suggestive manner by defining the SM VEV through the Fermi constant

$$v^2 \equiv \frac{1}{\sqrt{2}G_F}. \quad (2.119)$$

We then have

$$v = \begin{cases} v \text{ SM} \left(1 + \frac{\sin^2 2\beta}{2x} \right), & (\text{for LRD, LPD, HPD, FPD}) \\ v \text{ SM} \left(1 + \frac{\sin^2 2\beta}{4x} \right), & (\text{for LRT, LPT, HPT, FPT}) \\ v \text{ SM}. & (\text{for SQ, TF, UU}) \end{cases} \quad (2.120)$$

2.4.1.3 Z-Mass

The expression of the Z mass can be written as

$$M_Z^2 = \begin{cases} \frac{ev}{2 \sin \theta \cos \theta} \left(1 - \frac{\cos^4 \phi}{2x} \right), & (\text{for LRD, LPD, HPD, FPD}) \\ \frac{ev}{2 \sin \theta \cos \theta} \left(1 - \frac{\cos^4 \phi}{8x} \right), & (\text{for LRT, LPT, HPT, FPT}) \\ \frac{ev}{2 \sin \theta \cos \theta} \left(1 - \frac{\sin^4 \phi}{2x} \right), & (\text{for UU and TF}) \end{cases} \quad (2.121)$$

Thus we have

$$M_Z^2 = \begin{cases} \frac{e \text{ SM}_v \text{ SM}}{2 \sin \theta \cos \theta} \left(1 + \frac{\sin^2 2\beta}{2x} - \frac{\cos^4 \phi}{2x} \right), & (\text{for LRD, LPD, HPD, FPD}) \\ \frac{e \text{ SM}_v \text{ SM}}{2 \sin \theta \cos \theta} \left(1 + \frac{\sin^2 2\beta}{4x} - \frac{\cos^4 \phi}{8x} \right), & (\text{for LRT, LPT, HPT, FPT}) \\ \frac{e \text{ SM}_v \text{ SM}}{2 \sin \theta \cos \theta} \left(1 - \frac{\sin^4 \phi}{2x} \right), & (\text{for UU and TF}) \end{cases} \quad (2.122)$$

While in the SM Z mass can be written as

$$M_Z^{\text{SM}} = \frac{e \text{ SM}_v \text{ SM}}{2 \sin \theta \text{ SM}_{\cos \theta} \text{ SM}}. \quad (2.123)$$

Here $\sin \theta_{\text{SM}}$ is the SM weak coupling angle, and its value can be obtained by

$$\sin^2 \theta_{\text{SM}} \cos^2 \theta_{\text{SM}} = \frac{\pi \alpha(M_Z)_{\text{SM}}}{\sqrt{2} G_F^{\text{SM}} (M_Z^{\text{SM}})^2}, \quad (2.124)$$

Using $\frac{1}{\alpha(M_Z)_{\text{SM}}} = 128.91 \pm 0.02$, yields $\sin^2 \theta_{\text{SM}} = 0.23108 \pm 0.00005$. Since M_Z is defined in both the SM and the proposed model through the Z peak at LEP $M_Z = M_Z^{\text{SM}}$, we can solve for θ in terms of the reference and fit parameters

$$\sin^2 \theta \cos^2 \theta = \begin{cases} \sin^2 \theta_{\text{SM}} \cos^2 \theta_{\text{SM}} \left(1 - \frac{\cos^4 \phi}{x} + \frac{\sin^2 2\beta}{x} \right), \\ \text{(for LRD, LPD, HPD, FPD)} \\ \sin^2 \theta_{\text{SM}} \cos^2 \theta_{\text{SM}} \left(1 - \frac{\cos^4 \phi}{4x} + \frac{\sin^2 2\beta}{2x} \right), \\ \text{(for LRT, LPT, HPT, FPT)} \\ \sin^2 \theta_{\text{SM}} \cos^2 \theta_{\text{SM}} \left(1 - \frac{\sin^4 \phi}{x} \right), \\ \text{(for SQ, TF, UU).} \end{cases} \quad (2.125)$$

Hereafter, solving for $\sin^2 \theta = 1 - \cos^2 \theta$ in terms of $\sin^2 \theta_{\text{SM}}$ (the solutions of $x(1-x) = a$ are $x = \frac{1}{2}(1 \pm \sqrt{1-4a})$), one finds that

$$\begin{aligned} \sin^2 \theta &= \sin^2 \theta_{\text{SM}} \left[1 - \frac{\cos^2 \theta_{\text{SM}}}{\cos^2 \theta_{\text{SM}} - \sin^2 \theta_{\text{SM}}} \Delta\theta \right], \\ \cos^2 \theta &= \cos^2 \theta_{\text{SM}} \left[1 + \frac{\sin^2 \theta_{\text{SM}}}{\cos^2 \theta_{\text{SM}} - \sin^2 \theta_{\text{SM}}} \Delta\theta \right], \end{aligned} \quad (2.126)$$

where the correction Δ_θ is

$$\Delta_\theta = \begin{cases} \left(\frac{\cos^4 \phi}{x} - \frac{\sin^2 2\beta}{x} \right), & (\text{for LRD, LPD, HPD, FPD}) \\ \left(\frac{\cos^4 \phi}{4x} - \frac{\sin^2 2\beta}{2x} \right), & (\text{for LRT, LPT, HPT, FPT}) \\ \left(\frac{\sin^4 \phi}{x} \right), & (\text{for SQ, TF, UU}). \end{cases} \quad (2.127)$$

2.4.2 Mass Spectra

With the input parameters defined as above, we can calculate the corrections to the experimental observables. We take the mass spectrum as an example and collect the formula of the masses of the W -boson, W' -boson and Z' -boson.

2.4.2.1 Breaking Pattern I with Doublet Higgs

The mass spectrum in the Breaking Pattern I has the form of

$$M_W^2 = \frac{e_m^2 v^2}{4s_W^2} \left(1 - \frac{s_{2\beta}^2}{x} \right), \quad (2.128)$$

$$M_Z^2 = \frac{e_m^2 v^2}{4s_W^2 c_W^2} \left(1 - \frac{c_\phi^4}{x} \right), \quad (2.129)$$

and

$$M_{W'}^2 = \frac{e_m^2 v^2 x}{4c_W^2 s_\phi^2} \left(1 + \frac{1}{x} \right), \quad (2.130)$$

$$M_{Z'}^2 = \frac{e_m^2 v^2 x}{4c_W^2 s_\phi^2 c_\phi^2} \left(1 + \frac{c_\phi^4}{x} \right). \quad (2.131)$$

More specifically, in terms of the input parameters, we can convert all the model parameters to reference and fit parameters

$$M_W^2 = \frac{e_m^2 v^2}{4s_W^2} \left(1 + \frac{c_W^2}{c_W^2 - s_W^2} \left(\frac{c_\phi^4}{x} - \frac{s_{2\beta}^2}{x} \right) \right), \quad (2.132)$$

$$M_Z^2 = \frac{e_m^2 v^2}{4s_W^2 c_W^2} = M_Z^2 \text{ SM}, \quad (2.133)$$

and

$$M_{W'}^2 = \frac{e_m^2 v^2}{4c_W^2 s_\phi^2} \left(1 + \frac{1}{x} + \frac{c_W^2 s_{2\beta}^2 - s_W^2 c_\phi^4}{(c_W^2 - s_W^2)x} \right), \quad (2.134)$$

$$M_{Z'}^2 = \frac{e_m^2 v^2}{4c_W^2 s_\phi^2 c_\phi^2} \left(1 + \frac{c_\phi^4}{x} + \frac{c_W^2 s_{2\beta}^2 - s_W^2 c_\phi^4}{(c_W^2 - s_W^2)x} \right). \quad (2.135)$$

2.4.2.2 Breaking Pattern I with Triplet Higgs

The mass spectrum has the form of

$$M_W^2 = \frac{e_m^2 v^2}{4s_W^2} \left(1 - \frac{s_{2\beta}^2}{2x} \right), \quad (2.136)$$

$$M_Z^2 = \frac{e_m^2 v^2}{4s_W^2 c_W^2} \left(1 - \frac{c_\phi^4}{4x} \right), \quad (2.137)$$

and

$$M_{W'}^2 = \frac{e_m^2 v^2}{4c_W^2 s_\phi^2} \left(1 + \frac{1}{2x} \right), \quad (2.138)$$

$$M_{Z'}^2 = \frac{e_m^2 v^2}{4c_W^2 s_\phi^2 c_\phi^2} \left(1 + \frac{c_\phi^4}{4x} \right). \quad (2.139)$$

More specifically, in terms of the input parameters, we can convert all the model parameters to reference and fit parameters

$$M_W^2 = \frac{e_m^2 v^2}{4s_W^2} \left(1 + \frac{c_W^2}{c_W^2 - s_W^2} \left(\frac{c_\phi^4}{4x} - \frac{s_{2\beta}^2}{2x} \right) \right), \quad (2.140)$$

$$M_Z^2 = \frac{e_m^2 v^2}{4s_W^2 c_W^2} = M_Z^2 \text{ SM}, \quad (2.141)$$

and

$$M_{W'}^2 = \frac{2e_m^2 v^2}{4c_W^2 s_\phi^2} \left(1 + \frac{1}{2x} + \frac{2c_W^2 s_{2\beta}^2 - s_W^2 c_\phi^4}{4(c_W^2 - s_W^2)x} \right), \quad (2.142)$$

$$M_{Z'}^2 = \frac{4e_m^2 v^2}{4c_W^2 s_\phi^2 c_\phi^2} \left(1 + \frac{c_\phi^4}{4x} + \frac{2c_W^2 s_{2\beta}^2 - s_W^2 c_\phi^4}{4(c_W^2 - s_W^2)x} \right). \quad (2.143)$$

2.4.2.3 Breaking Pattern II

The mass spectrum in the Breaking Pattern II have

$$M_W^2 = \frac{e_m^2 v^2}{4s_W^2} \left(1 - \frac{s_\phi^4}{x} \right), \quad (2.144)$$

$$M_Z^2 = \frac{e_m^2 v^2}{4s_W^2 c_W^2} \left(1 - \frac{s_\phi^4}{x} \right), \quad (2.145)$$

and

$$M_{W'}^2 = \frac{e_m^2 v^2 x}{4s_W^2 s_\phi^2 c_\phi^2} \left(1 + \frac{s_\phi^4}{x} \right), \quad (2.146)$$

$$M_{Z'}^2 = \frac{e_m^2 v^2 x}{4s_W^2 s_\phi^2 c_\phi^2} \left(1 + \frac{s_\phi^4}{x} \right). \quad (2.147)$$

More specifically, in terms of the input parameters, we can convert all the model parameters to reference and fit parameters

$$M_W^2 = \frac{e_m^2 s_v^2}{4s_W^2} \left(1 + \frac{s_W^2}{c_W^2 - s_W^2} \frac{s_\phi^4}{x} \right), \quad (2.148)$$

$$M_Z^2 = \frac{e_m^2 s_v^2}{4s_W^2 c_W^2} = M_Z^2 \text{ SM}, \quad (2.149)$$

and

$$M_{W'}^2 = \frac{e_m^2 s_v^2 s_x^2}{4s_W^2 s_\phi^2 c_\phi^2} \left(1 + \frac{(2c_W^2 - s_W^2)s_\phi^4}{(c_W^2 - s_W^2)x} \right), \quad (2.150)$$

$$M_{Z'}^2 = \frac{e_m^2 s_v^2 s_x^2}{4s_W^2 s_\phi^2 c_\phi^2} \left(1 + \frac{(2c_W^2 - s_W^2)s_\phi^4}{(c_W^2 - s_W^2)x} \right). \quad (2.151)$$

2.5 Indirect and Direct Constraints on Parameter Spaces

Even though the W' and Z' bosons are not observed yet, they could contribute to a few observables, which can be measured precisely at low energy, via quantum effects. In this section we perform a global-fit analysis of 37 electroweak precision test observables (EWPTs) to derive the allowed model parameter space of those NP models of our interests. In addition, we also include direct search limits from the Tevatron and LHC.

Note that $m_{W'}$ and $m_{Z'}$ are not independent in the $G(221)$ model. In this study we choose $M_{W'}$ as an input parameter. In addition, other independent parameters are the gauge mixing angle ϕ , and the mixing angle β in the EWSB scale between two Higgs VEVs $s_2\beta = \sin(2\beta)$ that only exists in BP-I. Our parameter scan is not sensitive to the parameter β as it contributes to physical observables only at the order of $1/x = v/u$. We then present

our scan results in the plane of $(M_{W'}, c_\phi)$ or $(M_{W'}, M_{Z'})$.

2.5.1 Indirect Constraints from Electroweak Precision Tests

For a measured observable O^{exp} , the SM prediction can be broken down into the tree- and loop-level components

$$O_{\text{SM}}^{\text{th}} = O_{\text{SM}}^{\text{th,tree}} + O_{\text{SM}}^{\text{th,loop}}(\bar{m}_t, M_H), \quad (2.152)$$

where O^{th} is expressed in terms of the reference parameters. Since the top quark mass (\bar{m}_t) and the mass of the Higgs boson (M_H) enter into the loop-calculations in the SM, a global analysis of precision data and direct detection data can be used to constrain M_H . In the $G(221)$ models, we can express the theoretical prediction as

$$O^{\text{th}} = O_{\text{SM}}^{\text{th,tree}} + O_{\text{SM}}^{\text{th,loop}}(\bar{m}_t, M_H) + O_{\text{NP}}^{\text{th,tree}}(x, \phi, \beta), \quad (2.153)$$

where $O_{\text{NP}}^{\text{th,tree}}$ is of the order $\mathcal{O}(1/x)$, and we assume that

$$x^{-1} \sim \frac{1}{16\pi^2} \sim O_{\text{SM}}^{\text{th,loop}}. \quad (2.154)$$

That is, the Born-level new physics contributions from the $G(221)$ models are numerically of one-loop order, and loop corrections involving new physics are of two-loop order $\mathcal{O}\left(\frac{1}{16\pi^2 x}\right)$, which we discard in our analysis.

To compare with precision data (from LEP-1 and SLD) and low-energy observables, we calculate the shifts in observables $O_{\text{NP}}^{\text{th,tree}}(x, \phi, \beta)$, as in the previous examples of the

partial decay widths of the Z -boson and the mass of the W -boson, and we adapt these corrections into a numerical package GAPP [37]. GAPP then computes $O_{\text{SM}}^{\text{th,tree}}$ and $O_{\text{SM}}^{\text{th,loop}}(\bar{m}_t, M_H)$ ¹, together with the $O_{\text{NP}}^{\text{th,tree}}(x, \phi, \beta)$ to find the best-fit values of the fit parameters and the confidence level contours using the CERN library MINUIT [38].

We perform a global fit over the following classes of observables

- LEP-I Z -pole observables: the total Z -width (Γ_Z), left-right asymmetries (A_{LR}), and related observables,
- the mass (M_W) and decay width (Γ_W) of the W -boson,
- the tau lifetime τ_τ ,
- the ratios of neutral-to-charged current cross sections measured from neutrino-hadron deep-inelastic scattering (DIS) experiments ($R_\nu \equiv \sigma_{\nu N}^{\text{NC}}/\sigma_{\nu N}^{\text{CC}}$ and similarly defined for $\bar{\nu}$),
- effective vector and axial-vector neutrino-electron couplings ($g_V^{\nu e}$ and $g_A^{\nu e}$),
- weak charges (Q_W) of atoms and the electron measured from atomic parity experiments.

Detailed information on these observables can be found in PDG [39], and here we only briefly summarize the observables. The set of the observables included in our analysis is the same as that used in the PDG analysis [39], with two exceptions.

- First, we do not include the anomalous magnetic moment of the muon and the decay branching ratio $b \rightarrow s\gamma$. At leading order, these observables are of one-loop order, and

¹The higher order SM corrections included in our analysis are the same as those in the default GAPP code used for the PDG analysis.

they depend on the details of the extended flavor structure of the $G(221)$ models. In this work, we assume W' bosons only couple to fermions in the same generation.

- Second, we include the measurements of the decay width of the W -boson, which are not included in the PDG analysis. However, because of the comparatively low precision of these measurements, this observable turns out to be insensitive to the new physics contributions from the $G(221)$ models.

In total, we include a set of 37 experimental observables in our global-fit analysis.

Before we give a brief discussion on each of these classes of observables, we note that for some low-energy observables, such as the measurements from the atomic parity violation and neutrino-nucleus DIS experiments, we implement the shifts in the coefficients of the relevant four-fermion interactions, and rely on GAPP to compute the theoretical predictions based on these modified coefficients.

For the ease of typesetting in the following subsections, we introduce the abbreviation for the various forms of the fermionic currents

$$\begin{aligned}
 (\bar{f}_1 f_2)_L^\mu &\equiv \bar{f}_1 \gamma^\mu (1 - \gamma_5) f_2, \\
 (\bar{f}_1 f_2)_R^\mu &\equiv \bar{f}_1 \gamma^\mu (1 + \gamma_5) f_2,
 \end{aligned}
 \tag{2.155}$$

and

$$\begin{aligned}
 (\bar{f}_1 f_2)_V^\mu &\equiv \bar{f}_1 \gamma^\mu f_2, \\
 (\bar{f}_1 f_2)_A^\mu &\equiv \bar{f}_1 \gamma^\mu \gamma_5 f_2.
 \end{aligned}
 \tag{2.156}$$

2.5.1.1 Precision Measurements at the Z -Pole

The precision measurements at the Z -pole (including LEP-1 and SLD experiments) fall into two broad classes: observables that can be constructed from the partial widths and the asymmetry. We discuss these two classes in turn.

In the first class, we consider the $Z \rightarrow f\bar{f}$ partial width, which at tree-level has the expression in the Standard Model

$$\Gamma(Z \rightarrow f\bar{f}) = \frac{n_c}{12\pi} M_Z \left(g_V^2 + g_A^2 \right), \quad (2.157)$$

where $n_c = 3$ if f is a quark, and $n_c = 1$ for leptons, and $g_V(f)$, and $g_A(f)$ depend on the details of the model. In addition to the total width Γ_Z , there are also the following measurements:

$$\sigma_{\text{had}} = \frac{12\pi}{M_Z^2 \Gamma_Z^2} \cdot \Gamma_Z(e^-e^+) \Gamma_Z(\text{had.}), \quad (2.158)$$

$$R(\ell) = \frac{\Gamma_Z(\text{had.})}{\Gamma_Z(\ell\bar{\ell})}, \quad \text{for } \ell = e, \mu, \tau, \quad (2.159)$$

$$R(q) = \frac{\Gamma_Z(q\bar{q})}{\Gamma_Z(\text{had.})}, \quad \text{for } q = u, d, c, s, b, \quad (2.160)$$

$$\mathcal{R}(s) = \frac{R(s)}{R(u) + R(d) + R(s)}, \quad (2.161)$$

where $\Gamma_Z(f\bar{f})$ is the partial decay width $\Gamma(Z \rightarrow f\bar{f})$, and

$$\Gamma_Z(\text{had.}) = \sum_{q=u,d,c,s,b} \Gamma_Z(q\bar{q}). \quad (2.162)$$

The left-right asymmetry $A_{LR}(f)$ is defined as

$$A_{LR}(f) \equiv \frac{[g_L^Z(f)]^2 - [g_R^Z(f)]^2}{[g_L^Z(f)]^2 + [g_R^Z(f)]^2}, \quad (2.163)$$

where $g_L^Z(f)$ and $g_R^Z(f)$ are the couplings of the fermion f to the Z -boson:

$$\mathcal{L} \supset Z_\mu (g_L^Z(f) \bar{f}_L \gamma^\mu f_L + g_R^Z(f) \bar{f}_R \gamma^\mu f_R). \quad (2.164)$$

From the quark branching ratios $R(q)$ defined above, the hadronic left-right asymmetry Q_{LR} can be defined as [37] [40]

$$Q_{LR} \equiv \sum_{q=d,s,b} R(q) A_{LR}(q) - \sum_{q=u,c} R(q) A_{LR}(q). \quad (2.165)$$

A second class of asymmetries, the forward-backward asymmetries $A_{FB}(f)$, emerges from the convolution of the $A_{LR}(f)$ asymmetries with the polarization asymmetry $A_{LR}(e)$ of the electron. The hadronic charge asymmetry Q_{FB} is defined accordingly [37] [40]

$$A_{FB}(f) \equiv \frac{3}{4} A_{LR}(e) A_{LR}(f), \quad (2.166)$$

$$Q_{FB} \equiv \frac{3}{4} A_{LR}(e) Q_{LR}. \quad (2.167)$$

2.5.1.2 The Tau Lifetime

In terms of model parameters, the expression of the tau (τ) lifetime is similar to the muon (μ) lifetime in the $G(221)$ models, with the obvious replacement of m_μ in the μ lifetime by m_τ in the τ lifetime. This is true even in the top-flavor model, in which third generation

fermions transform under a different gauge group compared to the first two generations. In the four-fermion effective theory of the TF model, only interactions involving two pairs of third-generation fermions receive new physics contributions, and the interactions involving one pair of third-generation fermions with one pair of light-flavor fermions (those responsible for the decay of the τ) are the same as those between two pairs of first two generations of fermions (those responsible for the decay of μ). This is similar to the case of the un-unified model, where only interactions involving two pairs of quarks $(\bar{q}q)(\bar{q}q)$ receive new physics contributions, while the $(\bar{q}q)(\bar{\ell}\ell)$ interactions are the same as the $(\bar{\ell}\ell)(\bar{\ell}\ell)$. The lifetime τ_τ can be calculated at tree level as

$$\tau_\tau^{-1} \simeq \frac{G_F^2 m_\tau^5}{192\pi^3} \left(1 + 3 \frac{m_\tau^2}{M_W^2} \right), \quad (2.168)$$

in the SM. The dominant new physics contribution from $G(221)$ models can be captured in the shift of M_W .

2.5.1.3 νN Deep Inelastic Scattering

The νN deep inelastic scattering experiments probe the coefficients $\varepsilon_L(q)$ and $\varepsilon_R(q)$ (for q being u or d) that parameterize the neutral current $\bar{\nu}\nu\bar{q}q$ interactions below the electroweak scale

$$\mathcal{L} \supset -\frac{G_F}{\sqrt{2}} (\bar{\nu}\nu)_{L,\mu} \sum_{q=u,d} \left[\varepsilon_L(q) (\bar{q}q)_L^\mu + \varepsilon_R(q) (\bar{q}q)_R^\mu \right]. \quad (2.169)$$

The DIS experiments measure the ratios of neutral-to-charged current cross sections

$$R_\nu \equiv \sigma_{\nu N}^{\text{NC}} / \sigma_{\nu N}^{\text{CC}}, \quad R_{\bar{\nu}} \equiv \sigma_{\bar{\nu} N}^{\text{NC}} / \sigma_{\bar{\nu} N}^{\text{CC}}, \quad (2.170)$$

which can be written in terms of $\varepsilon_L(q)$ and $\varepsilon_R(q)$ as

$$R_\nu = (1 - \delta) \left[a_L(u) \varepsilon_L^2(u) + a_L(d) \varepsilon_R^2(d) + a_R(u) \varepsilon_R^2(u) + a_R(d) \varepsilon_L^2(d) \right], \quad (2.171)$$

$$R_{\bar{\nu}} = (1 - \bar{\delta}) \left[\bar{a}_L(u) \varepsilon_R^2(u) + \bar{a}_L(d) \varepsilon_L^2(d) + \bar{a}_R(u) \varepsilon_R^2(u) + \bar{a}_R(d) \varepsilon_L^2(d) \right]. \quad (2.172)$$

The coefficients δ and $a_{L,R}$ are related to the nuclei form factors that are experiment specific.

These coefficients are included in GAPP, and we implement only the corrections to $\varepsilon_L(q)$

and $\varepsilon_R(q)$.

2.5.1.4 νe Scattering

The most precise data on neutrino-electron scattering comes from the CHARM II [41] experiment at CERN that utilized ν_μ and $\bar{\nu}_\mu$. The relevant parameters $\varepsilon_L(e)$ and $\varepsilon_R(e)$ are defined similarly as in the νN scattering

$$\mathcal{L} \supset -\frac{G_F}{\sqrt{2}} (\bar{\nu}\nu)_{L,\mu} \left[\varepsilon_L(e) (\bar{e}e)_L^\mu + \varepsilon_R(e) (\bar{e}e)_R^\mu \right]. \quad (2.173)$$

We can further define

$$g_V^{\nu e} \equiv \varepsilon_R(e) + \varepsilon_L(e), \quad (2.174)$$

$$g_A^{\nu e} \equiv \varepsilon_R(e) - \varepsilon_L(e), \quad (2.175)$$

which are related to the measured total cross sections $\sigma_{\nu e}^{\text{NC}}$ and $\sigma_{\bar{\nu} e}^{\text{NC}}$ or their ratio $\sigma_{\nu e}^{\text{NC}}/\sigma_{\bar{\nu} e}^{\text{NC}}$.

In the limit of large incident neutrino energies, $E_\nu \gg m_e$, the cross sections are given as

$$\sigma_{\nu e}^{\text{NC}} = \frac{G_F^2 m_e E_\nu}{2\pi} \left[(g_V^{\nu e} + g_A^{\nu e})^2 + \frac{1}{3} (g_V^{\nu e} - g_A^{\nu e})^2 \right], \quad (2.176)$$

$$\sigma_{\bar{\nu} e}^{\text{NC}} = \frac{G_F^2 m_e E_\nu}{2\pi} \left[(g_V^{\nu e} - g_A^{\nu e})^2 + \frac{1}{3} (g_V^{\nu e} + g_A^{\nu e})^2 \right]. \quad (2.177)$$

We implement corrections to the couplings due to new physics in GAPP and compute the cross sections that are used in the global-fit analysis.

2.5.1.5 Parity Violation Experiments

We consider observables from three different measurements: atomic parity violation (APV), Møller scattering ($e^- e^- \rightarrow e^- e^-$) [42], and eN DIS. These experiments measure the weak charge (Q_W) of the electron [42], caesium-133 [43][44] and thallium-205 nuclei [45][46]. Before defining the weak charge, it is useful to parameterize the coefficients of the $(\bar{e}e)(\bar{q}q)$ and $(\bar{e}e)(\bar{e}e)$ interactions in terms of C_{1q} , C_{2q} , and C_{1e} as

$$\mathcal{L} \supset -\frac{G_F}{\sqrt{2}} \sum_q \left[C_{1q} (\bar{e}e)_{A,\mu} (\bar{q}q)_A^\mu + C_{2q} (\bar{e}e)_{A,\mu} (\bar{q}q)_A^\mu \right] - \frac{G_F}{\sqrt{2}} C_{1e} (\bar{e}e)_{A,\mu} (\bar{e}e)_A^\mu \quad (2.178)$$

The weak charges of the quark and electron are defined as

$$Q_W(q) = 2C_{1q}, \quad Q_W(e) = 2C_{1e}. \quad (2.179)$$

We can express the SM tree-level couplings of quarks to the Z -boson as $\mathcal{L} \supset Z^\mu J_\mu^Z$, where

$$J_\mu^Z = \left| g_A^Z(q) \right| \cdot \left[Q_W(q) (\bar{q}q)_{V,\mu} \pm (\bar{q}q)_{A,\mu} \right], \quad (2.180)$$

and the \pm on the axial-vector term is the opposite sign of the T_L^{3q} . Hence $Q_W(q)$ can be interpreted as the ratio of the vector current to axial-vector current coupling of quark q to the Z -boson:

$$Q_{W, \text{SM}}(q) = \frac{g_V^Z(q)}{\left| g_A^Z(q) \right|}. \quad (2.181)$$

The weak charges of the nucleons and nuclei can be built up from those of the quarks

$$Q_W(p) = 2Q_W(u) + Q_W(d), \quad (2.182)$$

$$Q_W(n) = Q_W(u) + 2Q_W(d), \quad (2.183)$$

and for nucleus A_Z (with atomic number Z and mass number A), which contains Z protons and $N(= A - Z)$ neutrons,

$$Q_W({}^A_Z) = Z \cdot Q_W(p) + N \cdot Q_W(n) \quad (2.184)$$

$$= 2 \left[(Z + A) \cdot C_{1u} + (2A - Z) \cdot C_{1d} \right]. \quad (2.185)$$

There are also measurements of certain linear combinations of the coupling coefficients C_{1u} and C_{1d} from polarized electron-hadron scattering data [47]. The particular linear

combinations, determined by the experimental data,

$$\begin{aligned} \mathcal{C}_1 &= 9C_{1u} + 4C_{1d}, \\ \mathcal{C}_2 &= -4C_{1u} + 9C_{1d}, \end{aligned} \tag{2.186}$$

are included in our global analysis.

2.5.2 Direct Searches at the Tevatron and LHC

Another important bound on the $G(221)$ model originates from direct searches at the Tevatron and LHC. Searches for the W' and Z' bosons as a s -channel resonance have been carried out at the Tevatron and LHC in leptonic decay modes, quark decay channels and diboson decays. For the constraints from Tevatron, we use the latest Tevatron data:

- DØ: $p\bar{p} \rightarrow Z' \rightarrow e^+e^-$ ($\int \mathcal{L}dt=5.4 \text{ fb}^{-1}$) [59];
- CDF: $p\bar{p} \rightarrow W'^{\pm} \rightarrow e\nu$ ($\int \mathcal{L}dt=5.3 \text{ fb}^{-1}$) [50];
- CDF: $p\bar{p} \rightarrow W'^{\pm} \rightarrow t\bar{b}$ ($\int \mathcal{L}dt=1.9 \text{ fb}^{-1}$) [51];
- CDF: $p\bar{p} \rightarrow Z' \rightarrow t\bar{t}$ ($\int \mathcal{L}dt=955 \text{ pb}^{-1}$) [53].

and LHC7 data:

- ATLAS: $pp \rightarrow W'^{\pm} \rightarrow l\nu$ ($\int \mathcal{L}dt=1.04 \text{ fb}^{-1}$) [54];
- ATLAS: $pp \rightarrow Z' \rightarrow l^+l^-$ ($\int \mathcal{L}dt=1.1 \text{ fb}^{-1}$) [55];
- CMS: $pp \rightarrow Z'^{\pm} \rightarrow t\bar{t}$ in the electron + jets channel ($\int \mathcal{L}dt=4.33 \text{ fb}^{-1}$) [56].

We will discuss the direct searches in the next chapter in more details.

2.5.3 Parameter constraints

Using all the indirect and direct searches mentioned above, we scan over the parameter space of a few $G(221)$ models to find allowed parameter contours at the 95% confidence level (CL). The NLO QCD corrections to new heavy gauge boson productions are included in the approach described in Sec. III. For each individual NP model the total width is calculated with all the possible decay channels included; see the discussion in Sec. III.

The parameter scan results are plotted in Figs. 2.5, 2.6, 2.7, 2.8, 2.9, 2.10, and 2.11, 2.12, 2.13, 2.14, 2.15, 2.16, and 2.17, 2.18, 2.19, 2.20, 2.21, 2.22. In order to better understand the impact of various experiment data on the parameter space of the $G(221)$ model, we separate the indirect and direct search constraints into three categories: the electroweak indirect constraints (green region) and the direct search constraints from the Tevatron (red region) and the LHC7 (blue region). In Figs. 2.5, 2.6, 2.7, 2.8, 2.9, 2.10, we note the following points:

- For the LRD (LRT) model, the LHC7 data gives stronger constraints on W' and Z' masses than both EWPT and Tevatron data, and excludes the region where the W' mass is smaller than 1.7 TeV (1.8 TeV) and Z' mass is smaller than 2.3 TeV (3.3 TeV);
- For the SQD model, although the W' and Z' with degenerate masses 500 GeV can be allowed by the EWPTs at large c_ϕ , the limits from the Tevatron and the LHC exclude the region where the W' and Z' masses are smaller than 1.5 TeV.
- For all the models except the flavor universal models, such as LRD(T) and SQD, the EWPT data still gives the strongest constraints on the W' and Z' masses, because of the non-universal flavor structure in these models.

- In BP-I, with combined constraints, all the phobic models, in which the couplings of W' to either quarks or leptons are suppressed, can still have relatively light W' around 500 GeV, but heavier Z' (about 1.5 TeV);
- For the non-universal models, such as TFD and UUD, the electroweak indirect constraints are tighter than Tevatron and LHC7 direct search constraints, and push the new gauge boson mass up to more than 2 TeV (TFD) and 3 TeV (UUD), respectively.

In Figs. 2.11, 2.12, 2.13, 2.14, 2.15, 2.16, and 2.17, 2.18, 2.19, 2.20, 2.21, 2.22, we also want to point out:

- In BP-I, the $M_{W'}-c_\phi$ plane shows that small c_ϕ is favored by direct search constraints because the W' coupling is proportional to $1/s_\phi$, which leads to a small W' production rate. However, in the $M_{Z'}-c_\phi$ plane, small c_ϕ is disfavored by direct search constraints because the mass relation $M_{Z'} \simeq M_{W'}/c_\phi$, push the exclusion region of small c_ϕ to larger $M_{Z'}$.
- In BP-II, the shape of the excluded bounds in the small c_ϕ region are very similar for all models because the production cross section of W' and Z' are proportional to $\tan \phi$ in all models such as SQD, TFD, and UUD. Because quarks and leptons are un-unified in UUD, the gauge couplings to leptons are proportional to $\cot \phi$, which implies the large c_ϕ region is also disfavored.
- Within the direct searches, for LRD(T) the most sensitive constraint comes from the W' leptonic decay channel, while for phobic models, the tightest constraints comes from the Z' leptonic decay channel. This explains why the contours in the phobic models have similar shapes, but different from those in the LRD(T) models.

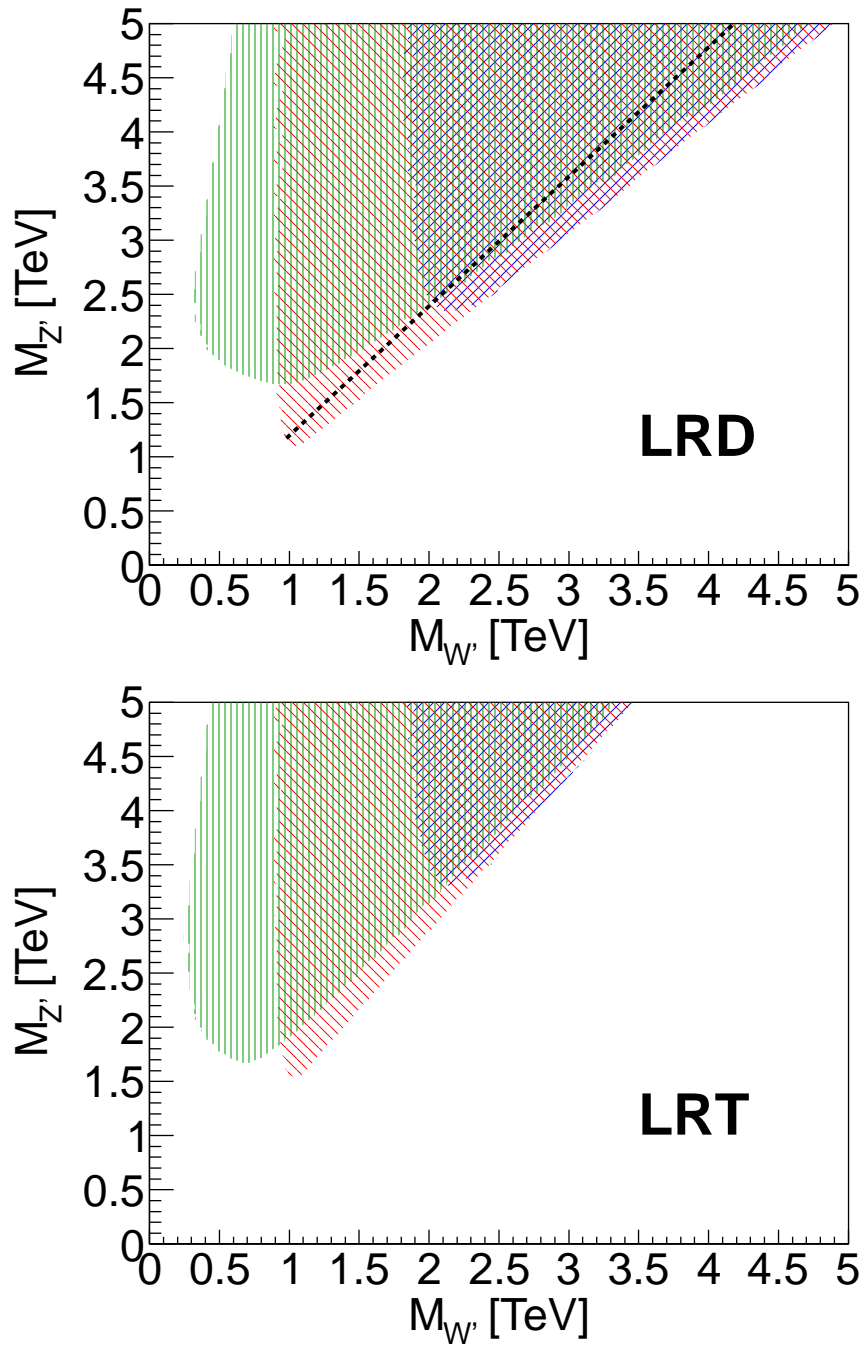


Figure 2.5: Allowed parameter space of the LRD and LRT models at 95% CL in the $M_{W'}$ – $M_{Z'}$ plane after including indirect and direct constraints: EWPTs (green), Tevatron (red) and LHC7 (blue).

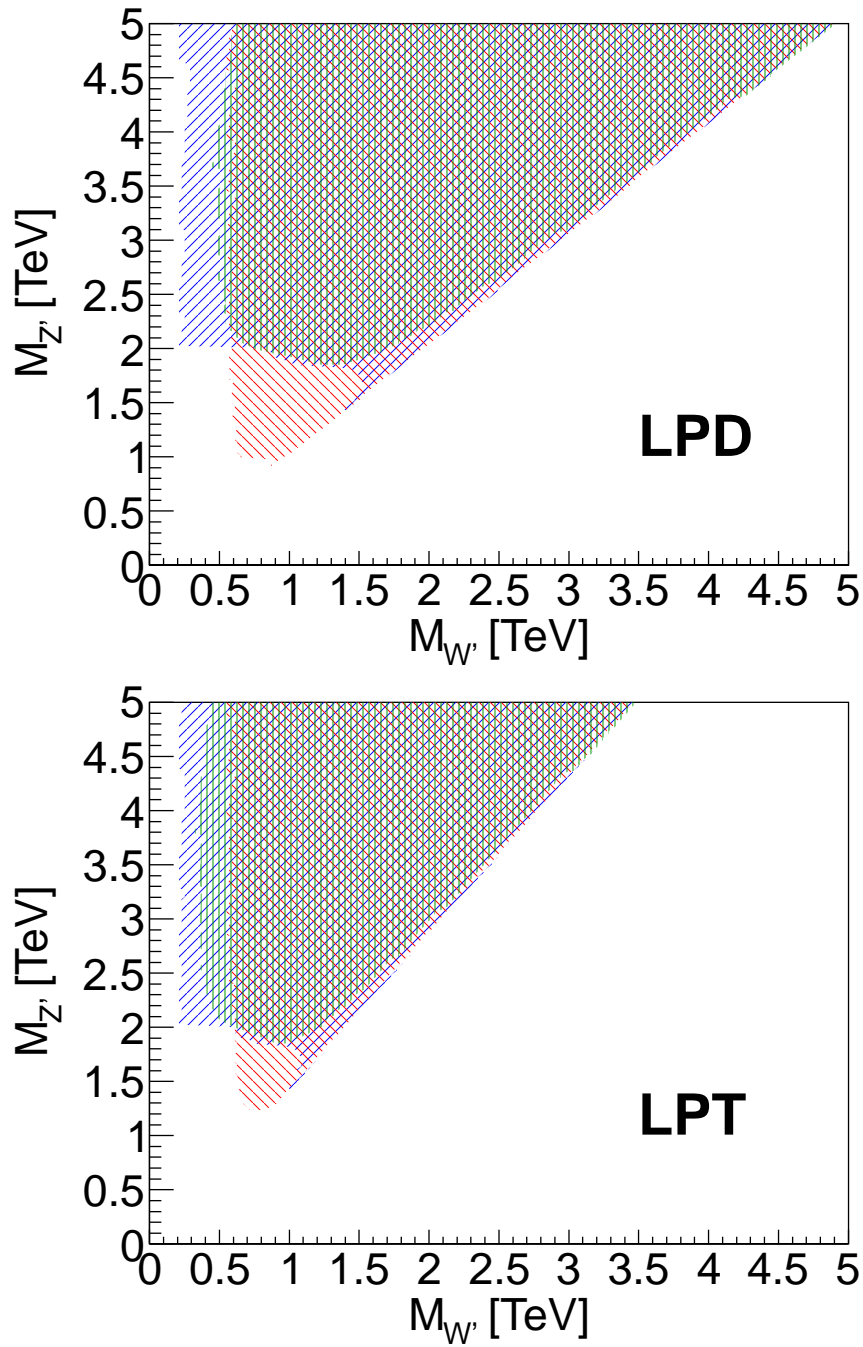


Figure 2.6: Allowed parameter space of the LPD and LPT models at 95% CL in the $M_{W'}$ – $M_{Z'}$ plane after including indirect and direct constraints: EWPTs (green), Tevatron (red) and LHC7 (blue).

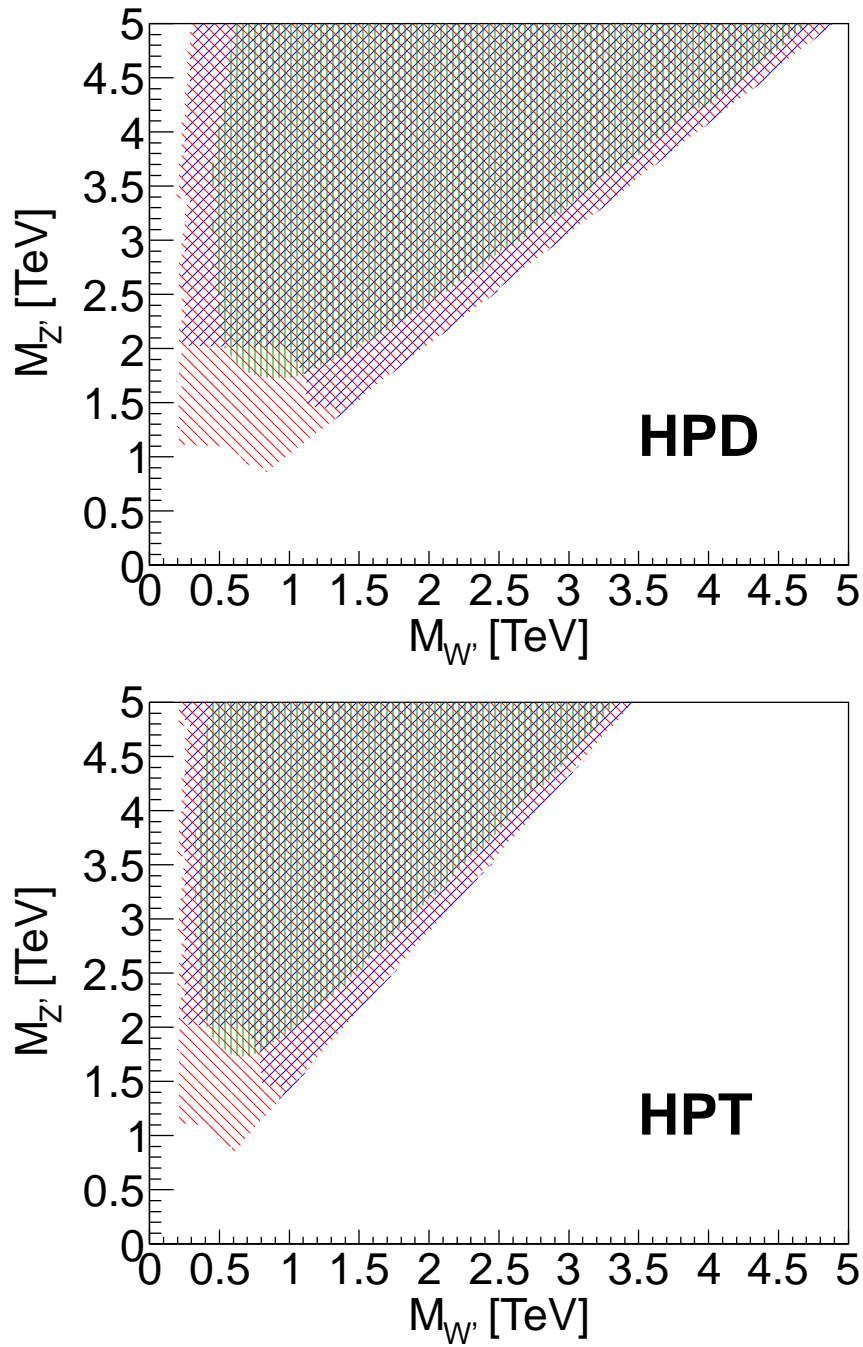


Figure 2.7: Allowed parameter space of the HPD and HPT models at 95% CL in the $M_{W'}$ – $M_{Z'}$ plane after including indirect and direct constraints: EWPTs (green), Tevatron (red) and LHC7 (blue).

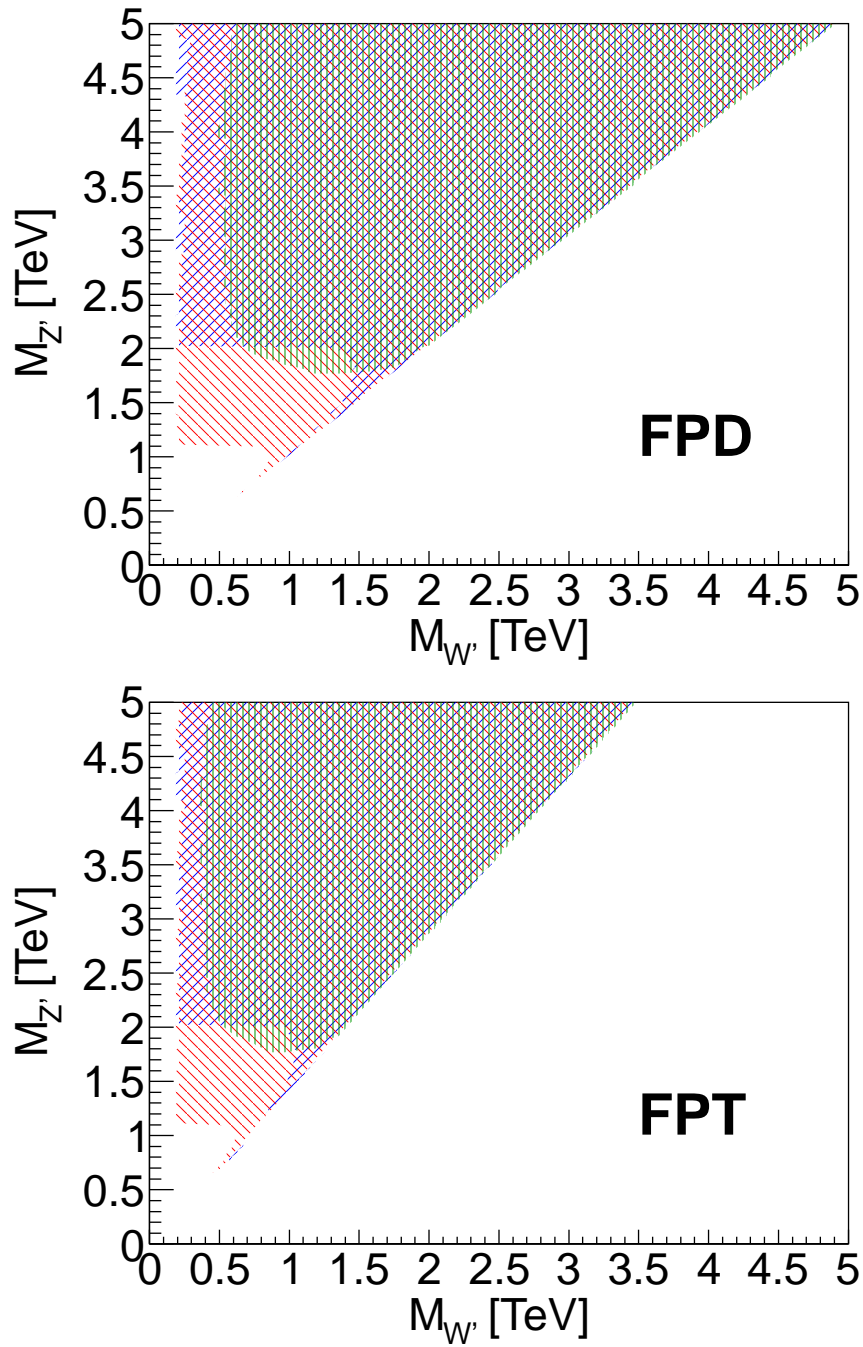


Figure 2.8: Allowed parameter space of the FPD and FPT models at 95% CL in the $M_{W'}$ – $M_{Z'}$ plane after including indirect and direct constraints: EWPTs (green), Tevatron (red) and LHC7 (blue).

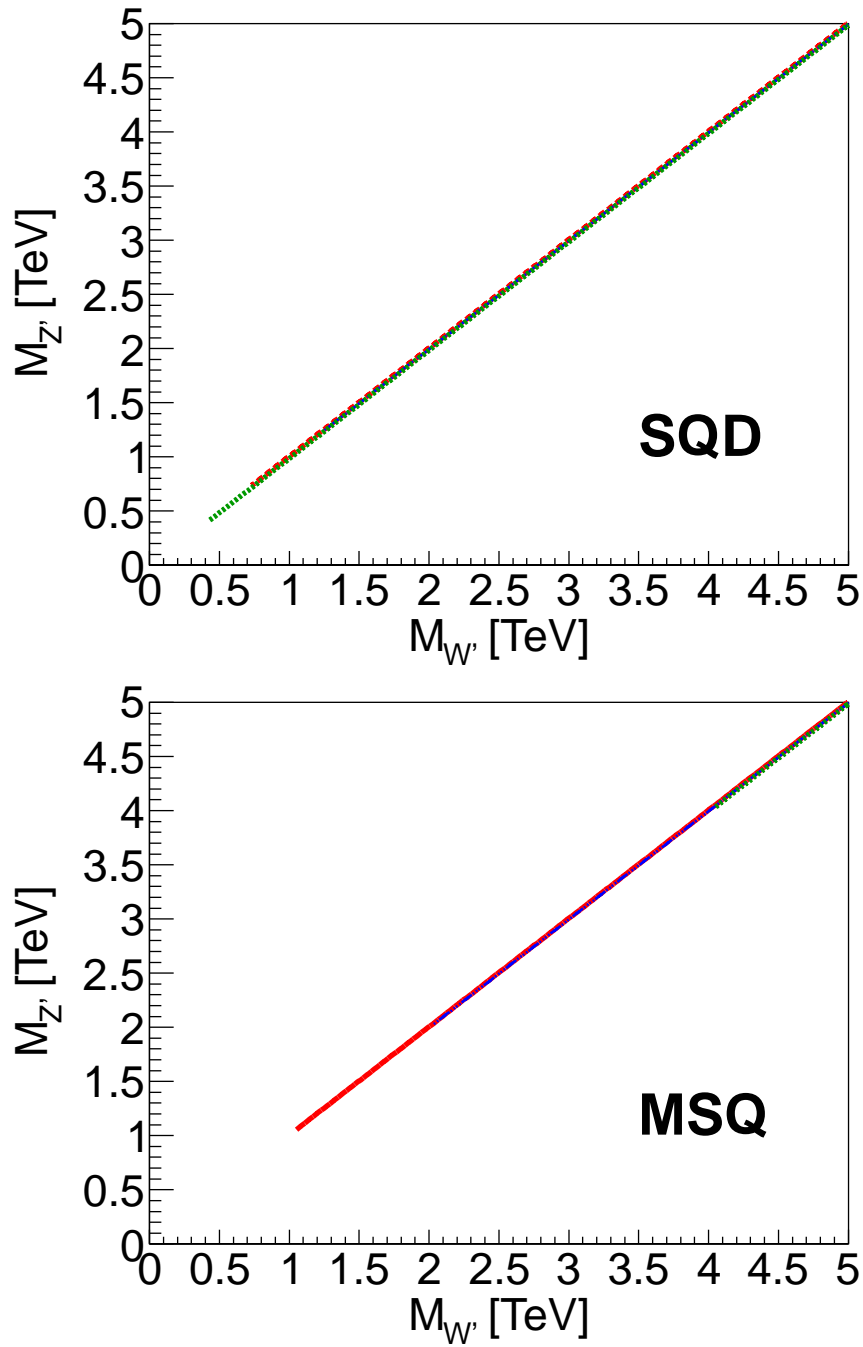


Figure 2.9: Allowed parameter space of the SQD and MSQ models at 95% CL in the $M_{W'}$ – $M_{Z'}$ plane after including indirect and direct constraints: EWPTs (green), Tevatron (red) and LHC7 (blue).

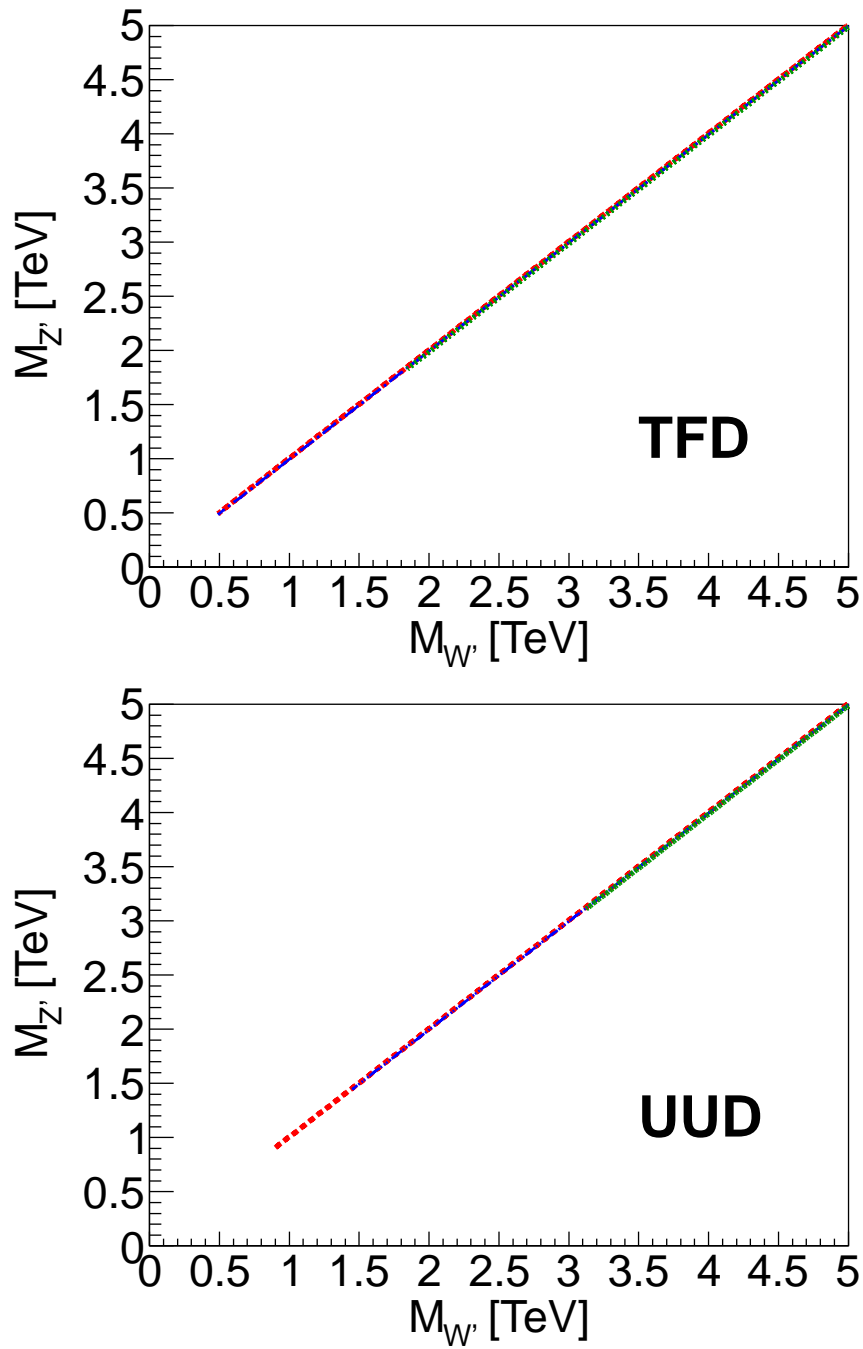


Figure 2.10: Allowed parameter space of the TFD and UUD models at 95% CL in the $M_{W'} - M_{Z'}$ plane after including indirect and direct constraints: EWPTs (green), Tevatron (red) and LHC7 (blue).

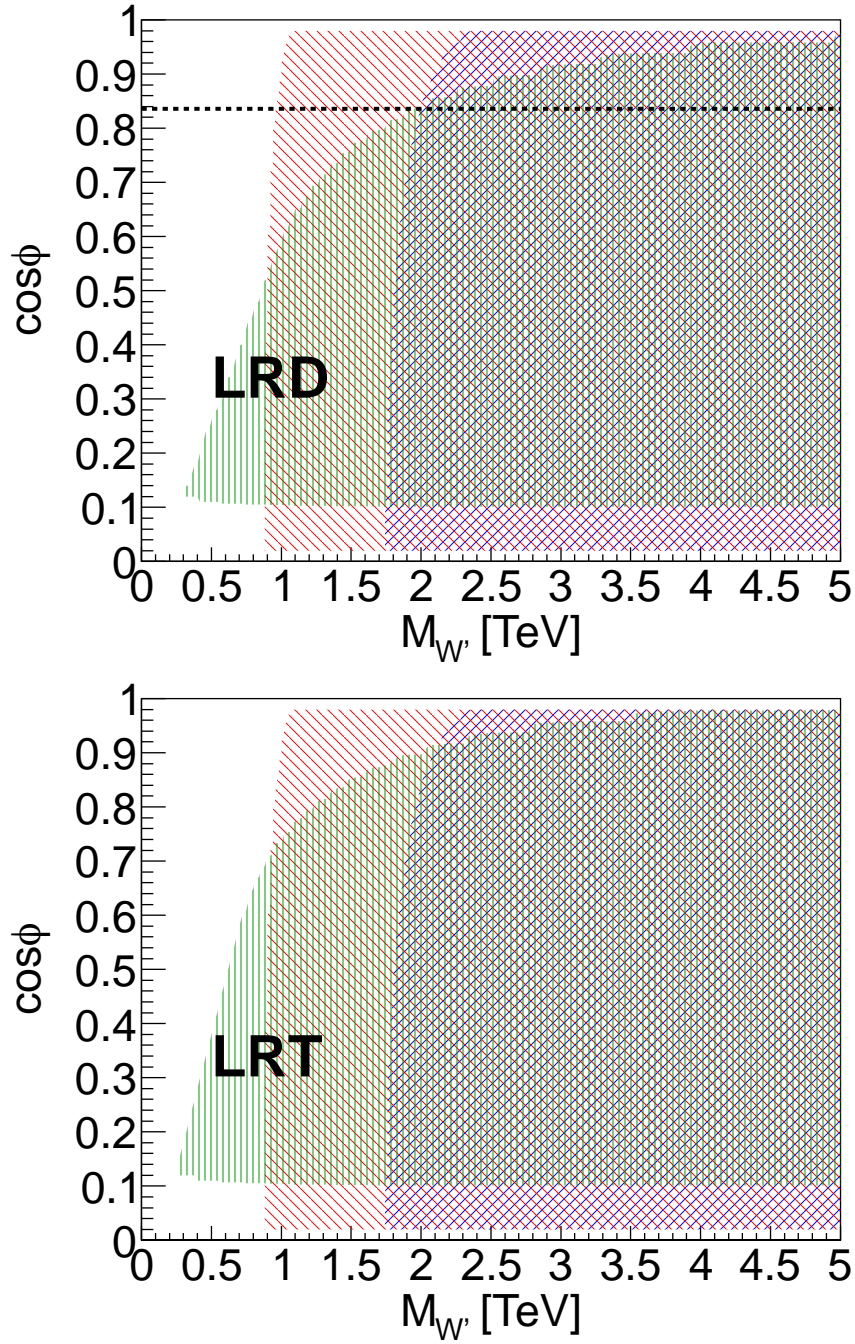


Figure 2.11: Allowed parameter space of the LRD and LRT models at 95% CL in the $M_{W'} - c_\phi$ plane after including indirect and direct constraints: EWPTs (green), Tevatron (red) and LHC7 (blue). The dashed black lines in LRD represent MLR models.

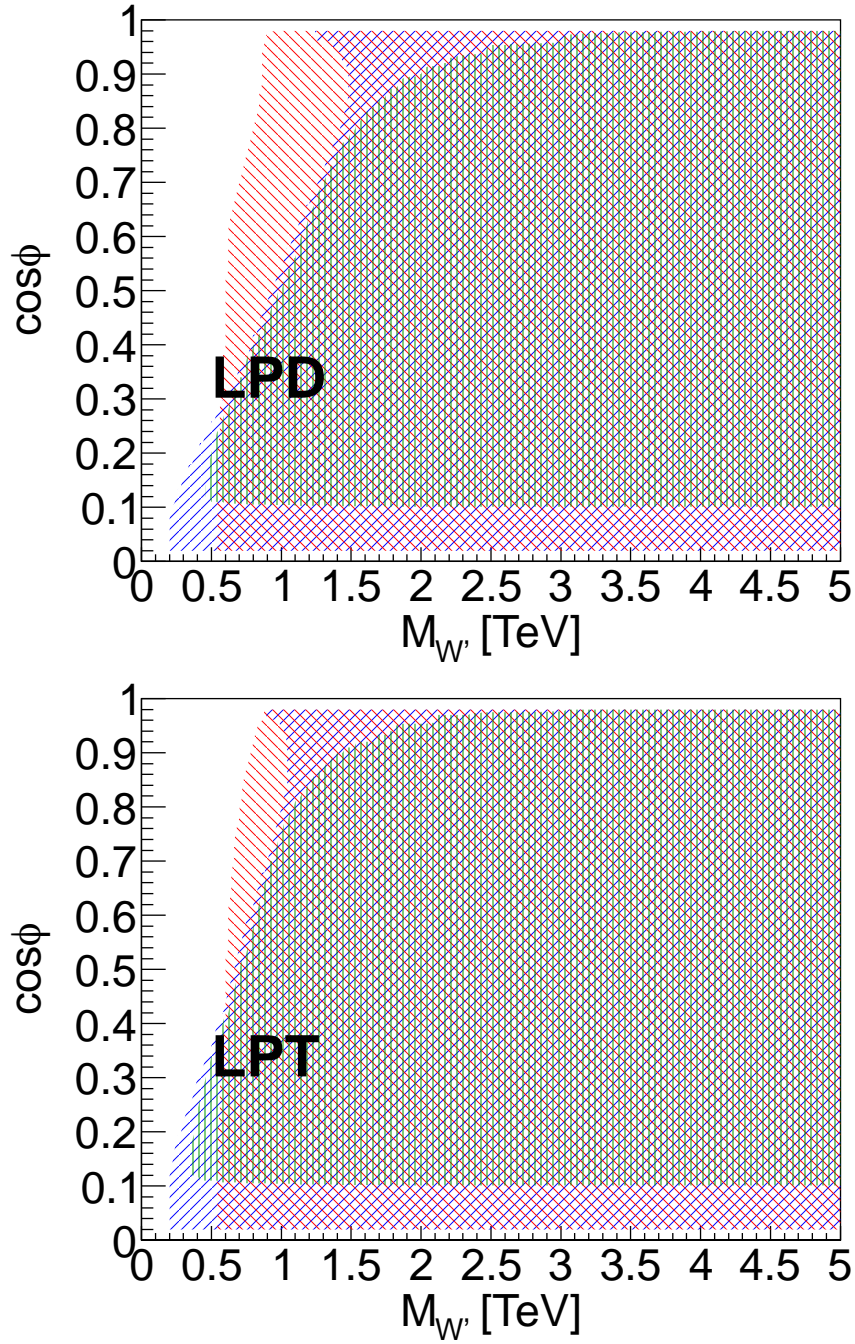


Figure 2.12: Allowed parameter space of the LPD and LPT models at 95% CL in the $M_{W'} - c_\phi$ plane after including indirect and direct constraints: EWPTs (green), Tevatron (red) and LHC7 (blue).

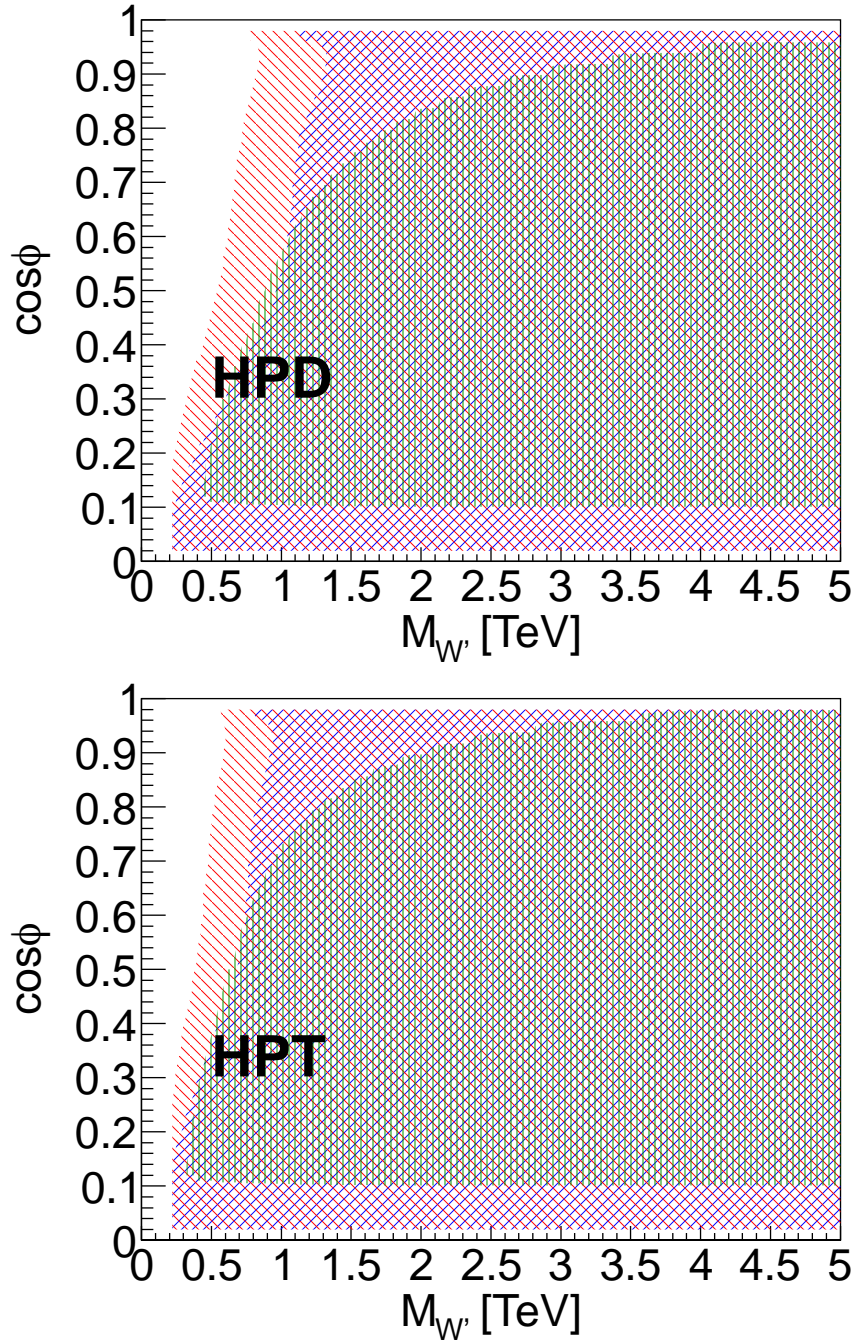


Figure 2.13: Allowed parameter space of the HPD and HPT models at 95% CL in the $M_{W'} - c_\phi$ plane after including indirect and direct constraints: EWPTs (green), Tevatron (red) and LHC7 (blue).

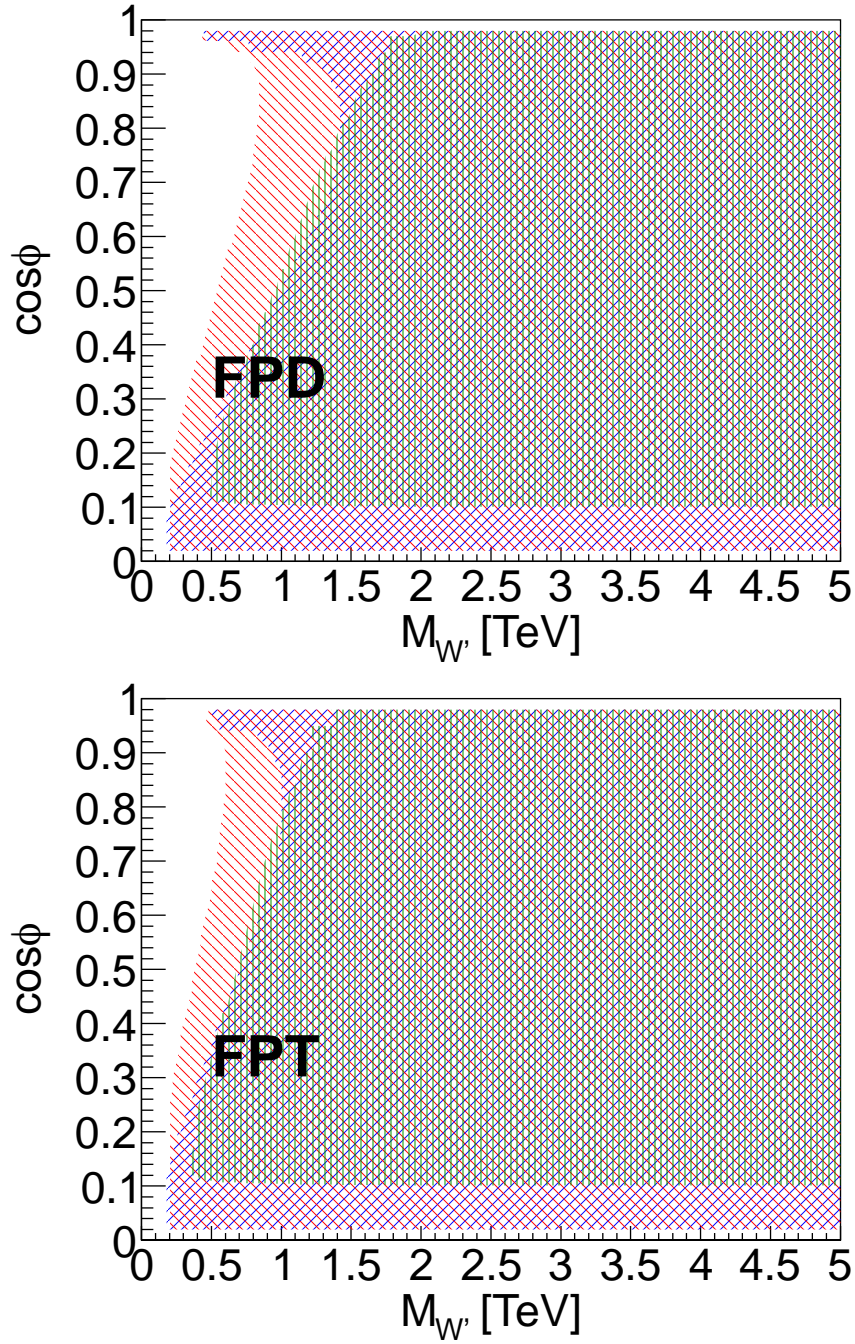


Figure 2.14: Allowed parameter space of the FPD and FPT models at 95% CL in the $M_{W'} - c_\phi$ plane after including indirect and direct constraints: EWPTs (green), Tevatron (red) and LHC7 (blue).

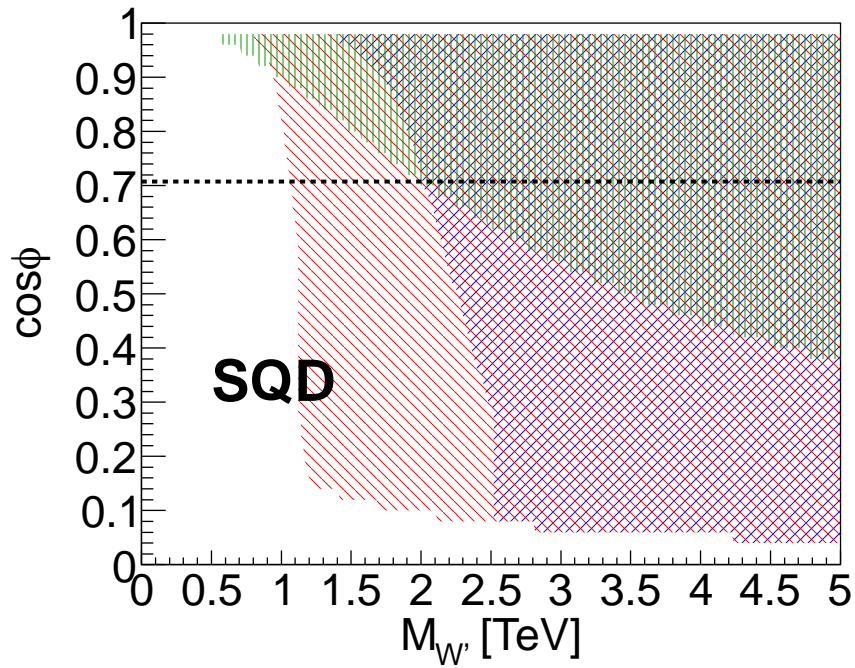


Figure 2.15: Allowed parameter space of the SQD models at 95% CL in the $M_{W'} - c_\phi$ plane after including indirect and direct constraints: EWPTs (green), Tevatron (red) and LHC7 (blue). The dashed black lines represent MSQ models.

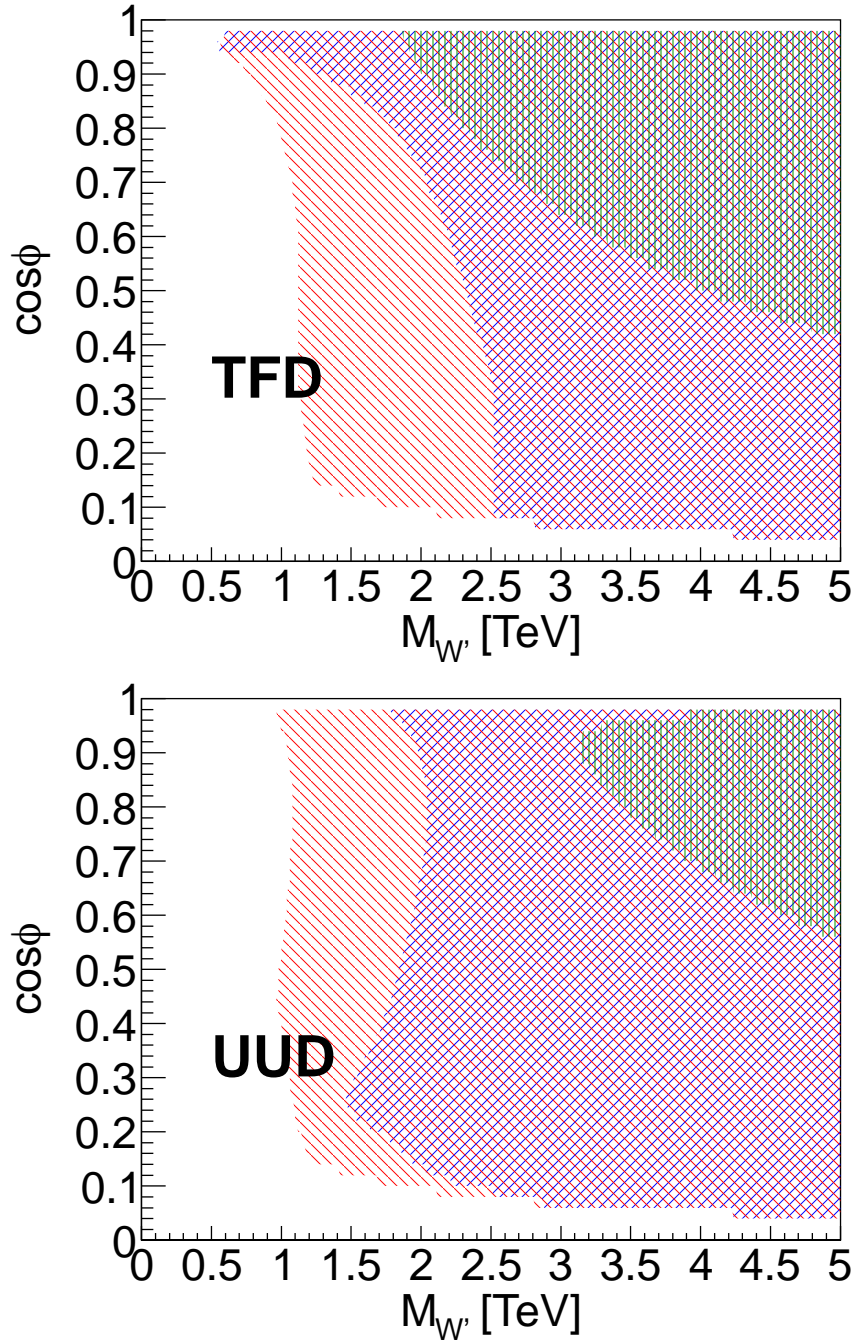


Figure 2.16: Allowed parameter space of the TFD and UUQ models at 95% CL in the $M_{W'} - c_\phi$ plane after including indirect and direct constraints: EWPTs (green), Tevatron (red) and LHC7 (blue).

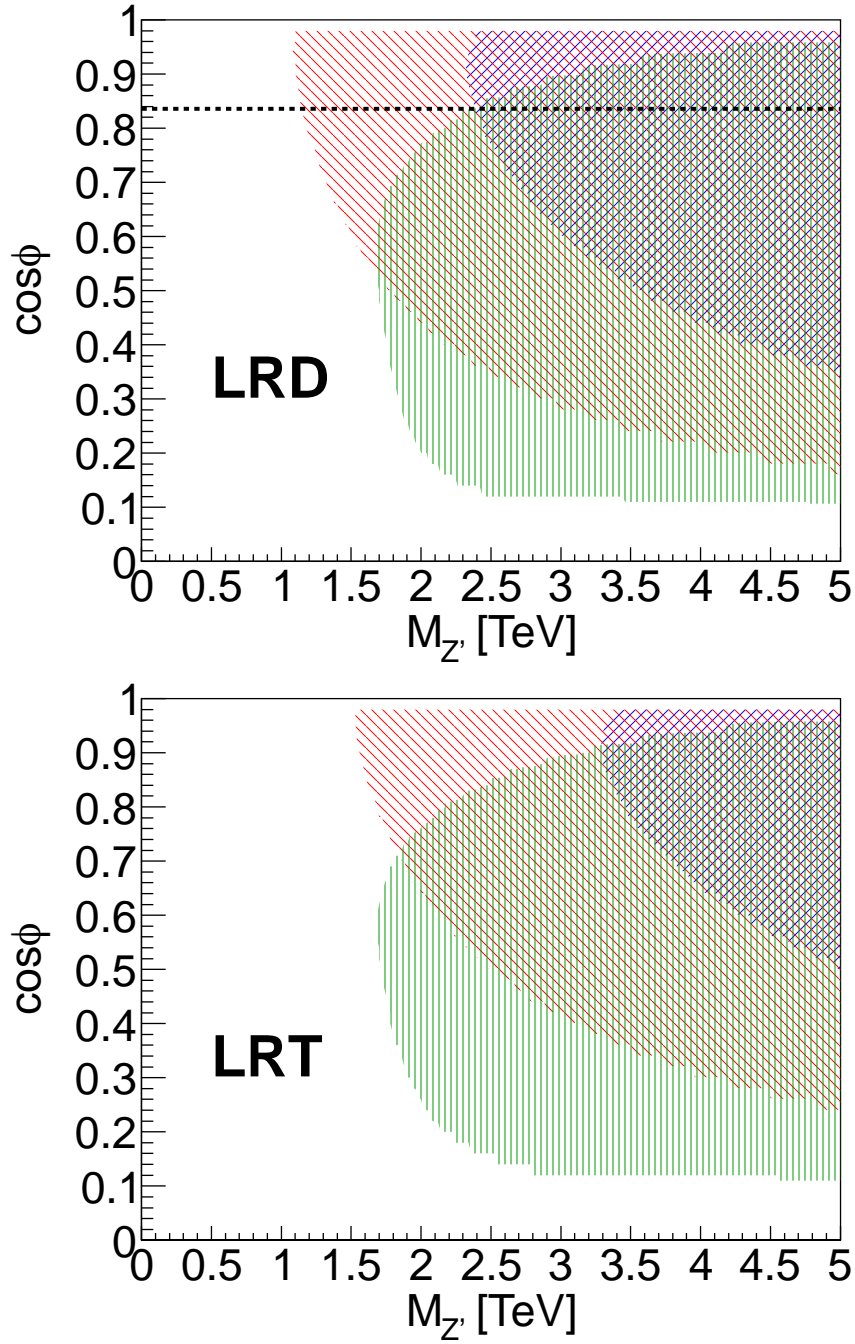


Figure 2.17: Allowed parameter space of the LRD and LRT models at 95% CL in the $M_{Z'} - c_\phi$ plane after including indirect and direct constraints: EWPTs (green), Tevatron (red) and LHC7 (blue). The dashed black lines in LRD represent MLR models.

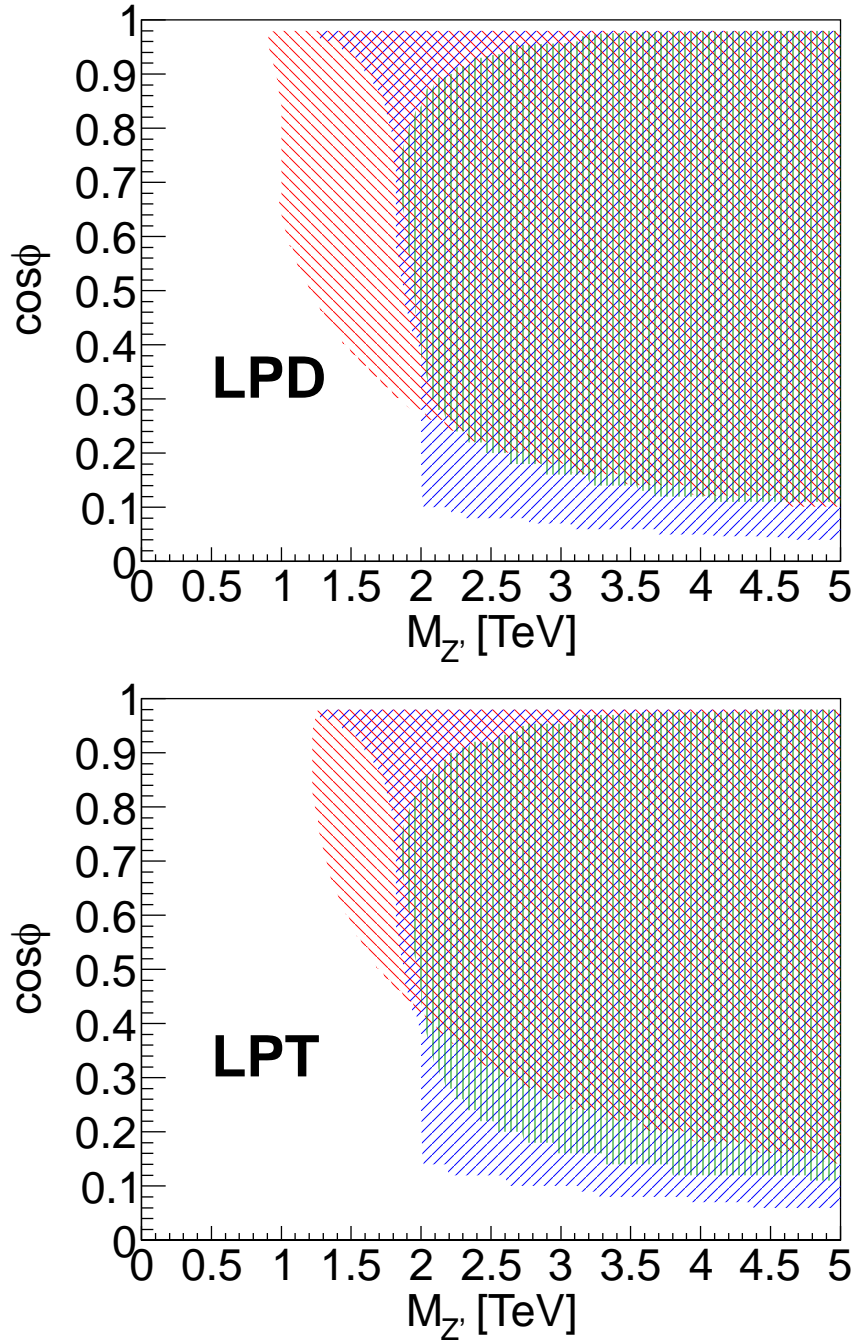


Figure 2.18: Allowed parameter space of the LPD and LPT models at 95% CL in the $M_{Z'} - c_\phi$ plane after including indirect and direct constraints: EWPTs (green), Tevatron (red) and LHC7 (blue).

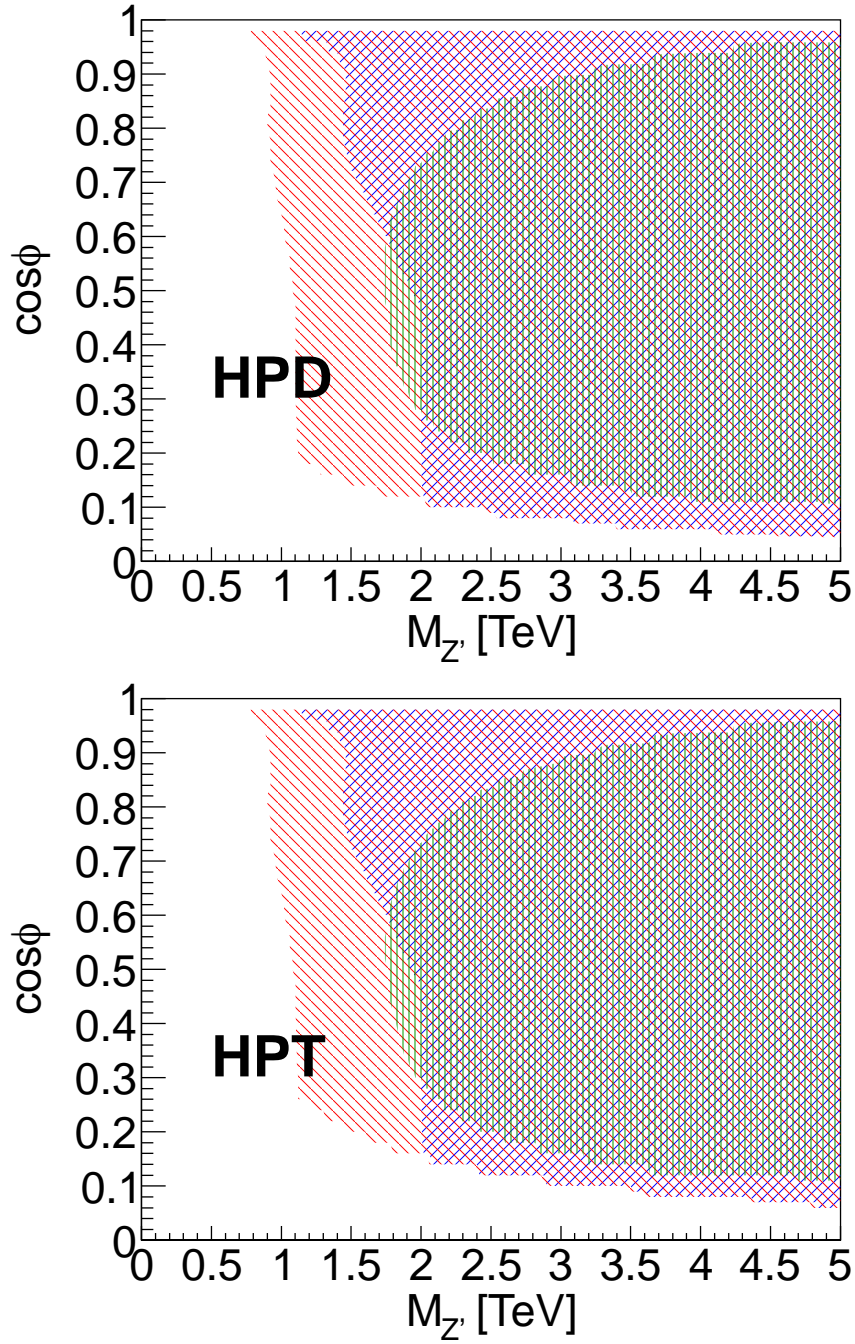


Figure 2.19: Allowed parameter space of the HPD and HPT models at 95% CL in the $M_{Z'} - c_\phi$ plane after including indirect and direct constraints: EWPTs (green), Tevatron (red) and LHC7 (blue).

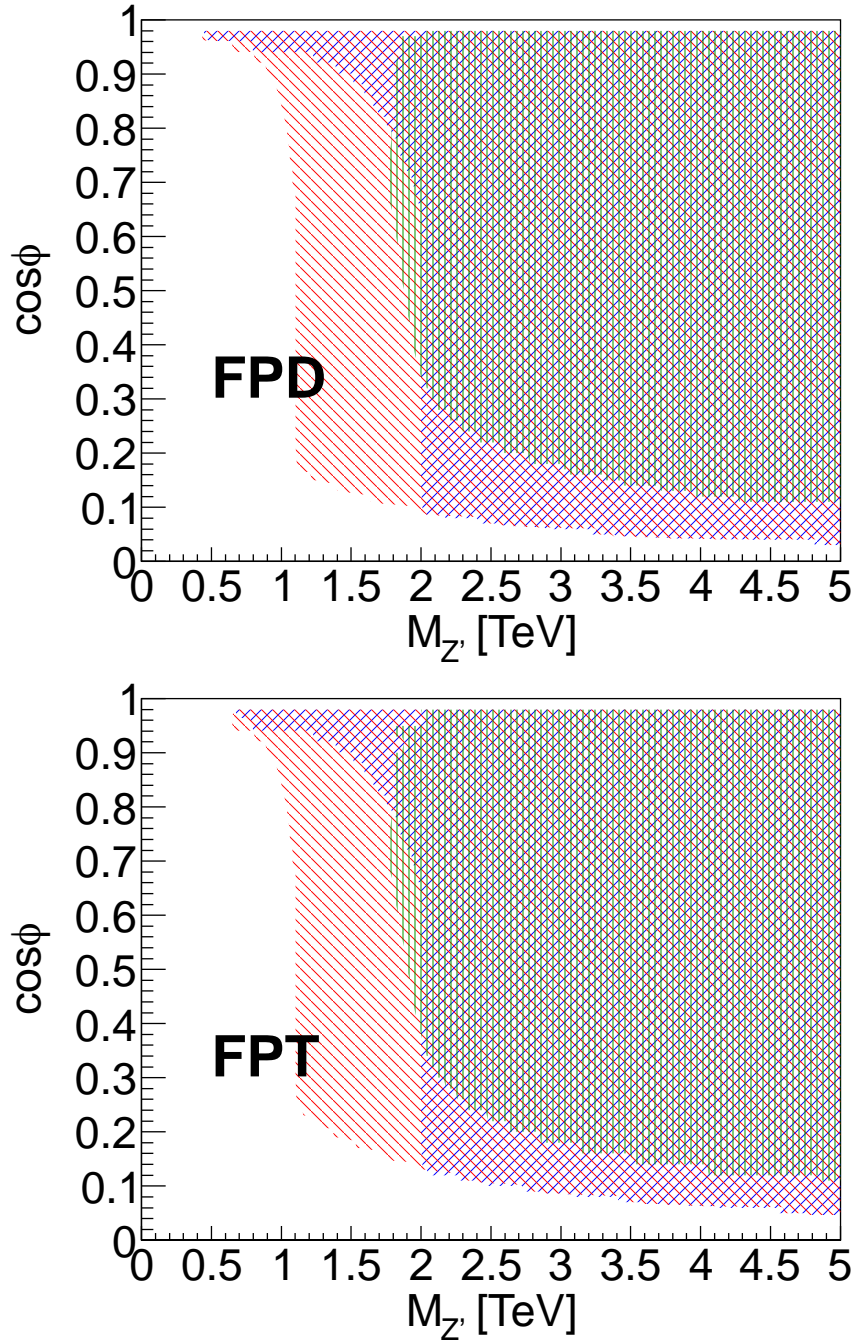


Figure 2.20: Allowed parameter space of the FPD and FPT models at 95% CL in the $M_{Z'} - c_\phi$ plane after including indirect and direct constraints: EWPTs (green), Tevatron (red) and LHC7 (blue).

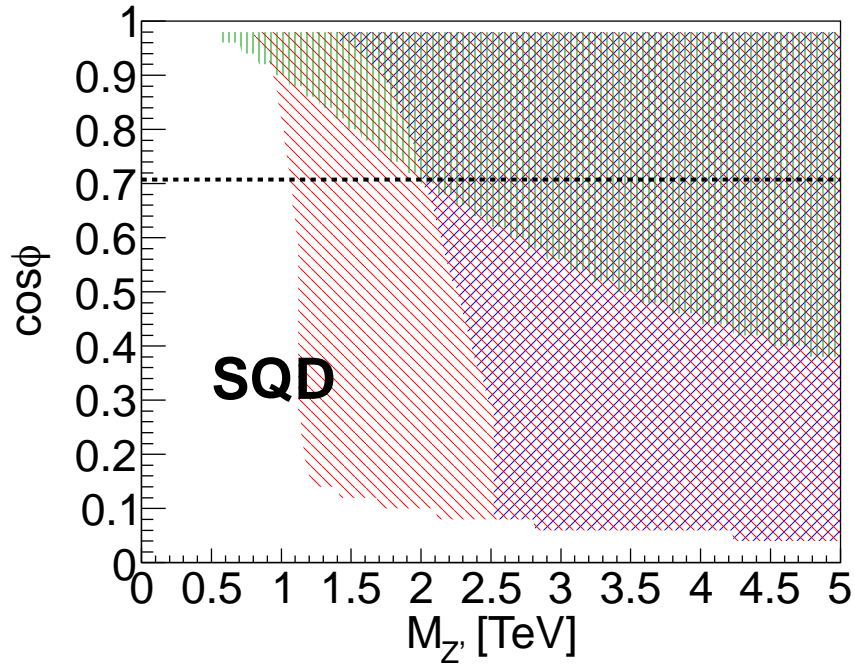


Figure 2.21: Allowed parameter space of the SQD models at 95% CL in the $M_{Z'} - c_\phi$ plane after including indirect and direct constraints: EWPTs (green), Tevatron (red) and LHC7 (blue). The dashed black lines represent MSQ models.

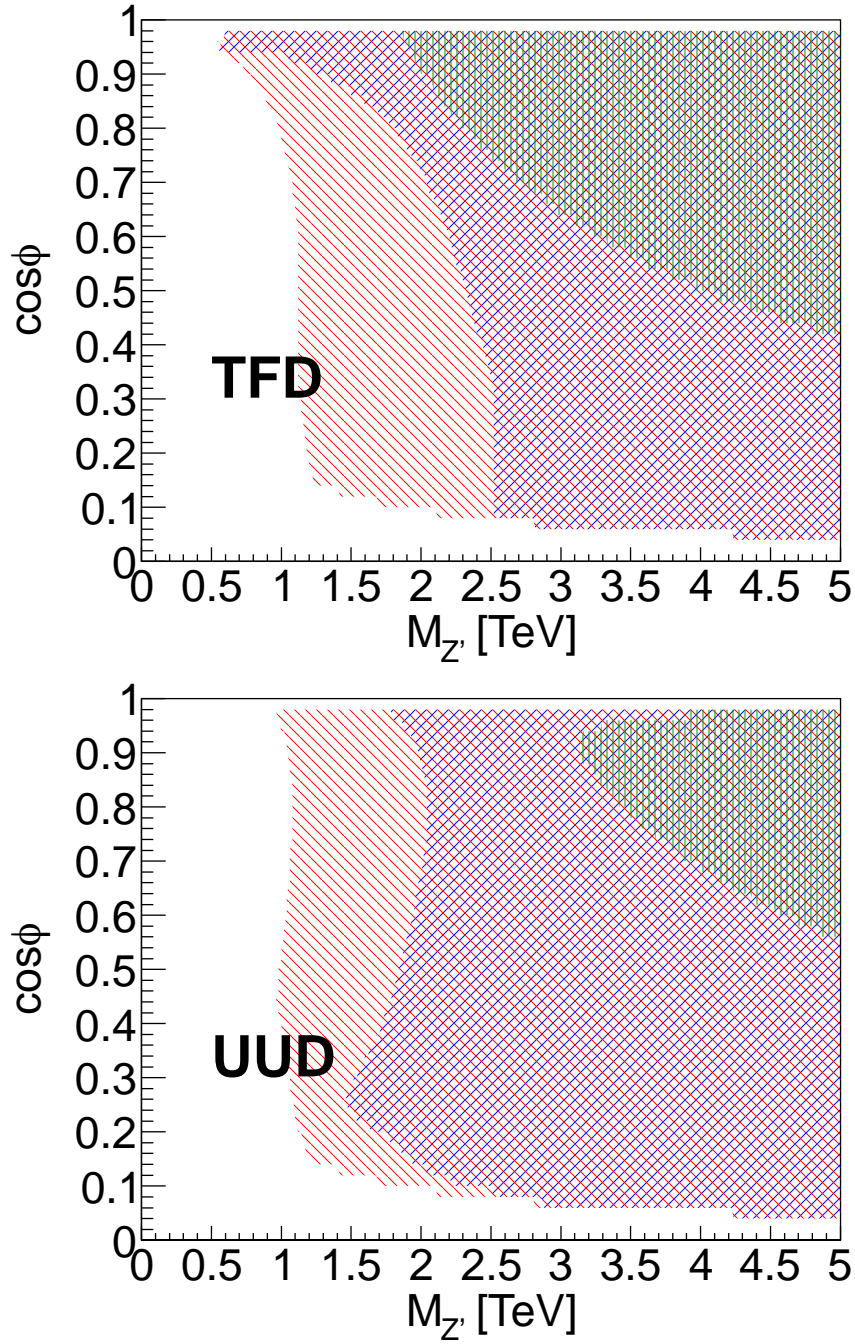


Figure 2.22: Allowed parameter space of the TFD and UUQ models at 95% CL in the $M_{Z'} - c_\phi$ plane after including indirect and direct constraints: EWPTs (green), Tevatron (red) and LHC7 (blue).

2.6 Summary

We classified the $G(221)$ models (including the left-right (LR), leptophobic (LP), hadrophobic (HP) and fermiophobic (FP) as well as the ununified (UU) and top-flavor(TF)) models in a unified view in terms of the patterns of symmetry breaking and the gauge couplings of fermions. We analyzed the constraints on the masses of the heavy gauge bosons of the $G(221)$ models. We performed a global-fit analysis about a set of 37 electroweak observables, including Z pole data, the mass and the width of the W^\pm boson, and various low-energy observables. Moreover, the direct search for the W' and Z' bosons at the Fermilab Tevatron and CERN LHC could further constrain the $G(221)$ model parameter space. The experimental precision with which these observables have been measured allows us to put strong bounds on the parameter space of the $G(221)$ models and to constrain the masses of the Z' and W'^\pm bosons. We presented our key results in terms of 95% C.L. contours of the allowed regions both on the $M_{W'}-\cos\phi$ plane, as well as on the $M_{Z'}-M_{W'}$ plane, from which we can readily give the lower bounds on the masses of the W' and Z' , which can be used as a guide for future collider searches.

Chapter 3

DISCOVERY OF HEAVY CHARGED GAUGE BOSONS

3.1 Introduction

At the Large Hadron Collider (LHC), it is very promising to search for the heavy Z' and W' bosons through their single production channel as an s -channel resonance with their subsequent leptonic decays [65]. It yields the simplest event topology to discover the Z' and/or W' with a large production rate and clean experimental signature. These channels may be one of the most promising early discoveries at the LHC [48, 49, 54, 55]. There are many theoretical studies of searching for the Z' boson at the LHC [33, 62, 64, 63, 67]. However, the study the discovery potential of the W' boson at the LHC has fared somewhat less well [66]. In many NP models with extended gauge groups, the W' boson emerges together with the Z' boson after symmetry breaking, and usually, the W' boson is lighter than, or equal to, the Z' boson. It is therefore possible to discover the W' prior to the Z' .

More often, the masses of the W' and Z' bosons are not generally independent, and so as their couplings to the SM fermions. Hence, the discovery potential of the W' and Z' at the LHC could be highly correlated. In this paper we present a comprehensive study of discovery potentials of both the W' and Z' bosons in the $G(221)$ model at the LHC.

The $G(221)$ model is the minimal extension of the SM gauge group to include both the W' and Z' bosons. Its gauge structure is $SU(2) \otimes SU(2) \otimes U(1)$ [11, 12, 13, 27, 25, 26, 28, 29, 31, 30, 32, 24]. The model can be viewed as the low energy effective theory of many NP models with extended gauge structure when all the heavy particles other than the W' and Z' decouple. In this chapter, based on a linearized effective theory including the $SU(2) \times SU(2) \times U(1)$ gauge group, we present the collider phenomenology related to the simplest event topology in the resonance Z' and W' processes aimed at the early discovery.

In the TeV scale, different symmetry breaking patterns will induce different Z' and W' mass relations. In breaking pattern I, which has the $SU(2) \otimes U(1)$ breaking down to $U(1)_Y$, the W' mass is always smaller than the Z' mass; while in breaking pattern II, the $SU(2) \otimes SU(2)$ breaking down to $SU(2)_L$ requires the W' and Z' have the same mass at tree level. This feature could assist us to distinguish these two breaking patterns after the W' and Z' are discovered.

3.2 Drell-Yan Production and Decay at Next-to-Leading Order

At the hadron collider, the total cross section can be written as the convolution of the parton cross section and parton distribution functions, as follows,

$$\sigma = \int dx_1 dx_2 \sum_{i,j} f_{i/A}(x_1) f_{j/B}(x_2) \cdot \sigma_{ij}(x_1 x_2 s), \quad (3.1)$$

with s is the Lab energy of (A, B) , and the c.m. energy of (a, b) is determined by $\hat{s} = x_1 x_2 s$.

One can also keep the x_2 unintegrated, with $x_1 = \frac{\tau}{x_2}$. With this variable change, the

Jacobian is

$$\frac{\partial(\tau, x)}{\partial(x_1, x_2)} = \begin{vmatrix} x_2 & x_1 \\ 0 & 1 \end{vmatrix} = x_2. \quad (3.2)$$

So the integration will be

$$\int_{\tau_0}^1 d\tau \int_{\tau}^1 \frac{dx_2}{x_2}. \quad (3.3)$$

Taking into account the $\frac{1}{\hat{s}}$ behavior of the hard-scattering processes as $\hat{s}\hat{\sigma}(\hat{s})$, the parton luminosity \mathcal{L} is

$$\sigma = \int_{\tau_0}^1 \frac{d\tau}{\tau} \cdot \mathcal{L}(\tau) \cdot [\hat{s}\hat{\sigma}(\hat{s})] \quad (3.4)$$

with

$$\mathcal{L}(\tau) = \frac{\tau}{\hat{s}} \frac{1}{1 + \delta_{ij}} \int_{\tau}^1 \frac{dx}{x} \sum (f_i(\tau/x) f_j(x) + f_i(x) f_j(\tau/x)). \quad (3.5)$$

where i and j denote the initial state partons and $f_i^{(a)}(x)$ is the parton distribution of the parton i inside the hadron a with a momentum fraction of $x = p_i/p_a$. The parton luminosity

has dimensions of a cross section, is a convenient measure of the reach of a collider of given energy and hadron-hadron luminosity.

At the LHC, the cross section of $pp \rightarrow V' \rightarrow \bar{f}f'$ ($V' = W'/Z'$) is

$$\sigma_{pp \rightarrow V' \rightarrow \bar{f}f'} = \sum_{\{ij\}} \int_{\tau_0}^1 \frac{d\tau}{\tau} \cdot \mathcal{L}_{ij}(\tau) \cdot [\hat{s} \hat{\sigma}_{ij \rightarrow V' \rightarrow \bar{f}f'}(\hat{s})], \quad (3.6)$$

where $\tau \equiv \hat{s}/s$. The lower limit of the τ variable is determined by the kinematic threshold of the V' production, i.e. $\tau_0 = M_{V'}^2/s$. Using the narrow width approximation (NWA) one can factorize the $pp \rightarrow V' \rightarrow \bar{f}f'$ process into the V' production and the V' decay,

$$\sigma_{pp \rightarrow V' \rightarrow \bar{f}f'} = \left(\sum_{\{ij\}} \int_{\tau_0}^1 \frac{d\tau}{\tau} \cdot \frac{1}{s} \frac{d\mathcal{L}_{ij}}{d\tau} \cdot [\hat{s} \hat{\sigma}_{ij \rightarrow V'}(\hat{s})] \right) \times \text{Br}(V' \rightarrow \bar{f}f'), \quad (3.7)$$

where the branching ratio (Br) is defined as $\text{Br}(V' \rightarrow \bar{f}f') = \Gamma(V' \rightarrow \bar{f}f')/\Gamma_{\text{tot}}$. As to be shown later, the decay widths of Z' and W' bosons in most of the allowed parameter space are much smaller than their masses, which validates the NWA adapted in this work.

3.2.1 Drell-Yan Production at the NLO

At the next-to-leading-order (NLO) the partonic cross section of the V' production is

$$\hat{\sigma}_{ij \rightarrow V'}(\hat{s}) = \frac{\pi}{6\hat{s}} g_2^2 (g_L^2 + g_R^2) H_{ij} \left(\frac{M_{V'}^2}{\hat{s}} \right), \quad (3.8)$$

where the functions $H_{ij}(z)$ for different parton flavors $ij = (\bar{q}q', qq, \bar{q}g)$ are

$$\begin{aligned}
H_{\bar{q}q'}(z) &= \delta(1-z) \\
&+ \frac{\alpha_s}{2\pi} C_F \left[\left(\frac{2\pi^2}{3} - 8 \right) \delta(1-z) - \frac{2(1+z^2)}{1-z} \log(z) \right. \\
&\left. + 4(1+z^2) \left(\frac{\log(1-z)}{1-z} \right)_+ \right], \tag{3.9}
\end{aligned}$$

and

$$H_{qg}(z) = H_{\bar{q}g}(z) = \frac{\alpha_s}{2\pi} T_F \left[\left(z^2 + (1-z)^2 \right) \log \frac{(1+z)^2}{z} + \frac{1}{2} + 3z - \frac{7}{2}z^2 \right]. \tag{3.10}$$

Here, C_F and T_F are the color factor defined as $C_F = 4/3$ and $T_F = 1/2$. The plus function has the properties such as

$$\begin{aligned}
\int_{z_0}^1 dz f(z) \left(\frac{\log(1-z)}{1-z} \right)_+ &= \int_{z_0}^1 dz f(z) \frac{\log(1-z)}{1-z} \\
&- \int_{z_0}^1 f(z) \delta(1-z) \int_{z_0}^1 dz' \frac{\log(1-z')}{1-z'}, \tag{3.11}
\end{aligned}$$

where $f(z)$ is a function including parton luminosity. In the soft limit $z \rightarrow 1$, the plus function is still finite.

It is convenient to parametrize the V' production cross section into one model-dependent piece $C_q^{V'}$ and another model-independent piece $F_q^{V'}(M_{V'}, \sqrt{s})$. The first piece consists of model couplings, while the second piece, which includes all the hadronic contributions [62], depends on $m_{V'}$ and \sqrt{s} only. We separate the up-quark and down-quark contributions in the Z' production because Z' couples quite differently to up- and down-quarks in a few NP

models. The NLO cross sections of Z' and W' production then can be expressed as

$$\begin{aligned}\sigma_{pp \rightarrow Z' \rightarrow ff} &= \frac{\pi}{6} [C_u^{Z'} F_u^{Z'}(M_{V'}, \sqrt{s}) + C_d^{Z'} F_d^{Z'}(M_{V'}, \sqrt{s})], \\ \sigma_{pp \rightarrow W' \rightarrow ff'} &= \frac{\pi}{6} [C_q^{W'} F_q^{W'}(M_{V'}, \sqrt{s})],\end{aligned}\tag{3.12}$$

where

$$C_q^{V'} = g_2^2 (f_L^2 + f_R^2) \times \text{Br}(V' \rightarrow ff'),\tag{3.13}$$

$$\begin{aligned}F_q^{V'}(M_{V'}, \sqrt{s}) &= \int_{\tau_0}^1 \frac{d\tau}{\tau} \cdot \left[\mathcal{L}_{q\bar{q}}(\tau) \cdot H_{\bar{q}q'}(z) + \mathcal{L}_{qg}(\tau) \cdot H_{\bar{q}g}(z) + (\bar{q} \rightarrow q) \right], \\ &= \int_{\frac{M^2}{s}}^1 \frac{dz}{z} \cdot \left[\mathcal{L}_{q\bar{q}}\left(\frac{M^2}{zs}\right) \cdot H_{\bar{q}q'}(z) + \mathcal{L}_{qg}\left(\frac{M^2}{zs}\right) \cdot H_{\bar{q}g}(z) \right. \\ &\quad \left. + (\bar{q} \rightarrow q) \right]\end{aligned}\tag{3.14}$$

$$\tag{3.15}$$

Note that the decay branching ratio is allocated to the model-dependent piece $C_q^{V'}$. After convoluting with PDFs, the model-independent piece $F_q^{V'}$ is merely a function of $m_{V'}$ and the collider energy \sqrt{s} .

As the model dependent couplings can be factorized out, the total cross section in the sequential W' and Z' models can be used as the reference cross section. The upper panels of Fig. 3.1 show the LO and NLO production cross sections of the sequential W' (left) and Z' boson (right) as a function of the extra gauge boson mass at the Tevatron, the 7 TeV and 14 TeV LHC. The lower panels display the K-factor, defined as the ratio of the NLO and LO cross sections. In the upper panels of Fig. 3.3 we plot the cross section of Z' production induced by $u\bar{u}$ (left) and $d\bar{d}$ (right) initial state, respectively. Again, the lower panels show the corresponding K -factors. Note that the K -factors are model independent

once one separates the up-quark and down-quark contributions in the Z' production. The K -factor is defined as

$$K_q = \frac{\sigma_{NLO}}{\sigma_{LO}} = \frac{F_q^{V'}(M_{V'}, \sqrt{s})_{NLO}}{F_q^{V'_{\text{seq}}}(M_{V'}, \sqrt{s})_{LO}}. \quad (3.16)$$

Here we adopt the CTEQ6.6M parton distribution package [68] for both the LO and NLO calculations. Both the factorization and renormalization scales are set to be $M_{V'}$.

The NLO cross section of other NP models can be obtained easily from the sequential W' and Z' cross sections plotted in Figs. 3.1, 3.2 and 3.3, 3.4 by:

- scaling the model-dependent $C^{V'}$ -coefficients ($C_u^{Z'}/C_u^{Z'_{\text{seq}}}$, $C_d^{Z'}/C_d^{Z'_{\text{seq}}}$, $C_q^{W'}/C_q^{W'_{\text{seq}}}$),
- including the NLO QCD correction with the inclusive K -factors (K_u , K_d and K_q).

To be more specific, the NLO cross sections of new gauge boson productions in the $G(221)$ model are

$$\begin{aligned} \sigma_{W'} &= \frac{C_q^{W'}}{C_q^{W'_{\text{seq}}}} \left(F_q^{W'} \right)_{\text{LO}} \times K_q, \\ \sigma_{Z'} &= \frac{C_u^{Z'}}{C_u^{Z'_{\text{seq}}}} \left(F_u^{Z'} \right)_{\text{LO}} \times K_u + \frac{C_d^{Z'}}{C_d^{Z'_{\text{seq}}}} \left(F_d^{Z'} \right)_{\text{LO}} \times K_d. \end{aligned} \quad (3.17)$$

3.2.2 V' Decay

In the $G(221)$ model the W' and Z' bosons can decay into SM fermions, gauge bosons, or a pair of SM gauge boson and Higgs boson. In this subsection we give detailed formula of partial decay widths of the extra gauge bosons.

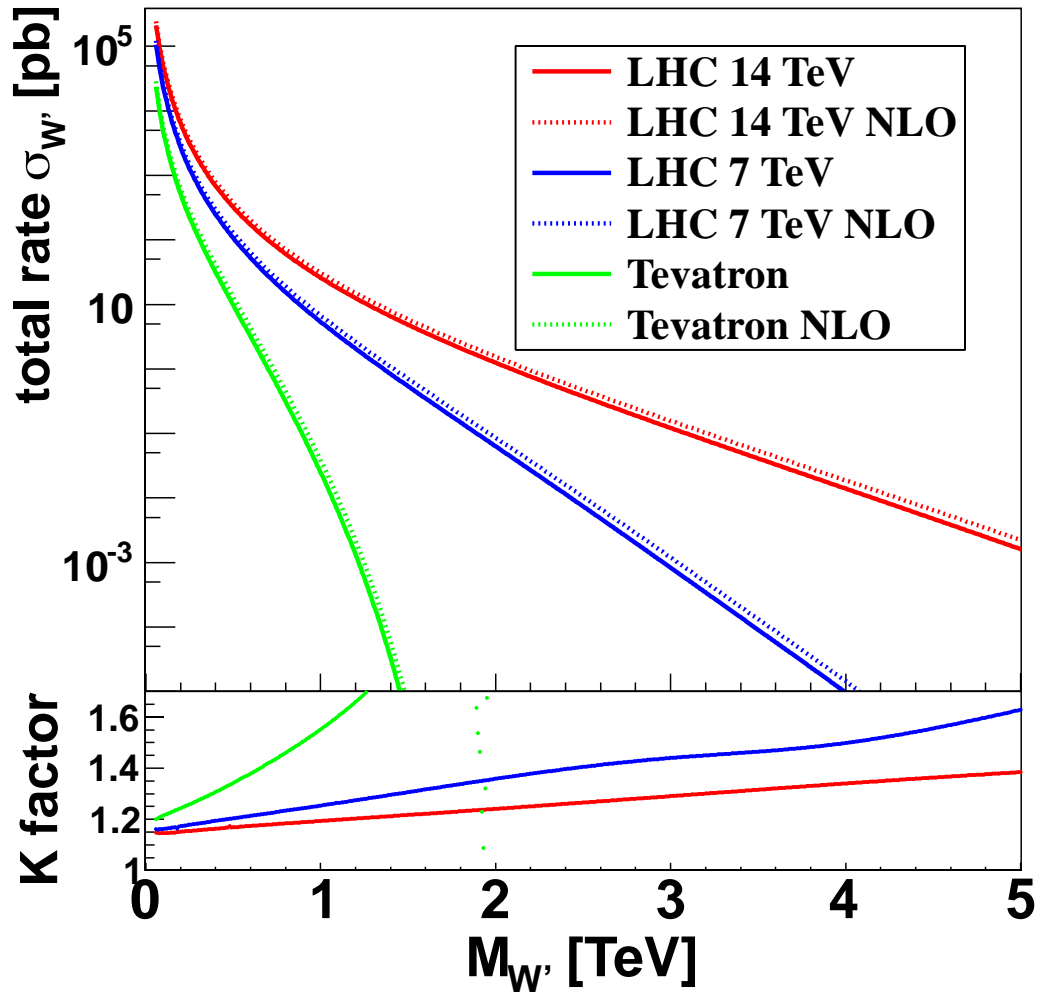


Figure 3.1: Upper panel: the LO and NLO cross sections of $pp \rightarrow W'$ process with a SM like coupling as a function of new heavy gauge boson mass ($m_{W'}$) in hadron collisions. Lower panel: the K -factor as a function of $m_{W'}$.

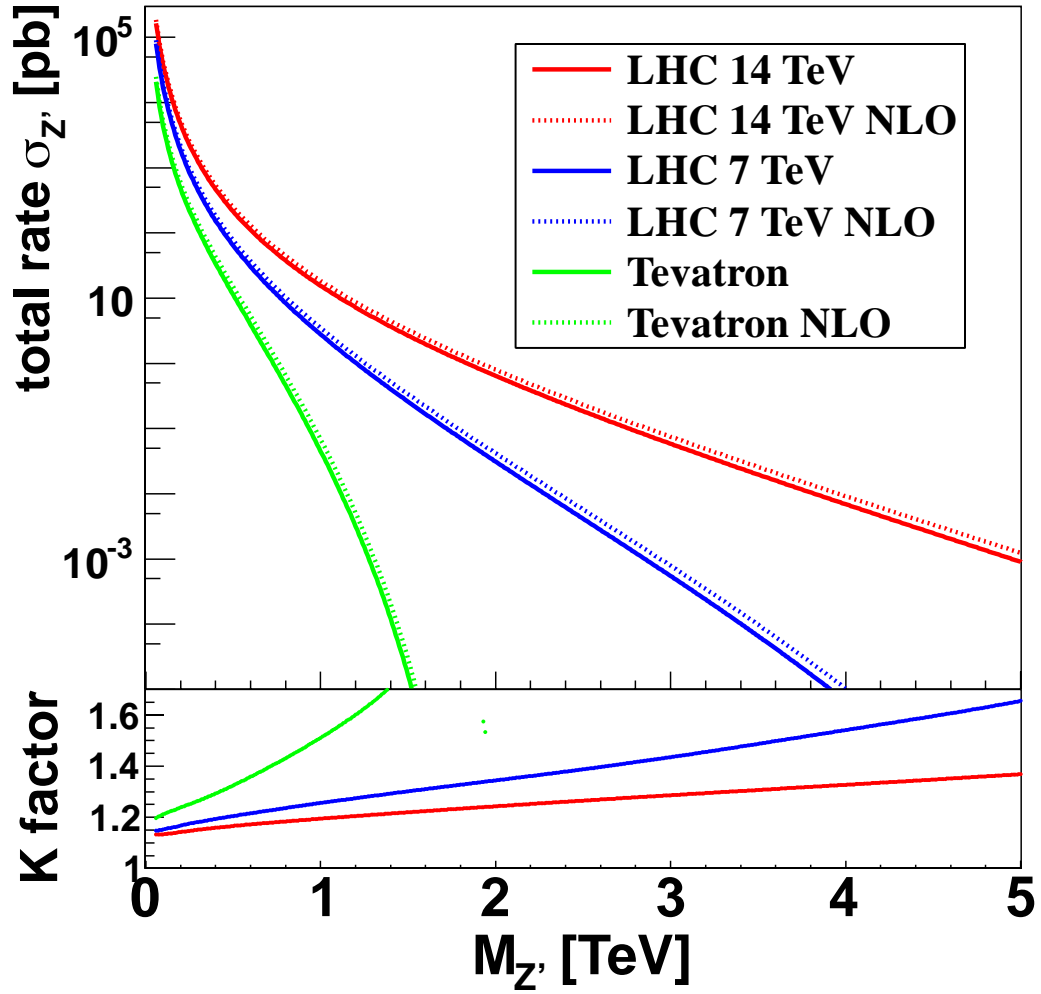


Figure 3.2: Upper panel: the LO and NLO cross sections of $pp \rightarrow Z'$ process with a SM like coupling as a function of new heavy gauge boson mass ($m_{Z'}$) in hadron collisions. Lower panel: the K -factor as a function of $m_{Z'}$.

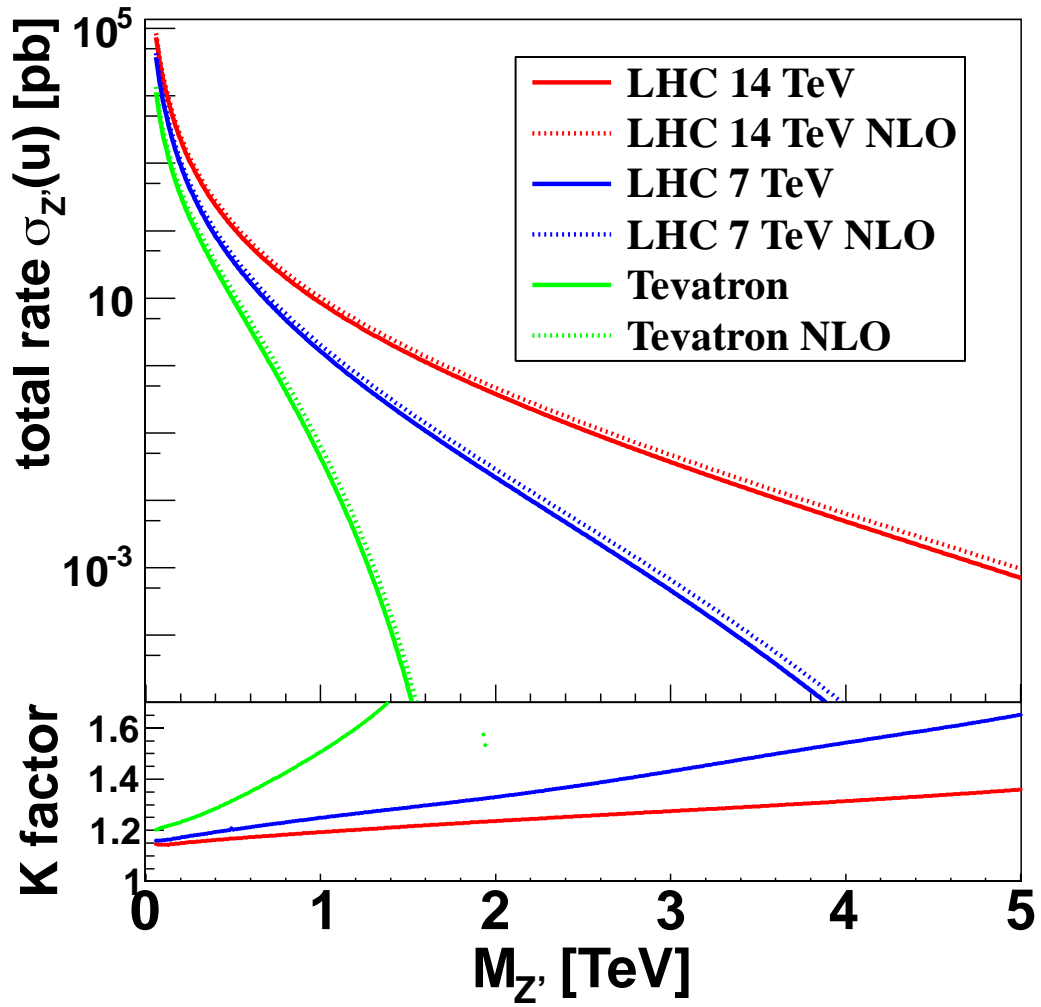


Figure 3.3: Upper panel: the LO and NLO cross sections of $pp \rightarrow Z'$ process with a SM-like couplings as a function of $m_{Z'}$ in hadron collision: induced by up-type quark initial state Lower panel: the K -factor as a function of $m_{Z'}$.

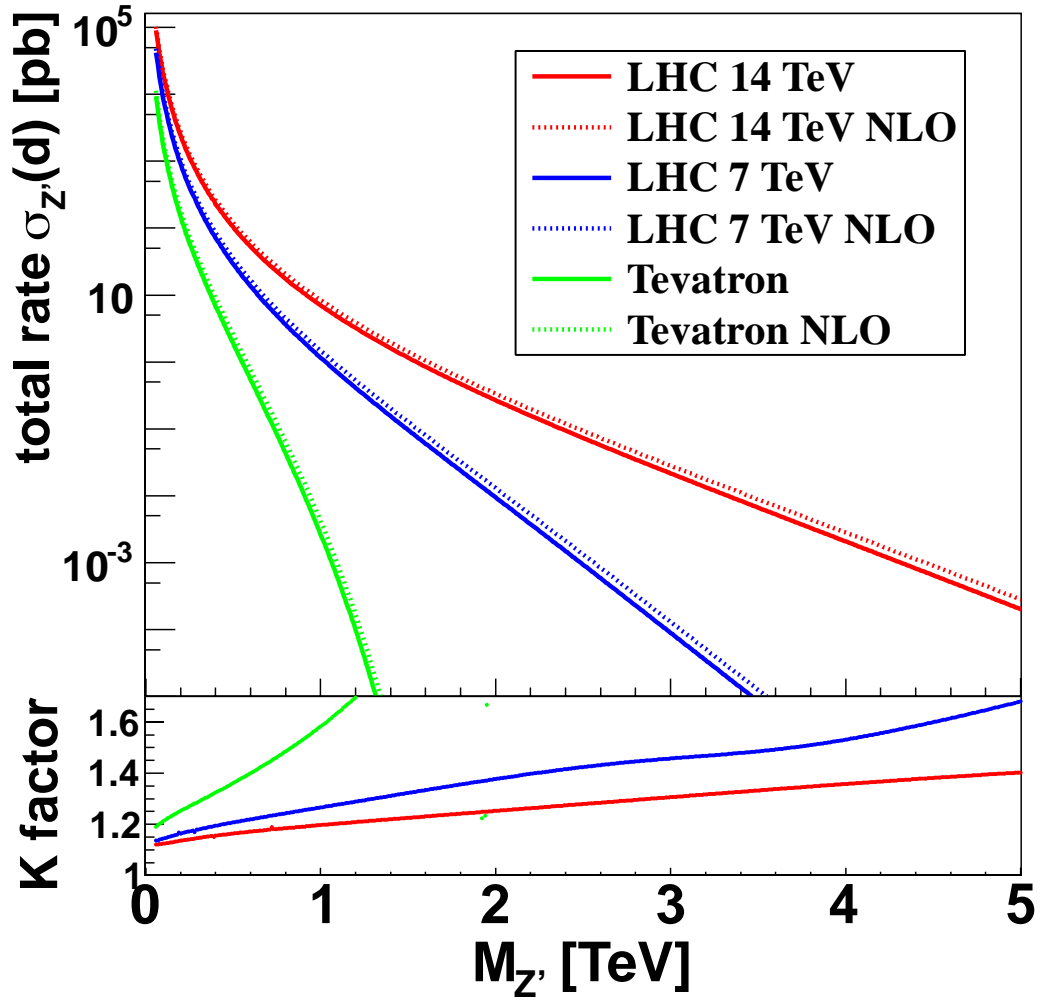


Figure 3.4: Upper panel: the LO and NLO cross sections of $pp \rightarrow Z'$ process with a SM-like couplings as a function of $m_{Z'}$ in hadron collision: induced by down-type quark initial state. Lower panel: the K -factor as a function of $m_{Z'}$.

First, consider the fermionic mode. The decay width of $V' \rightarrow \bar{f}_1 f_2$ is

$$\Gamma_{V' \rightarrow \bar{f}_1 f_2} = \frac{M_{V'}}{24\pi} \beta_0 \left[(g_L^2 + g_R^2) \beta_1 + 6g_L g_R \frac{m_{f_1} m_{f_2}}{M_{V'}} \right] \Theta(M_{V'} - m_{f_1} - m_{f_2}), \quad (3.18)$$

where

$$\begin{aligned} \beta_0 &= \sqrt{1 - 2 \frac{m_{f_1}^2 + m_{f_2}^2}{M_{V'}^2} + \frac{(m_{f_1}^2 - m_{f_2}^2)^2}{M_{V'}^4}}, \\ \beta_1 &= 1 - \frac{m_{f_1}^2 + m_{f_2}^2}{2M_{V'}^2} - \frac{(m_{f_1}^2 - m_{f_2}^2)^2}{2M_{V'}^4}. \end{aligned} \quad (3.19)$$

Note that the color factor is not included in Eq. 3.18 and the third generation quark decay channel opens only for a heavy Z' and W' .

Second, consider the bosonic decay mode, e.g. W' and Z' decay to gauge bosons and Higgs bosons. Such decay modes are induced by gauge interactions between the extra gauge boson and the SM gauge boson after symmetry breaking. Even though the couplings $g_{V'V_1V_2}$ and $g_{V'V_1H}$ are suppressed by the gauge boson mixing term $1/x$, the bosonic decay channel could be the major decay channel in certain models, e.g. fermio-phobic model in which the extra gauge boson does not couple to fermions at all.

The decay width of $V' \rightarrow V_1 V_2$ is

$$\Gamma_{V' \rightarrow V_1 V_2} = \frac{M_{V'}^5}{192\pi M_{V_1}^2 M_{V_2}^2} g_{V'V_1V_2}^2 \beta_0^3 \beta_1 \Theta(M_{V'} - M_{V_1} - M_{V_2}), \quad (3.20)$$

where

$$\begin{aligned}
\beta_0 &= \sqrt{1 - 2\frac{M_{V_1}^2 + M_{V_2}^2}{M_{V'}^2} + \frac{(M_{V_1}^2 - M_{V_2}^2)^2}{M_{V'}^4}}, \\
\beta_1 &= 1 + 10\frac{M_{V_1}^2 + M_{V_2}^2}{2M_{V'}^2} + \frac{M_{V_1}^4 + 10M_{V_2}^2M_{V_1}^2 + M_{V_1}^4}{M_{V'}^4}.
\end{aligned} \tag{3.21}$$

The width of $V' \rightarrow V_1 H$ (where $V_1 = W$ or Z boson and H is the lightest Higgs boson) is

$$\Gamma_{V' \rightarrow V_1 H} = \frac{M_{V'}}{192\pi} \frac{g_{V'V_1H}^2}{M_{V_1}^2} \beta_0 \beta_1 \Theta(M_{V'} - M_{V_1} - M_{V_2}), \tag{3.22}$$

where

$$\begin{aligned}
\beta_0 &= \sqrt{1 - 2\frac{M_{V_1}^2 + m_H^2}{M_{V'}^2} + \frac{(M_{V_1}^2 - m_H^2)^2}{M_{V'}^4}}, \\
\beta_1 &= 1 + \frac{10M_{V_1}^2 - 2m_H^2}{2M_{V'}^2} + \frac{(M_{V_1}^2 - m_H^2)^2}{M_{V'}^4}.
\end{aligned} \tag{3.23}$$

The couplings $g_{V'V_1V_2}$ and $g_{V'V_1H}$ for various models are listed in Table II for reference. In this study only left-handed neutrinos are considered while the possible right-handed neutrinos are assumed to be very heavy. In addition we also assume all the heavy Higgs bosons, except the SM-like Higgs boson, decouple from the TeV scale. As a result, the total decay width of the W' boson is

$$\Gamma_{W',\text{tot}} = 3\Gamma_{W' \rightarrow \bar{e}\nu} + 2N_C\Gamma_{W' \rightarrow \bar{u}d} + N_C\Gamma_{W' \rightarrow \bar{t}b} + \Gamma_{W' \rightarrow WZ} + \Gamma_{W' \rightarrow WH}, \tag{3.24}$$

while the width of the Z' boson is

$$\begin{aligned} \Gamma_{Z',\text{tot}} &= 3\Gamma_{Z'\rightarrow\bar{e}e} + 3\Gamma_{Z'\rightarrow\bar{\nu}\nu} + 2N_C\Gamma_{Z'\rightarrow\bar{u}u} + 3N_C\Gamma_{Z'\rightarrow\bar{d}d} \\ &+ N_C\Gamma_{Z'\rightarrow\bar{t}t} + \Gamma_{Z'\rightarrow WW} + \Gamma_{Z'\rightarrow ZH}, \end{aligned} \quad (3.25)$$

where $N_C = 3$ originates from summation of all possible color quantum number.

3.3 Event Simulation and Search Limits

3.3.1 Signal and Backgrounds

At hadron colliders, searches for a heavy resonance decaying to a charged lepton and missing transverse energy are always a primary task because of their simple final states. In the final states, the charged lepton can be electron or muon. The tau lepton is not considered here, because of the complicated hadronic decays of the tau lepton. The neutrino in the final states results in missing transverse energy in the detector.

One can not reconstruct the invariant mass of the final states, due to the missing transverse energy in the final states. The kinematic variable reconstructed instead is the transverse mass

$$M_T = \sqrt{(E_T^\ell + E_T^{\text{miss}})^2 - (p_T^\ell + p_T^{\text{miss}})^2} = \sqrt{2p_T E_T^{\text{miss}}(1 - \cos\varphi_{l\nu})}, \quad (3.26)$$

where p_T is the lepton transverse momentum, E_T^{miss} is the magnitude of the missing transverse momentum (E_T^{miss}), and $\varphi_{l\nu}$ is the angle between the p_T and E_T^{miss} vectors. The transverse mass distribution displays a Jacobian peak that falls sharply above the resonance

mass, as can be seen by the differential cross section

$$\frac{d\sigma}{dM_T} = \frac{d\sigma}{d\cos\theta} \frac{d\cos\theta}{dM_T} = \frac{d\sigma}{d\cos\theta} \frac{M_T}{2M_{W'}\sqrt{M_{W'}^2 - M_T^2}}, \quad (3.27)$$

where θ is the polar decay angle in the center of mass (COM) frame of the system. The Jacobian peak will become broad when the width of the W' boson and the effect of detector smearing are taken into account. Since there is a relation between p_T^ℓ and the polar angle θ in the COM frame with COM energy \hat{s} ,

$$p_T^\ell = \frac{\sqrt{\hat{s}}}{2} \sin\theta \quad (3.28)$$

a similar Jacobian peak will show up in the transverse momentum distribution of the final state lepton, as can be seen by the differential cross section

$$\frac{d\sigma}{dp_T^\ell} = \frac{d\sigma}{d\cos\theta} \frac{d\cos\theta}{dp_T^\ell} = \frac{d\sigma}{d\cos\theta} \frac{2p_T^\ell}{M_{W'}\sqrt{\frac{M_{W'}^2}{4} - p_T^{\ell 2}}}, \quad (3.29)$$

where the peak position is at $p_T^\ell = \frac{M_{W'}}{2}$. Measuring the Jacobian peak is complicated when the width of the W' boson and the effect of detector smearing are taken into account. From the above kinematic consideration, one would like to consider three variables, p_T^ℓ , M_T , and E_T^{miss} , to describe the characteristic feature of this process.

We choose the benchmark point as 1500 GeV mass, and coupling $f_L = \frac{e}{\sqrt{2}\sin\theta_W}$ and $f_R = 0$. The total decay width is $\Gamma_{W'} = 51$ GeV. Other couplings can be scaled using the scaling formula discussed in above. The CTEQ6L1 parton distribution functions are used in

our calculation with the renormalization and factorization scales chosen as $m_{W'}$. The final state of this channel is

$$pp \rightarrow W' \rightarrow \ell\nu. \quad (3.30)$$

For the signal, we choose the renormalization and factorization scales as the W' mass $M_{W'}$. The following SM backgrounds are considered:

$$pp \rightarrow W \rightarrow \ell\nu, \quad \text{main background} \quad (3.31)$$

$$pp \rightarrow Z/\gamma^* \rightarrow \ell\bar{\ell}, \quad (3.32)$$

$$pp \rightarrow VV \rightarrow \ell X, \quad (3.33)$$

$$pp \rightarrow t\bar{t} \rightarrow \ell X, \quad (3.34)$$

and, of course, the QCD background estimated from experimental data. The main background comes from the high energy tail of the SM W decays to the same lepton and missing energy. After basic event selection, other backgrounds than W decays are only estimated to be less than 10%. The p_T^ℓ , and E_T^{miss} distributions for the signal are shown in Figs. 3.5 and 3.6. The M_T distribution for the signal is shown in the left panel of the Fig. 3.7.

For the purpose of our study, we will only simulate the signal process using the benchmark point as a template to justify the simulation procedure. Then we will adopt the event simulations at the Tevatron and LHC for both signal and backgrounds to reproduce the search limits on the W' resonance. To illustrate the procedure, we summarize the results at the LHC with the energy 7 TeV and the luminosity 1 fb^{-1} using the ATLAS detector. We refer to the ATLAS paper in ref. [54] for all the details.

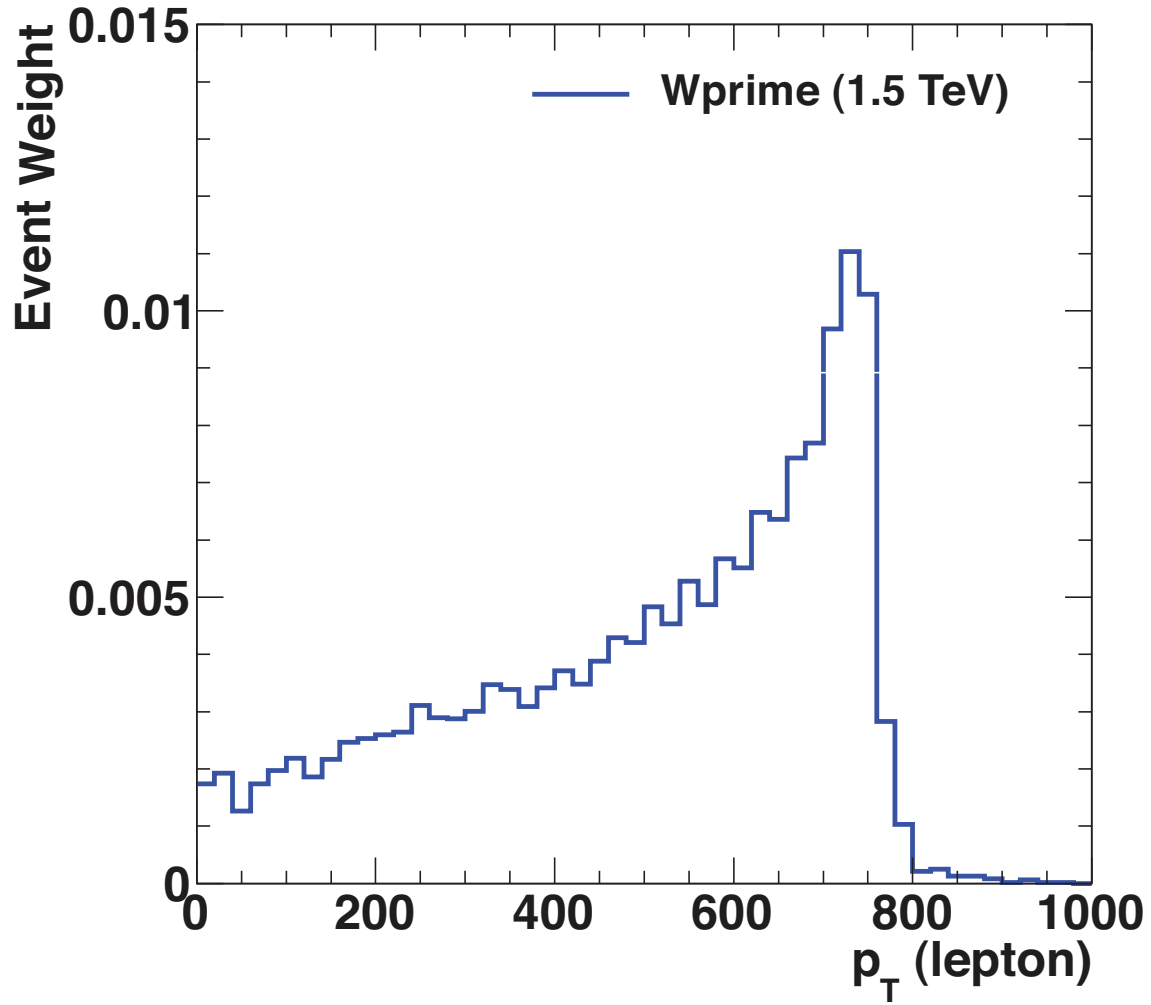


Figure 3.5: The p_T^{ℓ} distribution for 1500 GeV W' in the charged lepton and missing transverse energy final states.

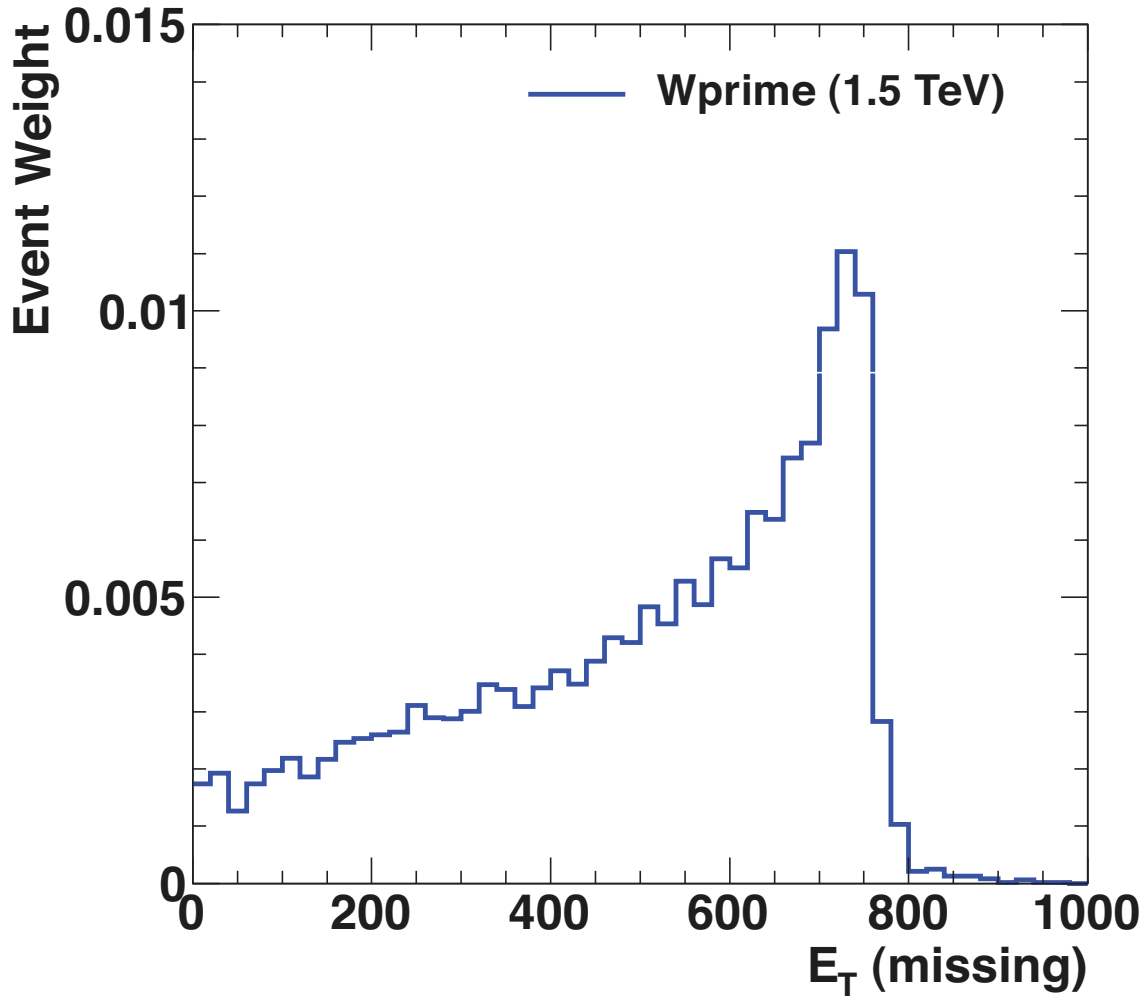


Figure 3.6: The E_T^{miss} distribution for 1500 GeV W' in the charged lepton and missing transverse energy final states.

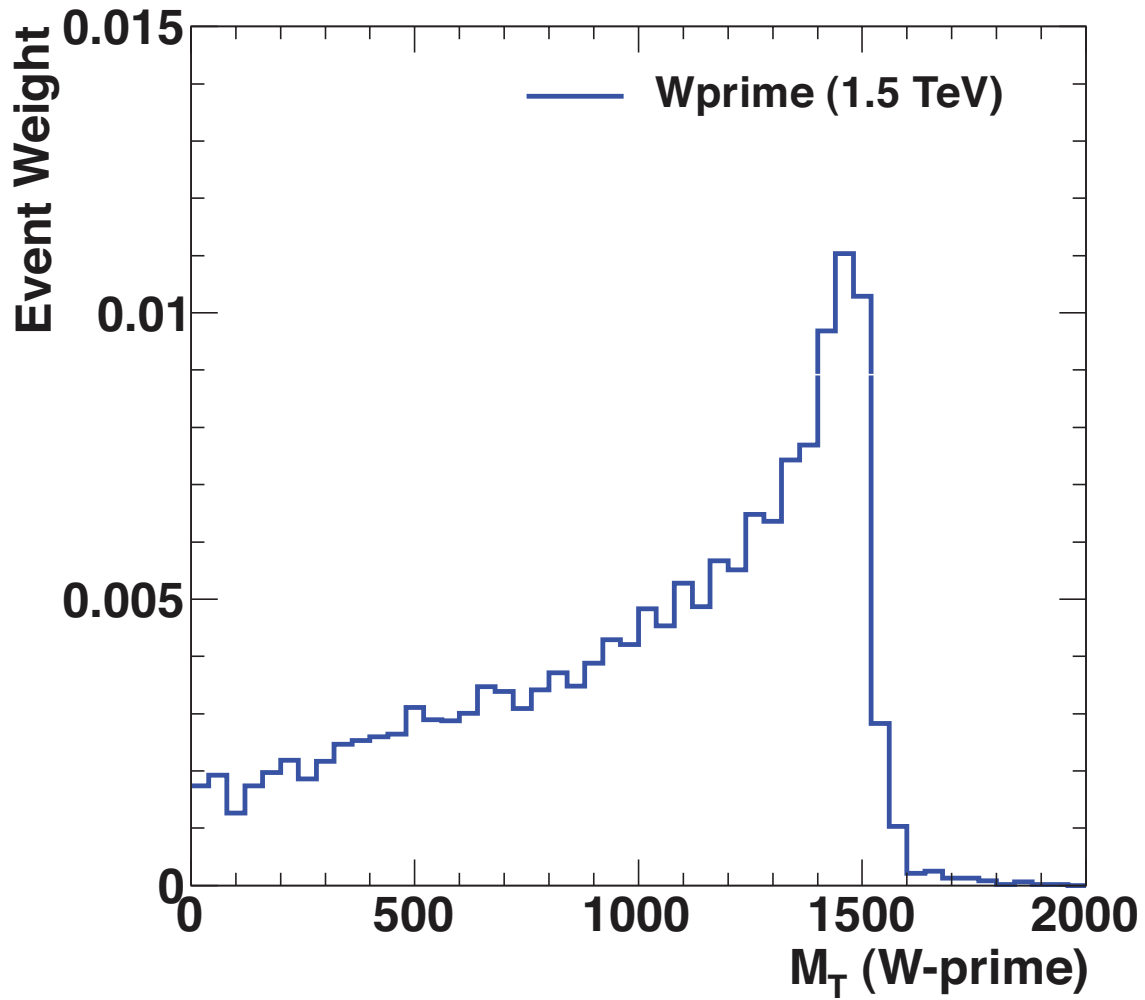


Figure 3.7: The M_T distribution for 1500 GeV W' in the charged lepton and missing transverse energy final states is shown.

3.3.2 Object Reconstructions and Event Selections at the LHC

The ATLAS detector has three major components: the inner tracking detector, the calorimeter and the muon spectrometer. Events are required to have their primary vertex reconstructed from at least three tracks with $p_{\text{T}} > 0.4$ GeV and longitudinal distance less than 200 mm from the center of the collision region.

Events are required to have exactly one candidate electron or one candidate muon satisfying the requirements described below:

- Electron candidate:
 - tracks with $p_{\text{T}} > 20$ GeV
 - electromagnetic compartment of calorimeter with $E_{\text{T}} > 25$ GeV and $|\eta| < 1.37$ or $1.52 < |\eta| < 2.47$ if matches with an inner detector track;
 - The resolution of the energy measurement is 2% for $E_{\text{T}} \approx 50$ GeV and approaches 1% in the high- E_{T} range relevant to this analysis.
 - the isolation energy is measured with the calorimeter in a cone $\Delta R < 0.4$ ($\Delta R \equiv \sqrt{(\Delta\eta)^2 + (\Delta\varphi)^2}$) around the electron track, and the requirement is $\sum E_{\text{T}} < 9$ GeV, where the sum includes all calorimeter energy clusters in the cone excluding the core energy deposited by the electron.

- Muon candidates:
 - matching tracks in the muon spectrometer and inner detector with combined $p_{\text{T}} > 22$ GeV. Muon tracks can be reconstructed independently in both the inner detector and muon spectrometer, and the muons used in this study are required to have matching tracks in both systems. The muons are required to

have $p_T > 25$ GeV, where the momentum of the muon is obtained by combining the inner detector and muon spectrometer measurements.

- approximately $|\eta| < 1.0$ and $1.3 < |\eta| < 2.0$.
- The average momentum resolution is currently about 15% at $p_T = 1$ TeV.
- the isolation energy is measured using inner detector tracks with $p_T^{track} > 1$ GeV in a cone $\Delta R < 0.3$ around the muon track. The isolation requirement is $\sum p_T^{track} < 0.05 p_T$, where the muon track is excluded from the sum.

The E_T^{miss} in the electron channel is obtained from a vector sum over calorimeter cells

$$E_T^{\text{miss}} = E_T^{\text{miss}}(\text{calo}). \quad (3.35)$$

Muons only deposit a small fraction of their energy in the calorimeter, and so, in the muon channel, the E_T^{miss} is obtained from

$$E_T^{\text{miss}} = E_T^{\text{miss}}(\text{calo}) - p_T(\mu). \quad (3.36)$$

The second term in this vector sum subtracts the muon transverse momentum. The missing E_T^{miss} requirements are imposed to be $E_T^{\text{miss}} > 25\text{GeV}$ in both channels. In the electron channel, to avoid the misidentification of hadronic jets as a lepton, a tighter cut is imposed with $E_T^{\text{miss}} > 0.6 p_T^\ell$.

After the lepton reconstruction and the basic event selections, one will notice that the M_T distributions, shown in the right panel of the Fig. 3.7, accumulate more data for the signal than the backgrounds in the high- M_T tails. To search for a W' with a mass of 1500

	$e\nu$	$\mu\nu$
$\sigma B\mathcal{L}$	92.248	92.248
ϵ_{sig}	0.541 \pm 0.026	0.347 \pm 0.024
N_{sig}	49.6 \pm 6.0	34.4 \pm 4.4
$W \rightarrow l\nu$	1.59 \pm 0.13	1.36 \pm 0.13
$Z \rightarrow ll$	0.00010 \pm 0.00004	0.095 \pm 0.005
diboson	0.08 \pm 0.08	0.11 \pm 0.08
$t\bar{t}$	0.08 \pm 0.08	0
QCD	0 $\begin{smallmatrix} +0.17 \\ -0 \end{smallmatrix}$	0.01 $\begin{smallmatrix} +0.02 \\ -0.01 \end{smallmatrix}$
Total N_{bg}	1.75 $\begin{smallmatrix} +0.24 \\ -0.18 \end{smallmatrix}$	1.57 \pm 0.15
N_{obs}	2	2

Table 3.1: Expected and observed numbers of events in 1.04 fb^{-1} in ref. [54] from the various background sources in each decay channel for $M_T > 891 \text{ GeV}$, the region used to search for a W' with a mass of 1500 GeV. In the table, the signal selection efficiency, ϵ_{sig} , and the prediction for the number of signal events, N_{sig} , obtained with this efficiency. The last two columns are the expected number of background events, N_{bg} , and the number of events observed in data, N_{obs} . The uncertainties are statistical.

GeV, the hard cut on M_T is required to be

$$M_T > 891 \text{ GeV}, \quad \text{for } M_{W'} = 1500 \text{ GeV}. \quad (3.37)$$

The rate for signal and backgrounds are listed in the Table 3.1. We notice that after all the cuts, the significance is large in the simulations. For the M_T cut imposed for other masses of W' , we refer to the ATLAS paper [54] for details.

3.3.3 Upper Limits on W' masses at the LHC

At the current LHC, since there is no excess on searching for the heavy resonance in the charged lepton and missing transverse energy final states, one would like to set the limits on this heavy resonance in this final states. Based on the expected and observed numbers of events after all the cuts, the Bayesian or frequentist analysis is used to set the limits at the 95% confidence level (CL). Here we will take the W' signal with 1500 GeV mass at the LHC as an example to show how to calculate the upper limit. From the Table 3.1, we can read out the signal selection efficiency ϵ_{sig} after all the cuts, the simulated numbers of signal N_{sig} , the simulated numbers of background N_{bg} , and the observed numbers N_{obs} . Then the expected number of events is

$$N_{\text{exp}} = \epsilon_{\text{sig}} \mathcal{L}_{\text{int}} \sigma B + N_{\text{bg}}, \quad (3.38)$$

where σ is the production cross section, B is the decay branching ratio, and \mathcal{L}_{int} is the integrated luminosity of the data sample. Using Poisson statistics, the likelihood to observe N_{obs} events is

$$\mathcal{L}(N_{\text{obs}}|\sigma B) = \frac{(\epsilon_{\text{sig}} \mathcal{L}_{\text{int}} \sigma B + N_{\text{bg}})^{N_{\text{obs}}} e^{-(\epsilon_{\text{sig}} \mathcal{L}_{\text{int}} \sigma B + N_{\text{bg}})}}{N_{\text{obs}}!}. \quad (3.39)$$

Taking a flat prior probability density, the posterior probability can be obtained. From the appendix, we know that the 95% CL upper limit $\sigma_{95\%CL}$, is given by

$$\int_0^{(\sigma B)^{95\%CL}} \mathcal{P}(\sigma B|N_{\text{obs}}) d(\sigma B) = 95\%. \quad (3.40)$$

If one don't take the uncertainties of signal and backgrounds into account, the upper limit has a simple formula to calculate for a single channel,

$$1 - \frac{\Gamma(N_{\text{obs}} + 1, (\sigma B)_{95\%CL} \epsilon_{\text{sig}} \mathcal{L}_{\text{int}})}{\Gamma(N_{\text{obs}} + 1, N_{\text{bg}})} = 95\%. \quad (3.41)$$

Using the numbers in the Table 3.1, we obtain the upper limit at the 95% CL is

$$(\sigma B)_{\text{up}} = 8.79184 \text{ fb} \quad \text{in the electron channel ,} \quad (3.42)$$

$$(\sigma B)_{\text{up}} = 12.968 \text{ fb} \quad \text{in the muon channel ,} \quad (3.43)$$

which are the same as the results in the ATLAS paper [54]. In principle, one can calculate the combined limit using the equations in appendix. Here we will only use an approximate formula in the Gaussian limit:

$$\mu_{\text{up}}^2 = \frac{1}{\sum_i^N \frac{1}{\mu_{i\text{up}}^2}}. \quad (3.44)$$

The combined limit is

$$(\sigma B)_{\text{up}} = 7.277 \text{ fb}, \quad (3.45)$$

which is still close to the results in the ATLAS paper [54].

3.4 Discovery Potential and Significance

In the early LHC7 experiment, the combined constraints from current direct searches and indirect EWPTs play the crucial role to specify the unexplored parameter space. Given the

allowed parameter space discussed in the previous chapter, we are able to predict the time scale to probe the W' and Z' at 5σ discovery evidence. We are able to provide the following information:

- The integrated luminosities, with which the LHC can discover the W' and/or Z' for certain masses in different $G(221)$ models.
- The region of the parameter space that could be accessed for different luminosities and energies in the LHC run.
- The possibility to identify different models in our classification once the W' and/or Z' are discovered.

To be specific, we consider two different scenarios: an early run with $\sqrt{s} = 7$ TeV and an integrated luminosity of 5.61 fb^{-1} ; a long run with $\sqrt{s} = 14$ TeV and $\mathcal{O}(10^3) \text{ fb}^{-1}$ integrated luminosity is expected finally.

To get the expected luminosity contour, one has to calculate the signal and background cross sections at LHC7 and LHC14 for each point in the parameter space of the models. In principle, the complete Monte Carlo simulations for the signal and background including efficiency analysis in the $G(221)$ models have to be used to obtain the needed luminosity for the discovery or exclusion at 7 TeV and 14 TeV. However, in the Drell-Yan production process, all the model-independent effects, including the kinematic cuts, can be factorized out from the model-dependent part, which only depends on the gauge couplings and branching ratios. Therefore, the simulation on one benchmark model, such as the sequential W' and Z' model, can provide the needed luminosity information for the other models. At the LHC7, the complete simulation on the signal and backgrounds including detection efficiency have

been done in Refs. [54, 55]. At the LHC14, the ATLAS TDR [58] have done the detailed studies on the discovery potentials for the sequential W' and Z' model. The luminosity needed for other new physics models can be obtained by properly scaling the luminosity obtained for the sequential model.

Here we summarize the event analysis procedures at the current LHC and in the ATLAS TDR. At the LHC7, we adopt the ATLAS simulation and analysis with integrated luminosity at about 1 fb^{-1} . Both electron and muon channels are considered in both W' and Z' searches. For the W' searches, the missing energy in both channels are required to be above the threshold energy of 25 GeV. Furthermore, the cut on the transverse mass of the lepton and missing energy system varies as the W' mass increases. For more detailed information, please refer to Refs. [54, 55]. In the ATLAS TDR, for the sequential W' , the simulation on the lepton plus missing transverse energy signal at high mass region is performed. We list the event selection and cut-based analysis as follows:

- Events are required to have exactly one reconstructed lepton with $p_T > 50 \text{ GeV}$ within $|\eta| < 0.25$, and isolated from jets with $\Delta R_{\ell j} = 0.5$;
- The lepton reconstruction is smeared by $\sigma(1/p_T) = 0.011/p_T \otimes 0.00017$, while the jet resolution is taken as $\sigma(E_T) = 0.45 \times \sqrt{E_T} \otimes 5\%$;
- Missing transverse energy $E_T^{\text{mis}} > 50 \text{ GeV}$;
- To reduce the di-jet and $t\bar{t}$ backgrounds, a lepton fraction is required to be

$$\sum p_T / \left(\sum p_T + \sum E_T \right) > 0.5 \tag{3.46}$$

;

- Transverse mass $m_T = \sqrt{2p_T E_T^{\text{mis}}(1 - \cos \Delta\phi)} > 0.7 \times M_{W'}$, where $\Delta\phi$ is the angle between the momentum of the lepton and the missing momentum.

For the sequential Z' , we list the event selection and analysis on the di-lepton final states as follows:

- Events are required to have exactly two reconstructed same-flavor opposite-charged leptons with at least one lepton $p_T > 30$ GeV, within $|\eta| < 0.25$;
- Di-lepton invariant mass window $|m_{\ell\ell} - M_{Z'}| < 4 \times \Gamma_{Z'}$.

Next we explore the LHC sensitivity to W' and Z' bosons. We can quantify the sensitivity to new physics discovery or set exclusion limits on it based on statistics. Specifically, for the case of discovery we would like to know the statistical significance (S) for discovery, which characterizes the inconsistency of the experiment data with a background-only hypothesis. If there is no discovery at a given luminosity, we set exclusion limits on new physics. In the counting experiments, suppose one has an experiment that counts n events, modeled as a Poisson distribution with mean $s + b$, where s is the expected signal rate, b is the expected background rate. The probability of measuring n events is therefore

$$P(n|s, b) = \frac{(s + b)^n}{n!} e^{-(s+b)}. \quad (3.47)$$

Using a profile likelihood ratio as the test statistic, the expected significance is obtained as follows [117]

$$S = \sqrt{2((s + b) \ln(1 + s/b) - s)}. \quad (3.48)$$

For sufficiently large b we can expand the logarithm in s/b and obtain the widely-used significance formula

$$S = \frac{s}{\sqrt{b}} (1 + \mathcal{O}(s/b)) . \quad (3.49)$$

In addition to establishing discovery by rejecting the background hypothesis, we can consider the signal hypothesis as well. It is common to use confidence level (CL) α and the related p -value to quantify the level of incompatibility of data with a signal hypothesis. The profile likelihood ratio q_μ is used as the test statistic [117]. For a sufficiently large data sample the probability density of q_μ takes on a well defined χ^2 distribution with mean $\hat{\mu}$ and variance $\hat{\sigma}$ for one degree of freedom. Given the p -value for each number of signal events s , we can obtain the upper limit s^{UP} on the number of signal events,

$$s^{\text{UP}} = \hat{\mu} + \hat{\sigma} \Phi^{-1}(1 - \alpha) , \quad (3.50)$$

where the mean and variance of the χ^2 distribution are $\hat{\mu} = n - b$, and $\hat{\sigma} = \sqrt{b}$ for large data sample, and Φ is the cumulative distribution of the standard Gaussian with zero mean and unit variance. For the expected upper limit, in which the data count is taken as the background sum, the upper limit at confidence level $\alpha = 95\%$ is

$$s^{\text{UP}} = \Phi^{-1}(0.05) \cdot \sqrt{b} = 1.64 \times \sqrt{b} . \quad (3.51)$$

So for a sufficiently large data sample the equivalent significance Z for excluding a signal hypothesis is given by

$$Z = \frac{s^{\text{UP}}}{\sqrt{b}} = 1.64. \quad (3.52)$$

For instance, when expressing the significance for 5σ discovery with the exclusion upper limit at the 95% CL, a factor $S/Z = 5/1.64 \simeq 3$ needs to be applied.

Denoting by σ_s (σ_b) the inclusive cross section of the signal (background), ϵ_s (ϵ_b) the cut acceptance of the signal (background), and \mathcal{L} the integrated luminosity, the number of signal (background) events can be written as

$$s = \sigma_s \epsilon_s \mathcal{L} , \quad (3.53)$$

$$b = \sigma_b \epsilon_b \mathcal{L} . \quad (3.54)$$

For a sufficiently large data sample, both S and Z have a scaling behavior on the integrated luminosity,

$$S \simeq Z \simeq \frac{s}{\sqrt{b}} = \frac{\sigma_s \epsilon_s}{\sqrt{\sigma_b \epsilon_b}} \times \sqrt{\mathcal{L}} . \quad (3.55)$$

Figures 3.8, 3.9, 3.10, 3.11, 3.12, 3.13 displays the 5σ discovery potential (fb^{-1}) for LHC7 via W' leptonic decay channel, and current combined constraints are within solid black contour. The LRD(T) and MLR models can be further constrained when the integrated luminosity for LHC7 reaches its maximum 5.6 fb^{-1} . However, the other models need much more luminosity, which even exceeds the total integrated luminosity (5.6 fb^{-1}) at LHC7. Therefore, the W' leptonic decay channel cannot make further contributions to discovering these $G(221)$ models, except in some small region in LRD(T) and MLR. In Figs. 2.5, 2.6, 2.7, 2.8, 2.9, 2.10, it shows that the EWPTs constraints are stronger than those from the Tevatron and the LHC7, except LRD(T) and MLR. This means that compared to EWPTs, the LHC7 direct search via the W' leptonic decay channel for the new physics models with $G(221)$ gauge group structure can put further constraint only on LRD(T) and

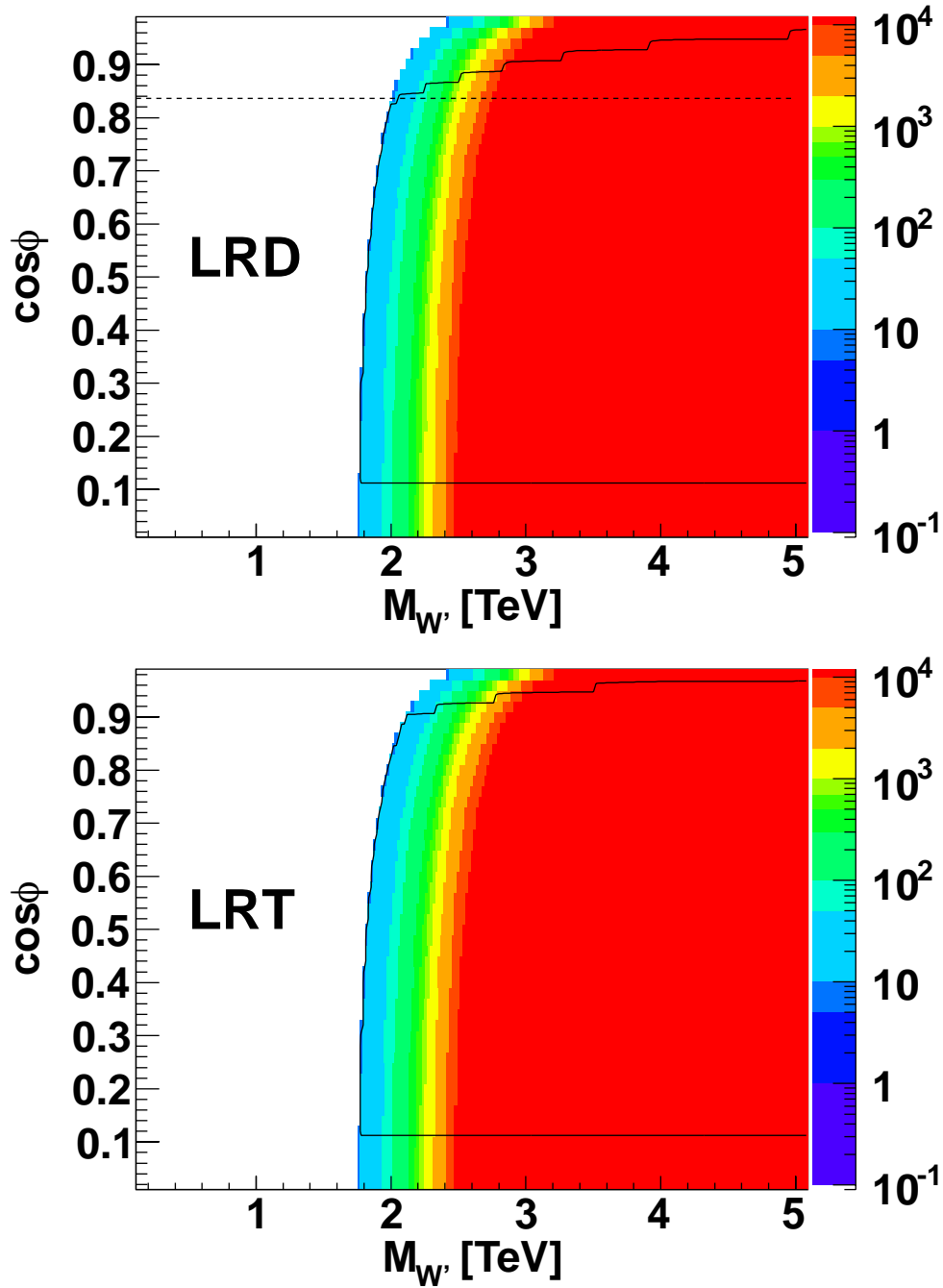


Figure 3.8: 5σ Discovery potential (fb^{-1}) in the LRD and LRT models for different luminosity at LHC7 via W' leptonic decay channel. The current combined constraints are within solid black contour. The dashed black lines in LRD represent MLR models.

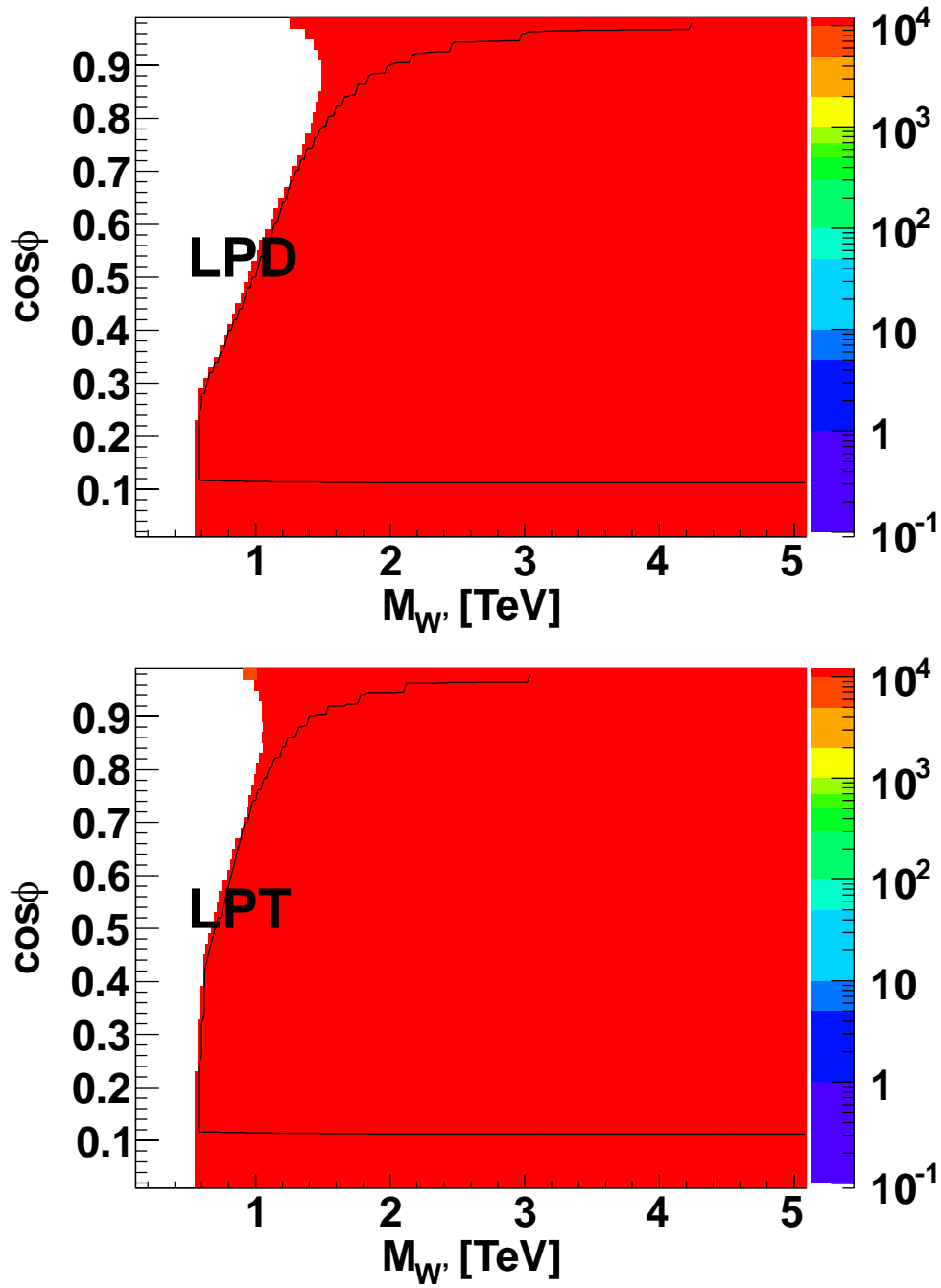


Figure 3.9: 5σ Discovery potential (fb^{-1}) in the LPD and LPT models for different luminosity at LHC7 via W' leptonic decay channel. The current combined constraints are within solid black contour.

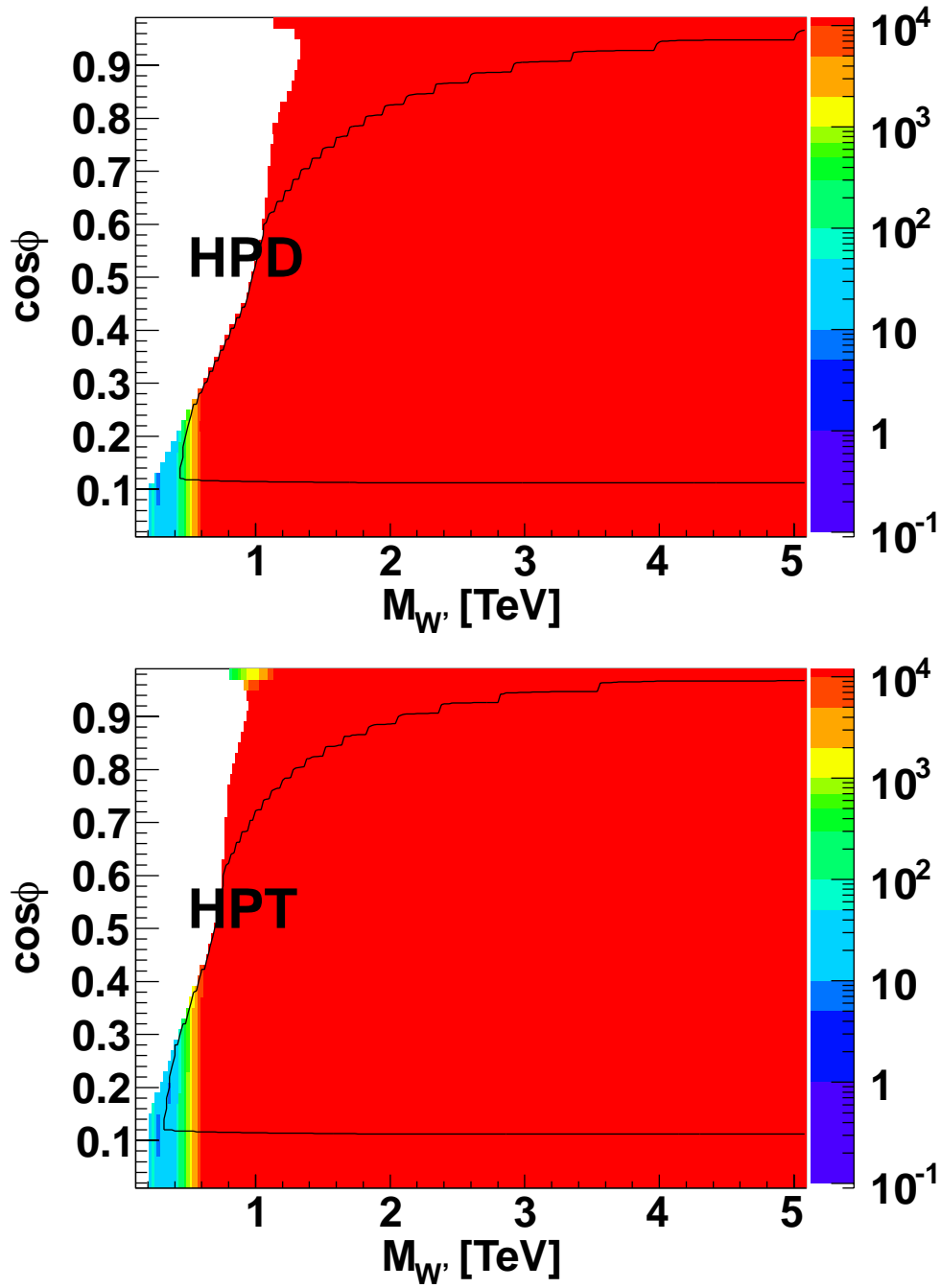


Figure 3.10: 5σ Discovery potential (fb^{-1}) in the HPD and HPT models for different luminosity at LHC7 via W' leptonic decay channel. The current combined constraints are within solid black contour.

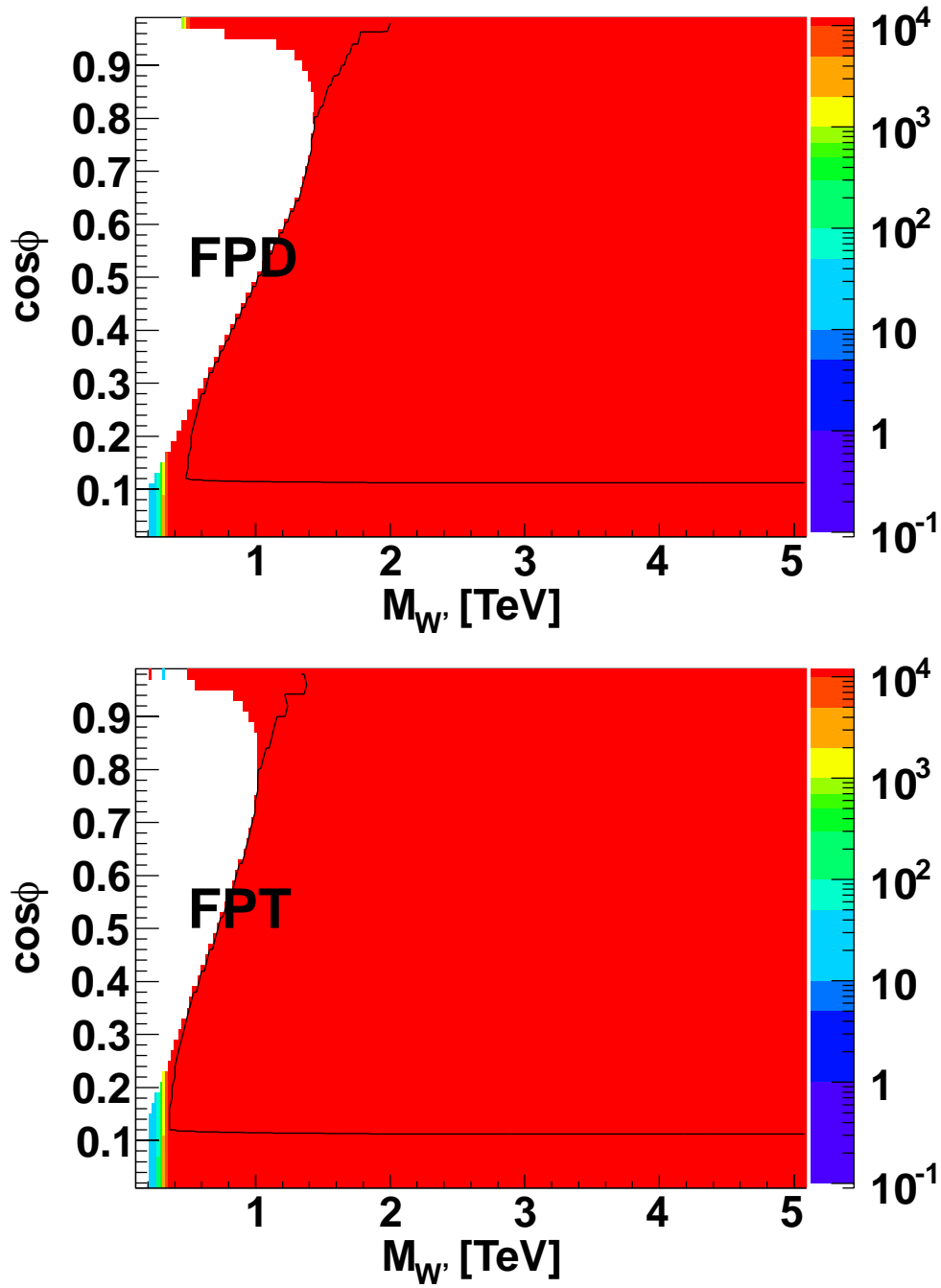


Figure 3.11: 5σ Discovery potential (fb^{-1}) in the FPD and FPT models for different luminosity at LHC7 via W' leptonic decay channel. The current combined constraints are within solid black contour.

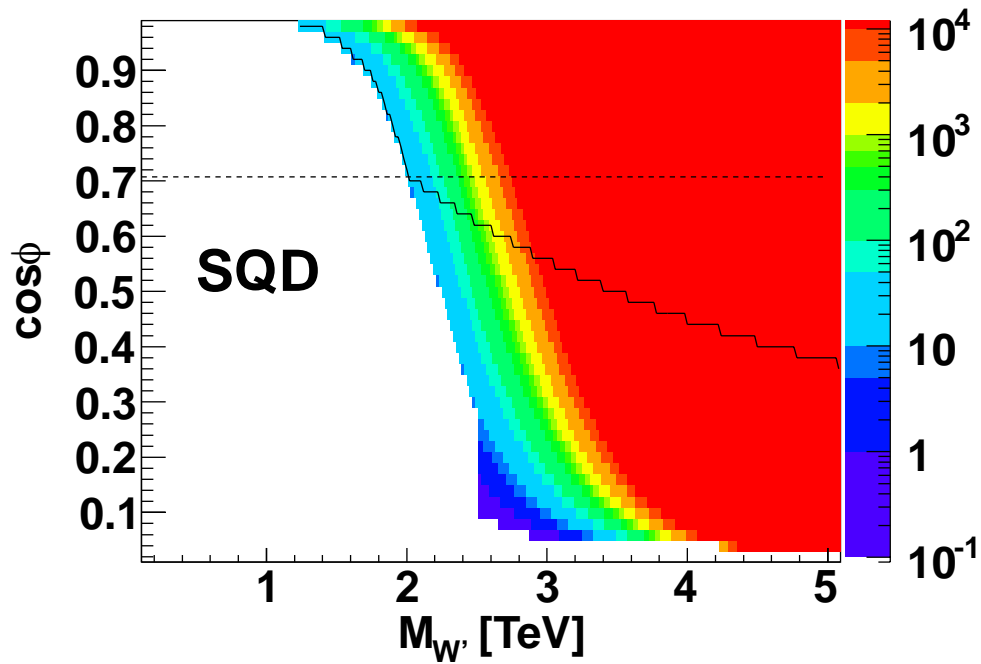


Figure 3.12: 5σ Discovery potential (fb^{-1}) in the SQD models for different luminosity at LHC7 via W' leptonic decay channel. The current combined constraints are within solid black contour. The dashed black lines in SQD represent MSQ models.

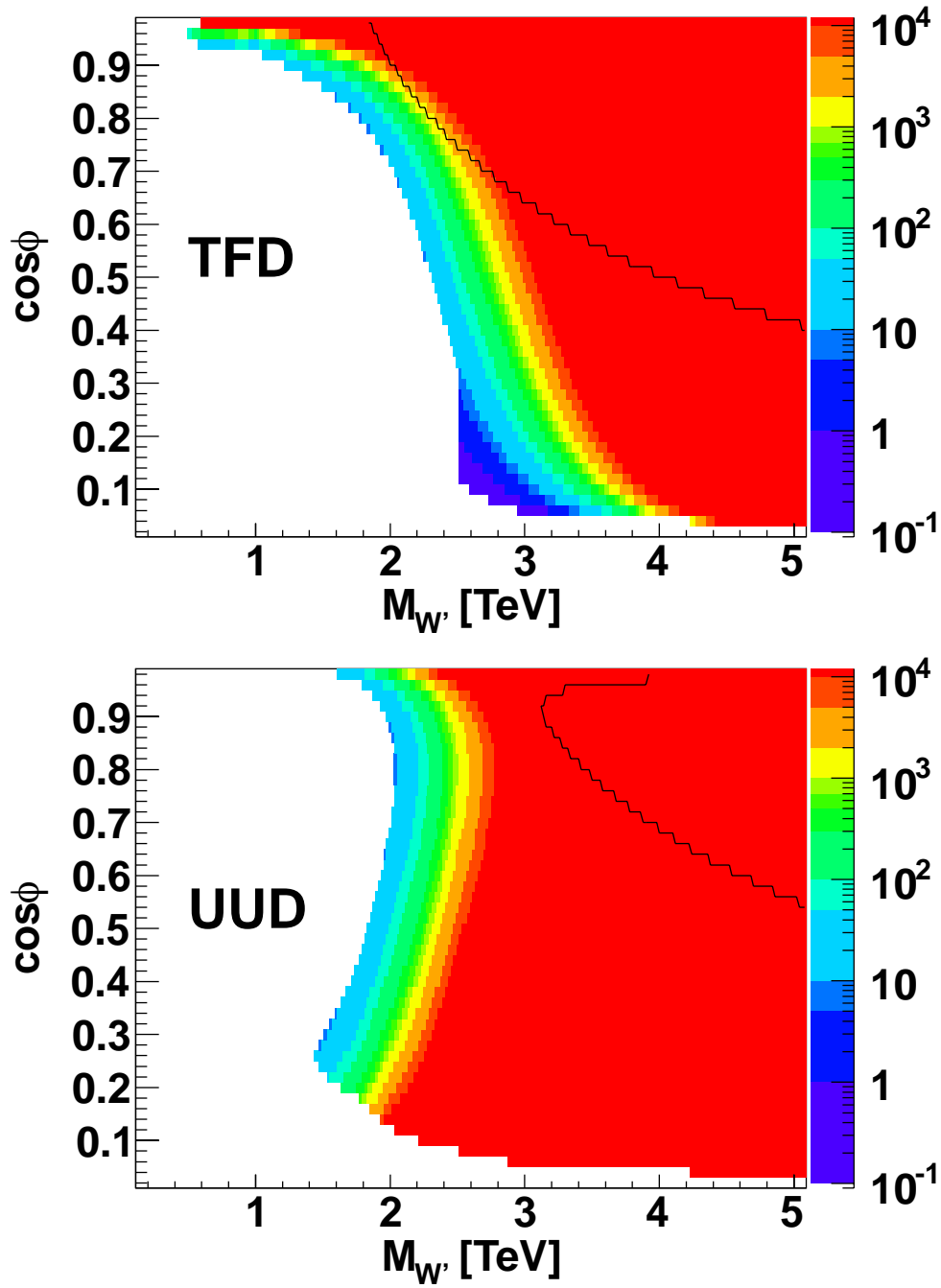


Figure 3.13: 5σ Discovery potential (fb^{-1}) in the TFD and UUD models for different luminosity at LHC7 via W' leptonic decay channel. The current combined constraints are within solid black contour.

MLR. For the other models, the direct search at LHC7 for s-channel W' production with leptonic decay cannot compete with seeking for deviation from SM predictions via EWPTs.

Figures 3.14, 3.15, 3.16, 3.17, 3.18, 3.19 shows the 5σ discovery potential (fb^{-1}) shows the 5σ discovery potential (fb^{-1}) at the LHC7 via the Z' leptonic decay channel, and the current combined constraints are within solid black contour. We can see that for LRD(T), SQD, TFD, UUD, MLR and MSQ, further discovery via the Z' leptonic decay channel needs more than 100 fb^{-1} , which is definitely far beyond the total integrated luminosity before LHC switches away from 7 TeV. However, some corner of the parameter space of LPD(T), HPD(T) and FPD(T) can be further tested when LHC7 reaches 5.6 fb^{-1} . Especially, for HPD(T) and FPD(T), there are small regions where Z' can be discovered with a few fb^{-1} luminosity or these parameters can be excluded with less than one fb^{-1} luminosity. At the LHC7, the Z' leptonic decay channel is more efficient than EWPTs on constraining the parameter regions in the LPD(T), HPD(T) and FPD(T). For LRD(T), LPD(T) and HPD(T), EWPTs are more sensitive to the large c_ϕ region, where LHC7 cannot compete with EWPTs. For SQD, TFD and UUD, both W' and Z' leptonic decay channel at LHC7 cannot help further, because the constraint from EWPTs for UUD is much stronger than Tevatron or LHC7 data, as shown in Figs. 2.5, 2.6, 2.7, 2.8, 2.9, 2.10.

Figures 3.20, 3.21, 3.22, 3.23, 3.24, 3.25 presents the 5σ discovery potential (fb^{-1}) at the LHC14 via the W' leptonic decay channel, and current constraints are within the solid black contour. After the LHC14 collects 10 fb^{-1} , a sizable region of parameter space will be further tested, except for all the phobic models, LPD(T), HPD(T) and FPD(T). For the phobic models, very large integrated luminosity is needed to have 5σ discovery because of the small total cross section in the W' leptonic decay channel, which is either suppressed by

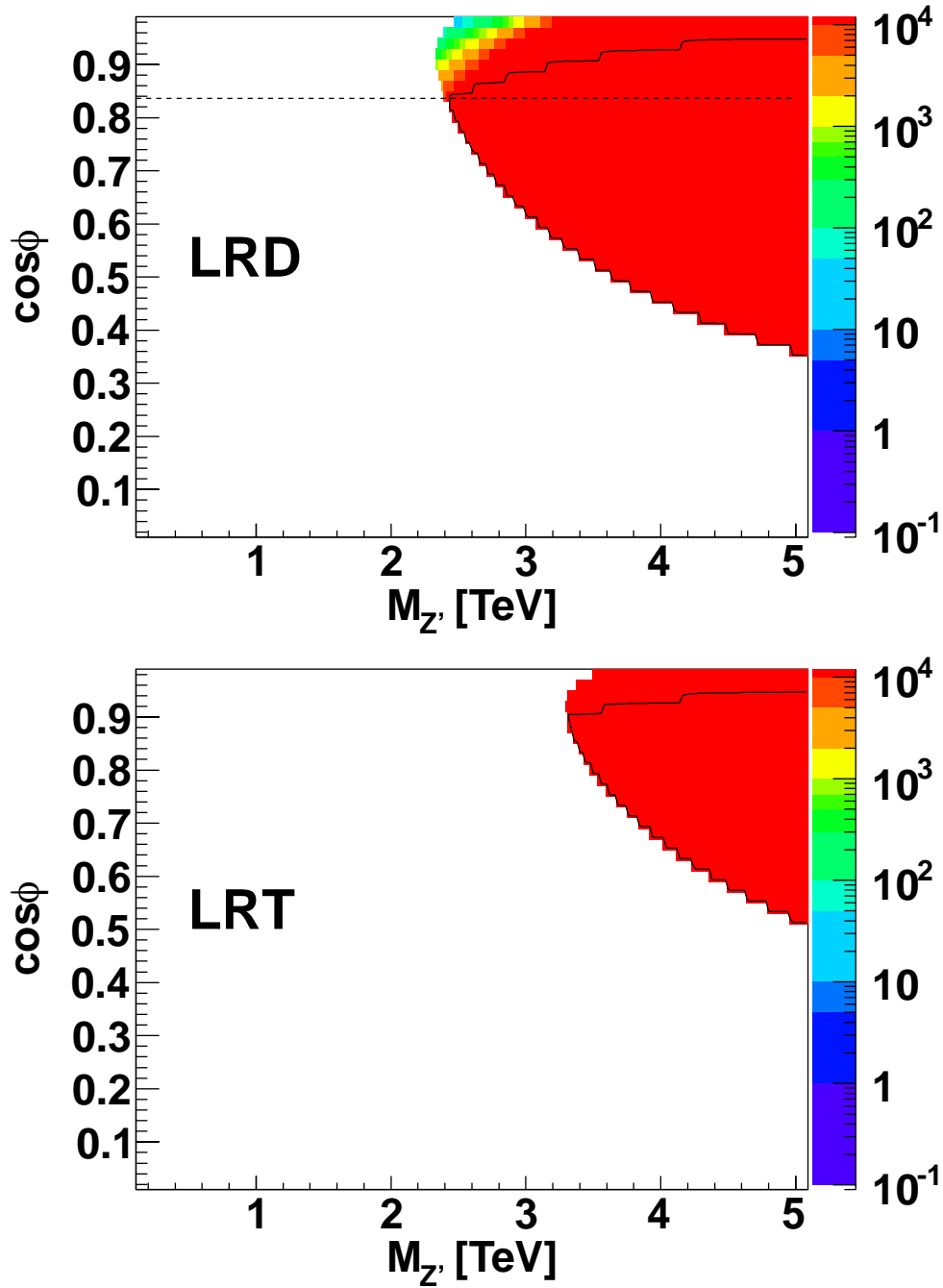


Figure 3.14: 5σ Discovery potential (fb^{-1}) in the LRD and LRT models for different luminosity at LHC7 via Z' leptonic decay channel. The current combined constraints are within solid black contour. The dashed black lines in LRD represent MLR models.

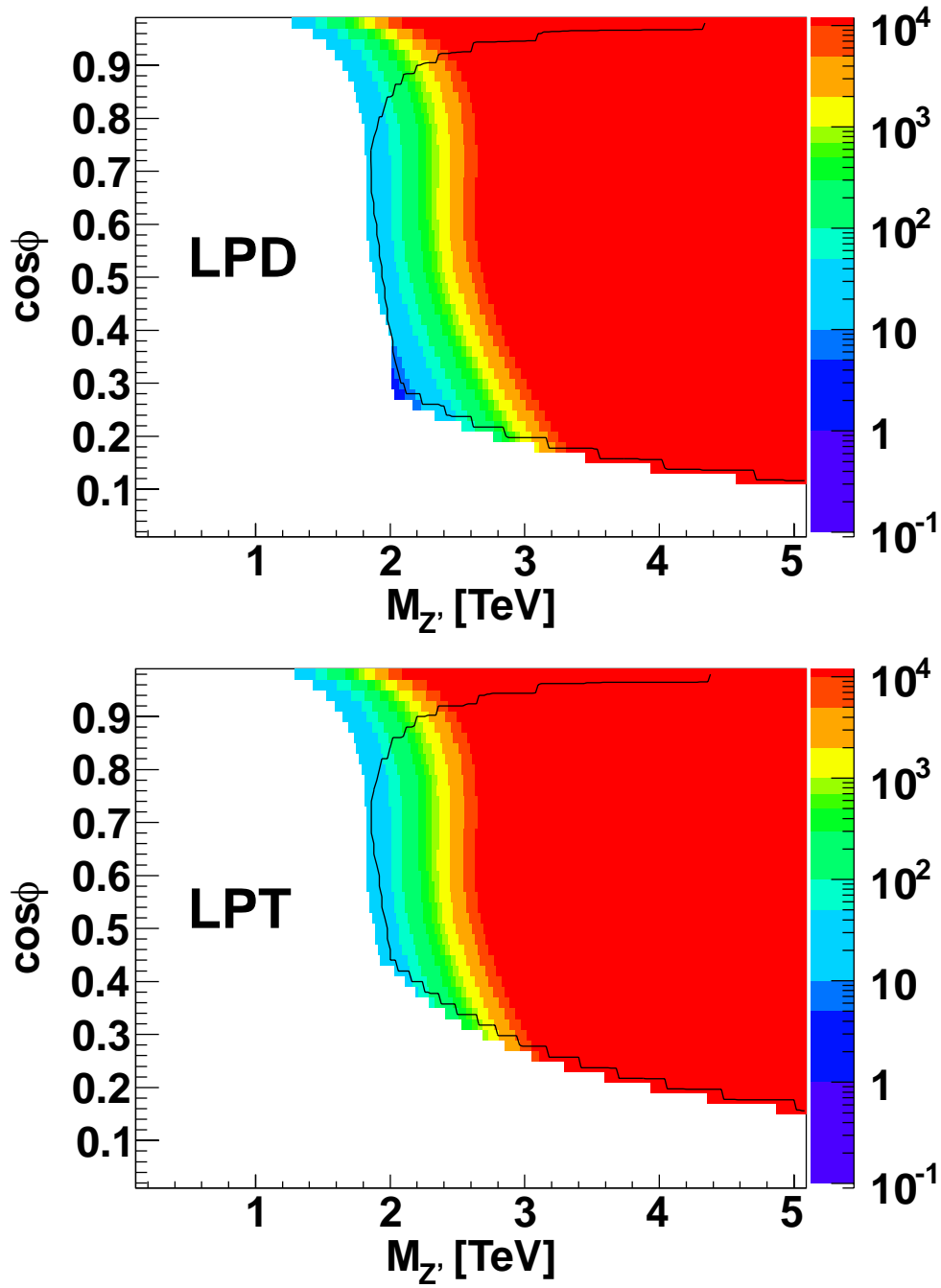


Figure 3.15: 5σ Discovery potential (fb^{-1}) in the LPD and LPT models for different luminosity at LHC7 via Z' leptonic decay channel. The current combined constraints are within solid black contour.

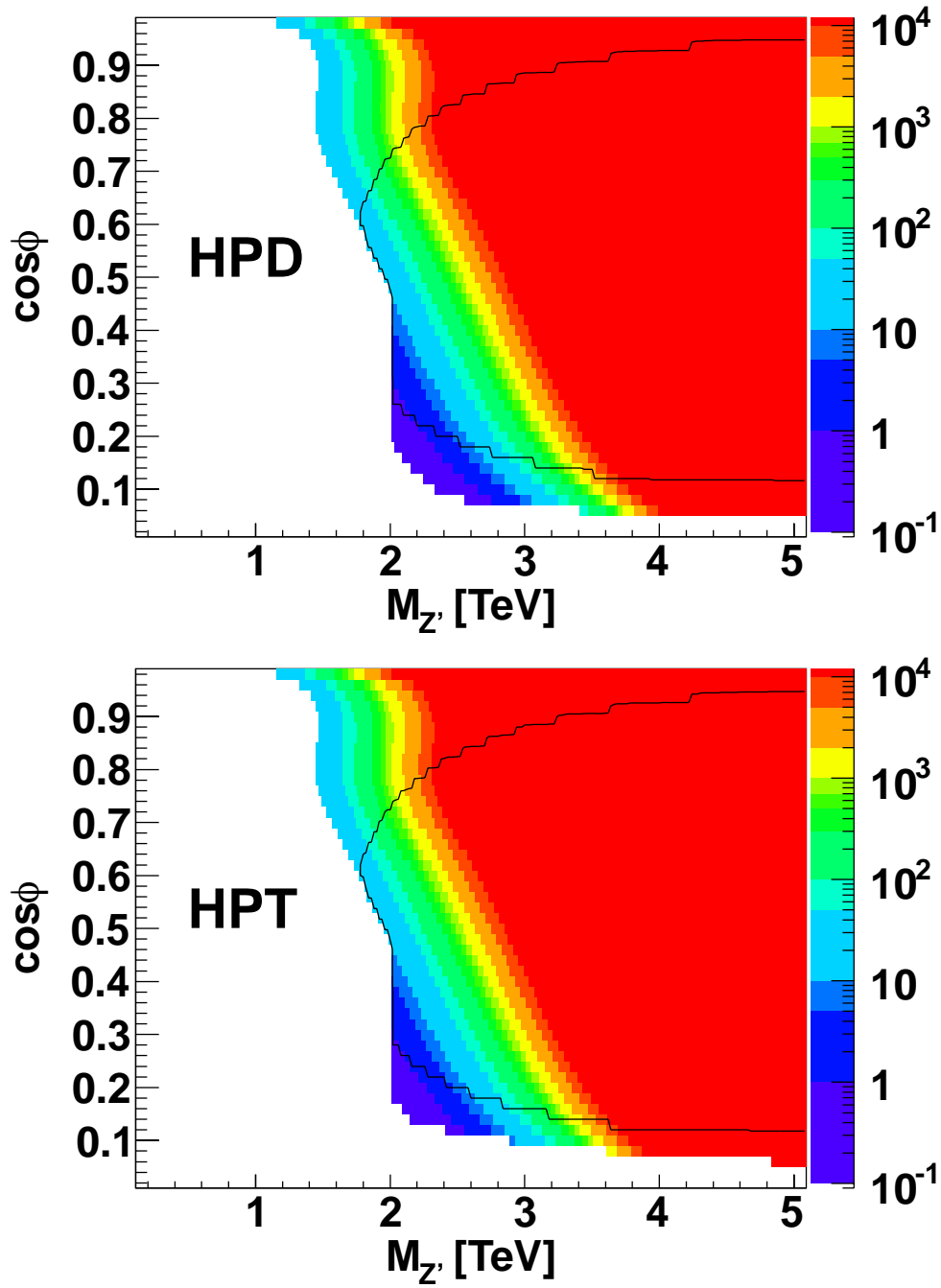


Figure 3.16: 5σ Discovery potential (fb^{-1}) in the HPD and HPT models for different luminosity at LHC7 via Z' leptonic decay channel. The current combined constraints are within solid black contour.

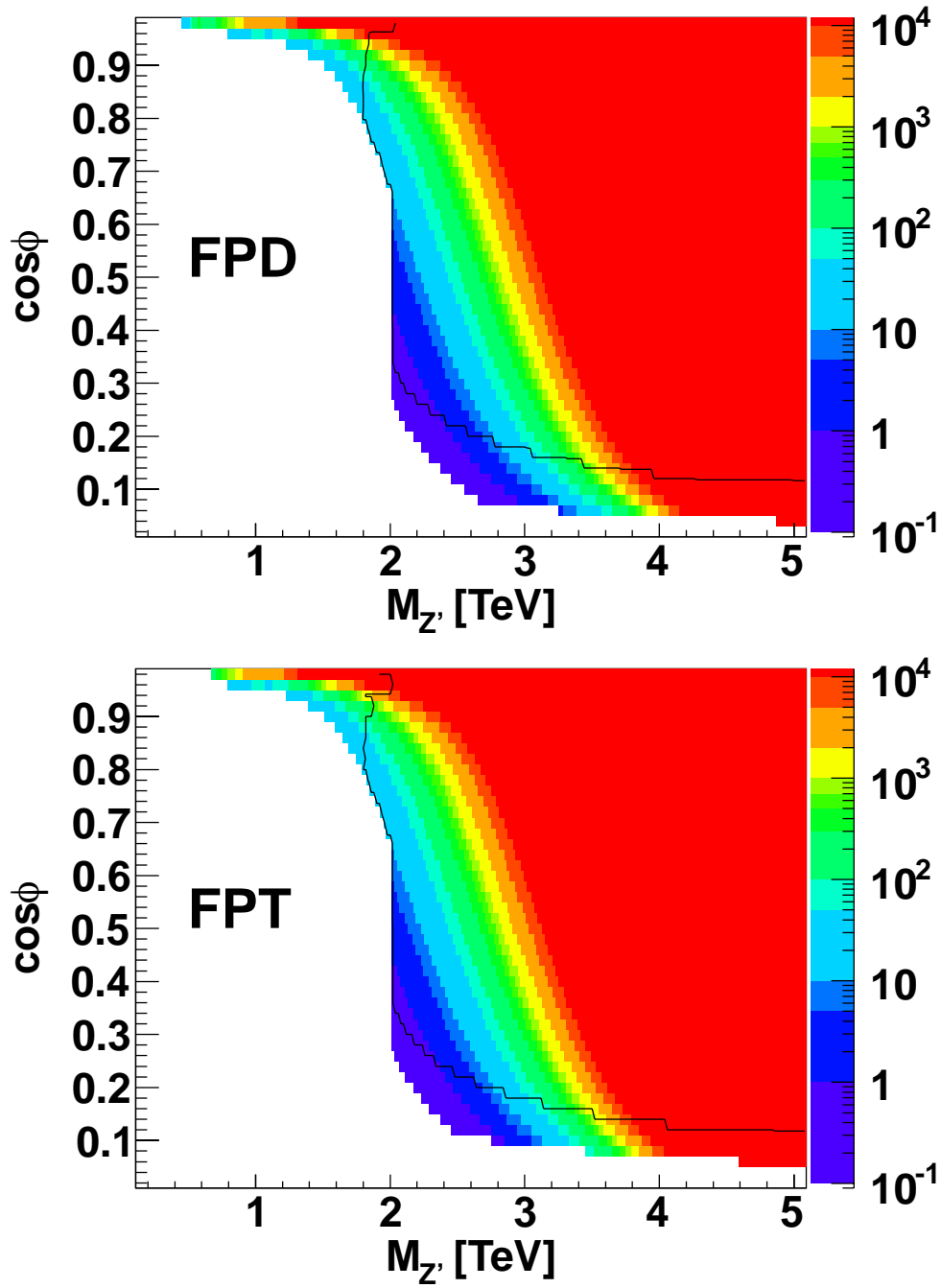


Figure 3.17: 5σ Discovery potential (fb^{-1}) in the FPD and FPT models for different luminosity at LHC7 via Z' leptonic decay channel. The current combined constraints are within solid black contour.

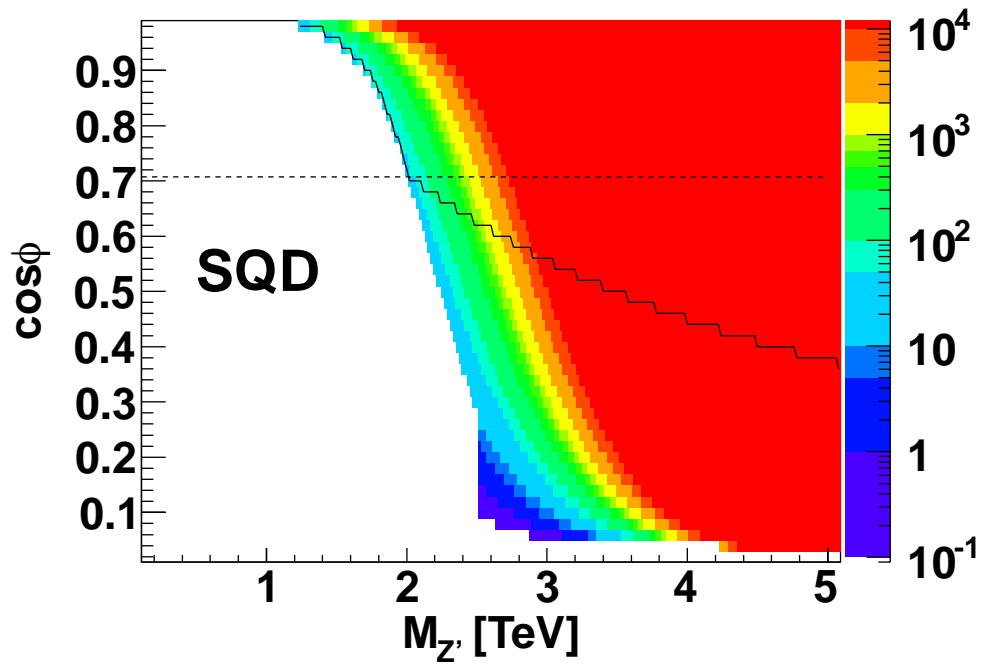


Figure 3.18: 5σ Discovery potential (fb^{-1}) in the SQD models for different luminosity at LHC7 via Z' leptonic decay channel. The current combined constraints are within solid black contour. The dashed black lines in SQD represent MSQ models.

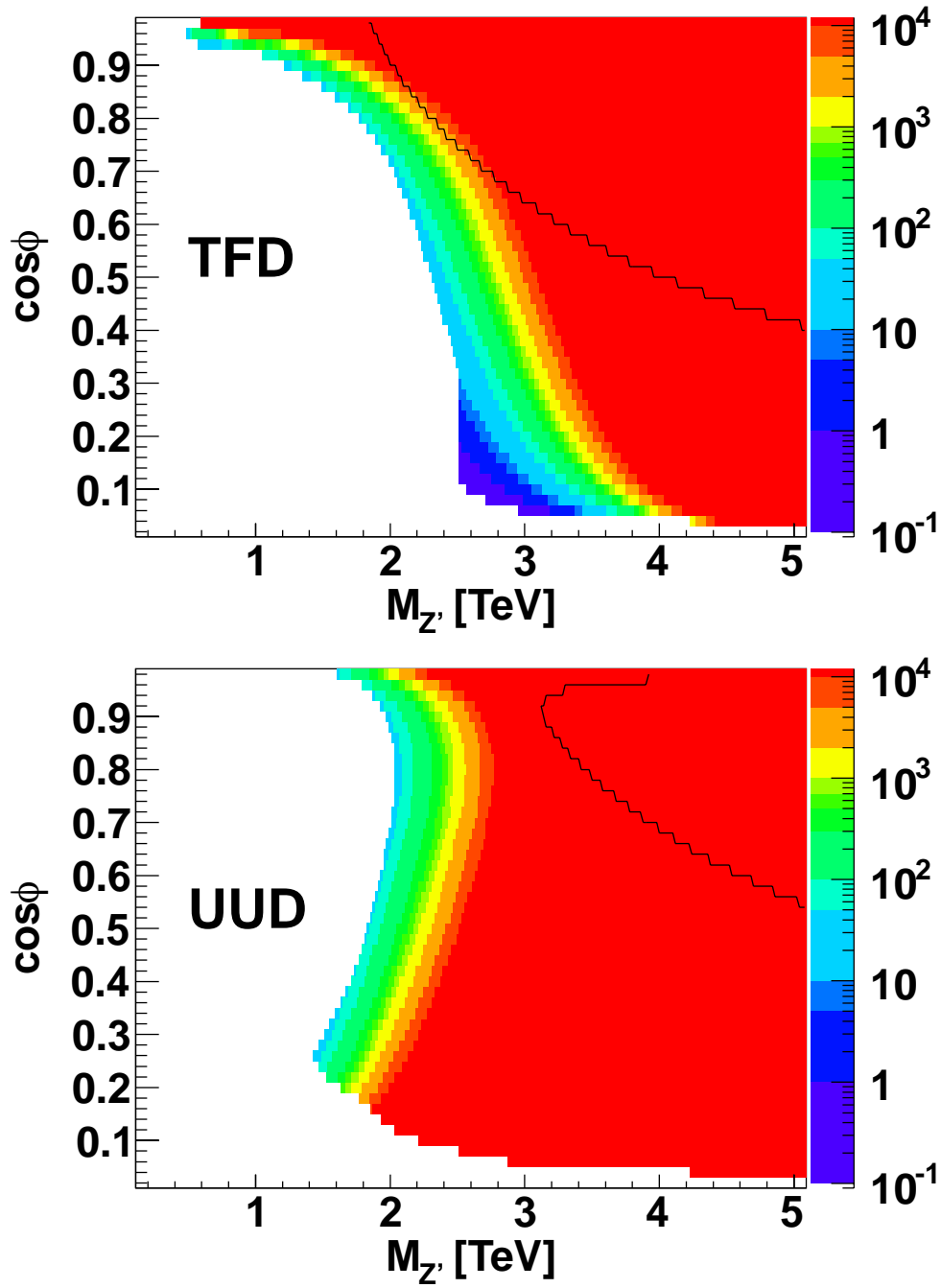


Figure 3.19: 5σ Discovery potential (fb^{-1}) in the TFD and UUD models for different luminosity at LHC7 via Z' leptonic decay channel. The current combined constraints are within solid black contour.

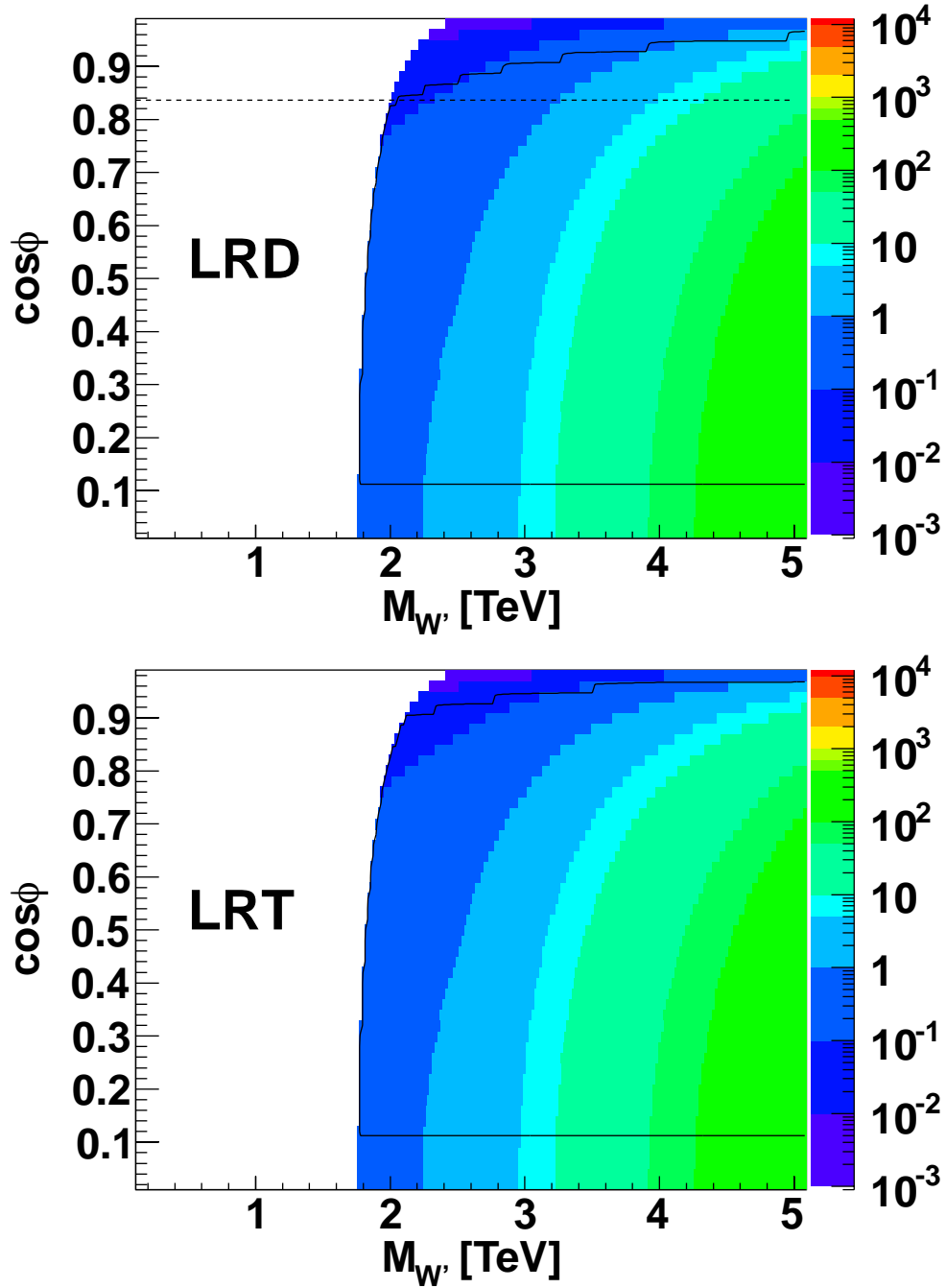


Figure 3.20: 5σ Discovery potential (fb^{-1}) in the LRD and LRT models for different luminosity at LHC14 via W' leptonic decay channel. The current combined constraints are within solid black contour. The dashed black lines in LRD represent MLR models.

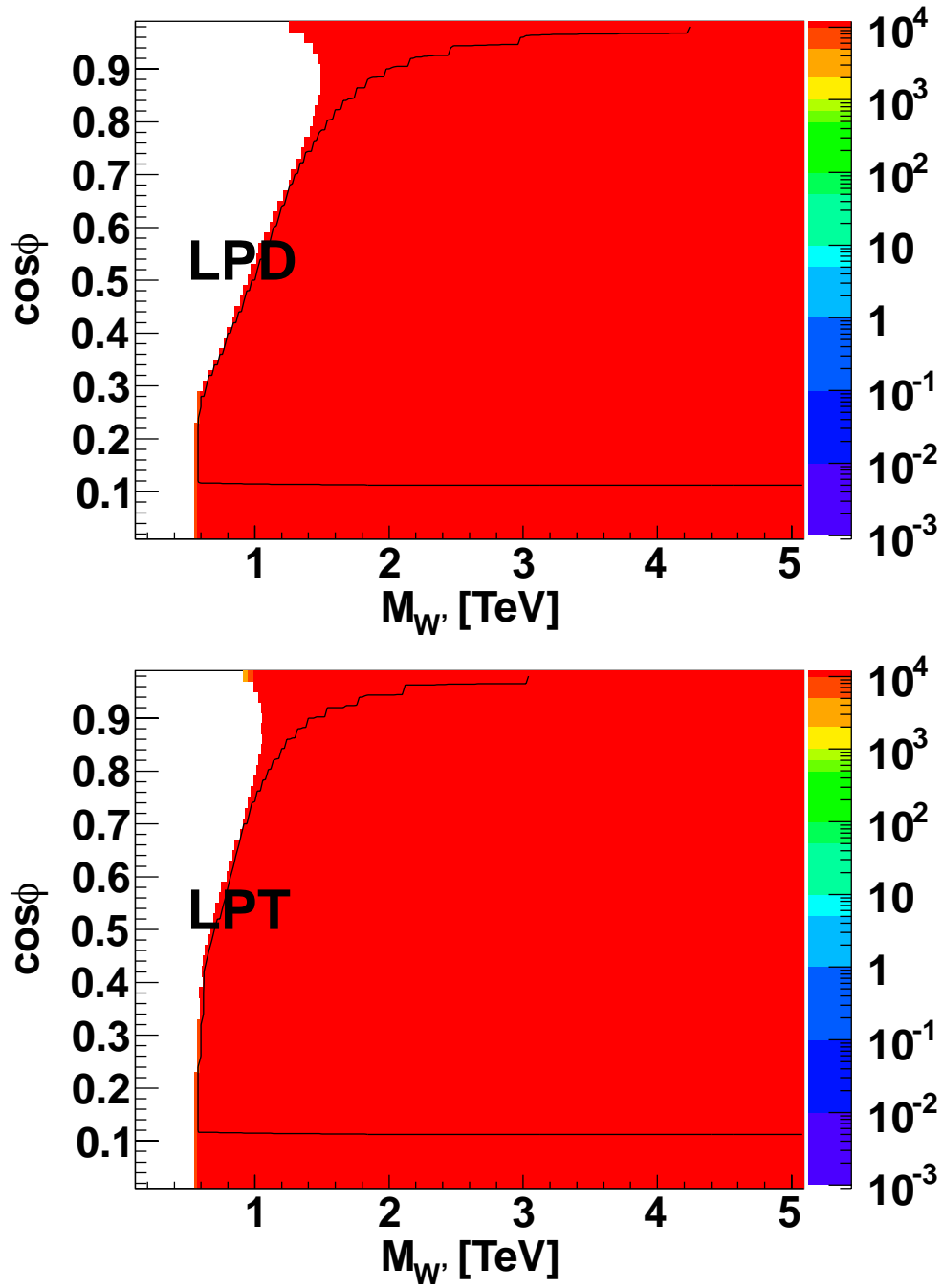


Figure 3.21: 5σ Discovery potential (fb^{-1}) in the LPD and LPT models for different luminosity at LHC14 via W' leptonic decay channel. The current combined constraints are within solid black contour.

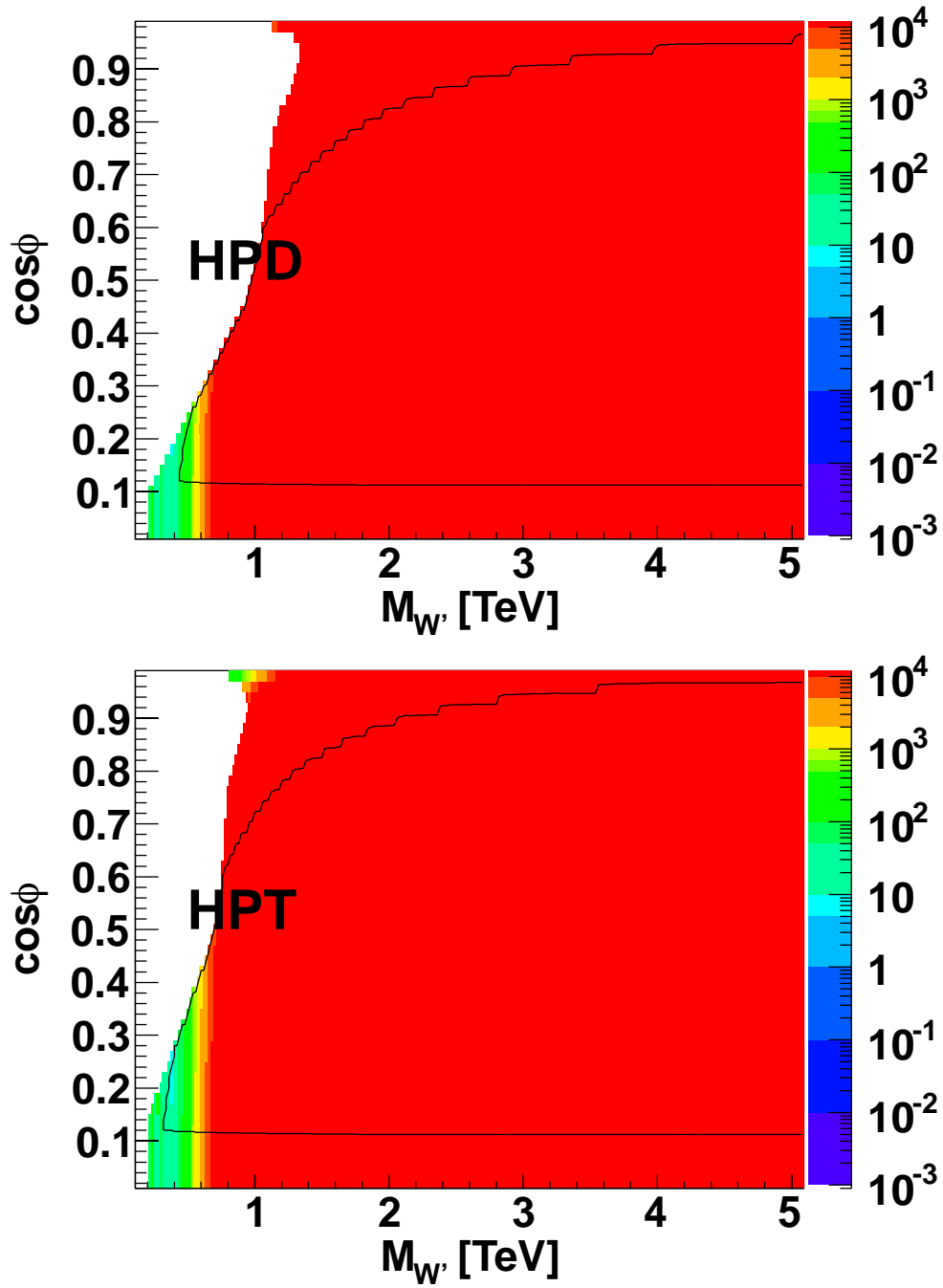


Figure 3.22: 5σ Discovery potential (fb^{-1}) in the HPD and HPT models for different luminosity at LHC14 via W' leptonic decay channel. The current combined constraints are within solid black contour.

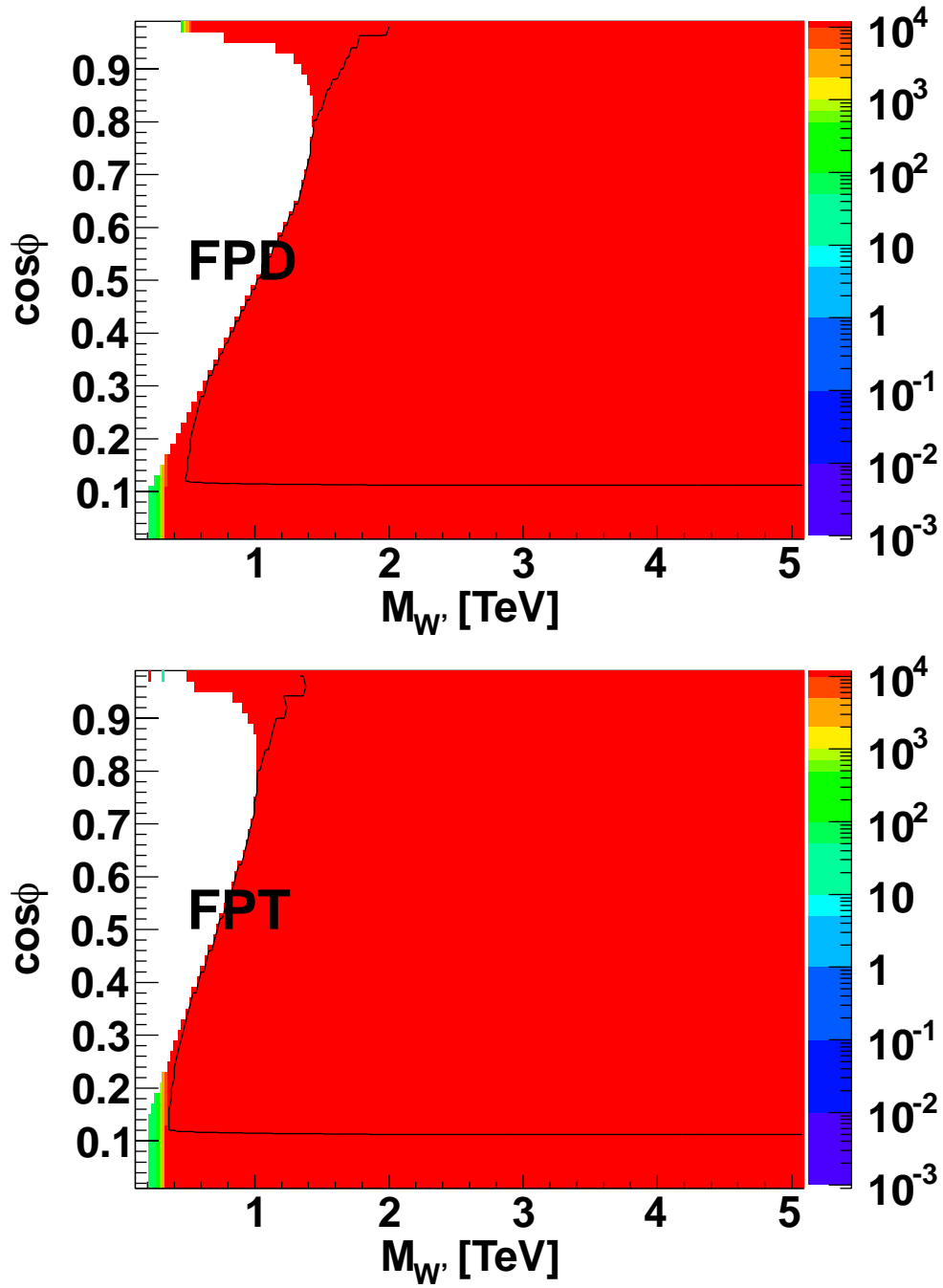


Figure 3.23: 5σ Discovery potential (fb^{-1}) in the FPD and FPT models for different luminosity at LHC14 via W' leptonic decay channel. The current combined constraints are within solid black contour.

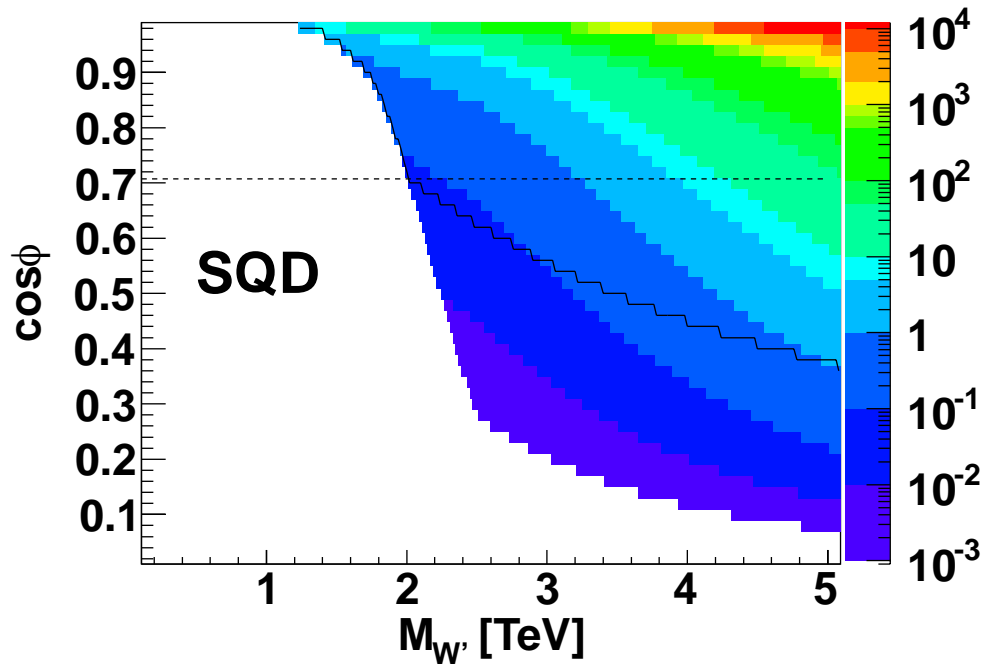


Figure 3.24: 5σ Discovery potential (fb^{-1}) in the SQD models for different luminosity at LHC14 via W' leptonic decay channel. The current combined constraints are within solid black contour. The dashed black lines in SQD represent MSQ models.

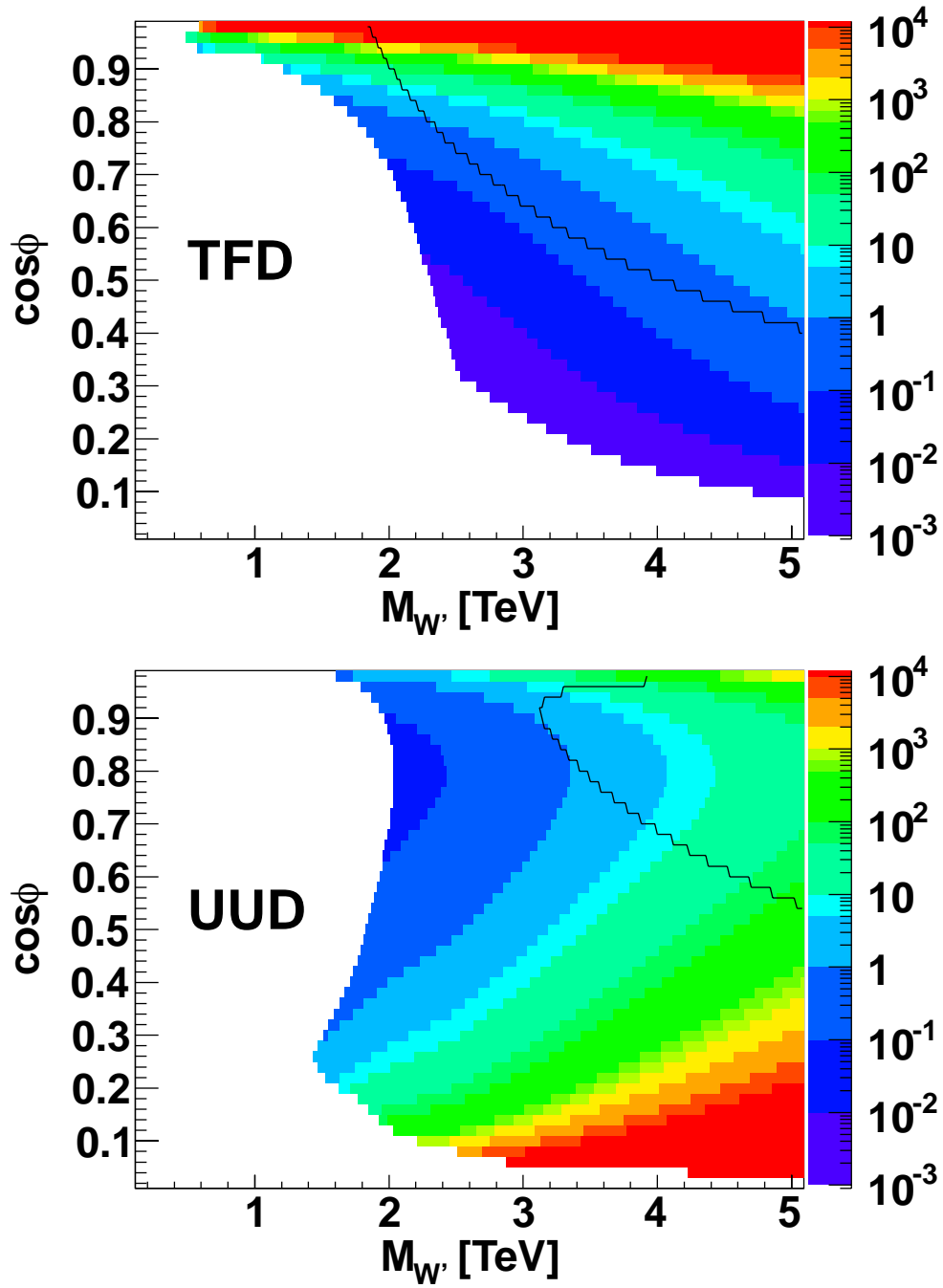


Figure 3.25: 5σ Discovery potential (fb^{-1}) in the TFD and UUD models for different luminosity at LHC14 via W' leptonic decay channel. The current combined constraints are within solid black contour.

the production rate of the W' , such as HPD(T) and FPD(T), or suppressed by the decay branching ratio, such as LPD(T) and FPD(T). With a 10 fb^{-1} luminosity, for LRD(T), the discovery potential for W' mass can reach more than 3 TeV, and the W' mass discovery for MLR can reach more than 4 TeV. Furthermore, for the large c_ϕ region in LRD(T), LHC14 search via W' leptonic decay channel can easily probe the large $M_{W'}$ region with several fb^{-1} . In BP-II, the current constraints already pushed the W' to the large mass region. However, with a 10 fb^{-1} integrated luminosity, for SQD, TFD and UUD models, most of the allowed region below 5 TeV W' mass can be further tested. For relatively small c_ϕ in SQD and TFD, a few fb^{-1} luminosity can even probe W' boson beyond 5 TeV. When the LHC is upgraded to 14 TeV, SQD, TFD and UUD can be further tested, exploring the region where current constraints cannot reach. This shows that the capability of LHC14 is far beyond LHC7. However, even LHC14 cannot test all the phobic models, such as LPD(T), HPD(T) and FPD(T), via only W' leptonic decay channel.

Figures 3.26, 3.27, 3.28, 3.29, 3.30, 3.31 shows the 5σ discovery potential (fb^{-1}) for the LHC14 via the Z' leptonic decay channel, and current combined constraints are within solid black contour. For the models other than LRD(T), UUD and MLR, the LHC14 can already test the parameter space effectively with the integrated luminosity less than 1 fb^{-1} . However, for the FPD(T), SQD and TFD models, EWPTs are more sensitive to the large c_ϕ region. Also if the luminosity can reach 10 fb^{-1} , we can test a large parameter space region, where we can either discover new physics based on these models or constrain the parameters in the relevant region. For LRD(T), UUD and MLR, when integrated luminosity is accumulated to more than 100 fb^{-1} , LHC14 data can have sizable parameter space further tested up to even beyond 5 TeV $M_{Z'}$. For LRD(T) Z' leptonic decay channel is less effective

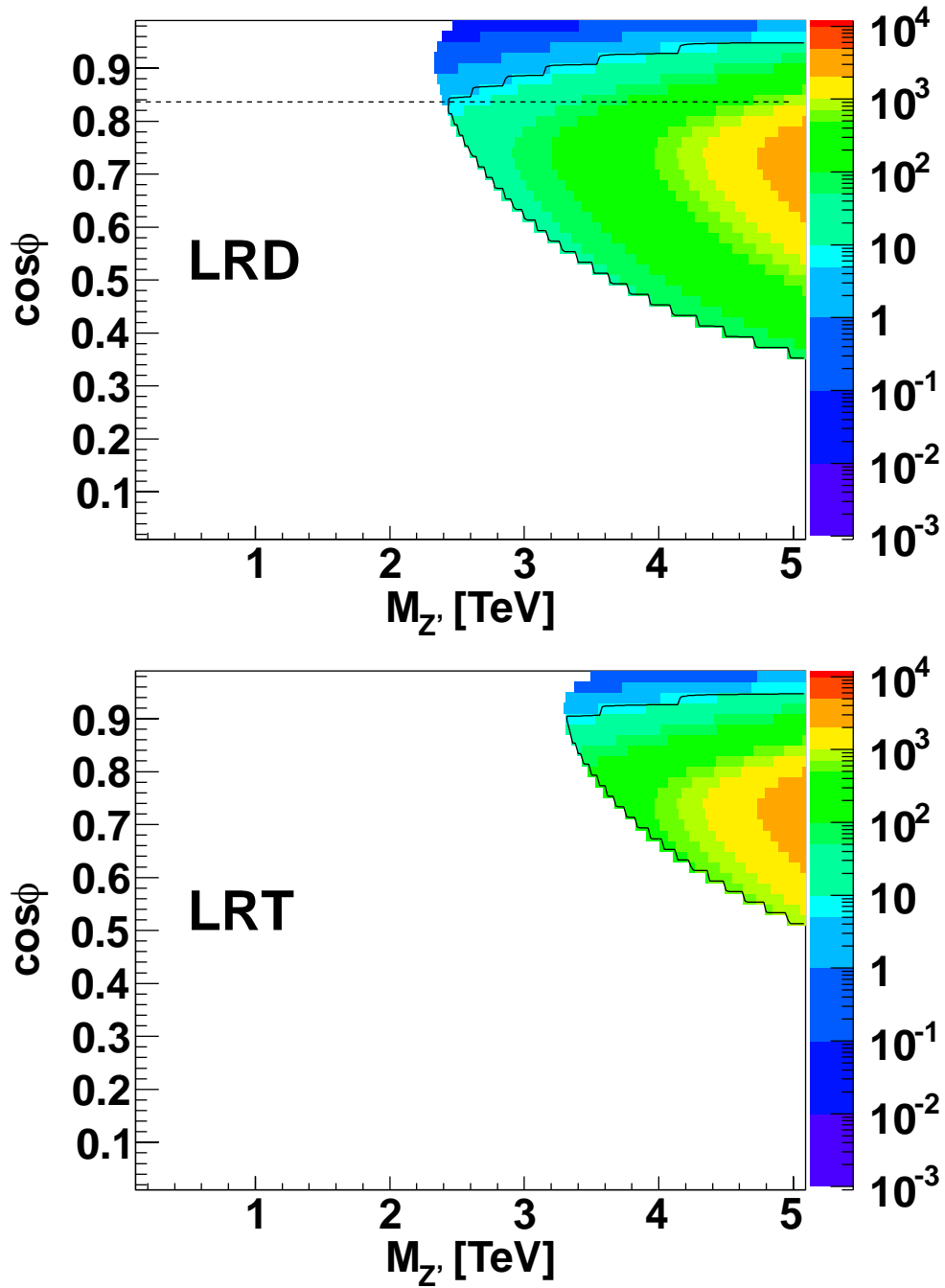


Figure 3.26: 5σ Discovery potential (fb^{-1}) in the LRD and LRT models for different luminosity at LHC14 via Z' leptonic decay channel. The current combined constraints are within solid black contour. The dashed black lines in LRD represent MLR models.

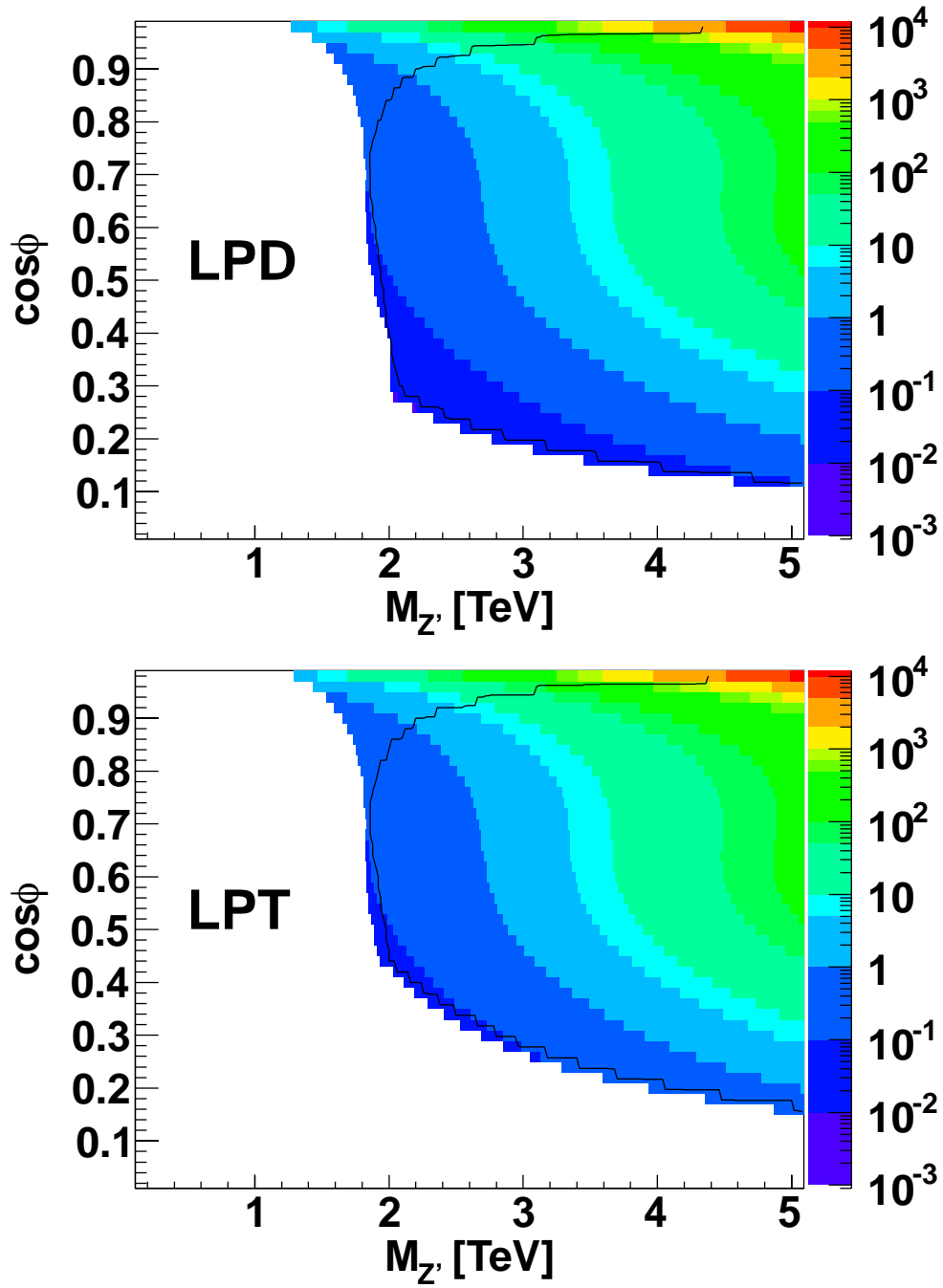


Figure 3.27: 5σ Discovery potential (fb^{-1}) in the LPD and LPT models for different luminosity at LHC14 via Z' leptonic decay channel. The current combined constraints are within solid black contour.

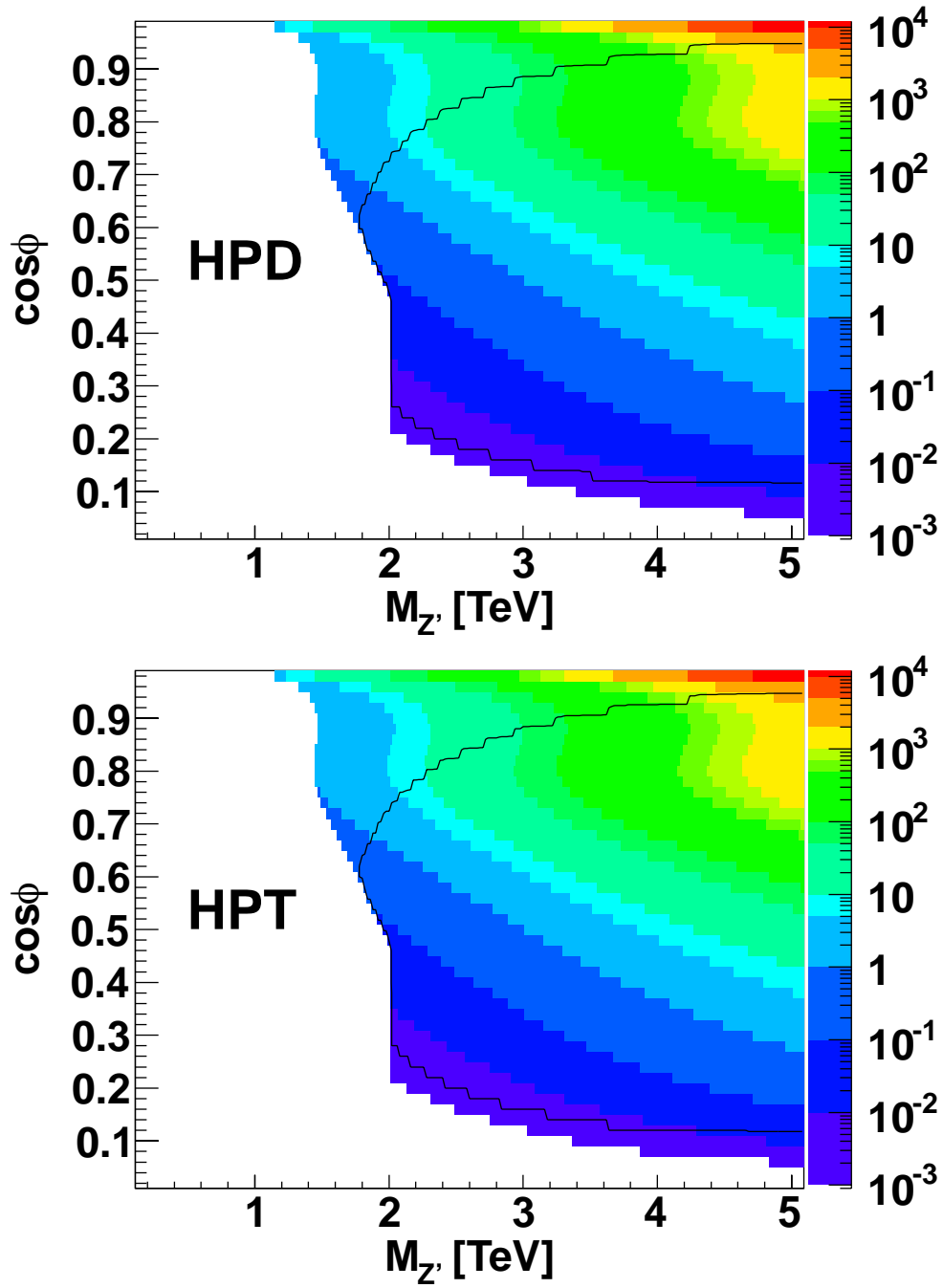


Figure 3.28: 5σ Discovery potential (fb^{-1}) in the HPD and HPT models for different luminosity at LHC14 via Z' leptonic decay channel. The current combined constraints are within solid black contour.

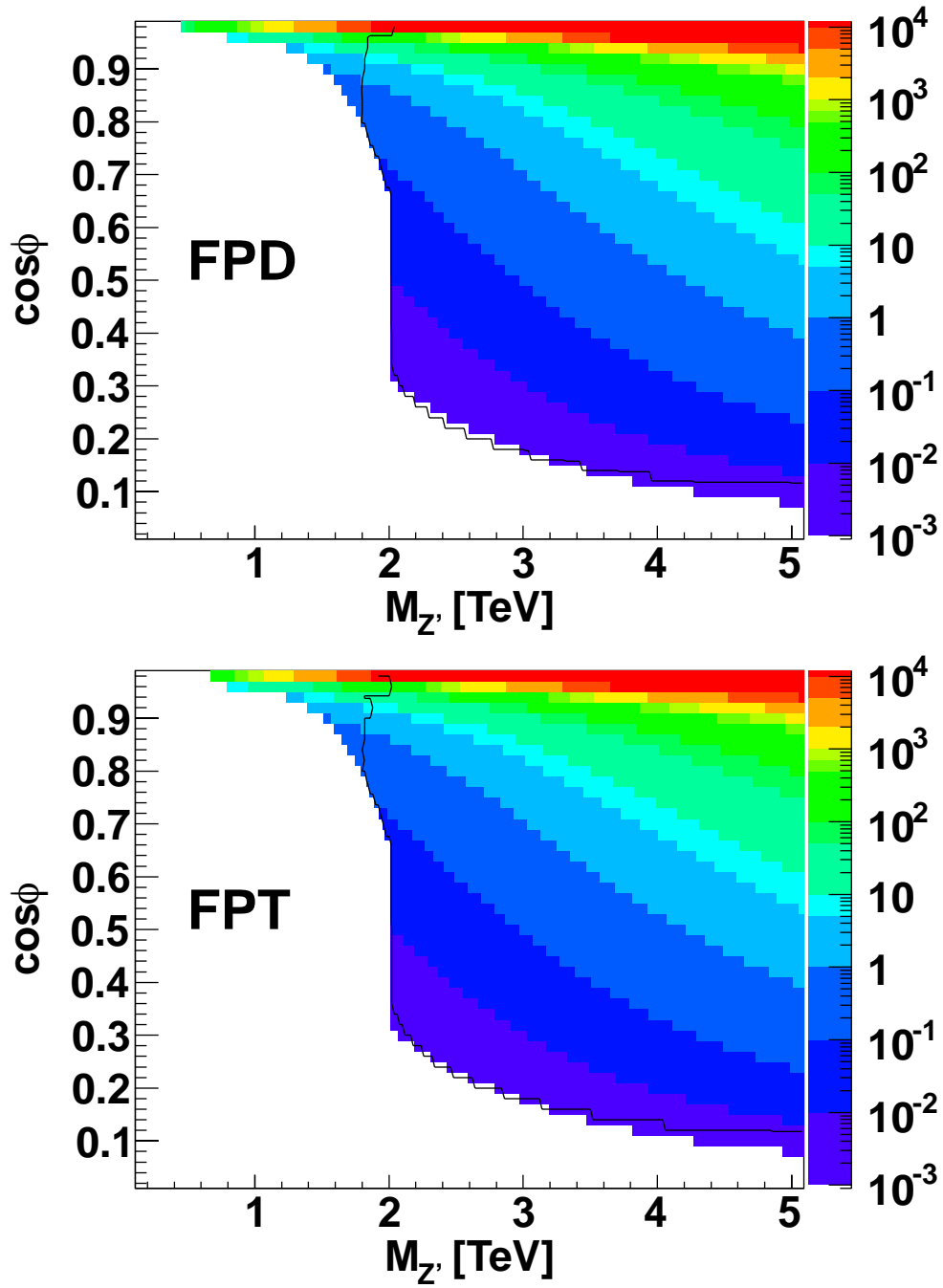


Figure 3.29: 5σ Discovery potential (fb^{-1}) in the FPD and FPT models for different luminosity at LHC14 via Z' leptonic decay channel. The current combined constraints are within solid black contour.

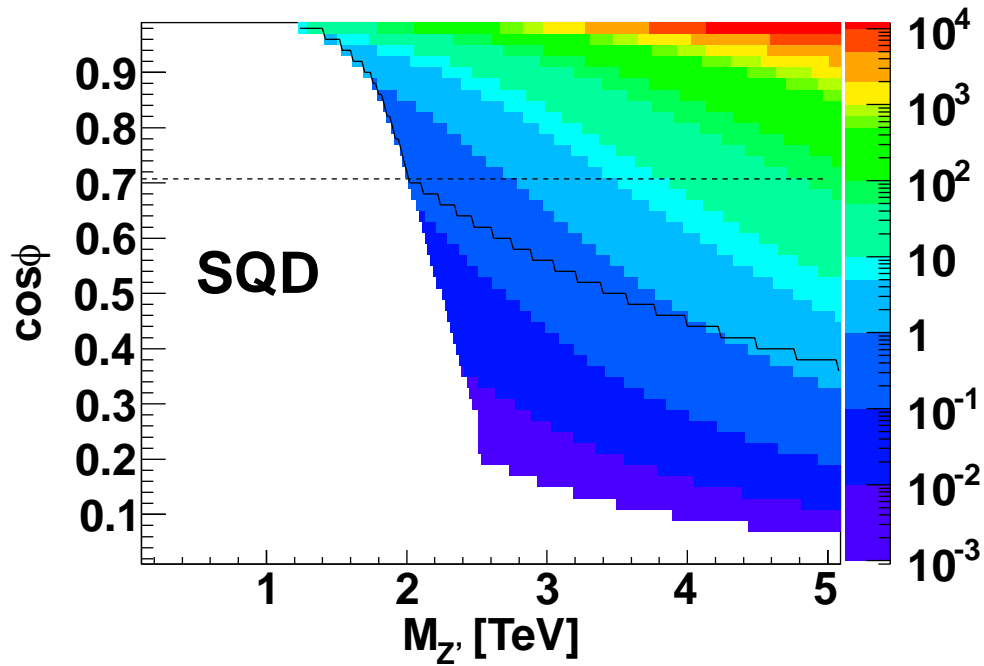


Figure 3.30: 5σ Discovery potential (fb^{-1}) in the SQD models for different luminosity at LHC14 via Z' leptonic decay channel. The current combined constraints are within solid black contour. The dashed black lines in SQD represent MSQ models.

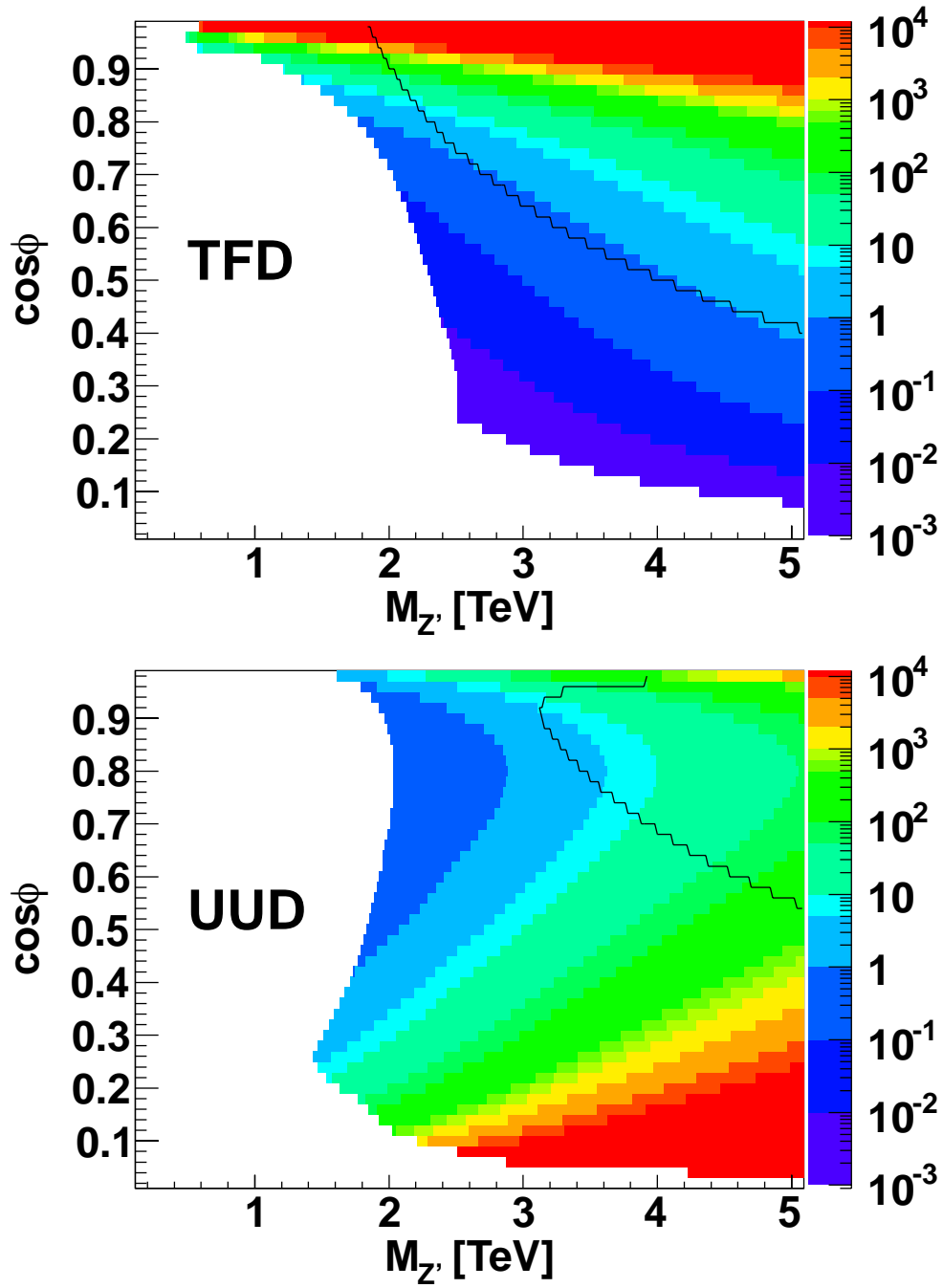


Figure 3.31: 5σ Discovery potential (fb^{-1}) in the TFD and UUD models for different luminosity at LHC14 via Z' leptonic decay channel. The current combined constraints are within solid black contour.

than W' channel. However, for the phobic models, such as LPD(T), FPD(T) and HPD(T), there is no $\mathcal{O}(1/x)$ suppression on the couplings of Z' to fermions, unlike the couplings of W' to fermions. So Z' leptonic decay channel is much more effective than W' for the investigation based on the LHC14 data. Especially, for the small c_ϕ region, a few pb^{-1} luminosity can probe very large $M_{Z'}$. In the phobic models, observing a Z' alone cannot rule out the possibility of a non-Abelian gauge extension of new physics.

In BP-II, both Z' and W' leptonic decay channel are suitable to explore the allowed parameter space of the models. Since the mass of W' and Z' are degenerate in BP-II, discovering degenerate W' and Z' in the leptonic decay channels at the same time will be the distinct feature compared to the models in BP-I. Compared to the LHC7 discovery potentials in Figs. 3.8, 3.9, 3.10, 3.11, 3.12, 3.13 and 3.14, 3.15, 3.16, 3.17, 3.18, 3.19. Figs. 3.20, 3.21, 3.22, 3.23, 3.24, 3.25 and 3.26, 3.27, 3.28, 3.29, 3.30, 3.31 show that for LHC the upgrade of the CM energy from 7 TeV to 14 TeV is much more efficient than accumulation of luminosity. For instance, for FPD(T) the Z' leptonic decay channel at LHC14 with less than 1 fb^{-1} can explore some region of parameter space, while LHC7 needs more than 10^4 fb^{-1} luminosity to achieve the similar sensitivity. For all these $G(221)$ models, LHC14 can exceed the capability of current combined constraints and has promising discovery potential.

If the heavy gauge bosons W' and/or Z' are not discovered, the potential for discovery can be converted to the 95% CL exclusion limits on the heavy gauge bosons W' and/or Z' using the relations $Z = S/3$ as discussed above. Equivalently, the luminosity for exclusion limits is about one order of magnitude lower than the discovery luminosity. Therefore, as shown in Figs. 3.8, 3.9, 3.10, 3.11, 3.12, 3.13 supposing no signals found, via W' leptonic decay channel, W' mass in LRD(T) can be further excluded by about 100 GeV after the

LHC7 collects 5.61 fb^{-1} luminosity. Figs. 3.14, 3.15, 3.16, 3.17, 3.18, 3.19 shows that via Z' leptonic decay channel, one can expect slightly further exclusion on LPD(T), HPD(T) and FPD(T) at LHC7. At the LHC14, as show in Figs. 3.20, 3.21, 3.22, 3.23, 3.24, 3.25 and 3.26, 3.27, 3.28, 3.29, 3.30, 3.31, exclusion region can extend very fast when luminosity is accumulated. For instance, via W' leptonic decay channel, 1 fb^{-1} can exclude most of the parameter region for LRD(T), SQD, TFD and UUD, and 10 fb^{-1} can completely remove the possibility of $M_{Z'}$ less than 5 TeV in these models if there is no any sign of W' production. For LPD(T), HPD(T) and FPD(T), Z' leptonic decay channel at the LHC14 can be used to exclude most of the parameter space region with only 1 fb^{-1} luminosity. Then data with 10 fb^{-1} luminosity at LHC14 may leave LPD(T) and HPD(T) and FPD(T) only a corner of parameter space at large c_ϕ to survive. The shapes of the exclusion contours are the same as these at the discovery contours.

3.5 Summary

In this paper we have discussed the potential for discovering, or setting limits on, the extra heavy gauge bosons W' and/or Z' using two different scenarios at the LHC: an early run with $\sqrt{s} = 7 \text{ TeV}$ and total integrated luminosity of 5.61 fb^{-1} ; a long run with $\sqrt{s} = 14 \text{ TeV}$ and 100 fb^{-1} integrated luminosity. The EWPTs, Tevatron and LHC data have been used to set bounds on the allowed parameter space. We showed that direct searches give tighter bounds than EWPTs in BP-I. Although constraints from LHC data surpasses Tevatron and EWPTs constraints in LRD, LRT models, in other models the parameter space depends non-trivially on the present bounds, especially during the early LHC runs. The unexplored parameter space will become accessible for 5σ discovery at different time scales. In LRD(T) it is more

Models	Current $M_{W'}$ Limit	$M_{W'}$ LHC14 Reach
LRD (LRT)	1.72 (1.76) TeV	3.2 - 5 TeV
LPD (LPT)	0.55 (0.55) TeV	No improvement
HPD (HPT)	0.46 (0.35) TeV	0.55 TeV
FPD (FPT)	0.5 (0.4) TeV	No improvement
SQD	1.25 TeV	3.5 - 5 TeV
TFD	1.7 TeV	2 - 5 TeV
UUD	3.1 TeV	4 - 5 TeV

Table 3.2: The current lowest limits and discovery reaches at the LHC14 with 100 fb^{-1} luminosity on W' masses.

Models	Current $M_{Z'}$ Limit	$M_{Z'}$ LHC14 Reach
LRD (LRT)	2.25 (3.2) TeV	2.8 - 5 TeV
LPD (LPT)	1.8 (1.8) TeV	3.5 - 5 TeV
HPD (HPT)	1.7 (1.7) TeV	3 - 5 TeV
FPD (FPT)	1.75 (1.75) TeV	1.75 - 5 TeV
SQD	1.25 TeV	1.5 - 5 TeV
TFD	1.7 TeV	2 - 5 TeV
UUD	3.1 TeV	3.3 - 5 TeV

Table 3.3: The current lowest limits and discovery reaches at the LHC14 with 100 fb^{-1} luminosity on W' and Z' masses.

efficient to use W' leptonic decay channel for discovery or exclusion than Z' leptonic decay channel. In the phobic models, it is challenging to discover a W' decaying into leptonic mode. Hence, observing a Z' alone cannot rule out the possibility of NP models with non-Abelian gauge extension of the standard model. In BP-II models, both Z' and W' leptonic decay channel are suitable to explore the allowed parameter space. Discovering degenerate W' and Z' in the leptonic decay channels at the same time will be the distinct feature in BP-II. In Tabs. 3.2 and 3.3, we summarize the current constraints and LHC14 reaches with 100 fb^{-1} luminosity on the W' and Z' masses in various models. If one needs to identify new physics models more precisely, one has to combine different discovery channels, such as top quark pair, single top quark production for the heavy resonances, or study angular distributions, or other properly defined asymmetries, in the most promising regions of parameter space of the models considered. For example, the LPD(T), HPD(T), and FPD(T) models can be further explored by examining the single-top production, the associate production of W' and W (or Z) bosons, and the production of weak gauge boson pairs from electroweak gauge boson fusion processes.

Chapter 4

PROPERTIES OF HEAVY CHARGED GAUGE BOSONS

4.1 Introduction

The leptonic channel is the golden channel to discover heavy charged gauge bosons at hadron colliders. The most sensitive observable to discover this heavy resonance is the transverse invariant mass of the lepton and missing energy system. After discovery, using the smeared peak behavior, it is possible to determine its basic properties, such as the mass and width. At the same time, the angular distribution of the final state lepton can be used to determine its spin, although it is difficult to do the angular analysis for the charged gauge boson due to the missing neutrino in the final state. To study its properties in detail, it is more efficient to look at other decay channel, such as the top quark channel.

The top quark plays a special role in the standard model, and offers a window into possible new physics beyond the SM. In many models, because the top quark is naturally

related to EWSB, new physics is very sensitive to the top quark observables. The observables such as angular, spin correlations and polarization of the top quark can be used to determine the particle properties and its chiral structures. Since t -channel single top production with W' exchange are much more suppressed than s -channel single top process if W' masses are larger than the top mass, one can reconstruct the invariant mass from the resonance peaks of the final state top and bottoms. Therefore, for a lepto-phobic W' , the single top channel will be the best channel to do discovery and further identification. Furthermore, in the top quark channel, because the final state lepton of the decaying top quark is sensitive to the chiral structure of the charged gauge bosons, it is possible to probe the chiral structure of the charged gauge bosons using the top quark polarization. We will study the heavy charged gauge bosons in the single top final states.

The forward-backward asymmetry indicates the chiral structures in the process. Both CDF and DØ at the FermiLab Tevatron observed the large forward-backward asymmetry of the top quark in the top pair final states, deviated by about two standard deviation (2σ) from the standard model expectations. Many new physics models have been proposed to explain the enhanced asymmetry. One possible model suggests that this large asymmetry might come from t -channel flavor-changing W' exchange in the top pair production. Measuring the forward-backward asymmetry will give us the information on the chiral structure of the W' -boson.

4.2 s -channel Production of W' : Resonances in Single Top Channel

4.2.1 New Physics Models

In the typical W' models, the leptonic final state will be the primary channel. However, because the W' searches in the leptonic final states at the LHC are pushing to higher and higher W' mass region, it is also worth to search W' in the quark channel, especially single top quark channel in the low mass region. For example, in some special models in which the W' is lepto-phobic, the third generation quark final state will be the best channel to look at. We list the following possible models which prefer the single top final state,

- In some models, the top quark is involved in the electroweak breaking. In this case, the top quark couplings of new gauge bosons will be larger than the light quark couplings. In the top-flavor model, the W' prefer to couple with the third generation quarks.
- Motivated from the Wjj anomaly at the LHC, it is possible that heavy gauge boson can be lepto-phobic. From the di-jet final states, the resonance of di-jet can not tell us whether it is a W' or neutral gauge bosons, such as Z' or axi-gluon. In this case, the single top process will be the discovery channel for the lepto-phobic W' .
- Motivated from top pair forward-backward asymmetry, it is possible to have the flavor-violating couplings between the first generation quarks and the third generation quarks, such as $t - \bar{u} - Z'$, and $b - \bar{d} - Z'$. So through $d\bar{b}$ initial state, there is a s channel single top by decaying to $t\bar{u}$ final state. On the other hand, through ud initial state,

there is a t channel single top by decaying to tb final state.

In this thesis, we focus on a lepto-phobic W' model. To keep this analysis model independent, the most general effective Lagrangian is written as

$$\mathcal{L} = i\frac{g_2}{\sqrt{2}} \begin{pmatrix} \bar{u} & \bar{c} & \bar{t} \end{pmatrix} \gamma^\mu (f_L P_L + f_R P_R) \begin{pmatrix} d \\ s \\ b \end{pmatrix} W'_\mu{}^+ + \text{h.c.} \quad , \quad (4.1)$$

where $g_2 = e/\sin\theta_W$ is the weak coupling, while $P_{L/R}$ are the usual chirality projection operators. For simplicity, we consider only the case with a purely left-handed current ($f_L = 1$, and $f_R = 0$), but our study can be extended easily to other cases. The triple gauge interaction of the W' and SM gauge bosons is included although such a non-abelian interaction is suppressed for large W' mass ($m_{W'}$) by W - W' mixing effects, which are of order $\mathcal{O}(m_W^2/m_{W'}^2)$.

This W' decays to quarks with decay width

$$\Gamma_{W' \rightarrow qq'} \simeq \frac{9g_2^2 m_{W'}}{48\pi} (f_L^2 + f_R^2). \quad (4.2)$$

For $f_L^2 + f_R^2 = 1$, $\Gamma_{W'} \sim m_{W'}/40$, indicating that the W' is narrow.

The parameter constraints are listed here. Previous studies of W' 's decaying to tops have focused on the LHC at center of mass energies of 14 TeV [71]. We examine the potential of the early LHC to identify W' 's during the early LHC as well as the experimental reach. Many natural models of new physics beyond the SM have relatively light W' bosons. They are needed to cancel quadratic divergences induced by SM W bosons on the higgs potential.

However, the closest exclusion limits come from leptophobic W' 's which decay to dijets [70, 69]

$$280 < m_{W'} < 1500 \text{ GeV.} \quad (4.3)$$

and direct searches from single top production.

4.2.2 Cross Section and Event Simulation

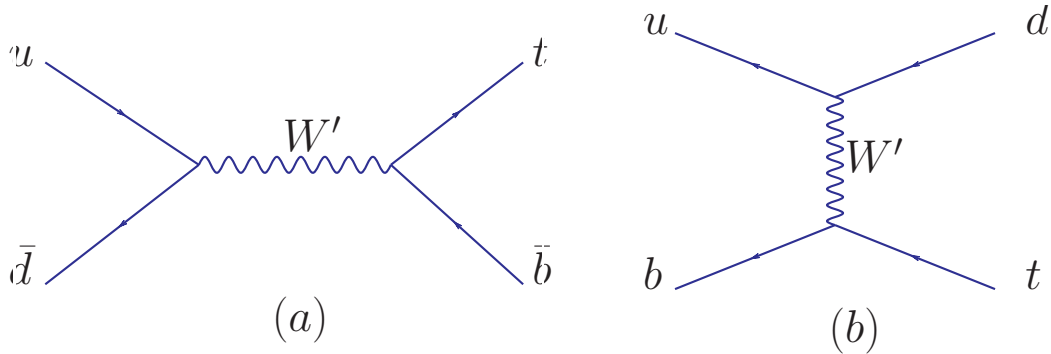


Figure 4.1: Feynman diagrams of the s -channel and t -channel single top production with exchanging a W' .

The s - and t -channel signal processes are

$$pp \rightarrow t\bar{b} + \text{h.c.} \quad pp \rightarrow tq \quad \text{or} \quad \rightarrow \bar{t}q, \quad (4.4)$$

Feynman diagrams are shown in the Fig. 4.1. From the current constraints on the W' mass in the top quark channel, one notes that the allowed W' mass is larger than the threshold energy of the top and bottom system. Therefore, the s -channel contribution will dominate, while the t -channel contribution is small. Considering the semi-leptonic decay of the top

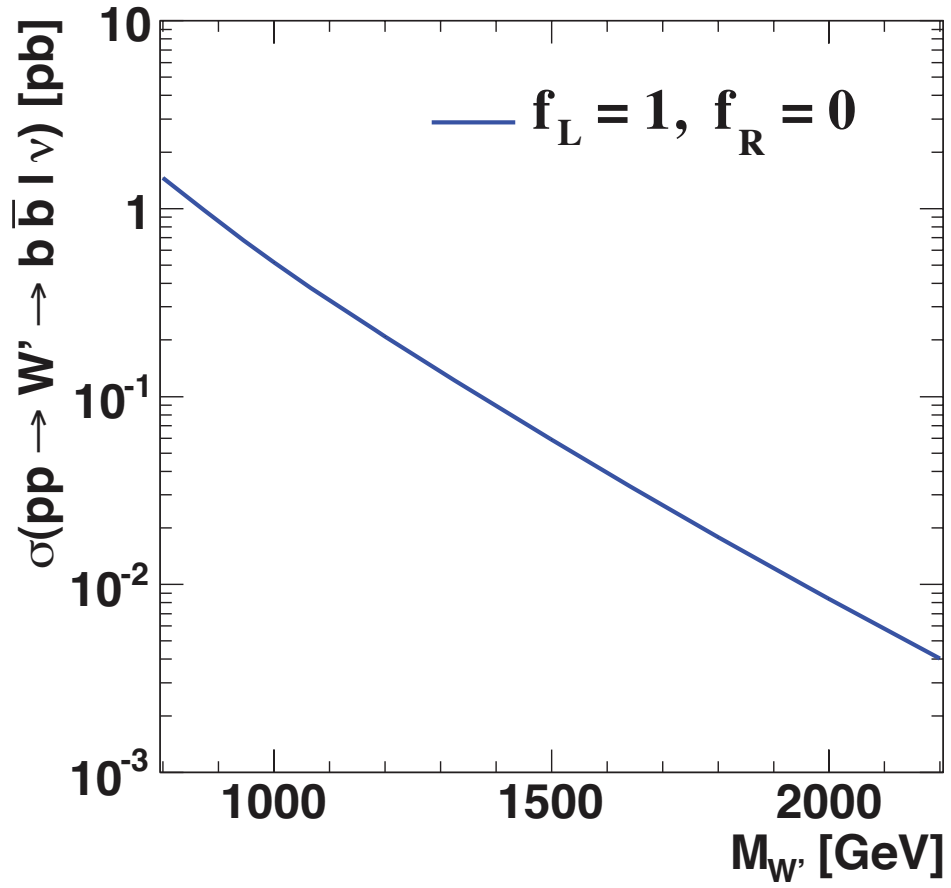


Figure 4.2: Total cross section of W' for $f_L = 1, f_R = 0$ at the LHC.

quark, the final state of this channel is

$$pp \rightarrow W' \rightarrow t\bar{b}(\bar{t}b) \rightarrow bl\nu\bar{b}. \quad (4.5)$$

The total cross section for W' production and subsequent decay to a top quark and bottom quark at the LHC are computed with Madgraph [107], which is shown in Fig. 4.2. We use the CTEQ6L1 set of parton distribution functions [74] and set the factorization and renormalization scales to the W' mass.

Signal and background events are generated with Madgraph [107] and are normalized to the corresponding LO cross sections. We choose the benchmark point as 1500 GeV mass, and coupling $f_L = \frac{g_2}{\sqrt{2}}$ and $f_R = 0$. The total decay width is $\Gamma_{W'} = 7.21$ GeV. The dominant backgrounds to the final state of lepton and two jets are from top quark pair production and W boson production in association with jets. For top pair production we include the lepton+jets final state, $t\bar{t} \rightarrow bl\nu\bar{b}jj$. Smaller backgrounds are from single top quark production in association with a W boson ($t + W$) or with jets ($t + jets$, t -channel and s -channel) and from diboson+jet (WV) production.

We use the anti-kt algorithm in the FastJet [75] package to cluster quarks and gluons into final state jets with parameter $R = 0.4$. Detector resolution effects are simulated by smearing jet and leptonic energies according to a Gaussian:

$$\frac{\delta E}{E} = \frac{\mathcal{A}}{\sqrt{E/\text{GeV}}} \oplus \mathcal{B}, \quad (4.6)$$

where $\frac{\delta E}{E}$ is the energy resolution, \mathcal{A} is a sampling term, \mathcal{B} is a constant term, \oplus represents addition in quadrature, and all energies are measured in GeV. For leptons we take $\mathcal{A} = 5\%$

and $\mathcal{B} = 0.55\%$, while for jets we take $\mathcal{A} = 100\%$ and $\mathcal{B} = 5\%$, chosen to represent the ATLAS and CMS detector performance [76, 77]. We do not smear \cancel{E}_T . We model b -tagging as a flat 60% probability to tag b -quark jets and a 0.5% probability to mistag non- b -quark jets (including charm quarks).

At the analysis level, all the signal and background events are required to pass the *basic* selection cuts listed here:

$$\begin{aligned}
\text{At least two jets with} & \quad p_T^j \geq 25 \text{ GeV}, & \quad |\eta_j| \leq 2.5 \\
\text{Exactly one lepton with} & \quad p_T^\ell \geq 25 \text{ GeV}, & \quad |\eta_\ell| \leq 2.5, \\
\text{Missing energy} & \quad \cancel{E}_T > 25 \text{ GeV}, \\
\text{Separation with} & \quad \Delta R_{jj,j\ell} > 0.4, & \quad \Delta R_{\ell\ell} > 0.2.
\end{aligned} \tag{4.7}$$

The kinematic distribution of the W' signal and the various backgrounds after these cuts are shown in Figs. 4.3 and 4.4.

To isolate the W' signal and suppress the SM backgrounds, a set of final cuts is applied on the jet P_T and on H_T , listed as follows,

$$\begin{aligned}
p_T^{j1st} & \geq 200 \text{ GeV}, \\
p_T^{j2st} & \geq 80 \text{ GeV}, \\
H_T & \geq 600 \text{ GeV},
\end{aligned} \tag{4.8}$$

where H_T is the scalar sum of the system p_T . These cuts effectively suppress most of the SM backgrounds while passing much of the W' signal.

In order to further improve the sensitivity of the analysis, the reconstruction of the W'

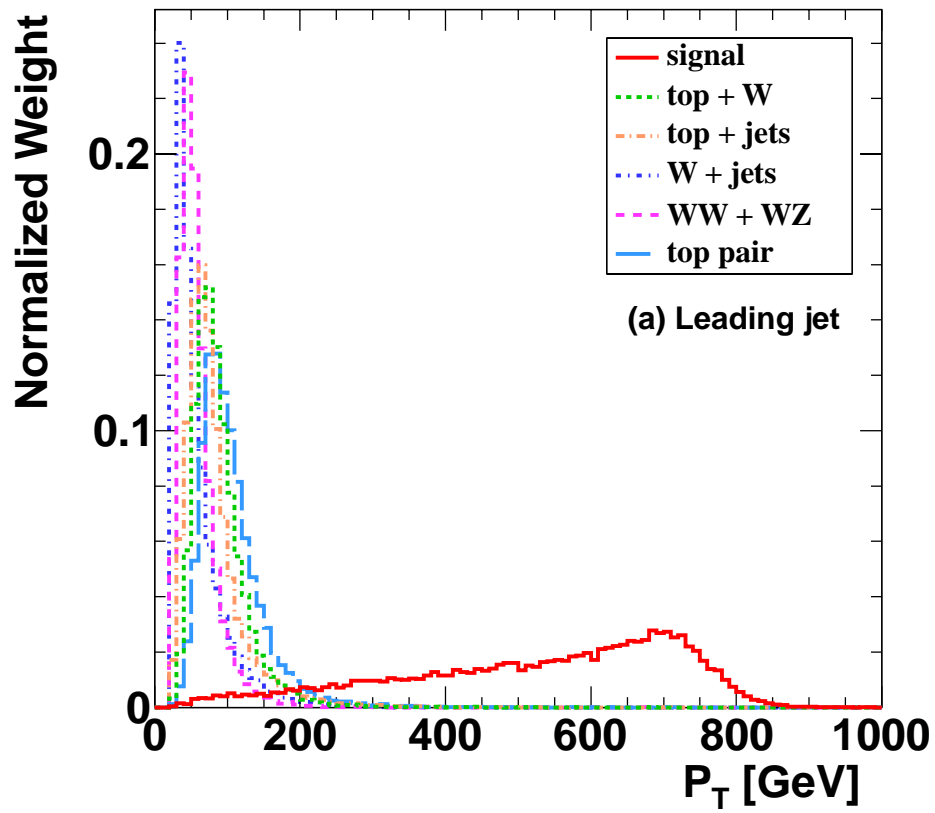


Figure 4.3: The normalized P_T distributions of the leading jet for signal and backgrounds.

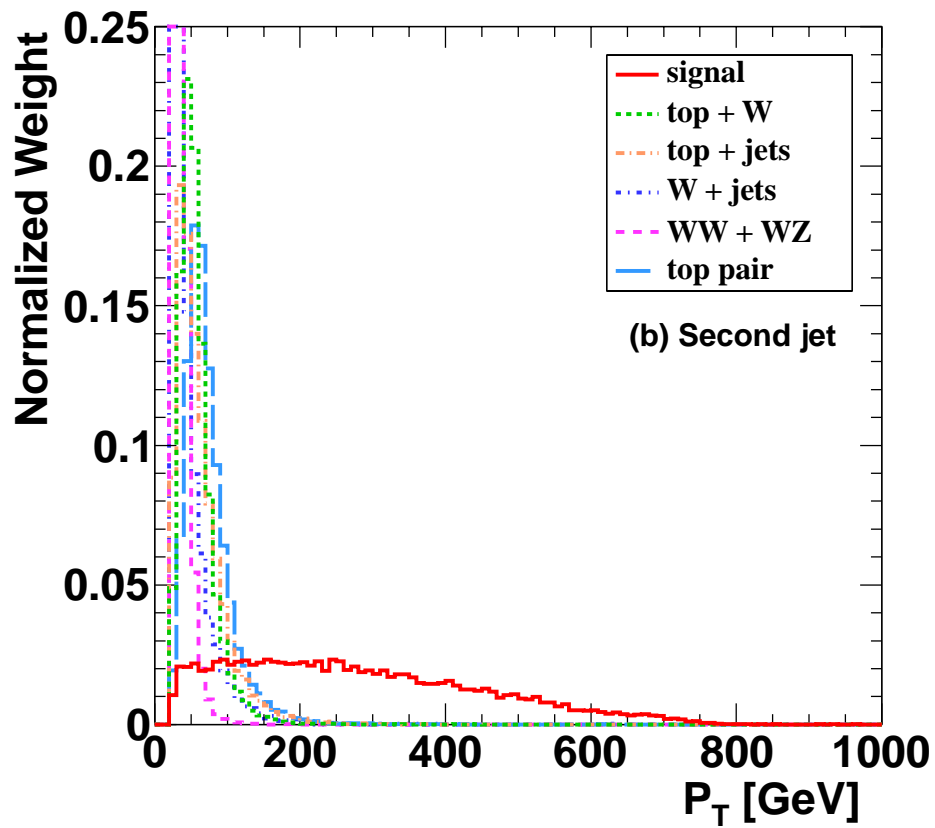


Figure 4.4: The normalized P_T distributions of the subleading jet for signal and backgrounds.

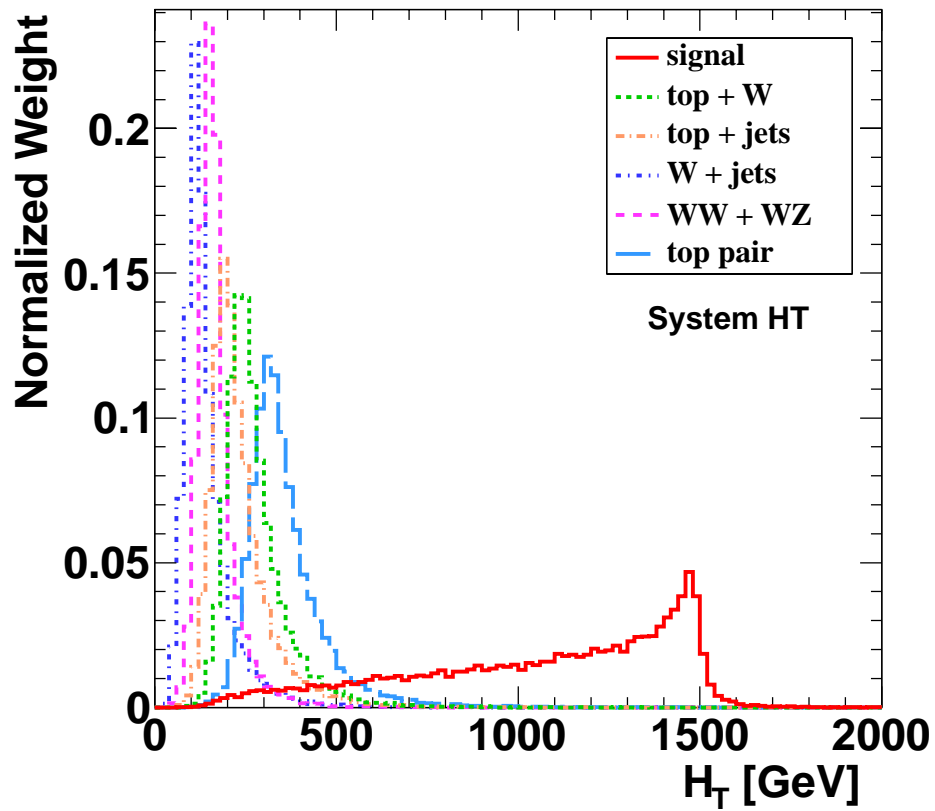


Figure 4.5: The normalized H_T distributions of the system for signal and backgrounds.

and its invariant mass is required. For this reconstruction it is necessary to first obtain the neutrino momentum. In the top quark reconstruction, we demand $m_{l\nu}^2 = M_W^2$ first. The longitudinal momentum of the neutrino is formally expressed as

$$p_{\nu L} = \frac{1}{2p_{eT}^2} \left(A p_{eL} \pm E_e \sqrt{A^2 - 4p_{eT}^2 \cancel{E}_T^2} \right), \quad (4.9)$$

where $A = M_W^2 + 2\vec{p}_{eT} \cdot \vec{\cancel{E}}_T$. If $A^2 - 4p_{eT}^2 \cancel{E}_T^2 \geq 0$. If there are two solutions, we will pick up the solution with central rapidity. If the solution is complex, we will pick up the real part of this solution. With the neutrino identified properly, we reconstruct the mass of the W' as

$$m_{W'}^{\text{rec}} = m(\vec{p}_\nu + \vec{p}_l + \vec{p}_{\text{jet } 1} + \vec{p}_{\text{jet } 2}) \quad (4.10)$$

Figure 4.6 shows the reconstructed invariant mass. The signal peak is clearly visible above the smoothly falling background.

To increase the local significance of this process, after all the optimized cuts one will select certain bins of the invariant mass distributions. We then impose a window cut on the invariant mass difference between the reconstructed invariant mass and the theory W' mass under consideration,

$$\left| m_{l\nu jj} - M_{W'} \right| < 400 \text{ GeV}. \quad (4.11)$$

Table 4.1 shows the number of events passing each set of cuts, in units of fb.

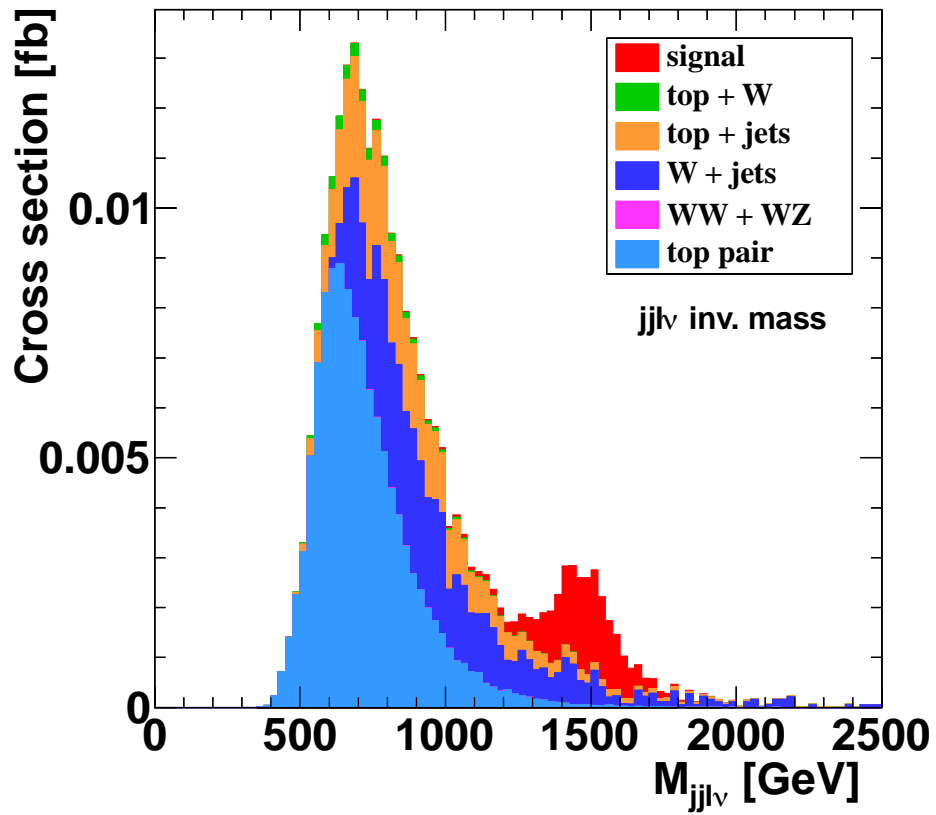


Figure 4.6: After all the cuts, the reconstructed invariant mass distributions of the system for W' signal and backgrounds.

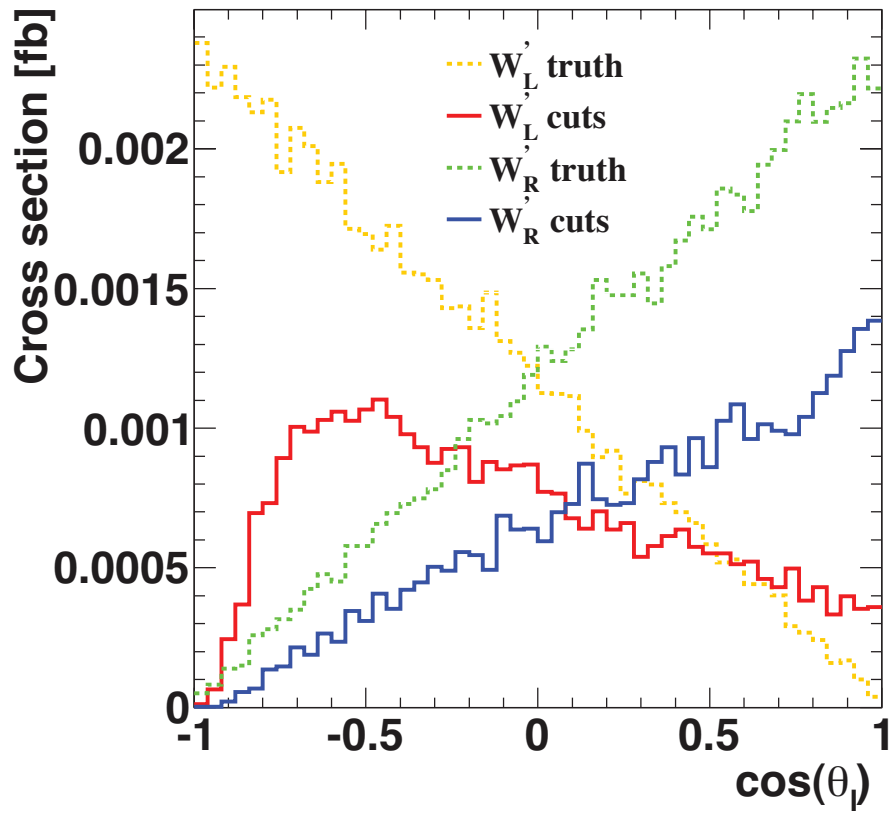


Figure 4.7: Before and after basic cuts, the $\cos\theta$ angular distributions of the final state leptons for left-handed W' and right-handed W' .

$\sigma(\text{fb})$	Signal	$t + \text{jets}$	$t + W$	$t\bar{t}$	WV	$W + \text{jets}$
no cuts	58.96	18877	2861	25840.	9888	4018600
basic cuts	33.38	4049.	833.	7206.7	2265	284516
+ smearing	33.83	4067.	815.	6878.6	2193	296371
+ hard cuts	28.65	158.5	11.1	232.56	3.67	7836.2
+ H_T cuts	26.45	59.80	5.69	137.6	3.51	3782.
+ b -tagging	22.26	44.79	3.44	115.7	0.19	61.98
+ mass window	21.59	7.80	0.13	3.97	0.03	16.02

Table 4.1: Cross sections for the signal and various background processes at the 7 TeV LHC in different cut levels are listed.

4.2.3 Lepton Angular Distribution and Chiral Structure

The charged lepton from top-quark decay is maximally correlated with top-quark spin. The connection between top-quark spin and the charged lepton can be found from the distribution in θ_{hel} , the angle of the lepton in the rest frame of top quark relative to the top-quark direction of motion in the overall c.m. frame. This is usually named as ‘‘helicity’’ basis. The angular correlation of the lepton ℓ^+ is given by

$$\frac{1}{\sigma} \frac{d\sigma}{d \cos \theta_{\text{hel}}} = \frac{1 \pm \cos \theta_{\text{hel}}}{2}, \quad (4.12)$$

with the (+) choice for right-handed and (−) for left-handed top-quarks; Clearly, the charged lepton from a right-handed top-quark prefers to move along the top-quark moving direction while the one from a left-handed top-quark is to against the top-quark moving direction. In the top-quark rest frame, 75% (25%) of charged lepton from t_R (t_L) decay follows top-quark moving direction.

After the discovery of the W' , one would like to know its mass, spin, and couplings. Angular distributions of its decay products can be investigated to definitively determine the spin and chiral structure of the W' to the SM fermions. The chirality of the W' coupling to SM fermions is best measured from the polarization of the top quark. Among the top quark decay products, the charged lepton from $t \rightarrow b + l + \nu$ is the best analyzer of the top quark spin. For a left-handed top quark, the charged lepton moves preferentially against the direction of motion of the top quark, while for a right-handed top quark the charged lepton moves along the direction of motion of the top quark. The angular correlation of the lepton is $(1 \pm \cos \theta_l)/2$, with the (+) choice for right-handed and (-) for left-handed top quarks, where θ_l is the angle of the lepton in the rest frame of top quark relative to the top quark direction of motion in the center-of-mass (c.m.) frame of the incoming partons. In Fig. 4.7, we plot the $\cos \theta_l$ for $f_L = 1, f_R = 0$ (W'_L) as well as $f_L = 0$ and $f_R = 1$ (W'_R). We expect a flat angular distribution for the SM background because the top quark and anti-top quark are not polarized. Therefore, the angular distributions of the lepton can be used to discriminate W' models in which the chirality of the W' coupling to SM fermions differs.

4.3 t -channel Production of W' : Top Quark Forward-backward Asymmetry

4.3.1 Forward-backward Asymmetry of Top Quark

The observed forward-backward asymmetry in rapidity A_{FB}^t of top quarks [72, 73] at the Fermilab Tevatron deviates by about two standard deviations (2σ) from standard model (SM) expectations [79]. After corrections for detector acceptance and resolution, A_{FB}^t in

the center-of-mass (c.m.) frame is $15.8 \pm 7.5\%$ at CDF [72] and is $19.6 \pm 6.5\%$ at D0 [73]. In addition to A_{FB}^t , the D0 group also reports a positive forward-backward asymmetry of charged leptons from top quark decays of $A_{FB}^\ell = (15.2 \pm 4.0)\%$ compared with the small value $2.1 \pm 0.1\%$ from simulations of the SM [73, 78]. The definition of A_{FB}^ℓ is

$$A_{FB}^\ell = \frac{n_F^\ell - n_B^\ell}{n_F^\ell + n_B^\ell}, \quad (4.13)$$

where n_F^ℓ (n_B^ℓ) is the number of events with $q_\ell y_\ell > 0$ ($q_\ell y_\ell < 0$), and q_ℓ and y_ℓ are the sign and rapidity respectively of the charged lepton from the semileptonic decay of a top or anti-top quark in the $t\bar{t}$ production.

In this thesis, we investigate the kinematic and dynamic relationship between the two asymmetries A_{FB}^t and A_{FB}^ℓ . We study quantitatively the influence of the top-quark boost on the kinematics of the charged lepton, showing how the distribution of leptons in the laboratory frame is related to the polarization state of the top quark parent. We show that current data on the ratio of the two asymmetries favor models in which more right-handed than left-handed top quarks are produced. The fact that A_{FB}^ℓ , A_{FB}^t , and the ratio A_{FB}^ℓ/A_{FB}^t are larger than the SM predictions indicates that the charged lepton strongly prefers to move in the same direction as the top quark from which it originates. This result can arise if right-handed top quarks [80, 81] play a significant role in A_{FB}^t or if a non-standard mechanism produces more highly boosted top quarks at the Tevatron, as we explain below.

Many new physics (NP) models have been proposed to explain the enhancement of A_{FB}^t , such as flavor-changing Z' [82], W' [83]¹, axigluon G' [84, 85, 86] models, etc [89, 90].

¹The next-to-leading order quantum chromodynamics corrections to the process of

The first two models produce predominantly right-handed top quarks, whereas the axigluon model generates unpolarized top quarks. It is important to validate these models at the Large Hadron Collider (LHC) and/or at the Tevatron. For example, the heavy flavor-changing Z' ($\gtrsim m_t$) model is disfavored because it predicts too many same-sign top quark pairs at the LHC [91, 92]. In this thesis, we focus on how consistently the W' models can describe both A_{FB}^t and A_{FB}^ℓ .

4.3.2 Kinematics

The charged lepton in top quark decay is a powerful analyzer of the polarization of the top quark [93]. In the rest frame of a top quark, the distribution in the polar angle θ_{hel} of a decay lepton ℓ^+ is

$$\frac{1}{\Gamma} \frac{d\Gamma}{d \cos \theta_{\text{hel}}} = \frac{1 + \lambda_t \cos \theta_{\text{hel}}}{2}, \quad (4.14)$$

where λ_t denotes the top quark helicity. Here, $\lambda_t = +$ is for a right-handed top quark (t_R) while $\lambda_t = -$ for a left-handed top quark (t_L). The angle θ_{hel} is measured with respect to the direction of motion of the top quark in the overall center-of-mass system of the $t\bar{t}$ production process. The distributions are shown in Fig. 4.8(a). The charged lepton from a right-handed top quark decay prefers to move along the top quark direction of motion, while a lepton from a left-handed top quark moves preferentially against the top quark direction of motion. In the rest frame of the top quark, 75% (25%) of charged leptons from t_R (t_L) decay follow the top quark direction of motion, i.e. $\cos \theta_{\text{hel}} > 0$.

Once the top quark is boosted, the angular distribution of the charged lepton relative to

$q\bar{q} \rightarrow t\bar{t}$ induced by the flavor-changing Z' and W' are calculated in Ref. [87] and Ref. [88], respectively, with the result that the NP prediction at the leading order is reliable.

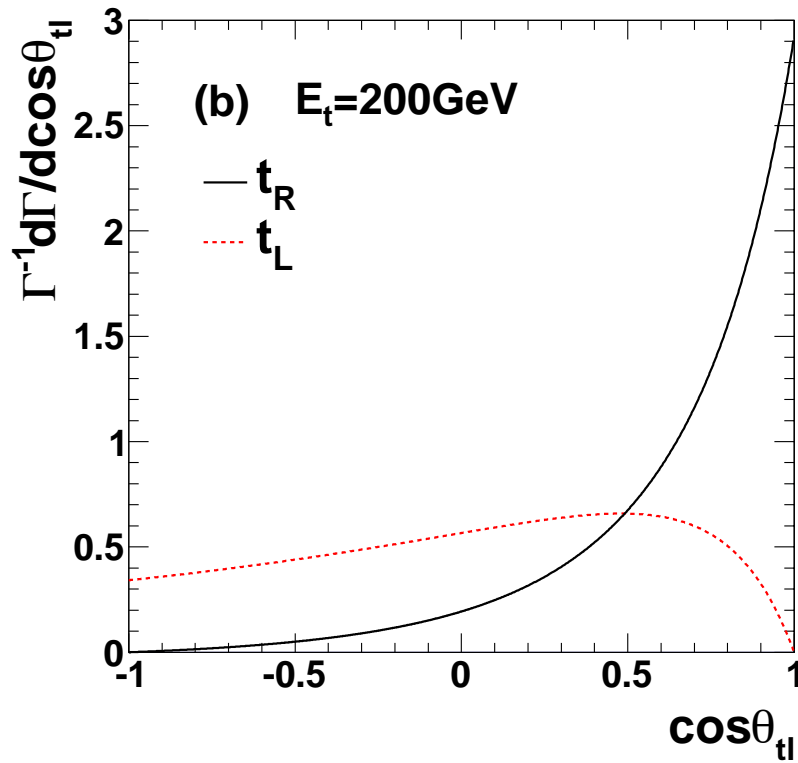
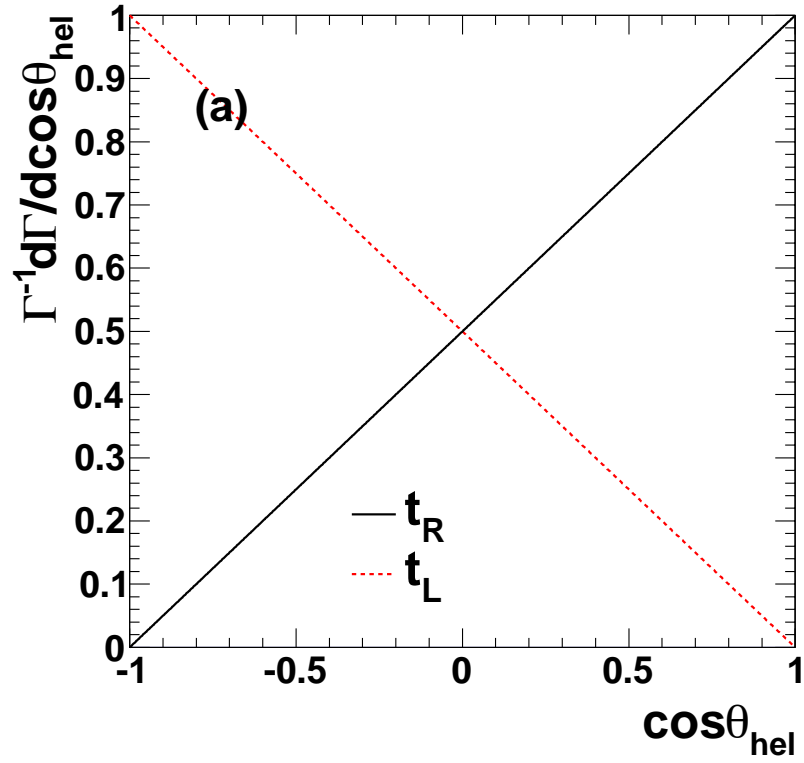


Figure 4.8: (a) $\cos\theta_{\text{hel}}$ distribution in the top quark rest frame for both t_L and t_R . (b) $\cos\theta_{t\ell}$ distribution in the boosted frame for a top quark with $E_t = 200\text{ GeV}$.

the direction of motion of the top quark is sensitive to the energy of the top quark E_t (or equivalently its velocity β). We derive

$$\frac{d\Gamma}{\Gamma d\cos\theta_{t\ell}} = \frac{1 - \beta \cos\theta_{t\ell} + \lambda_t (\cos\theta_{t\ell} - \beta)}{2\gamma^2 (1 - \beta \cos\theta_{t\ell})^3}, \quad (4.15)$$

where $\beta = \sqrt{1 - m_t^2/E_t^2}$, $\gamma = E_t/m_t$. As an illustration, we plot in Fig. 4.8(b) the distribution of $\cos\theta_{t\ell}$ of the charged lepton for a fixed energy of the top quark $E_t = 200$ GeV, where $\theta_{t\ell}$ is the angle between the charged lepton and the moving direction of its parent top quark in the laboratory frame. We find that about 60% of ℓ^+ follow (i.e., $\cos\theta_{t\ell} > 0$) the top quark moving direction for a t_L , and almost 100% for a t_R for $E_t = 200$ GeV.

The distribution of charged leptons in the laboratory frame depends on the top quark kinematics, including the top quark energy and its rapidity, and the top quark polarization. The probability for finding a positive charged lepton in the forward region when it originates from a top quark with a velocity β , rapidity y_t , and polarization λ_t is defined as

$$R_F^{\ell, \lambda_t}(\beta, y_t) = \frac{N_F^\ell}{N_F^\ell + N_B^\ell}, \quad (4.16)$$

where N_F^ℓ (N_B^ℓ) denotes the number of leptons ℓ in the forward (backward) region in the laboratory, and

$$y_t \equiv \ln \sqrt{\frac{E_t + p_z^t}{E_t - p_z^t}} \quad (4.17)$$

with p_z^t being the z -component of top quark momentum along the proton beam. After

lengthy algebra, it can be shown that the ratio $R_F^{\ell, \lambda_t}(\beta, y_t)$ is

$$R_F^{\ell, \lambda_t}(\beta, y_t) = \begin{cases} \frac{1}{2} + \frac{1}{2(1 + \gamma^{-2} \coth^2 y_t)^{1/2}} + \frac{\lambda_t \coth^2 y_t}{4\beta\gamma^2(1 + \gamma^{-2} \coth^2 y_t)^{3/2}}, \\ y_t \in [0, y_t^{\max}] \\ \\ \frac{1}{2} - \frac{1}{2(1 + \gamma^{-2} \coth^2 y_t)^{1/2}} - \frac{\lambda_t \coth^2 y_t}{4\beta\gamma^2(1 + \gamma^{-2} \coth^2 y_t)^{3/2}}, \\ y_t \in [-y_t^{\max}, 0] \end{cases} \quad (4.18)$$

where

$$y_t^{\max} = \frac{1}{2} \ln \frac{1 + \beta}{1 - \beta}. \quad (4.19)$$

To illustrate the effect of the top quark boost, we plot in Fig. 4.9 the fraction R_F as a function of y_t . We choose two characteristic top quark energies, $E_t = 200$ GeV (Fig. 4.9 (a)) and 600 GeV (Fig. 4.9 (b)). The former energy represents top quarks produced around the threshold region, while the latter pertains for highly boosted top quarks. Note that $y_t^{\max} = 0.53$ for $E_t = 200$ GeV. When a top quark moves perpendicular to the beam line, i.e. $y_t = 0$, there is an equal number of leptons in the forward and backward regions, leading to $R_F = 0.5$, independent of E_t and the polarization of the top quark.

We focus on the behavior of R_F in the region of $y_t > 0$, since the results for $R_F(y_t < 0)$ is just $(1 - R_F(y_t > 0))$. For right-handed top quarks t_R (black-solid lines in Fig. 4.9), R_F increases rapidly with y_t in the region of $y_t > 0$. This is because the charged lepton likes to follow the direction of motion of the top quark as we already see in Fig. 4.8. The direction of top quark can be used to well approximate that of the charged lepton in the laboratory

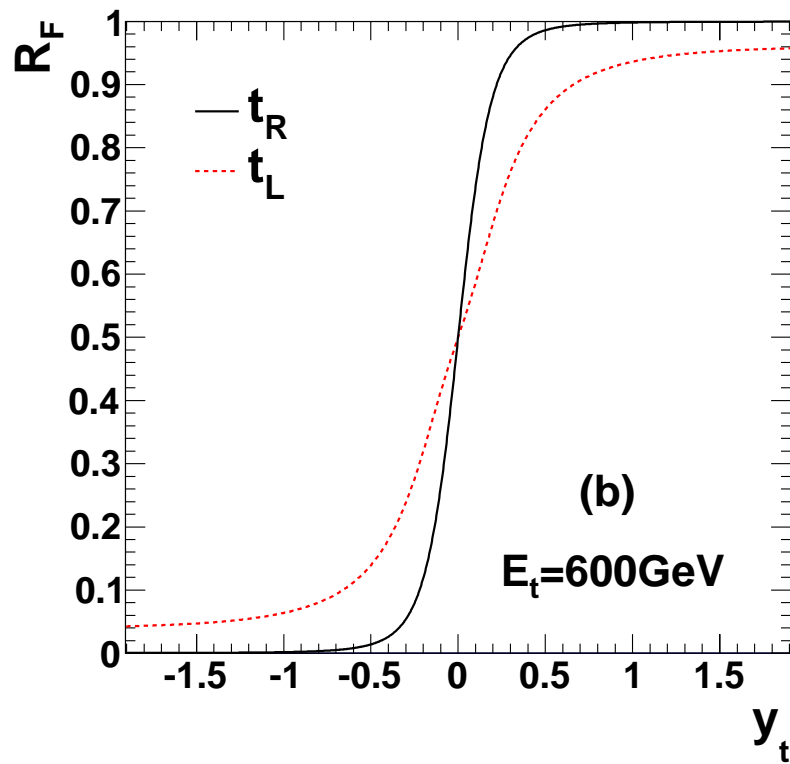
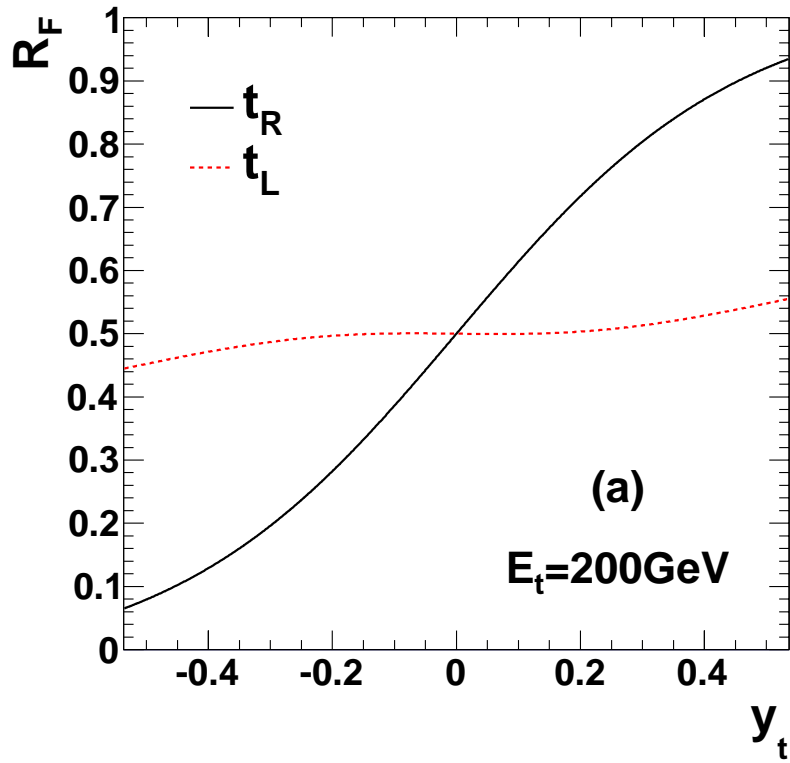


Figure 4.9: The ratio R_F as a function of y_t for a top quark with fixed energy: (a) $E_t = 200 \text{ GeV}$ and (b) $E_t = 600 \text{ GeV}$.

frame, and such an approximation works better for a highly energetic top quark. We can also see that when E_t becomes larger, i.e. the top quark is more energetic and the lepton is more boosted, R_F rapidly reaches its maximum value 1.

On the contrary, in the case of t_L 's, the ratio R_F does not significantly with y_t compared with t_R , owing to the anti-boost effect on the charged lepton. For $E_t = 200$ GeV, the boost causes charged leptons to distribute nearly uniformly (as seen in Fig. 4.8(b)), as a result, R_F is around 0.5 for all the allowed range of y_t , as seen in the red-dotted curve in Fig. 4.9(a). When the energy of top quark is large enough, the large boost forces most of the charged leptons from top quark decays to move along the top quark direction of motion, even if they move against the top quark direction of motion in the top quark rest frame. The boost yields a large value R_F in the region of large y_t , as shown by the red-dotted curve in Fig. 4.9(b). The competing influences leave the t_L curve slightly below the t_R curve. One can expect that, in the limit of $E_t \rightarrow \infty$, the direction of charged lepton is the same as its parent top quark, independent of polarization of the top quark.

Moreover, in Figs. 4.10 and 4.11, we show how R_F varies with top quark transverse momentum p_T^t and y_t . The distributions for right-handed top quarks t_R 's do not vary greatly with p_T^t due to the fact that most of the charged leptons like to follow t_R . However, the shapes of the curves for left-handed top quarks, which are the focus in the discussion below, are very different between the low p_T^t and high p_T^t regions, as is seen in the red-dotted lines. For the top quark away from $y_t = 0$ with fixed p_T^t , the boost becomes more significant because the energy of the top quark must be increased compared with $y_t = 0$. Therefore, more leptons are forced to move along the direction of the top quark in the laboratory frame. On the other hand, when y_t changes, a portion of the decay leptons which are initially in

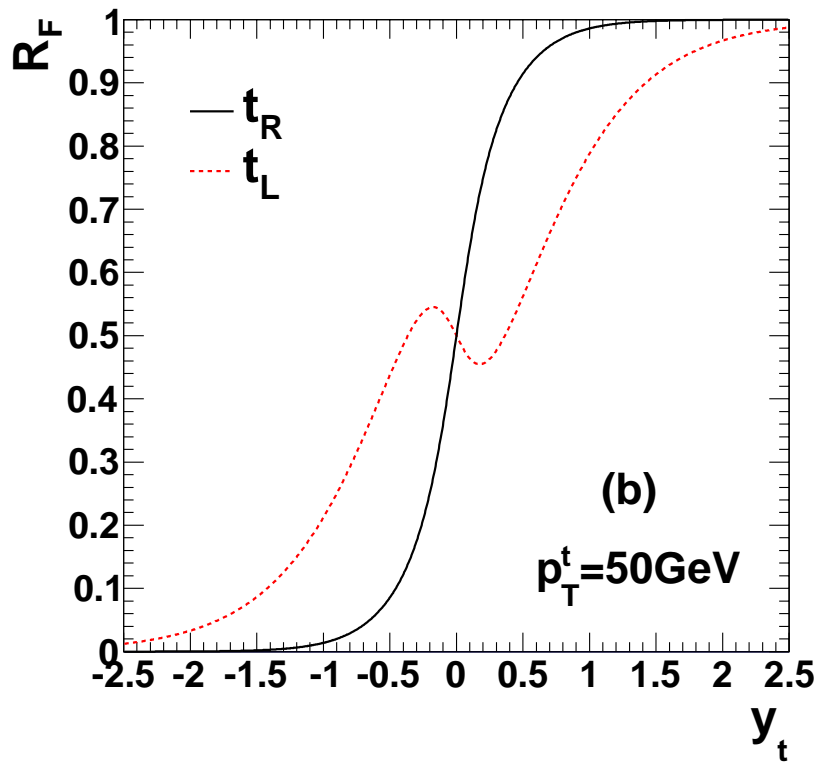
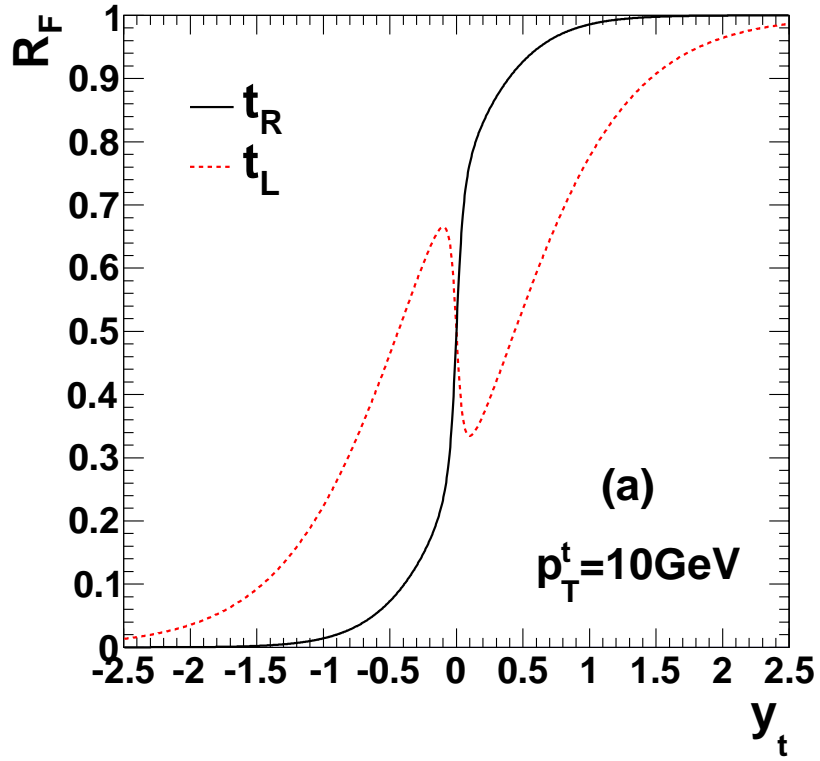


Figure 4.10: The ratio of the charged lepton in the forward and backward region as a function of the top quark rapidity for top quarks with fixed transverse momentum $p_T = 10, 50 \text{ GeV}$.

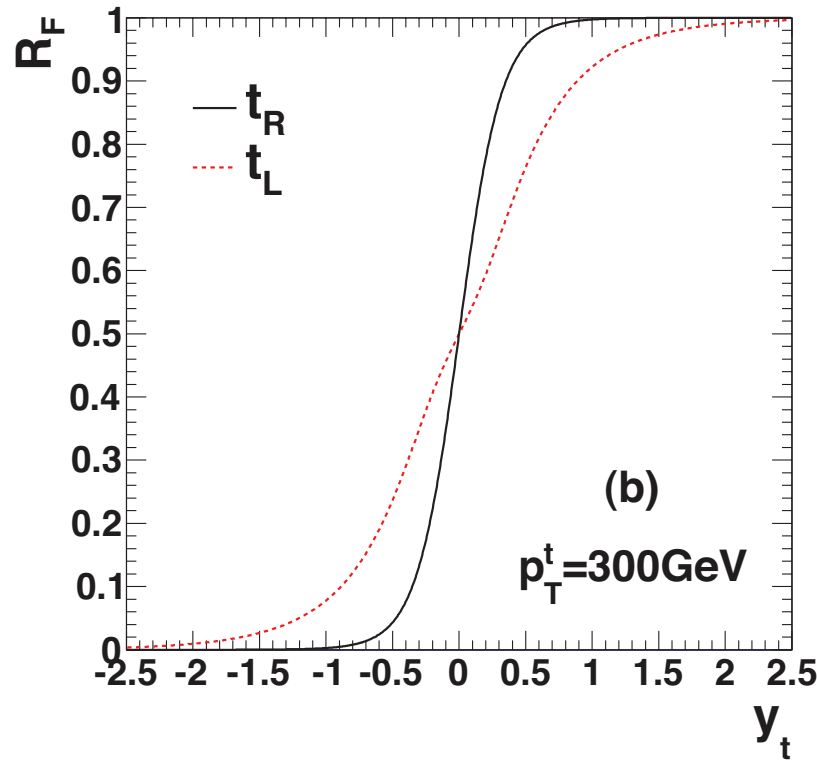
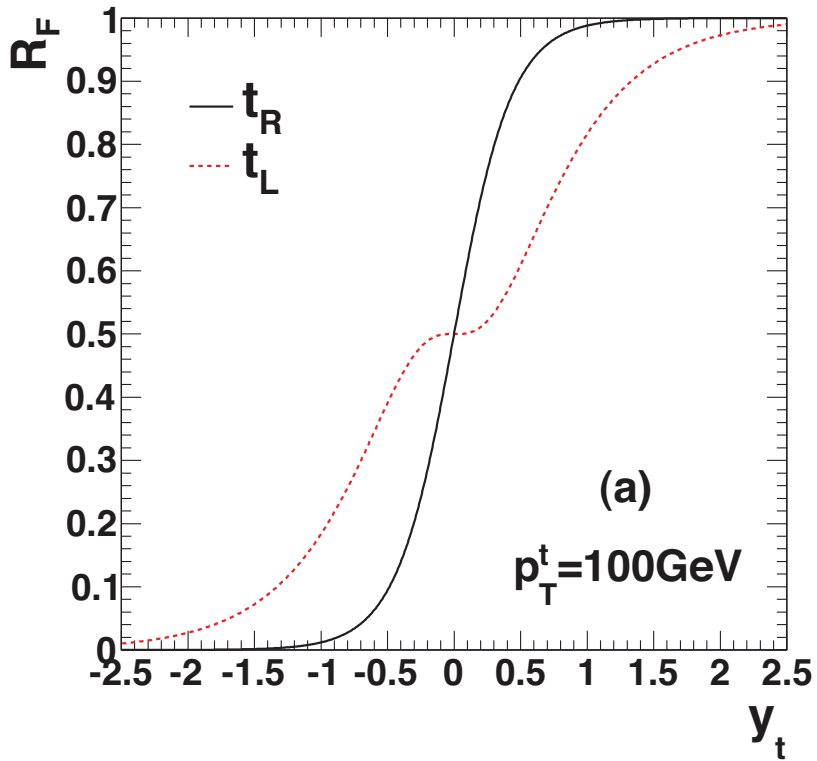


Figure 4.11: The ratio of the charged lepton in the forward and backward region as a function of the top quark rapidity for top quarks with fixed transverse momentum $p_T = 100, 300 \text{ GeV}$.

the forward/backward region ($y_\ell > 0/y_\ell < 0$) will then be in the backward/forward region. In summary, there are two factors which affect R_F : the boost and the rearrangement of the distribution of charged leptons in the forward ($y_\ell > 0$) and backward ($y_\ell < 0$) region. The former always increases R_F while the latter may increase or decrease the R_F depending on how energetic the top quark is at $y_t = 0$. Generally speaking, when the boost is not significant (low p_T^t and small y_t), R_F decreases when y_t increases from $y_t = 0$, as we can see in the drop in the red-dotted curves in Fig. 4.10(a) and 4.10(b). When the boost is big enough, R_F always increases with y_t . The platform-like behavior around $y_t \simeq 0$ in Fig. 4.11(a) arises because the leptons accumulate nearly uniformly around the axis of motion of the top quark when $p_T^t = m_t/\sqrt{3} \simeq 100$ GeV.² Therefore the ratio R_F is rather stable as the top quark changes its direction of motion direction around $y_t = 0$.

4.3.3 A_{FB}^t and A_{FB}^ℓ

The observed positive top-quark asymmetry A_{FB}^t indicates more top quarks are produced in the forward region than in the backward region of rapidity. Both t_R and t_L can generate a positive lepton asymmetry A_{FB}^ℓ with positive A_{FB}^t . However, as shown in Fig. 4.9, t_L would need a large boost along the proton beam line (i.e. in the large forward rapidity region) to overcome the fact that most of the charged leptons from its decay move against it in its rest frame. A right-handed top quark t_R can yield a positive A_{FB}^ℓ even for top quarks near the $t\bar{t}$ threshold region. Therefore, the large positive top quark and lepton asymmetries A_{FB}^t and A_{FB}^ℓ observed by the D0 collaboration indicate that the top quark polarization and kinematics of top quarks, like y_t and E_t , may be playing a non-trivial role. In this

²The critical value, $m_t/\sqrt{3}$ is obtained by solving $\frac{\partial R_F}{\partial y_t}|_{y_t=0} = 0$

section we present a general analysis of the correlation between A_{FB}^t and A_{FB}^ℓ so that one can have a better understanding about the numerical results derived from NP models to be shown in Sec. 4.3.4.

The top quark asymmetry A_{FB}^t can be expressed as a sum of contributions from the SM and NP as:

$$\begin{aligned} A_{FB}^t &= \frac{(N_F^{\text{NP}} + N_F^{\text{SM}}) - (N_B^{\text{NP}} + N_B^{\text{SM}})}{(N_F^{\text{NP}} + N_F^{\text{SM}}) + (N_B^{\text{NP}} + N_B^{\text{SM}})} \\ &= A_{FB}^{t, \text{NP}} \times R^{\text{NP}} + A_{FB}^{t, \text{SM}} \times (1 - R^{\text{NP}}), \end{aligned} \quad (4.20)$$

where

$$A_{FB}^{t, \text{SM}} = \frac{N_F^{\text{SM}} - N_B^{\text{SM}}}{N_F^{\text{SM}} + N_B^{\text{SM}}}, \quad A_{FB}^{t, \text{NP}} = \frac{N_F^{\text{NP}} - N_B^{\text{NP}}}{N_F^{\text{NP}} + N_B^{\text{NP}}}, \quad R^{\text{NP}} = \frac{N_{\text{tot}}^{\text{NP}}}{N_{\text{tot}}^{\text{SM}} + N_{\text{tot}}^{\text{NP}}}, \quad (4.21)$$

with $N_{F(B)}^{\text{SM}}$ and $N_{F(B)}^{\text{NP}}$ being the numbers of events in which the top quark moves with $y_t > 0$ ($y_t < 0$) in the SM and induced by NP, respectively, and $N_{\text{tot}}^{\text{SM(NP)}}$ is the total number of events predicted in the SM (induced by NP). The NLO QCD contribution to the production process $q\bar{q} \rightarrow t\bar{t}$ could generate a value $A_{FB}^{t, \text{SM}} \sim 5\%$ at the Tevatron, which is much less than the central value of experimental data.

To simplify the discussion of the correlation between A_{FB}^t and A_{FB}^ℓ , we assume in this section that A_{FB}^t is generated completely by NP, but all SM contributions (including the NLO QCD effects) are retained in the numerical calculations we present.

The contributions to A_{FB}^t from different polarizations of top quarks can be separated

as:

$$A_{FB}^t \approx \left[\rho_{tL} A_{FB}^{tL, \text{NP}} + \rho_{tR} A_{FB}^{tR, \text{NP}} \right] \times R^{\text{NP}}, \quad (4.22)$$

where

$$A_{FB}^{\lambda_t, \text{NP}} = \left[\frac{N_F^{\lambda_t} - N_B^{\lambda_t}}{N_F^{\lambda_t} + N_B^{\lambda_t}} \right]_{\text{NP}}, \quad \rho_{\lambda_t} = \frac{N^{\lambda_t, \text{NP}}}{N_{\text{tot}}^{\text{NP}}}. \quad (4.23)$$

Here, $A_{FB}^{\lambda_t, \text{NP}}$ denotes the forward-backward asymmetry of the top quark with polarization λ_t generated only by NP, while ρ_{λ_t} is the fraction of top quarks with polarization λ_t in $t\bar{t}$ events induced by NP. One advantage of decomposing A_{FB}^t into contributions of different top quark polarizations is to monitor the chirality of the couplings of NP particles to top quarks. Another advantage is to make the connection between A_{FB}^ℓ and A_{FB}^t more transparent.

As discussed in Sec. 4.3.2 the ratio R_F^ℓ depends on the top quark kinematics (β , y_t and λ_t). To compute the total probability of finding a charged lepton in the forward region, one must convolute the top quark production cross section with R_F^ℓ on an event-by-event basis, i.e.

$$\frac{1}{N_{\text{tot}}} N^{t\bar{t}} \otimes R_F^{\ell, \lambda_t} = \frac{1}{N_{\text{tot}}} \int N^{t\bar{t}}(\beta, y_t, \lambda_t) R_F^{\ell, \lambda_t}(\beta, y_t), \quad (4.24)$$

where $N^{t\bar{t}}$ labels the $t\bar{t}$ production rate for a top quark with specific kinematics (β , y_t , λ_t) and N_{tot} stands for total number of events. The lepton asymmetry A_{FB}^ℓ generated by a top quark with polarization λ_t can be therefore expressed as

$$\begin{aligned}
A_{FB}^{\ell, \lambda_t} \Big|_{\text{NP}} &= \frac{(N_F^{\lambda_t} \otimes R_F^{\ell, \lambda_t} + N_B^{\lambda_t} \otimes R_F^{\ell, \lambda_t}) - (N_F^{\lambda_t} \otimes R_B^{\ell, \lambda_t} + N_B^{\lambda_t} \otimes R_B^{\ell, \lambda_t})}{N_F^{\lambda_t} + N_B^{\lambda_t}} \Big|_{\text{NP}} \\
&= \frac{N_F^{\lambda_t} \otimes (2R_F^{\ell, \lambda_t} - 1) + N_B^{\lambda_t} \otimes (2R_F^{\ell, \lambda_t} - 1)}{N_F^{\lambda_t} + N_B^{\lambda_t}} \Big|_{\text{NP}} \\
&= \frac{(N_F^{\lambda_t} - N_B^{\lambda_t}) \otimes (2R_F^{\ell, \lambda_t} - 1)}{N_F^{\lambda_t} + N_B^{\lambda_t}} \Big|_{\text{NP}} . \tag{4.25}
\end{aligned}$$

Here,

$$R_B^{\ell, \lambda_t}(\beta, y_t) \equiv \frac{N_B^\ell}{N_F^\ell + N_B^\ell} = 1 - R_F^{\ell, \lambda_t}(\beta, y_t), \tag{4.26}$$

and we use the following relation between R_F^{ℓ, λ_t} and R_B^{ℓ, λ_t} in our derivation,

$$R_B^{\ell, \lambda_t}(y_t) = R_F^{\ell, \lambda_t}(-y_t). \tag{4.27}$$

The quantities $N_F^{\lambda_t}$ and $N_B^{\lambda_t}$ in the convolutions in Eq. (4.25) should be understood as the distributions $N^{t\bar{t}}(\beta, y_t, \lambda_t)\Theta(y_t)$ and $N^{t\bar{t}}(\beta, y_t, \lambda_t)\Theta(-y_t)$, respectively, where $\Theta(x)$ is the Heaviside step function. The quantity $N_F^{\lambda_t} - N_B^{\lambda_t}$ should be understood as

$$\left[N^{t\bar{t}}(\beta, y_t, \lambda_t) - N^{t\bar{t}}(\beta, -y_t, \lambda_t) \right] \Theta(y_t). \tag{4.28}$$

Because R_F^{ℓ, λ_t} in Eq. (4.25) cannot exceed 1, we have $A_{FB}^\ell \lesssim A_{FB}^t$. When R_F^{ℓ, λ_t} is close to a constant \mathcal{R}_C , e.g. $\mathcal{R}_C \sim 1/2$ around the $t\bar{t}$ threshold ($E_t \sim 200\text{GeV}$) for left-handed

top quark or $\mathcal{R}_C \sim 1$ for a highly boosted top quark, Eq. (4.25) can be simplified as

$$A_{FB}^{\ell, \lambda_t} \Big|_{\text{NP}} = \left[\frac{N_F^{\lambda_t} - N_B^{\lambda_t}}{N_F^{\lambda_t} + N_B^{\lambda_t}} \right]_{\text{NP}} \times (2\mathcal{R}_C - 1) = A_{FB}^{\lambda_t, \text{NP}} \times (2\mathcal{R}_C - 1). \quad (4.29)$$

Equation (4.29) and Fig. 4.9 show that:

- $A_{FB}^{\ell, tL} \sim 0$ when the $t\bar{t}$ pair is produced around the threshold region;
- $A_{FB}^{\ell, tL} \lesssim A_{FB}^{\ell, tR} \approx A_{FB}^t$ in the large $m_{t\bar{t}}$ region.

Although Eq. (4.29) is approximate, it helps in understanding the NP prediction obtained from a complete numerical calculation.

4.3.4 Flavor-changing W' Model

In this subsection we focus on a flavor-changing W' model [83]. We examine how this models can accommodate the values of both A_{FB}^t and A_{FB}^ℓ measured by the D0 collaboration.

A different class of NP models to explain the $t\bar{t}$ forward-backward asymmetry is based on t -channel kinematics. Such models involve large flavor-changing interactions. A model with a non-universal massive neutral vector boson Z' [82] is one of the possibilities. However, it is disfavored because it implies a large rate for same-sign top quark production at the 7 TeV LHC [91], not supported by data [92].

We consider a flavor-changing W' which couples an incident d -quark to the produced t -quark [83],

$$\mathcal{L} = g_2 g_R \bar{d} \gamma^\mu P_R t W'_\mu + h.c. , \quad (4.30)$$

where g_2 is the weak coupling. In the W' model, in addition to the SM process $q\bar{q} \rightarrow g \rightarrow t\bar{t}$,

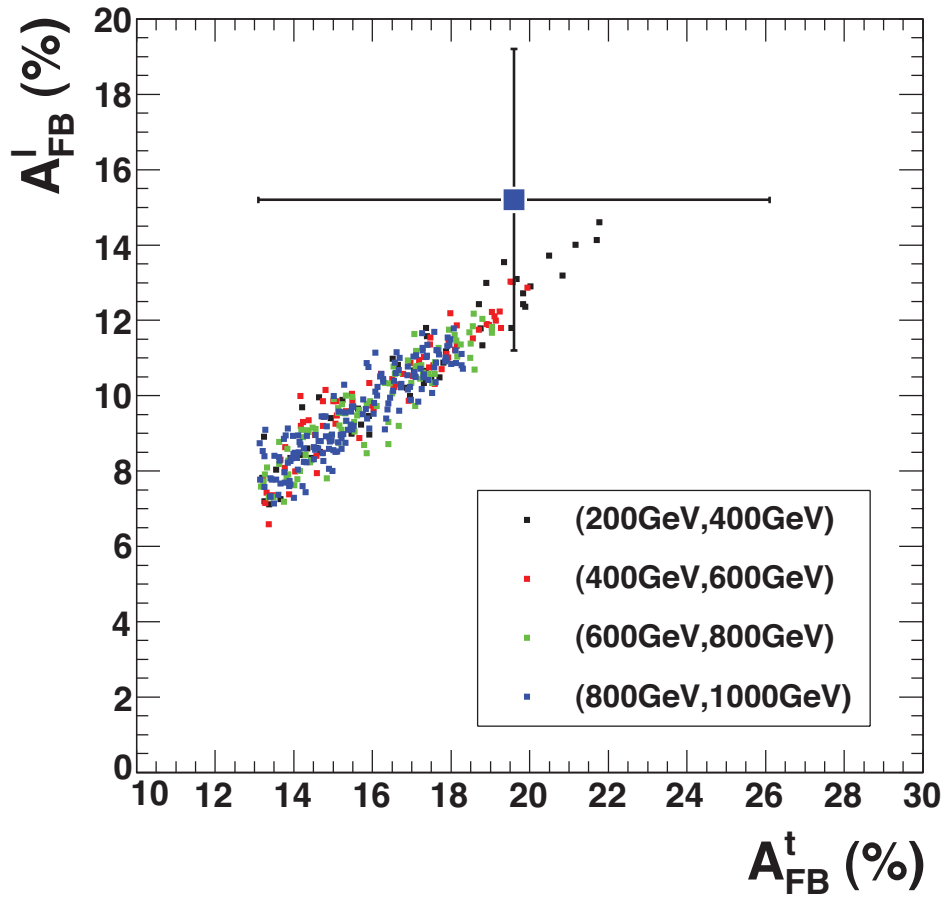


Figure 4.12: Correlation between A_{FB}^l and A_{FB}^t in the W' models. The point corresponding to the D0 data is also shown. The numbers within the parentheses label the lower and upper limits of the mass of the W' .

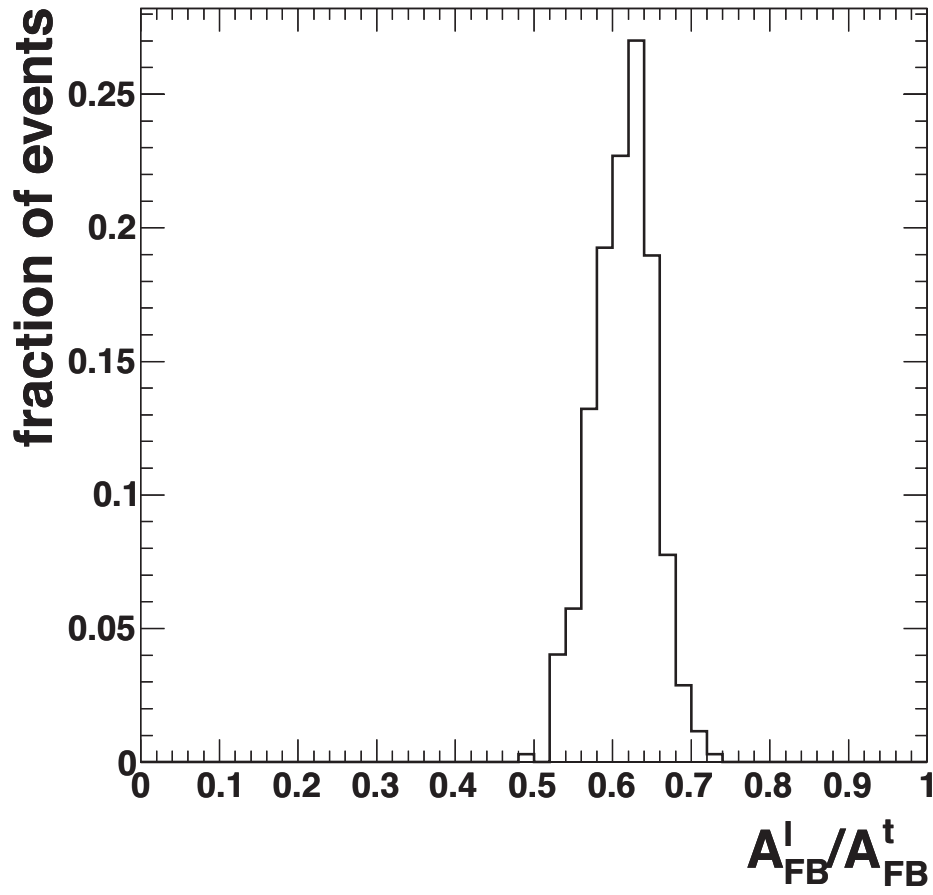


Figure 4.13: The statistics for the ratio of predicted A_{FB}^l to A_{FB}^t in the W' models.

the $t\bar{t}$ pair can also be produced via a t -channel process with a W' mediator. Apart from a common factor $\frac{g_2^2 g_R^2 \hat{s} \delta_{ac} \delta_{bd}}{4(\hat{t} - m_{W'}^2)}$, the helicity amplitude $M_{W'}^t(\lambda_q, \lambda_{\bar{q}}, \lambda_t, \lambda_{\bar{t}})$ is

$$\begin{aligned}
\mathcal{M}_{W'}^t(+ - - -) &= \left[2 + r_W^2\right] \sqrt{1 - \beta^2} \sin \theta, \\
\mathcal{M}_{W'}^t(+ - - +) &= \left[2(1 - \beta) + r_W^2(1 + \beta)\right] (1 - \cos \theta), \\
\mathcal{M}_{W'}^t(+ - + -) &= -\left[2(1 + \beta) + r_W^2(1 - \beta)\right] (1 + \cos \theta), \\
\mathcal{M}_{W'}^t(+ - + +) &= -\left[2 + r_W^2\right] \sqrt{1 - \beta^2} \sin \theta,
\end{aligned} \tag{4.31}$$

where $r_W = m_t/m_{W'}$.

4.3.5 Correlations on A_{FB}^ℓ and A_{FB}^t

In the region $\beta \simeq 1$, the nonzero helicity amplitudes are

$$\begin{aligned}
\mathcal{M}_{W'}^t(+ - - +) &\sim 2r_W^2(1 - \cos \theta), \\
\mathcal{M}_{W'}^t(+ - + -) &\sim 4(1 + \cos \theta).
\end{aligned} \tag{4.32}$$

In order to produce top quarks in the forward region, one needs $2r_W^2 < 4$, which is always true for the region of W' masses (heavier than the top quark) considered in this paper. At the Tevatron the β distribution of the top quark in $t\bar{t}$ production peaks around 0.6, and therefore most of the top quarks are not significantly boosted. We can also easily see that more right-handed top quarks are produced compared to left-handed ones in the W' model, $\rho_{t_R} > \rho_{t_L}$. Since the t -channel propagator contributes a minus sign, the total forward-backward asymmetry results from a competition between the square of the purely NP term

and the interference term of NP with the SM. The former is proportional to g_R^4 and the latter to g_R^2 . We plot the correlation between A_{FB}^t and A_{FB}^ℓ for the W' model in Fig. 4.13. The strong correlation is fit well by

$$A_{FB}^\ell \simeq 0.75 \times A_{FB}^t - 2.1\% . \quad (4.33)$$

Moreover, for a relatively light W' ($\lesssim 600$) GeV, both A_{FB}^t and A_{FB}^ℓ can be consistent with the D0 data within 1σ .

For the W' model, Fig. 4.13 shows the statistics for the ratio of the predicted A_{FB}^ℓ to A_{FB}^t , based on the scattered points in Fig. 4.12. The total number of events is normalized to 1. The data from D0 shows A_{FB}^ℓ/A_{FB}^t about $78 \pm 33\%$. The ratio in the SM is close to 40%. The comparison to the D0 point shown in Fig. 4.12 indicates that top quark events with a large proportion of right-handed top quarks are favored. Constraints on flavor-changing currents in the W' model allow only right-handed couplings to the top quark, consistent with the D0 A_{FB}^ℓ results. Improved statistics would help, as well as a measurement of A_{FB}^ℓ by the CDF collaboration. For W' model, since the events that contribute to A_{FB}^t are almost locate region of $2R_F - 1 > 0$, it is very transparent from Eq. (4.25) that A_{FB}^ℓ/A_{FB}^t can be as large as 0.75, see Eq. (4.33). For SM, one may expect that $A_{FB}^\ell/A_{FB}^t > 0.5$. However, the predicted values are about and 0.4 for SM, respectively. Therefore, one should be more careful to take in to account the boost effect due to different frames, i.e.

$$\frac{A_{FB}^\ell(lab)}{A_{FB}^t(c.m.)} = \frac{A_{FB}^\ell(lab)}{A_{FB}^t(lab)} \frac{A_{FB}^t(lab)}{A_{FB}^t(c.m.)} . \quad (4.34)$$

It is known that the boost effect will reduce A_{FB}^t in laboratory frame related to the c.m.

frame [95]. For SM, the reduction is about 30%. One can then easily understand that the predicted values $A_{FB}^\ell(lab)/A_{FB}^t(c.m.) < 0.5$ even $A_{FB}^\ell(lab)/A_{FB}^t(lab) > 0.5$. We therefore encourage D0 collaboration to measure the A_{FB}^t in the laboratory frame as well, in order to have a more transparent comparison with NP prediction, and we expect the value of A_{FB}^ℓ/A_{FB}^t in the laboratory frame will be larger than 78% which is the result of current data measured from two different frame. Combined with the results from CDF measurements, if large A_{FB}^ℓ and A_{FB}^ℓ/A_{FB}^t are confirmed, it would be a strong evidence for the new physics signal and the chirality of coupling between new particle(s) with SM particles.

4.4 Summary

The deviation of the top quark forward-backward asymmetry A_{FB}^t from its SM prediction may indicate the presence of new physics. Based simply on the large value of A_{FB}^t , the charged lepton forward-backward asymmetry A_{FB}^ℓ should also be expected to be larger than the SM expectation. Indeed, the D0 collaboration reports $A_{FB}^\ell = 15.2\%$, about 3σ away above the SM value. In this paper, we study the kinematic and dynamic aspects of the relationship between the asymmetries A_{FB}^t and A_{FB}^ℓ based on the spin correlation between charged leptons and the top quark with different polarization states. Owing to the spin correlation in top quark decay, A_{FB}^ℓ and A_{FB}^t are strongly positively correlated for *right-handed* top quarks. However, for *left-handed* top quarks, the nature of the correlation depends on how boosted the top quark is. For large enough top quark energy, left-handed top quarks will also generate a large charged-lepton asymmetry, similar to that for right-handed quarks. However, if the top quark is not boosted ($E_t \lesssim 200$ GeV), A_{FB}^ℓ from

left-handed top quarks will be less than $A_{FB}^t/2$ for a positive A_{FB}^t . Since most of the $t\bar{t}$ events are produced in the threshold region, one may use the large positive values of A_{FB}^t and A_{FB}^ℓ measured at D0 to conclude that production of left-handed top quarks is disfavored. Confirmation of the D0 result and greater statistics are desirable. There is great value in making measurements of both A_{FB}^t and A_{FB}^ℓ because their correlation can be related through top quark polarization to the underlying dynamics of top quark production.

We focused on a flavor-changing W' model which produced dominantly right-handed top quarks. To determine free parameters, we required that these new physics models fit A_{FB}^t as well as the $t\bar{t}$ total cross section at the Tevatron at 1σ level of accuracy. As we have shown, there is a strong correlation between A_{FB}^t and A_{FB}^ℓ in both models. The best fit to the relationship is $A_{FB}^\ell \simeq 0.75 \times A_{FB}^t - 2.1\%$, within 2σ of the D0 result. To generate A_{FB}^ℓ satisfying the data to better than 1σ accuracy, a light W' (lighter than 600 GeV) is favored.

Chapter 5

EXOTIC HEAVY CHARGED GAUGE BOSONS

5.1 Introduction

In this chapter we study a different W' model, named a “top-philic” model, in which the W' couples only to third-generation quarks (top and bottom quarks) and is produced only in association with a top quark. It decays only into a top quark and a bottom quark pair. The collider signature of the events is a $t\bar{t}$ pair plus one b -jet. We explore the discovery potential of the top-philic W' boson at the LHC at a center of mass energy of 14 TeV with an integrated luminosity of 100 fb^{-1} . We compute the inclusive cross section, simulate the signal and backgrounds, and investigate a set of optimal cuts. Our study shows that the prospects are promising to discover the top-philic W' in tW' associated production despite the presence of SM backgrounds that exceed our signal by three or four orders of magnitude. The key is to identify as a b jet the extra jet produced in association with $t\bar{t}$. A 1 TeV W'

with the same coupling strength as the SM W - t - b interaction could be discovered with a statistical significance of 5 standard deviations at the LHC at 14 TeV.

Motivated by the observation of large parity violation in top quark pair-production at the Tevatron [72], several authors have recently proposed a W' boson with a flavor changing d - t - W' interaction [109, 110, 86, 111, 112]. This W' boson is also produced in association with a top quark, but it differs from the top-philic W' we discuss in that it decays into a top quark and a non- b quark, yielding a final state of $t\bar{t}$ plus a non- b jet [113]. This final state suffers from a huge $t\bar{t}j$ background that cannot be mitigated by b -tagging on the jet produced in association with the top quark pair. As a result, a large coupling strength would be needed for discovery of the flavor changing W' at the LHC.

5.2 The model

A top-philic W' can arise from a new non-abelian gauge symmetry which breaks generation universality [30, 31, 32]. A summary may be found in Ref. [24]. In this study we adopt an effective Lagrangian approach rather than focusing on specific NP models. The effective, renormalizable interaction of the W' to the SM third generation fermions is

$$\mathcal{L} = i\frac{g_2}{\sqrt{2}} \bar{t}\gamma^\mu(f_L P_L + f_R P_R)b W'_\mu{}^+ + \text{h.c.} \quad , \quad (5.1)$$

where $g_2 = e/\sin\theta_W$ is the weak coupling, while $P_{L/R}$ are the usual chirality projection operators. For simplicity, we consider only the case with a purely left-handed current ($f_L = 1$, and $f_R = 0$), but our study can be extended easily to other cases. The triple gauge interaction of the W' and SM gauge bosons is not included because such a non-abelian

interaction is suppressed for large W' mass ($m_{W'}$) by W - W' mixing effects, which are of order $\mathcal{O}(m_W^2/m_{W'}^2)$.

The W' decays entirely to a top quark and bottom quark pair with decay width

$$\Gamma_{W' \rightarrow t\bar{b}} \simeq \frac{3g_2^2 m_{W'}}{48\pi} (f_L^2 + f_R^2). \quad (5.2)$$

For $f_L^2 + f_R^2 = 1$, $\Gamma_{W'} \sim m_{W'}/100$, indicating that the W' is quite narrow.

The top-philic W' boson is produced predominately through a gluon-bottom-quark fusion process, as depicted in Fig. 5.1. The W' decays into a top and bottom quark pair, and the overall final state is then $t\bar{b}$. Since this final state has not been used to search for a W' at the Tevatron and LHC, none of the current collider limits constrain our top-philic W' model. It is possible the top-philic W' boson could be as light as a few hundred GeV.

The recent CDF measurement of the ratio of the cross sections for $t\bar{t} + 0$ jets to $t\bar{t} + n$ jets is consistent with the SM expectation [114]. Top-philic W' production will contribute to the $t\bar{t} + n$ jets rate. However, our numerical calculation shows that tW' production is too small to be of concern, e.g. $\sigma(tW'^- + \bar{t}W'^+) \sim 3$ fb for $m_{W'} = 200$ GeV, $f_L = 1$, and $f_R = 0$. Moreover, the cross section drops rapidly with $m_{W'}$. We conclude that the top-philic W' model is consistent with $t\bar{t}$ current measurements at the Tevatron.

In Fig. 5.2, we display the leading-order inclusive cross section for tW'^- and $\bar{t}W'^+$ production, $\sigma(tW'^- + \bar{t}W'^+)$, as a function of the W' mass ($m_{W'}$) at 14 TeV with a purely left-handed W' - t - b coupling, i.e. $f_L = 1$ and $f_R = 0$. Note that $\sigma(\bar{t}W'^+) = \sigma(tW'^-)$ owing to equality of the parton distribution functions for initial state b - and \bar{b} -quarks. The CTEQ6L parton distribution functions are used in our calculation with the renormalization and factorization scales chosen as $m_{W'}$. The production cross section is at the picobarn level

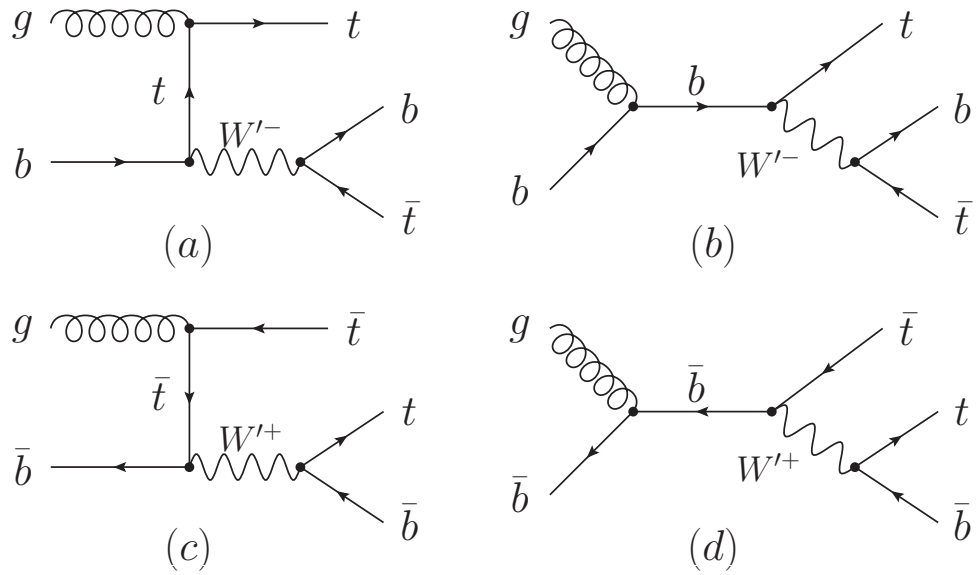


Figure 5.1: Feynman diagrams for the associated production of a W' and a top quark: (a, b) W'^-t , and (c, d) $W'^+\bar{t}$.

for a W' with a few hundred GeV mass and at the femtobarn level for a multiple TeV-scale W' .

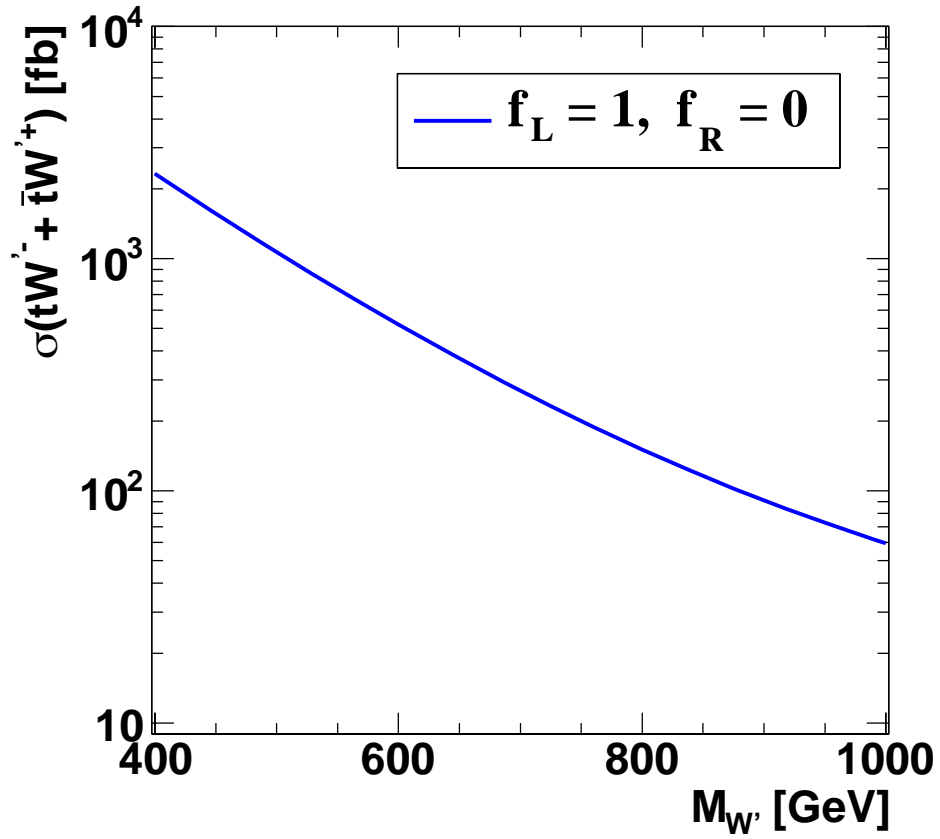


Figure 5.2: The inclusive cross section of the tW'^- and $\bar{t}W'^+$ associated production at a 14 TeV LHC with $f_L = 1$ and $f_R = 0$.

5.3 Collider phenomenology

Our signal consists of both tW'^{-} and $\bar{t}W'^{+}$ production channels because the two channels give rise to the same $t\bar{t}$ plus one b -jet collider signature after the W' decay. The b -jet could originate from a b or a \bar{b} as one cannot now distinguish b - and \bar{b} -jets experimentally. At the event reconstruction level the b -jet together with one top quark would yield a heavy W' resonance. The main SM background is from production of a $t\bar{t}$ pair plus one b jet. We also take into account the possibility that a light quark jet fakes a b jet. The signal and background events are generated with MadGraph5/MadEvent [107].

In order to trigger on the signal event, we demand a leptonic decay of the top quark $t \rightarrow b\ell^+\nu_\ell$ and hadronic decay of the antitop $\bar{t} \rightarrow \bar{b}jj$. The signal processes are

$$\begin{aligned}
 pp &\rightarrow tW'^{-} \rightarrow t\bar{t}b \rightarrow bW^+\bar{b}W^{-}b \rightarrow b\bar{b}\bar{b}\ell^+jj\nu, \\
 pp &\rightarrow \bar{t}W'^{+} \rightarrow t\bar{t}\bar{b} \rightarrow bW^+\bar{b}W^{-}\bar{b} \rightarrow b\bar{b}\bar{b}\ell^+jj\nu.
 \end{aligned}
 \tag{5.3}$$

The topology of our signal is characterized by one isolated positive charged lepton, five high energy jets, and a large missing transverse momentum ($E_{\text{T}}^{\text{miss}}$) from the missing neutrino.

Both electrons and muons are used in our analysis.

We separate the SM backgrounds according to the flavor of the jet produced in association with the $t\bar{t}$ pair:

$$t\bar{t}j \quad : \quad pp \rightarrow t\bar{t}j \rightarrow bW^+\bar{b}W^{-}j \rightarrow b\bar{b}jjj\ell^+\nu,
 \tag{5.4}$$

$$t\bar{t}b \quad : \quad pp \rightarrow t\bar{t}b \rightarrow bW^+\bar{b}W^{-}b \rightarrow b\bar{b}bjj\ell^+\nu.
 \tag{5.5}$$

$m_{W'}$	No cut	<i>basic</i>	<i>optimal</i>	<i>b-tagging</i>	ΔM cut	ϵ_{cut}
400	32920	6929	5240	3018	2166	6.6 %
$t\bar{t}b$	1.9×10^5	23849	2712	1537	297	0.15 %
$t\bar{t}j$	3.13×10^7	3×10^6	306062	6984	967	$3.1 \times 10^{-3}\%$
500	15115	3324	2621	1513	1120	7.4 %
$t\bar{t}b$	1.9×10^5	23849	2709	1529	449	0.23 %
$t\bar{t}j$	3.13×10^7	3×10^6	306057	6895	577	$1.8 \times 10^{-3}\%$
600	7361	1666	1300	754	565	7.7 %
$t\bar{t}b$	1.9×10^5	23849	2524	1429	437	0.23 %
$t\bar{t}j$	3.13×10^7	3×10^6	288098	6214	385	$1.2 \times 10^{-3}\%$
700	3843	874	638	369	282	7.4 %
$t\bar{t}b$	1.9×10^5	23849	1781	1026	303	0.16 %
$t\bar{t}j$	3.13×10^7	3×10^6	212153	4441	304	$9.7 \times 10^{-4}\%$
800	2110	490	405	197	154	7.3 %
$t\bar{t}b$	1.9×10^5	23849	1060	620	189	0.10 %
$t\bar{t}j$	3.13×10^7	3×10^6	130122	2346	214	$6.8 \times 10^{-4}\%$
900	1215	290	187	107	85	6.9 %
$t\bar{t}b$	1.9×10^5	23849	594	353	110	0.058 %
$t\bar{t}j$	3.13×10^7	3×10^6	74342	1052	62	$2.0 \times 10^{-4}\%$
1000	720	172	106	62	50	7.0 %
$t\bar{t}b$	1.9×10^5	23849	337	199	64	0.034 %
$t\bar{t}j$	3.13×10^7	3×10^6	42423	505	35	$5.4 \times 10^{-5}\%$

Table 5.1: The numbers of signal and background events at 14 TeV with an integrated luminosity of 100 fb^{-1} before and after cuts, with $f_L = 1$, for seven values of $m_{W'}$ (GeV). The top quark decay branching ratio $2/27$ is included in the “no cut” column, and the b tagging efficiency is included in the fifth column. The cut acceptances ϵ_{cut} are also listed.

The “extra” jet in association with the $t\bar{t}$ originates from a light-flavor quark or gluon in the first case and from a b or \bar{b} in the second case. As shown below, the two backgrounds are suppressed by different kinematic cuts. In the generation of background events, we demand the transverse momentum (p_T) of the extra jet to be harder than 10 GeV to avoid soft and collinear divergences from QCD radiation. After kinematic cuts, the contributions from other SM backgrounds, e.g. W^+W^-jjj , are quite small and are not included in our analysis.

For an integrated luminosity of 100 fb^{-1} , the numbers of signal and background events at the event generator level are shown in the second column of Table 5.1. The top quark decay branching ratio $\text{Br}(t\bar{t} \rightarrow b\bar{b}\ell^+\nu jj) = 2/27$ is included in the numbers. We choose six benchmark points for the mass $m_{W'}$. We set the W' - t - b couplings at $f_L = 1$ and $f_R = 0$. The rates for other values of f_L can be obtained from simple scaling

$$\sigma = f_L^2 \times \sigma(f_L = 1). \quad (5.6)$$

5.3.1 Selection cuts

At the analysis level, all the signal and background events are required to pass the *basic* selection cuts listed here:

$$\begin{aligned} p_T^j &\geq 25 \text{ GeV}, & |\eta_j| &\leq 2.5 \\ p_T^\ell &\geq 25 \text{ GeV}, & |\eta_\ell| &\leq 2.5, \\ \Delta R_{jj,j\ell,\ell\ell} &> 0.4, & \cancel{E}_T &> 25 \text{ GeV} \end{aligned} \quad (5.7)$$

where p_T denotes the transverse momentum, \cancel{E}_T is the missing transverse momentum from the invisible neutrino in the final state, and ΔR is the separation in the azimuthal angle (ϕ)-pseudorapidity (η) plane between the objects k and l

$$\Delta R_{kl} \equiv \sqrt{(\eta_k - \eta_l)^2 + (\phi_k - \phi_l)^2}. \quad (5.8)$$

We smear the final state hadronic and leptonic energy according to a fairly standard Gaussian-type detector resolution given by

$$\frac{\delta E}{E} = \frac{\mathcal{A}}{\sqrt{E/\text{GeV}}} \oplus \mathcal{B}, \quad (5.9)$$

where $\mathcal{A} = 5(100)\%$ and $\mathcal{B} = 0.55(5)\%$ for leptons (jets).

As shown in the third column of Table 5.1, roughly 1/3 of the signal events pass the basic analysis cuts. At this stage, the SM backgrounds are dominant over the signal. A set of optimized cuts, based on the kinematic differences between the signal and backgrounds, is needed to extract the small signal.

There are five jets in the final state. Jets from a heavy W' boson decay tend to have a harder p_T than jets in the backgrounds. We order the jets by their values of p_T . Jet charge would also be a possibility for labeling jets, but the charge of jets is not well measured experimentally. Figure 5.3(a) displays the normalized p_T distribution of the jet with largest p_T for a 1 TeV W' . The signal and background curves are normalized by their individual cross sections. The signal distribution (black solid curve) peaks around 450 GeV while the backgrounds peak around 60-80 GeV. The leading jet in the signal is mainly the b -jet from $W' \rightarrow tb$ decay. It shares energy with its top quark partner; therefore its p_T is about

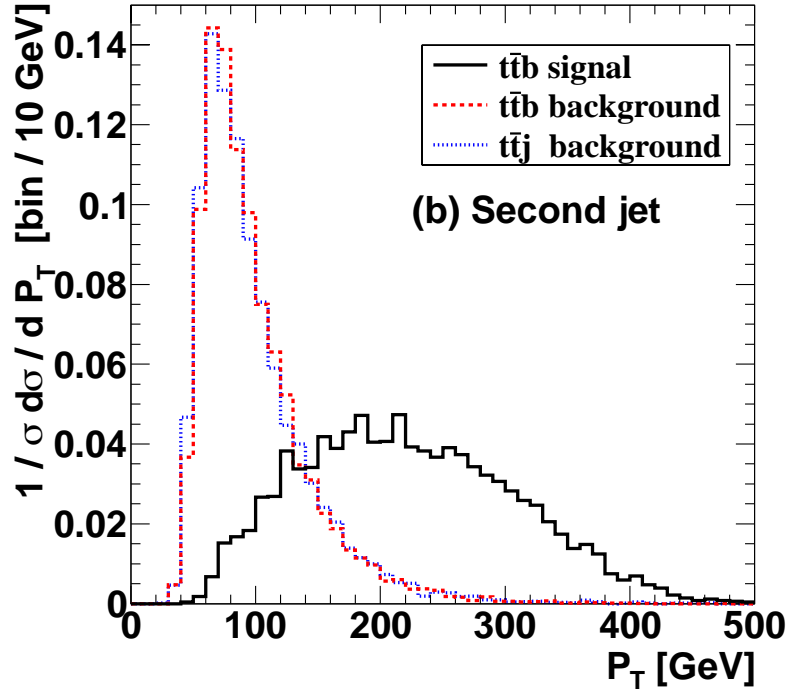
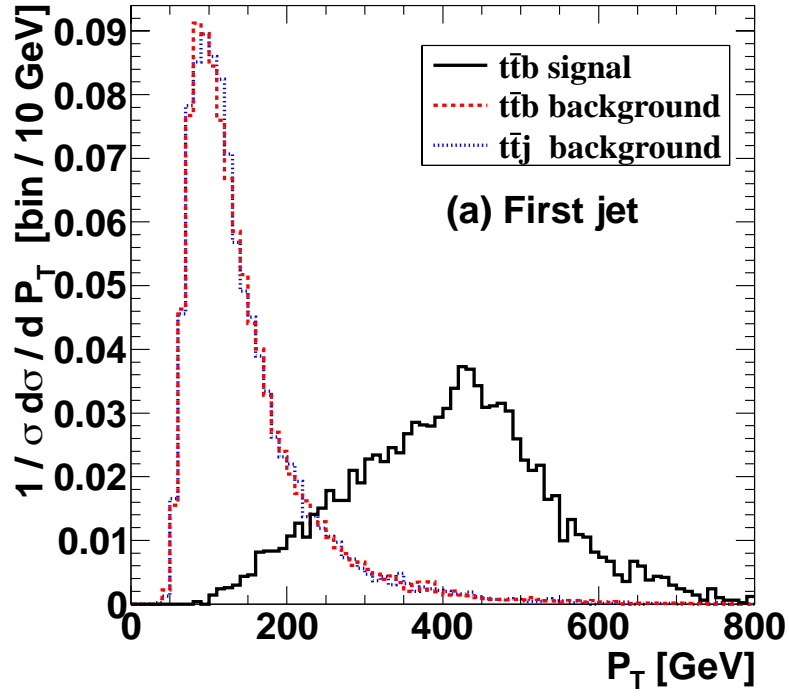


Figure 5.3: Normalized p_T distribution of (a) the leading jet, (b) the second leading jet distributions. The black-solid curves represent the signal ($m_{W'} = 1$ TeV), the red-dashed curves the $t\bar{t}b$ background, while the blue-dotted curves the $t\bar{t}j$ background.

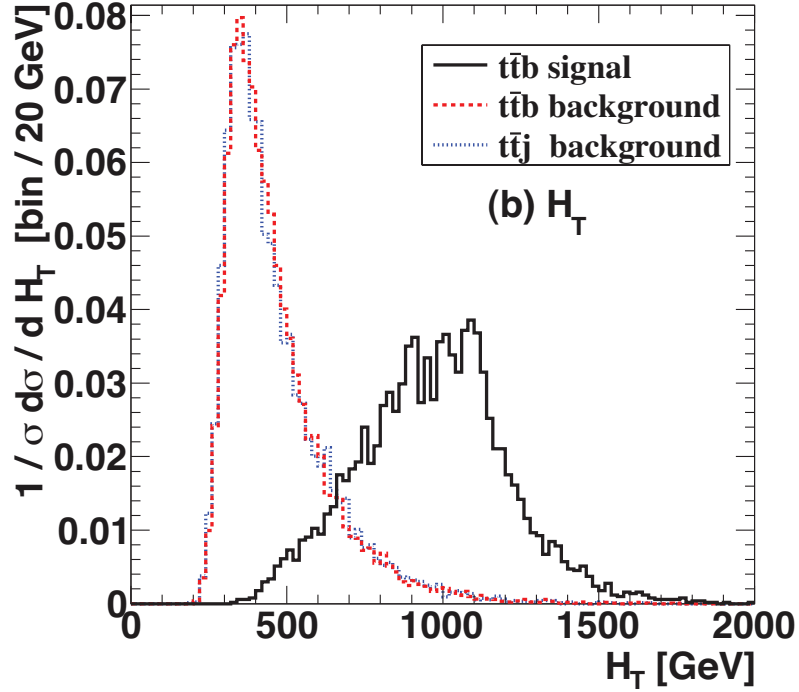
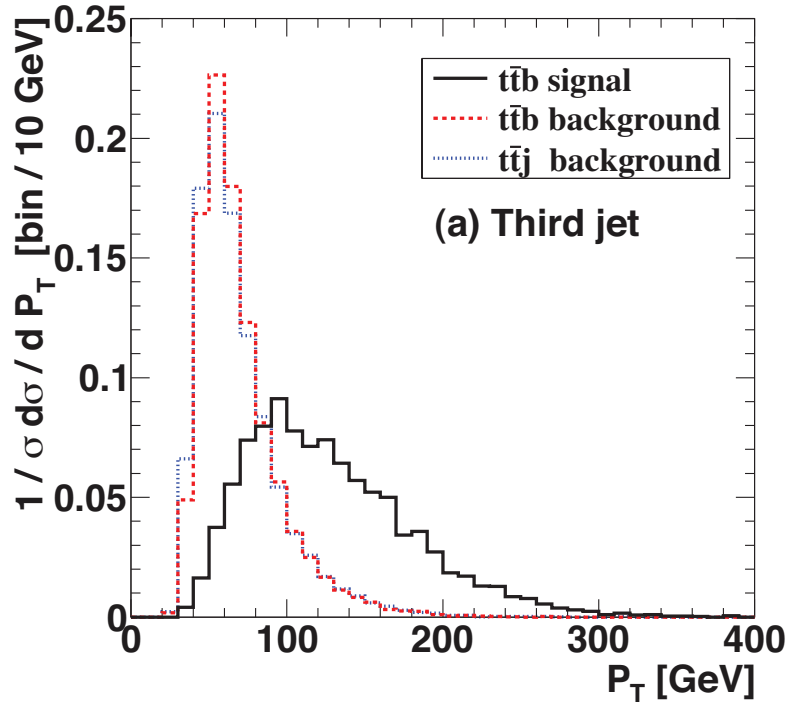


Figure 5.4: Normalized p_T distribution of (a) the third leading jet, as well as (b) the normalized H_T distribution. The black-solid curves represent the signal ($m_{W'} = 1$ TeV), the red-dashed curves the $t\bar{t}b$ background, while the blue-dotted curves the $t\bar{t}j$ background.

$m_{W'}/2$. On the other hand, the leading jet in the backgrounds is predominately from top quark decay. Its p_T spectrum peaks around $m_t/3 \sim 60$ GeV. These distinct p_T spectra motivate a hard cut on the leading jet p_T .

The p_T spectrum of the background is independent of $m_{W'}$ whereas the p_T spectrum of the leading jet in the signal is sensitive to $m_{W'}$. Absent prior knowledge of $m_{W'}$, a first step in a search might be to introduce a mass independent cut to suppress backgrounds, such as to require $p_T > 120$ GeV. This cut could then be increased or decreased to probe for a signal, as we expect experimental collaborations will do to search for heavy resonances.

Since the signal strength is much smaller than the background, we perform Monte Carlo simulations to find the best cut for each $m_{W'}$. This best cut is provided by the simple parameterization

$$p_T^{\text{1st}} \geq \left(50.0 + \frac{m_{W'}}{5} \right) \text{ GeV}, \quad (5.10)$$

which works well for $400 \text{ GeV} < m_{W'} < 1.0 \text{ TeV}$. We think of these $m_{W'}$ dependent cuts as different cut thresholds. Our $m_{W'}$ dependent cuts are optimized for discovery, and the numbers shown in the fourth column (labeled “optimal”) in Table 5.1 should be viewed as optimized results for each $m_{W'}$.

Figures 5.3(b) and 5.4(c) show the p_T spectra of the second and the third leading p_T jets. Similar to the leading jet, the 2nd and 3rd leading jets in the signal are harder than those in the backgrounds. We impose kinematic cuts on the 2nd and 3rd jets as follows:

$$\begin{aligned} p_T^{\text{2nd}} &\geq \left(20.0 + \frac{m_{W'}}{10} \right) \text{ GeV}, \\ p_T^{\text{3rd}} &\geq \left(20.0 + \frac{m_{W'}}{50} \right) \text{ GeV}. \end{aligned} \quad (5.11)$$

Another useful variable is H_T , the scalar sum of the p_T 's of all the visible particles in the final state,

$$H_T = p_T^{\ell^+} + \sum_j p_T^j. \quad (5.12)$$

Figure 5.4(d) shows the H_T distributions for the signal and backgrounds. Involving a massive W' in the final state, the signal distribution peaks above 1 TeV while the background distributions peak near the mass threshold of a $t\bar{t}$ pair (~ 400 GeV). This difference enables us to impose a hard cut on H_T to further suppress the SM background:

$$H_T > \left(m_{W'} - \frac{m_{W'}}{10} \right) \text{ GeV}, \quad (5.13)$$

The fourth column of Table 5.1 shows the number of signal and background events after the *optimized* cuts listed in Eqs. (5.10-5.13). The $t\bar{t}b$ background is suppressed significantly, but the $t\bar{t}j$ background still overwhelms the signal. However, as we now show, if b -tagging can be applied to the extra jet (the jet produced in association with the $t\bar{t}$ pair), the $t\bar{t}j$ background can be suppressed efficiently. This improvement arises because the extra jet in the signal originates from the b quark in the W' decay while the extra jet in the $t\bar{t}j$ background is from a non- b quark.

5.3.2 χ^2 -template and extra-jet tagging

Superficially, the only difference one sees among the final states in Eqs. (5.3-5.5) is that the signal and the $t\bar{t}b$ background produce final states with 3 b jets, whereas the $t\bar{t}j$ background has only 2 b jets. The key to suppressing the $t\bar{t}j$ background is to identify the extra b jet in the final state. To do this, we first exploit the difference in p_T between the extra jet and

the other jets, and then we require b tagging to identify it as a b jet.

The extra jet in the signal comes from the heavy W' decay and tends to have large p_T . The extra jet in the SM backgrounds, mainly from QCD radiation, tends to have a much softer p_T . However, a complication is that top quarks in the signal events are boosted and jets from top quark decay have large p_T . One of the jets from top quark decay could play the role of the leading jet. Our simulation shows that the extra jet (from heavy W' decay) serves as the leading p_T jet in 62% to 84 % of the cases for $m_{W'}$ ranging from 400 GeV to 1000 GeV. In view of small signal rate for a heavy W' , a more efficient method is needed to identify the extra-jet.

In this study we use a χ^2 -template method based on the W boson and top quark masses to select the extra jet. For each event we pick the combination which minimizes the following χ^2 :

$$\chi^2 = \frac{(m_W - m_{jj})^2}{\Delta m_W^2} + \frac{(m_t - m_{jl\nu})^2}{\Delta m_t^2} + \frac{(m_t - m_{jjj})^2}{\Delta m_t^2}. \quad (5.14)$$

There is two-fold ambiguity in the reconstruction of the longitudinal momentum of the neutrino from top quark decay. Making use of the W -boson on-shell condition, $m_{l\nu}^2 = m_W^2$, we can determine the longitudinal momentum of the neutrino ($p_{\nu L}$) as

$$p_{\nu L} = \frac{1}{2p_{eT}^2} \left(A p_{eL} \pm E_e \sqrt{A^2 - 4p_{eT}^2 \not{E}_T^2} \right), \quad (5.15)$$

where $A = m_W^2 + 2\vec{p}_{eT} \cdot \vec{E}_T$. If $A^2 - 4p_{eT}^2 \not{E}_T^2 \geq 0$, the value of $p_{\nu L}$ that best yields the known top mass is selected via $m_{l\nu b}^2 = m_t^2$. Once detector resolution is taken into account, this ideal situation need not hold. In this case, the value of $p_{\nu L}$ is chosen which yields the

minimum χ^2 . The reconstruction efficiencies (ϵ) for a 1 TeV W' compared with Monte Carlo truth are found to be:

$$\begin{aligned}
\epsilon_{\text{extra}} &= 99.8\%, \\
\epsilon_{t_{\text{lep}}} &= 98.9\%, \\
\epsilon_{t_{\text{had}}} &= 92.3\%.
\end{aligned}
\tag{5.16}$$

Such high efficiencies at the parton level arise mainly from the fact that the jets are highly boosted. Since there are combinatorial ambiguities in the final state, the efficiency for reconstruction of a top quark decaying leptonically (t_{lep}) is higher than for a top quark decaying hadronically (t_{had}).

Once the extra jet is identified by this kinematic method, one can require it to be a b -jet, reducing the $t\bar{t}j$ background by about a half, as is shown in the fifth column of Table 5.1. To retain as many signal events as possible, we require only one jet to be b -tagged. A tagging efficiency of 60% is used in our analysis. We take into account a mistag rate for a light non- b quark (including the charm quark) to mimic a b jet, with mistag efficiency $\epsilon_{j \rightarrow b} = 0.5\%$. For the Monte-Carlo truth events of the signal and backgrounds, we expect that 60% of the signal and $t\bar{t}b$ background events pass the b -tagging, while 0.5% of the $t\bar{t}j$ background events pass the b -tagging. Recall that the $t\bar{t}b$ background is suppressed by the hard p_T and H_T cuts. The b -tagging will further suppress the $t\bar{t}j$ background events with an efficiency 0.5%, if one can perfectly identify the extra-jet out of the five jets in the final state. However, the extra-jet identification with the χ^2 template method is not perfect. The jet identified as the extra-jet has three sources: the true extra-jet, b -quarks from top (antitop) quark decay, and the light-non- b quark from W^- -boson decay. Multiplying the extra-jet fraction with

the corresponding jet-tagging efficiency, we show below that one obtains a net jet-tagging efficiency of 1.2 % for the $t\bar{t}j$ background, cf. Eq. (5.20), about twice as large as the case of perfect extra-jet identification (0.5 %).

In Table 5.2 we show the tagging efficiency $\epsilon_{b\text{-tag}}$ of the extra jet after the χ^2 -template fit. It depends on the reconstruction efficiencies for the extra jet: $\epsilon_{\text{correct}}$ denotes the correct fraction from the χ^2 -fit, $\epsilon_{\text{wrong-}b}$ is the fraction of b jets from top quark decay that fake the extra jet, while $\epsilon_{\text{wrong-light}}$ is the fraction of light jets from top quark decay that fake the extra jet. As an example, consider the b -tagging efficiency in the signal process with 1 TeV W' mass. Since there are five jets in the final state, it is possible that after event reconstruction the extra jet is a b -jet from the top quark or anti-top quark decay (which we label “wrong- b ”), or a light-flavor jet from hadronic top quark decay (which we label “wrong - light”), or a b -jet from the W' decay (which we label “correct”). Note that the b -tagging is applied to the extra jet (which we call “extra-j-tagging”, to avoid confusion with the original b -tagging), but not to the truth b -jet from the W' decay. Taking the reconstruction efficiencies into account, we evaluate the net b -tagging efficiency of the extra jet $\epsilon_{\text{extra-j-tag}}$ as

$$\epsilon_{\text{extra-j-tag}} = (\epsilon_{\text{correct}} + \epsilon_{\text{wrong-}b}) \times 0.6 + \epsilon_{\text{wrong-light}} \times 0.005, \quad (5.17)$$

for the signal process. A similar analysis gives us the same formula for the $t\bar{t}b$ background. For a 1 TeV W' with hard cuts, we find the extra jet is a b -jet with 99.9% probability, and a light jet with 0.4% probability. Therefore, the b -tagging efficiency for the signal is

$$0.999 \times 0.6 + 0.004 \times 0.005 = 0.60. \quad (5.18)$$

For the $t\bar{t}j$ background, the correct jet is a light-flavor jet from the real radiation associated with top pair production. The formula changes to

$$\epsilon_{\text{extra-j-tag}} = (\epsilon_{\text{correct}} + \epsilon_{\text{wrong-light}}) \times 0.005 + \epsilon_{\text{wrong-b}} \times 0.6 \quad (5.19)$$

for the $t\bar{t}j$ background. For the $t\bar{t}j$ background, in the case of a 1 TeV W' with hard cuts, we find extra jet is a light jet with 98.8% probability, and a b -jet with 1.18% probability. Therefore, the b -tagging efficiency for the $t\bar{t}j$ background is

$$0.988 \times 0.005 + 0.012 \times 0.6 = 0.012. \quad (5.20)$$

We use Eqs. (5.17-5.20) to explain the numbers in the b -tagging column in Table 5.2. Table 5.2 shows that about 60% of the signal and $t\bar{t}b$ background events pass b -tagging even with the imperfect reconstruction of the extra jet. However, the extra-jet tagging efficiency for the $t\bar{t}j$ background is always larger than the b -tagging efficiency of 0.005 because it always is possible to mistag a b -jet when the extra-jet tagging is done.

5.3.3 Mass window ΔM cut

After full event reconstruction, one can compute the W' mass formed from the extra jet and the reconstructed t - or \bar{t} -quark. Since our signal events consist of both tW'^{-} and $\bar{t}W'^{+}$, one half of the signal events exhibit a peak in the invariant mass spectrum of the extra jet and t quark (denoted as m_{tj}) while the other half have a peak in the invariant mass of the extra jet and \bar{t} quark (denoted as $m_{\bar{t}j}$). Figure 5.5 shows the reconstructed m_{tj} and $m_{\bar{t}j}$ distributions for the signal (red), $t\bar{t}j$ (blue) and $t\bar{t}b$ (green) backgrounds. The signal distribution shows

$m_{W'}$	$\epsilon_{\text{correct}}$	$\epsilon_{\text{wrong}-b}$	$\epsilon_{\text{wrong}-\text{light}}$	$\epsilon_{\text{extra}-j-\text{tag}}$
400	98.15 %	1.63 %	0.22 %	59.9 %
$t\bar{t}b$	98.34 %	1.5 %	0.15 %	59.9 %
$t\bar{t}j$	96.67 %	2.96 %	0.37 %	2.26 %
500	98.53 %	1.35 %	0.12 %	59.9 %
$t\bar{t}b$	98.34 %	1.5 %	0.16 %	59.9 %
$t\bar{t}j$	96.7 %	2.92 %	0.37 %	2.23 %
600	99.32 %	0.59 %	0.08 %	59.9 %
$t\bar{t}b$	98.34 %	1.48 %	0.15 %	59.9 %
$t\bar{t}j$	96.75 %	2.88 %	0.36 %	2.22 %
700	99.4 %	0.51 %	0.09 %	59.9 %
$t\bar{t}b$	98.6 %	1.27 %	0.12 %	59.9 %
$t\bar{t}j$	97.15 %	2.55 %	0.29 %	2.02 %
800	99.66 %	0.31 %	0.03 %	60 %
$t\bar{t}b$	98.93 %	1.0 %	0.07 %	60 %
$t\bar{t}j$	97.6 %	2.17 %	0.23 %	1.79 %
900	99.87 %	0.12 %	0.01 %	60 %
$t\bar{t}b$	99.24 %	0.69 %	0.06 %	60 %
$t\bar{t}j$	98.17 %	1.63 %	0.2 %	1.46 %
1000	99.79 %	0.14 %	0.06 %	60 %
$t\bar{t}b$	99.5 %	0.43 %	0.07 %	60 %
$t\bar{t}j$	98.65 %	1.18 %	0.17 %	1.2 %

Table 5.2: The efficiency for extra jet reconstruction with the χ^2 -template method. The net b -tagging efficiencies ($\epsilon_{\text{extra}-j-\text{tag}}$), calculated with Eqs. (5.17) and (5.19), are shown in the last column.

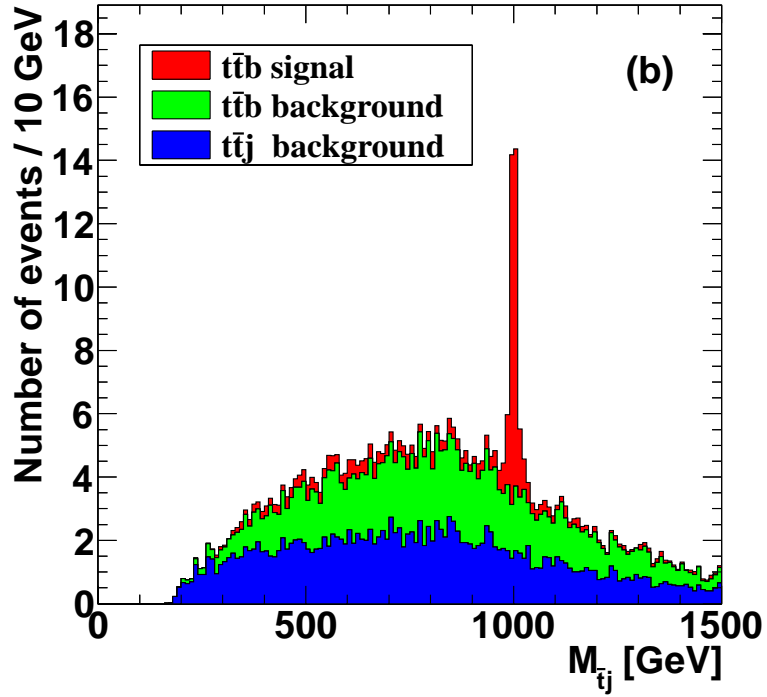
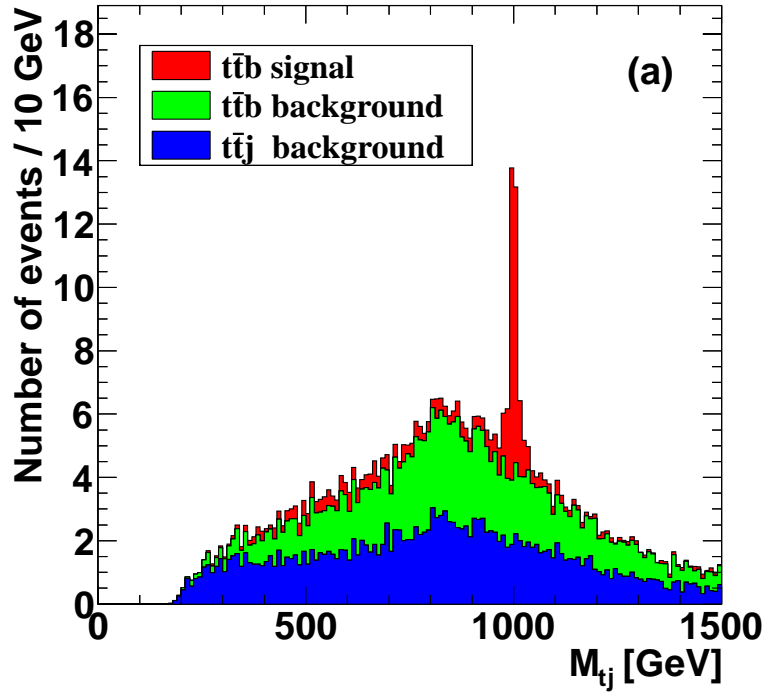


Figure 5.5: (a) Reconstructed invariant mass distribution of the leptonic decaying top and extra jet; (b) reconstructed hadronic decaying top and extra jet invariant mass distribution.

a sharp peak at the input value of $m_{W'}$. The pin shape reflects the narrow width of the top-philic W' boson, e.g. the W' width is about 8 GeV for a 1 TeV W' . The long tail into the small mass region comes from the one-half wrong combination. The peaks of the background distributions around 800 GeV are caused by the combination of hard kinematic cuts and jet identification (with combinatorial factors included).

Once $m_{W'}$ is known, we can impose cuts on m_{tj} or $m_{\bar{t}j}$ to further suppress backgrounds. We first demand large invariant masses for both tj and $\bar{t}j$,

$$m_{tj} > 250 + \frac{m_{W'}}{4}, \quad m_{\bar{t}j} > 250 + \frac{m_{W'}}{4}, \quad (5.21)$$

and that one of the following two mass window cuts be satisfied,

$$\left| m_{tj} - m_{W'} \right| < \frac{m_{W'}}{10}, \quad \text{or} \quad \left| m_{\bar{t}j} - m_{W'} \right| < \frac{m_{W'}}{10}. \quad (5.22)$$

The mass window suppress both SM backgrounds by a factor of 10 while it keeps most of the signal.

5.3.4 Discovery potential

The SM backgrounds are suppressed efficiently such that less than 1 background event survives after cuts with an integrated luminosity of 100 fb^{-1} . For a 1 TeV W' with the same coupling strength as the SM W - t - b interaction, we obtain a 5 standard deviations (σ) statistical significance, defined as S/\sqrt{B} where S and B denotes the number of signal and background events, respectively. For a lighter W' , the significance is larger for fixed coupling strength. The 3σ and 5σ discovery curves are plotted in Fig. 5.6. The region above

the 5σ curve is good for discovery.

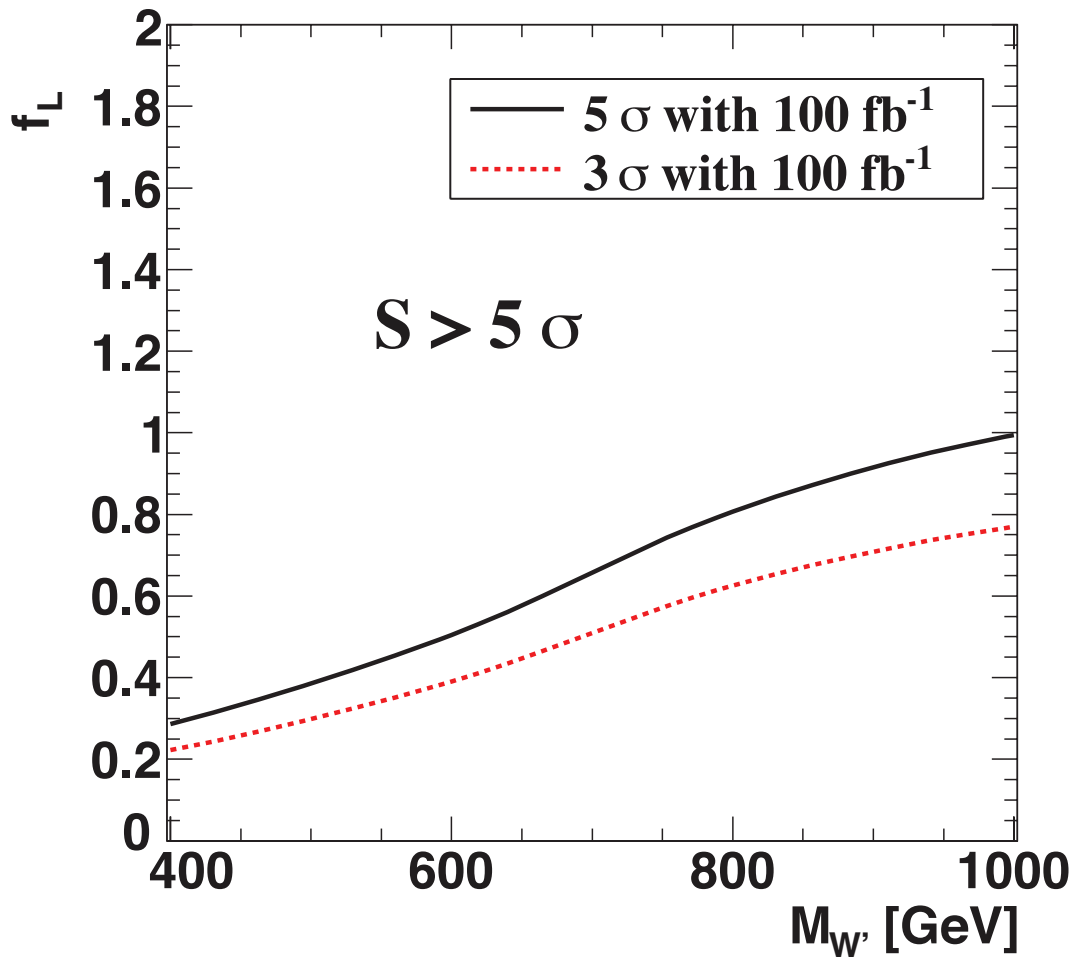


Figure 5.6: The discovery potential for the top-philic W' 14 TeV with an integrated luminosity of 100 fb^{-1} .

5.4 W' - t - b coupling and t -polarization

After the discovery of this W' boson, one would like to know its mass, spin, and couplings. The invariant mass or transverse momentum distributions of its decay products can be used to determine its mass. Angular distributions of its decay products can be investigated to confirm its spin and the chiral structure of the W' couplings to SM fermions. The chirality of the W' coupling to SM fermions is best measured from the polarization of the top quark [71, 94]. Among the top quark decay products, the charged lepton from $t \rightarrow bl\nu$ is the best analyzer of the top quark spin. For a left-handed top quark, the charged lepton moves preferentially against the direction of motion of the top quark, while for a right-handed top quark the charged lepton moves along the direction of motion of the top quark. The angular correlation of the lepton is $\frac{1}{2}(1 \pm \cos \theta_l)$, with the (+) choice for right-handed and (-) for left-handed top quarks, where θ_l is the angle of the lepton in the rest frame of top quark relative to the top quark direction of motion in the center-of-mass (cm) frame of the incoming partons. In Figs. 5.7 and 5.8 we plot the $\cos \theta_l$ distribution for $f_L = 1, f_R = 0$ and $f_L = 0, f_R = 1$ couplings. The curves clearly show the main characteristic features of the $\frac{1}{2}(1 \pm \cos \theta_l)$ behaviors for purely right- and left-handed polarized top quarks from W' decay, even after kinematic cuts are imposed. We note that due to the p_T and ΔR cuts, the distributions are distorted and drop significantly in the region $\cos \theta_l \sim -1$ for $f_L = 1$ and $f_R = 0$, and $\cos \theta_l \sim 1$ for $f_R = 1$ and $f_L = 0$. We expect a flat angular distribution for the SM background because the top quark and anti-top quark are not polarized. Therefore, the angular distributions of the lepton can be used to discriminate top-philic W' models in which the chirality of the W' coupling to SM fermions differs.

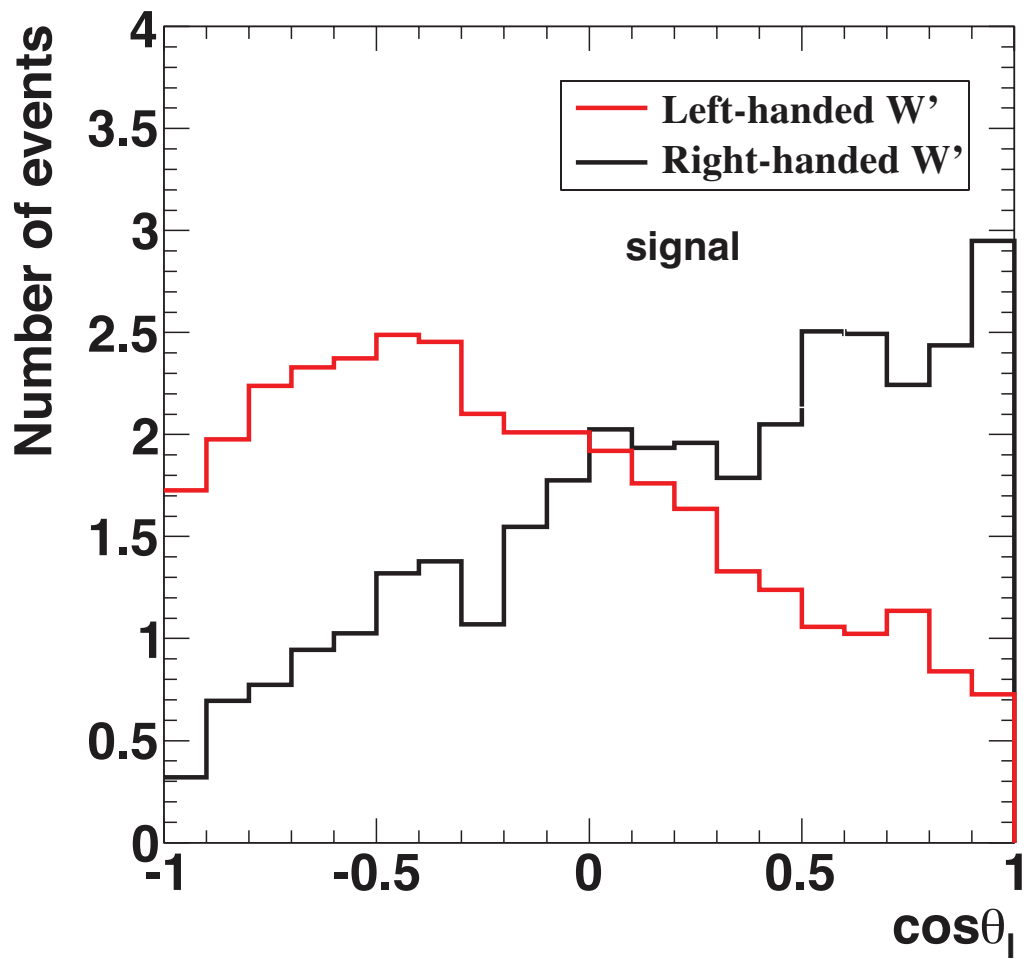


Figure 5.7: The angular distributions of the final lepton $\cos\theta_l$ for the left-handed and the right-handed W' .

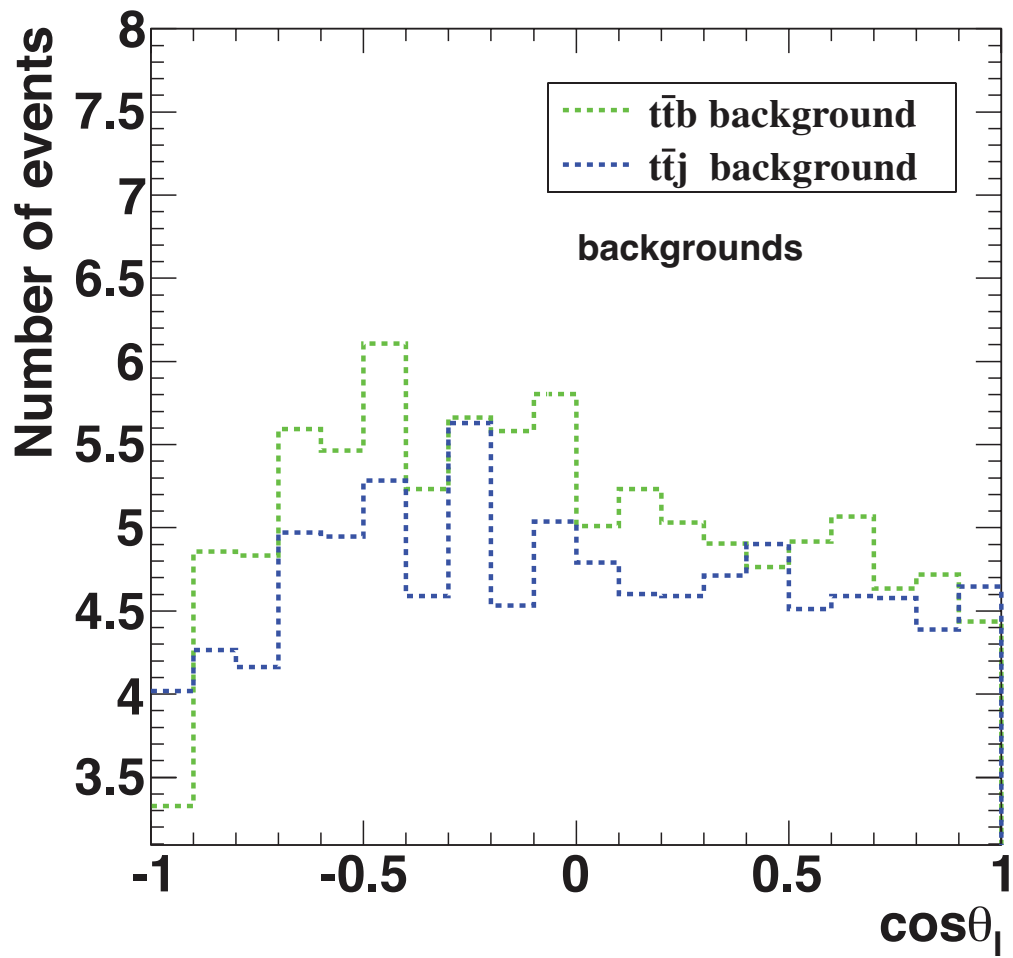


Figure 5.8: The angular distributions of the final lepton $\cos \theta_l$ for the SM background.

5.5 Summary

In this chapter we examined the LHC phenomenology of a top-philic W' model. In the model the W' boson is produced in association with a top-quark and it decays into a top quark and bottom quark pair, yielding a collider signature of $t\bar{t}$ plus one b -jet. We exploited the different kinematic features of the signal and backgrounds to suppress the large standard model backgrounds from $t\bar{t}j$ and $t\bar{t}b$ production. Examining the distributions of the signal and backgrounds, we found that hard p_T cuts and cuts on H_T can suppress the $t\bar{t}b$ background. After full event reconstruction, we showed that tagging the extra b -jet can further suppress the $t\bar{t}j$ background. We showed that discovery of a top-philic W' with SM-like coupling strengths is promising at 14 TeV with $\mathcal{L} = 100 \text{ fb}^{-1}$. A resonance peak in the top quark and b -jet invariant mass distribution is a distinct signature of W' discovery. Top quark polarization can be used to measure the chiral structure of the W' - t - b coupling. Top quark pair and hard b -jet final states are worth examining even in a model-independent way. This final state is a new unexploited channel at the LHC.

Chapter 6

CONCLUSION

This thesis presents a study of the phenomenology of heavy charged gauge bosons. We studied the heavy gauge bosons within the framework of an effective field theory with the gauge symmetries $SU(2)_1 \times SU(2)_2 \times U(1)_X$ models (the so-called $G(221)$ models). Such a formalism provides a unified view of the possible symmetry breaking patterns to recover the standard model as well as the gauge couplings of the fermions. The $G(221)$ models can be separated into two classes of breaking patterns: breaking pattern I (BP-I), and the breaking pattern II (BP-II). Examples of models in BP-I are the left-right (LR), leptophobic (LP), hadrophobic (HP) and fermiophobic (FP), while examples in BP-II are the sequential (SQ), the ununified (UU) and non-universal (NU) models.

We studied the parameter constraints on the $G(221)$ models and placed bounds on the masses of the heavy gauge bosons. For the electroweak precision constraints, we performed a global-fit analysis on a set of 37 electroweak observables, including Z pole data, the mass and the width of the W^\pm boson, and various low-energy observables. Moreover, the direct searches of the W' and Z' bosons at the Fermilab Tevatron and CERN LHC further con-

strained the $G(221)$ model parameter space. We summarized here the most important results from the indirect and direct constraints. For the left-right model, the direct search data at the LHC with 7 TeV energy gives a stronger constraint on W' and Z' masses than both the electroweak and Tevatron constraints. It excludes the region where the W' mass is smaller than 1.7 TeV, and where the Z' mass is smaller than 2.3 TeV. For the sequential model, although W' and Z' with degenerate masses below 500 GeV are allowed by the EWPTs at large c_ϕ , the limits from Tevatron and LHC exclude the region where W' and Z' masses are smaller than 1.5 TeV. For all other models, the electroweak precision data still gives the strongest constraint on the W' and Z' masses, because of the non-universal flavor structure in these models. In breaking pattern I, with all combined constraints, all the phobic models can still have relatively light W' with a mass of 500 GeV mass, but with a heavier Z' of mass 1.5 TeV. For the non-universal models, such as top-flavor and un-unified models, the electroweak indirect constraints are tighter than Tevatron and LHC7 direct constraints, and push the new gauge boson mass up to more than 2 TeV in top-flavor model and 3 TeV in un-unified model.

The Drell-Yan production, which has the simplest topology and very clean leptonic final states, is the most promising channel for early discovery of W' and Z' bosons. In the general $SU(2)_1 \times SU(2)_2 \times U(1)_X$ models, we calculated the Drell-Yan production cross section at the next-to-leading order. Our study revealed that the discovery potential of W' and Z' bosons is highly limited by the indirect constraints. With a full scan of the parameter space, we are able to predict the time scale to probe/exclude the W' and Z' by accessing more parameter region as the luminosity goes up at the LHC. In the left-right model it is more efficient to use the W' leptonic decay channel for discovery or exclusion than the Z' leptonic

decay channel. In theophobic models, observing a Z' alone cannot rule out the possibility of a non-abelian gauge extension of new physics. In BP-II models, both the Z' and the W' leptonic decay channel are suitable to explore the allowed parameter space. Discovering a degenerate W' and Z' in the leptonic decay channels at the same time will be the distinct feature in BP-II.

The top quark plays a special role in the standard model, and offers a window into possible new physics beyond the SM. In many models, because the top quark is naturally related to EWSB, new physics is very sensitive to the top quark observables. The observables such as angular, spin correlations and polarization of the top quark can be used to determine the particle properties and its chiral structures. We studied the heavy charged gauge bosons in the single top final states. We showed that it is possible to probe the chiral structure of the charged gauge bosons using the top quark polarization. As another example, since both CDF and D0 confirmed a large forward-backward asymmetry in the top pair production, we studied how a flavor-violating W' model might explain this asymmetry. We investigated the correlation between the top quark A_{FB}^t and the final-state lepton A_{FB}^l in the flavor-violating W' models. We studied the kinematic and dynamic aspects of the relationship between A_{FB}^t and A_{FB}^l , arising from the spin correlation between the charged lepton and the top quark with different polarization states. Our study revealed a strong correlation between these two asymmetries, and we conclude that a model which produces more right-handed than left-handed top quarks is favored by the present data.

We also looked for unexpected new signatures for the exotic W' discovery. We studied a "top-philic" model, in which the W' couples only to third-generation quarks and is produced only in association with a top quark. The final state, top quark pair plus a hard b-jet, is

a new unexploited channel at the LHC. We performed a detailed study on the top quark pair plus a hard b -jet final states, and expect that our analysis can be used in a model-independent study. To discriminate signal from the large background $t\bar{t}j$, we studied the distributions of the signal and backgrounds and found that several kinematic features, such as H_T and b -tagging, can be used to suppress the large $t\bar{t}j$ backgrounds. We showed that discovery of a top-philic W' with SM-like coupling strengths is promising at 14 TeV with $\mathcal{L} = 100 \text{ fb}^{-1}$. A resonance peak in the top quark plus b -jet invariant mass distribution is a distinct signature of W' discovery. Furthermore, top quark polarization can be used to measure the chiral structure of the W' - t - b coupling. The Top quark pair plus hard b -jet final state is a new unexploited channel at the LHC, which is worth continued examination in a model-independent way.

As a final outlook, we would like to mention several theoretical considerations left for future investigation. At the LHC, if there is enough luminosity, the vector boson pair production, and the vector boson and Higgs associated production channel will be the primary channels to study. The reason is that the vector boson channel is essential to explore the spontaneous symmetry breaking at the TeV scale. The vector boson channels will probe a different part of the theory about resonances, whether the resonance is a gauge boson or just a vector boson, whether the resonance is relevant to spontaneous symmetry breaking or not. In addition, there are also other kinds of W' -bosons, such as T-parity odd W' , and Kaluza-Klein W' resonances which can be studied in future.

With the start of the LHC, a new era of discovery in particle physics has just begun. It is the time to study the collider phenomenology of new physics beyond the standard model. Although in this thesis we focus on the charged gauge boson resonances, similar strategies can

be performed to study the collider phenomenologies for other kinds of new heavy particles. We look forward to how the LHC will revolutionize particle physics by opening the TeV energy region to direct experimental exploration.

APPENDICES

Appendix A

Statistics for Upper limit and Significance

In the high energy experiments, a very important aim is to search for new physics beyond the standard model. Statistical data analysis will be used either to set limits on new physics or to claim a new discovery. To distinguish a possible new physics signal s from the existing standard model background b , hypothesis testing in statistical method plays an important role. When setting limits, the model with signal plus background plays the role of null hypothesis, which is tested against the background-only hypothesis H_1 . When discovering a new signal process, one defines the null hypothesis as background, which is tested against the alternative signal hypothesis.

The Bayesian and the classical frequentist, are the two statistical approaches commonly used in high energy physics to do hypothesis testing. The difference between frequentist and Bayesian is:

- in frequentist statistics, data are repeatable random sample, while underlying param-

eters remains constant during this random process (parameters are fixed);

- in Bayesian statistics, parameters are unknown random variables, while data are observed from the realistic experiments (data are fixed).

They are different points of view: the frequentist statistician does many repeated trials given an underlying true theory, while the Bayesian tries to get the degree of belief of an incomplete theory given the existing measurements. For more details, we refer readers to refs. [115]. In the following, we will apply the hypothesis testing in the counting experiments to illustrate the two approaches. Suppose one has an experiment that counts n events, modeled as a Poisson distribution with mean $s + b$, where s is the expected signal rate, b is the expected background rate. The probability of measuring n events is therefore

$$P(n|s, b) = \frac{(s + b)^n}{n!} e^{-(s+b)}. \quad (\text{A.1})$$

A.1 Upper Limit

Both Bayesian and the classical frequentist methods use confidence level (CL) to quantify the level of incompatibility of data with a signal hypothesis. Usually one requires a 95% CL for excluding a signal hypothesis.

A.1.1 Bayesian Approach

In the signal hypothesis, one would like to set limit on the expected cross section σ of a signal process. Consider there are N channels (or bins), and for channel i , one observes n_i events, assuming the expected background rate is b_i , and the acceptance is ϵ_i with integrated

luminosity L_i .

In the absence of systematic errors from subsidiary measurements, the joint likelihood for combined N channels can be written as the product of individual likelihood

$$\mathcal{L}(\vec{n}|\sigma, \vec{b}, \vec{\epsilon}) = \prod_{i=1}^N \frac{(\sigma L_i \epsilon_i + b_i)^{n_i}}{n_i!} e^{-(\sigma L_i \epsilon_i + b_i)}, \quad (\text{A.2})$$

where the vectors indicate the variables are arrays carrying index i .

To quantify the degree of belief on this signal hypothesis, the posterior probability is defined to be related with the confidence level. Using Bayes' theorem, the posterior probability density can be obtained, given the likelihood and the prior probability density $\pi(\sigma)$ for the signal cross section. The posterior probability density is

$$\mathcal{P}(\sigma|\vec{n}, \vec{b}, \vec{\epsilon}) = \frac{1}{\mathcal{N}} \mathcal{L}(\vec{n}|\sigma, \vec{b}, \vec{\epsilon}) \pi(\sigma), \quad (\text{A.3})$$

where the normalization factor \mathcal{N} integrated all the possible σ . Typically the function $\mathcal{P}(\sigma)$ is commonly taken to be flat for $\sigma \geq 0$ and zero otherwise.

The limit is now obtained by integrating this posterior probability density for σ until we achieve the 95% of the total integral from zero to infinity. The 95% CL upper limit $\sigma_{95\%CL}$, is given by

$$\int_0^{\sigma_{95\%CL}} \mathcal{P}(\sigma'|\vec{n}, \vec{b}, \vec{\epsilon}) d\sigma' = 95\%. \quad (\text{A.4})$$

In the case of single channel with constant prior probability density, the final expression is

$$1 - \frac{\Gamma(n+1, \sigma_{95\%CL} \epsilon L)}{\Gamma(n+1, b)} = 95\%. \quad (\text{A.5})$$

To include the systematic errors (nuisance parameters), one would consider the prior probability density from the subsidiary measurements $\pi(\sigma, \vec{b}, \vec{\epsilon})$. Then one marginalizes the nuisance parameters by integrating over them. The posterior probability density can be rewritten as

$$\mathcal{P}(\sigma|\vec{n}) = \frac{1}{\mathcal{N}} \int \int \mathcal{L}(\vec{n}|\sigma, \vec{b}, \vec{\epsilon}) \pi(\sigma, \vec{b}, \vec{\epsilon}) d\vec{b} d\vec{\epsilon}. \quad (\text{A.6})$$

The 95% CL upper limit $\sigma_{95\%CL}$, is given by

$$\int_0^{\sigma_{95\%CL}} \mathcal{P}(\sigma'|\vec{n}) d\sigma' = 95\%. \quad (\text{A.7})$$

To get the expected limit, one would treat \vec{n} as \vec{b} in above integration.

If the number of observed events is large, the Poisson likelihood asymptotically tends to a Gaussian with mean n and standard deviation \sqrt{n} :

$$P(n|s, b) = \frac{(s+b)^n}{n!} e^{-(s+b)} \quad \rightarrow \quad e^{-\frac{(s+b-n)^2}{2n}}. \quad (\text{A.8})$$

In practice, the approximation is already good for $n \geq 10$. The integration

$$\int_0^{s_{95\%CL}} \mathcal{P}(s|n, b) ds = \frac{\int_0^{s_{95\%CL}} P(n|s, b) ds}{\int_0^\infty P(n|s, b) ds} \quad (\text{A.9})$$

can be calculated analytically

$$\frac{\text{ERF} \left[(s_{95\%CL} + b - n)/\sqrt{2n} \right] + \text{ERF}[(n - b)/\sqrt{2n}]}{1 + \text{ERF}[(n - b)/\sqrt{2n}]} = 95\%. \quad (\text{A.10})$$

The expected limit can be obtained through

$$\text{ERF} \left[(s_{95\%CL})/\sqrt{2b} \right] = 95\%. \quad (\text{A.11})$$

The final result is

$$s_{95\%CL} = 1.96 \times \sqrt{b} \quad \rightarrow \quad \sigma_{95\%CL} = 1.96 \times \frac{\sqrt{b}}{\epsilon L}, \quad (\text{A.12})$$

where one can infer a scaling behavior

$$\sigma_{95\%CL} \sim \frac{1}{\sqrt{L}}. \quad (\text{A.13})$$

For the combined upper limits of N channels, the combined likelihood can be written as

$$P(n|s, b) = \prod_{i=1}^N \frac{(\sigma \epsilon_i L_i + b_i)^{n_i}}{n_i!} e^{-(\sigma \epsilon_i L_i + b_i)} \quad \rightarrow \quad \prod_{i=1}^N e^{-\frac{(\sigma \epsilon_i L_i + b_i - n_i)^2}{2n_i}}. \quad (\text{A.14})$$

From the properties of product of Gaussian distribution, the Gaussian likelihood can be rewritten as

$$P(n|\sigma, \epsilon, b) = \prod_{i=1}^N e^{-\frac{\left(\sigma - \frac{n_i - b_i}{\epsilon_i L_i}\right)^2}{2n_i/(\epsilon_i L_i)^2}} = e^{-\frac{(\sigma - \mu)^2}{2\kappa^2}}. \quad (\text{A.15})$$

where

$$\mu = \frac{\sum_i^N \frac{n_i - b_i}{2n_i/(\epsilon_i L_i)}}{\sum_i^N \frac{1}{2n_i/(\epsilon_i L_i)^2}}, \quad (\text{A.16})$$

$$\kappa^2 = \frac{1}{\sum_i^N \frac{(\epsilon_i L_i)^2}{n_i}}. \quad (\text{A.17})$$

we can get the combined upper limit

$$s_{95\%CL} = 1.96 \times \kappa. \quad (\text{A.18})$$

From the above, we can obtain the following relation

$$\sigma_{95\%CL}^2 = \frac{1}{\sum_i^N \frac{1}{\sigma_{95\%CL\ i}^2}}. \quad (\text{A.19})$$

A.1.2 Frequentist Approach

The frequentist approach requires the selection of a test statistic q as measure of discrepancy between the data and the hypothesis, with higher values of q corresponding to increasing disagreement. As a signal-vs-background discriminator, there are many kinds of choices of the test statistic:

- a simple choice will be the possible observed number of events n during the trial measurement;
- By the Neyman-Pearson lemma, the likelihood ratio Q is the most powerful discrimi-

nator, defined as

$$q_\mu = -2 \ln \frac{\mathcal{L}(n|\mu s + b)}{\mathcal{L}(n|b)}, \quad (\text{A.20})$$

where μ is a strength parameter defined such that $\mu = 0$ is the background-only hypothesis and $\mu = 1$ is the hypothesis of background plus signal. This test statistic was used by LEP and the Tevatron. In references, there are various modifications of this method: Feldman-Cousins, CL_S , Power-Constrained Limits, etc.

- At the LHC, the profile-likelihood test statistic q_μ is used. The profile likelihood ratio is defined as

$$\lambda(\mu) = \frac{\mathcal{L}(\mu, \hat{\hat{b}})}{\mathcal{L}(\hat{\mu}, \hat{\hat{b}})}. \quad (\text{A.21})$$

Here $\mathcal{L}(\mu, \hat{\hat{b}})$ is the likelihood maximized $\hat{\hat{b}}$ for the specified μ i.e., it is the conditional maximum-likelihood (ML) estimator of b (and thus is a function of μ). $\mathcal{L}(\hat{\mu}, \hat{\hat{b}})$ is the maximized (unconditional) likelihood function, i.e., $\hat{\mu}$ and $\hat{\hat{b}}$ are their ML estimators. The profile likelihood ratio is thus

$$t_\mu = -2 \ln \lambda(\mu). \quad (\text{A.22})$$

In the absence of systematic errors, for the Poisson likelihood with given observable n

$$\mathcal{L}(\mu, b; n) = \frac{(\mu s + b)^n}{e^{-(\mu s + b)}} n!, \quad (\text{A.23})$$

the profile likelihood with given n is

$$t_\mu = -2 \ln \lambda(\mu) = 2 \left[(\mu s + b - n) + n \ln \frac{n}{\mu s + b} \right]. \quad (\text{A.24})$$

For large $\mu s + b$, the test statistic can be expanded around $x = (n - \mu s - b)/(\mu s + b)$ as

$$t_\mu = \frac{(n - \mu s - b)^2}{\mu s + b} \left(1 - \frac{x}{3} + \frac{x^2}{6} + \dots \right). \quad (\text{A.25})$$

Here the distribution for n is approximately a Gaussian distribution with mean $\mu s + b$ and variance $\sigma_0 = \sqrt{\mu s + b}$. So we can rewrite

$$t_\mu \simeq \frac{(\mu - \mu_0)^2}{\sigma_0^2}, \quad (\text{A.26})$$

where $\mu_0 = \frac{n - b}{s}$ and $\sigma_0 = \sqrt{\mu s + b}/s$. For the multi-channel case, the test statistic is

$$t_\mu = -2 \ln \lambda(\mu) = \sum_{i=1}^N 2 \left[(\mu s + b_i - n_i) + n_i \ln \frac{n_i}{\mu s + b_i} \right]. \quad (\text{A.27})$$

Having defined the test statistic, next one constructs the probability density $f(t_\mu|\mu)$ of the chosen test statistic q_μ under the signal hypothesis through many repeated pseudo-observations. Using the probability density $f(t_\mu|\mu)$ one can quantify the level of disagreement by defining the p -value

$$p_\mu = \int_{t_{\mu,\text{obs}}}^{\infty} f(t_\mu|\mu) dt_\mu, \quad (\text{A.28})$$

where $t_{\mu,\text{obs}}$ is the value of the statistic t_μ observed from the data. Such a p -value is denoted as CL_{s+b} , which relate to confidence level as $1 - CL_{s+b}$. The probability densities are different for different test statistics, such that in the simplest choice of test statistic n the probability density is a simple Poisson distribution.

At the LHC, the default test statistic is the profile likelihood ratio, because this method has the simplest way to incorporate systematics into hypothesis, and its known asymptotic properties. We will focus on this profile likelihood method and calculate the upper limit.

In order to find the p -value, the sampling distribution of the test statistic $f(q_\mu|\mu)$ need to be obtained. We also need the distribution $f(q_\mu|\mu')$ with $\mu' \neq \mu$ to find how this is distributed (the median) if the data correspond to a strength parameter different from the one being tested. Here we present an approximate distribution for the profile likelihood ratio, valid in the large sample limit. In the large sample limit, one can model $\hat{\mu}$, which is the value of μ that maximizes the likelihood, as a Gaussian distributed variable. If $\hat{\mu}$ follows a Gaussian distribution with a mean μ' and standard deviation σ , we can approximate the test statistic as

$$-2 \ln \lambda(\mu) = \frac{(\mu - \hat{\mu})^2}{\sigma^2} + \mathcal{O}(1/\sqrt{N}) . \quad (\text{A.29})$$

and determine its distributions of the test statistics. The standard deviation σ of $\hat{\mu}$ is obtained from the covariance matrix of the estimators for all the parameters,

$$V_{ij}^{-1} = -E \left[\frac{\partial^2 \ln L}{\partial \theta_i \partial \theta_j} \right] , \quad (\text{A.30})$$

where here the θ_j represent both μ as well as the nuisance parameters. If all nuisance parameters are fixed, $\hat{\mu}$ will be the value

$$E[\mu] = E\left[\frac{n-b}{s}\right] = \frac{n-b}{s}, \quad (\text{A.31})$$

which maximizes the likelihood. For the variance, one can take $\theta_0 = \mu$, so

$$V_{00}^{-1} = -E \left[\frac{\partial^2 \ln L}{\partial \mu \partial \mu} \right] = E \left[\frac{n\mu^2}{(\mu s + b)^2} \right] = \frac{s^2}{\mu s + b}, \quad (\text{A.32})$$

where L is a Poisson distribution, and $E[n] = \mu s + b$. Then we obtain

$$\sigma^2 = V_{00} = \frac{\mu s + b}{s^2}. \quad (\text{A.33})$$

If $\hat{\mu}$ is Gaussian distributed, one can show the statistic t_μ follows a non-central χ^2 distribution with one degree of freedom,

$$f(t_\mu; \Lambda) = \frac{1}{2\sqrt{t_\mu}} \frac{1}{\sqrt{2\pi}} \left[\exp \left(-\frac{1}{2} \left(\sqrt{t_\mu} + \sqrt{\Lambda} \right)^2 \right) + \exp \left(-\frac{1}{2} \left(\sqrt{t_\mu} - \sqrt{\Lambda} \right)^2 \right) \right], \quad (\text{A.34})$$

where the parameter Λ is

$$\Lambda = \frac{(\mu - \mu')^2}{\sigma^2}. \quad (\text{A.35})$$

For the special case $\mu' = \mu$ one has $\Lambda = 0$ and $-2 \ln \lambda(\mu)$ approaches a chi-square distribution for one degree of freedom.

For purposes of computing limits, we introduce a modification to the profile likelihood ratio definition as

$$q_\mu = \begin{cases} -2 \ln \lambda(\mu) & \hat{\mu} \leq \mu, \\ 0 & \hat{\mu} > \mu, \end{cases} \quad (\text{A.36})$$

The reason for setting $q_\mu = 0$ for $\hat{\mu} > \mu$ is we want to determine the smallest μ such that there is a fixed small p -value to find data as compatible with that value of μ or less. Similar

to the above, the pdf $f(q_\mu|\mu')$ can be written as

$$f(q_\mu|\mu') = \Phi\left(\frac{\mu' - \mu}{\sigma}\right) \delta(q_\mu) + \frac{1}{2} \frac{1}{\sqrt{2\pi}} \frac{1}{\sqrt{q_\mu}} \exp\left[-\frac{1}{2} \left(\sqrt{q_\mu} - \frac{\mu - \mu'}{\sigma}\right)^2\right], \quad (\text{A.37})$$

In the special case $\mu = \mu'$ is a half-chi-square distribution:

$$f(q_\mu|\mu) = \frac{1}{2} \delta(q_\mu) + \frac{1}{2} \frac{1}{\sqrt{2\pi}} \frac{1}{\sqrt{q_\mu}} e^{-q_\mu/2}. \quad (\text{A.38})$$

The cumulative distribution is

$$F(q_\mu|\mu') = \Phi\left(\sqrt{q_\mu} - \frac{\mu - \mu'}{\sigma}\right), \quad (\text{A.39})$$

and the corresponding special case $\mu' = \mu$

$$F(q_\mu|\mu) = \Phi\left(\sqrt{q_\mu}\right). \quad (\text{A.40})$$

The p -value can be calculated as

$$p_\mu = 1 - F(q_{\mu\text{obs}}|\mu) = 1 - \Phi\left(\sqrt{q_{\mu\text{obs}}}\right), \quad (\text{A.41})$$

and the upper limit is

$$\mu_{\text{up}} = \hat{\mu} + \sigma \Phi^{-1}(1 - \alpha). \quad (\text{A.42})$$

where α is the upper limit of p_μ . At a confidence level of 95%, p -value is $1 - \alpha = 5\%$, so one has

$$\mu_{\text{up}} = \hat{\mu} + \sigma \Phi^{-1}(0.05) = \hat{\mu} + 1.64\sigma . \quad (\text{A.43})$$

To determine $\hat{\mu}$ and σ one further take the Gaussian approximation. For large $\mu s + b$, the distribution of n is Gaussian distributed with mean $\hat{\mu}$ and σ . For given n , $\hat{\mu}$ is the maximized value of μ , with $\hat{\mu} = \frac{n - b}{s}$ and σ can be approximately treated as $\sigma = \frac{\sqrt{\hat{\mu}s + b}}{s} = \frac{\sqrt{n}}{b}$. For the expected upper limit $\hat{\mu} = 0$ and $\sigma = \sqrt{b}/s$, so we get

$$\mu_{\text{up}} = 1.64 \frac{\sqrt{b}}{s} . \quad (\text{A.44})$$

We then derive the combined upper limit. The test statistic for N multi-channel processes is

$$q_\mu = \sum_{i=1}^N \frac{(\mu_i - \hat{\mu}_i)^2}{\sigma_i^2} = \sum_{i=1}^N \chi_i^2, \quad (\text{A.45})$$

where μ is the is a strength parameter, or saying the ratio between Higgs cross section and reference standard model Higgs cross section. Since the product of Gaussian distribution has such a property:

$$\hat{\mu} = \frac{\sum_i^N \frac{\hat{\mu}_i}{\sigma_i^2}}{\sum_i^N \frac{1}{\sigma_i^2}}, \quad (\text{A.46})$$

$$\sigma^2 = \frac{1}{\sum_i^N \frac{1}{\sigma_i^2}}, \quad (\text{A.47})$$

the test statistic of N multi-channel can be rewritten based on $\hat{\mu}$ and σ^2 as

$$q_{\mu} = \frac{(\mu - \hat{\mu})^2}{\sigma^2}. \quad (\text{A.48})$$

At a confidence level of 95%, p -value is $1 - \alpha = 5\%$, so one has

$$\mu_{\text{up}} = \hat{\mu} + \sigma \Phi^{-1}(0.05) = \hat{\mu} + 1.64\sigma. \quad (\text{A.49})$$

For the expected upper limit $\hat{\mu} = 0$ and $\sigma = \sqrt{b}/s$, so we get the combined limit

$$\mu_{\text{up}} = 1.64 \frac{\sqrt{b}}{s} = 1.64 \times \sigma, \quad (\text{A.50})$$

and for each channel

$$\mu_{i\text{up}} = 1.64 \frac{\sqrt{b_i}}{s_i} = 1.64 \times \sigma_i. \quad (\text{A.51})$$

From Eq. A.46, one can get

$$\mu_{\text{up}}^2 = \frac{1}{\sum_i^N \frac{1}{\mu_{i\text{up}}^2}}. \quad (\text{A.52})$$

The result is the same as the one using Bayesian approach.

To include the systematic errors, one can define the complete profile likelihood ratio with background errors. When one does the maximization of the likelihood, one need to solve the ML estimators \hat{b} and $\hat{\theta}$. There is another method to include systematic errors, in which all the errors are included as nuisance parameters. In this case, one need to do the marginalization for the likelihood, and then take the ratio of the profile likelihood.

A.2 Discovery Significance

In the case of observing an excess of events, the statistical significance of an observed signal can be quantified by means of a p -value or its equivalent Gaussian significance in the frequentist approach, and Bayes Factor in the Bayesian approach.

A.2.1 Bayesian Approach

In the Bayesian approach, the Bayesian could define an interval that reflects the degree-of-belief for each hypothesis. The ratio of these intervals is defined as Bayes factor,

$$B = \frac{\text{likelihood with } s = 0, \text{ marginalized over } b}{\text{likelihood with } \mu = 0 \text{ marginalized over } s \text{ and } b}, \quad (\text{A.53})$$

which is quite similar to the definition of the profile likelihood ratio, with Bayesian marginalization replacing maximization. Unlike the frequentist approach, one doesn't need to know the probability density of all possible outcomes of the measurement for a given hypothesis. However, the disadvantages with this Bayesian approach are that one has to assume prior distributions for each hypothesis, and one is only allowed to make relative confidence statements about two hypotheses. Due to the above disadvantages, the Bayes factor only has limited usage on new physics discovery in high energy physics. We will focus on the discovery in the frequentist approach.

A.2.2 Frequentist Approach

For the discovery, the p -value is defined as the probability of getting an observation as or less compatible as seen in data for the background-only hypothesis, in the following

$$p_0 = \int_{t_{0,\text{obs}}}^{\infty} f(t_0|b) dt_0, \quad (\text{A.54})$$

where $t_{0,\text{obs}}$ is the value of the statistic t_0 observed from the data. The p -value can be converted into an equivalent significance Z , defined such that a Gaussian distributed variable via

$$Z = \Phi^{-1}(1 - p). \quad (\text{A.55})$$

For a signal process, one commonly regards the rejection of the background hypothesis with a significance of at least $Z = 5$ as an appropriate level to constitute a discovery. This corresponds to $p = 2.87 \times 10^{-7}$. For purposes of excluding a signal hypothesis, a threshold p -value of 0.05 (i.e., 95% confidence level) is often used, which corresponds to $Z = 1.64$.

We will focus on the test statistic q_0 used at the LHC [116]. From the modified definition of q_0 , we therefore have

$$q_0 = \begin{cases} \hat{\mu}^2/\sigma^2 & \hat{\mu} \geq 0, \\ 0 & \hat{\mu} < 0, \end{cases} \quad (\text{A.56})$$

where $\hat{\mu}$ follows a Gaussian distribution with mean μ' and standard deviation σ . One will get a similar probability density with $\mu = 0$. For the special case of $\mu' = 0$, the probability density reduces to

$$f(q_0|0) = \frac{1}{2}\delta(q_0) + \frac{1}{2}\frac{1}{\sqrt{2\pi}}\frac{1}{\sqrt{q_0}}e^{-q_0/2}, \quad (\text{A.57})$$

which is a mixture of a delta function at zero and a chi-square distribution for one degree of freedom. The corresponding cumulative distribution is

$$F(q_0|\mu') = \Phi\left(\sqrt{q_0} - \frac{\mu'}{\sigma}\right). \quad (\text{A.58})$$

and the special case $\mu' = 0$

$$F(q_0|0) = \Phi\left(\sqrt{q_0}\right). \quad (\text{A.59})$$

The p -value of the $\mu = 0$ hypothesis is

$$p_0 = 1 - F(q_0|0), \quad (\text{A.60})$$

and therefore the significance is

$$Z_0 = \Phi^{-1}(1 - p_0) = \sqrt{q_0}. \quad (\text{A.61})$$

In the counting experiment, if we regard b as known, the data consist only of n and thus the likelihood function is

$$L(\mu) = \frac{(\mu s + b)^n}{n!} e^{-(\mu s + b)}, \quad (\text{A.62})$$

The test statistic for discovery q_0 can be written

$$q_0 = \begin{cases} -2 \ln \frac{L(0)}{L(\hat{\mu})} & \hat{\mu} \geq 0, \\ 0 & \hat{\mu} < 0, \end{cases} \quad (\text{A.63})$$

where $\hat{\mu} = n - b$. For sufficiently large b we can use the asymptotic formula (A.61) for the

significance,

$$Z_0 = \sqrt{q_0} = \begin{cases} \sqrt{2 \left(n \ln \frac{n}{b} + b - n \right)} & \hat{\mu} \geq 0, \\ 0 & \hat{\mu} < 0. \end{cases} \quad (\text{A.64})$$

To approximate the expected (median) significance assuming the nominal signal hypothesis ($\mu = 1$) we replace n by the Asimov value $s + b$ to obtain

$$\text{med}[Z_0|s + b] = \sqrt{q_{0,A}} = \sqrt{2 \left((s + b) \ln(1 + s/b) - s \right)}. \quad (\text{A.65})$$

For large b , the test statistic can be expanded around $x = (n - b)/b$ as

$$q_0 \simeq \frac{(n - b)^2}{b}. \quad (\text{A.66})$$

Here the distribution for n is approximately a Gaussian distribution with mean b and variance $\sigma_0 = \sqrt{b}$. So we can rewrite

$$Z_0 = \sqrt{q_0} \sim \begin{cases} \frac{n - b}{\sqrt{b}} & \hat{\mu} \geq 0, \\ 0 & \hat{\mu} < 0. \end{cases} \quad (\text{A.67})$$

Expanding the logarithm in s/b one finds the expected (median) significance assuming signal rate

$$\text{med}[Z_0|s + b] = \frac{s}{\sqrt{b}} \left(1 + \mathcal{O}(s/b) \right). \quad (\text{A.68})$$

Although $Z_0 \approx s/\sqrt{b}$ has been widely used for cases where $s + b$ is large, one sees here that this final approximation is strictly valid only for $s \ll b$.

BIBLIOGRAPHY

BIBLIOGRAPHY

- [1] M. E. Peskin and D. V. Schroeder, “An Introduction to quantum field theory,” Reading, USA: Addison-Wesley (1995).
- [2] C. Quigg, “Gauge Theories of the strong, weak, and electromagnetic interactions,” Boulder, USA: Westview (1997).
- [3] T. Morii, C. S. Lim, and S. N. Mukherjee “The physics of the standard model and beyond,” Singapore: World Scientific (2004).
- [4] C. Quigg, *Ann. Rev. Nucl. Part. Sci.* **59**, 505 (2009) [arXiv:0905.3187 [hep-ph]].
- [5] H. Georgi, *Nucl. Phys. B* **266**, 274 (1986).
- [6] B. W. Lee, C. Quigg and H. B. Thacker, *Phys. Rev. D* **16**, 1519 (1977).
- [7] Y. -P. Yao and C. P. Yuan, *Phys. Rev. D* **38**, 2237 (1988).
- [8] M. Bustamante, L. Cieri and J. Ellis, CERN Yellow Report CERN-2010-001, 145-228 [arXiv:0911.4409 [hep-ph]].
- [9] J. Ellis, J. R. Espinosa, G. F. Giudice, A. Hoecker and A. Riotto, *Phys. Lett. B* **679**, 369 (2009) [arXiv:0906.0954 [hep-ph]].
- [10] K. Cheung, C. -W. Chiang and T. -C. Yuan, *Phys. Rev. D* **78**, 051701 (2008) [arXiv:0803.2661 [hep-ph]].
- [11] R. N. Mohapatra and J. C. Pati, *Phys. Rev. D* **11**, 2558 (1975).
- [12] R. N. Mohapatra and J. C. Pati, *Phys. Rev. D* **11**, 566 (1975).

- [13] R. N. Mohapatra and G. Senjanovic, Phys. Rev. D **23**, 165 (1981).
- [14] H. Georgi and S. L. Glashow, Phys. Rev. Lett. **32**, 438 (1974).
- [15] H. Georgi and A. Pais, “Calculability And Naturalness In Gauge Theories,” Phys. Rev. D **10**, 539 (1974).
- [16] H. Georgi and A. Pais, “Vacuum Symmetry And The Pseudogoldstone Phenomenon,” Phys. Rev. D **12**, 508 (1975).
- [17] N. Arkani-Hamed, A. G. Cohen, T. Gregoire and J. G. Wacker, “Phenomenology of electroweak symmetry breaking from theory space,” JHEP **0208**, 020 (2002) [arXiv:hep-ph/0202089].
- [18] L. Randall and R. Sundrum, Phys. Rev. Lett. **83**, 3370 (1999) [hep-ph/9905221].
- [19] C. Csaki, C. Grojean, L. Pilo and J. Terning, Phys. Rev. Lett. **92**, 101802 (2004) [hep-ph/0308038].
- [20] C. Csaki, C. Grojean, H. Murayama, L. Pilo and J. Terning, Phys. Rev. D **69**, 055006 (2004) [hep-ph/0305237].
- [21] R. Contino, Y. Nomura and A. Pomarol, “Higgs as a holographic pseudo-Goldstone boson,” Nucl. Phys. B **671**, 148 (2003) [arXiv:hep-ph/0306259].
- [22] K. Agashe, R. Contino and A. Pomarol, “The minimal composite Higgs model,” arXiv:hep-ph/0412089.
- [23] T. G. Rizzo, arXiv:hep-ph/0610104.
- [24] K. Hsieh, K. Schmitz, J. H. Yu and C. P. Yuan, Phys. Rev. D **82**, 035011 (2010) [arXiv:1003.3482 [hep-ph]].
- [25] V. D. Barger, W. Y. Keung and E. Ma, Phys. Rev. D **22**, 727 (1980).
- [26] V. D. Barger, W. Y. Keung and E. Ma, Phys. Rev. Lett. **44**, 1169 (1980).
- [27] R. S. Chivukula, B. Coleppa, S. Di Chiara, E. H. Simmons, H. J. He, M. Kurachi and M. Tanabashi, Phys. Rev. D **74**, 075011 (2006) [arXiv:hep-ph/0607124].

- [28] H. Georgi, E. E. Jenkins and E. H. Simmons, Phys. Rev. Lett. **62**, 2789 (1989) [Erratum-ibid. **63**, 1540 (1989)].
- [29] H. Georgi, E. E. Jenkins and E. H. Simmons, Nucl. Phys. B **331**, 541 (1990).
- [30] E. Malkawi, T. M. P. Tait and C. P. Yuan, Phys. Lett. B **385**, 304 (1996) [arXiv:hep-ph/9603349].
- [31] X. Li and E. Ma, Phys. Rev. Lett. **47**, 1788 (1981).
- [32] X. G. He and G. Valencia, Phys. Rev. D **66**, 013004 (2002) [Erratum-ibid. D **66**, 079901 (2002)] [arXiv:hep-ph/0203036].
- [33] P. Langacker, Rev. Mod. Phys. **81**, 1199 (2008) [arXiv:0801.1345 [hep-ph]].
- [34] P. Langacker and S. Uma Sankar, Phys. Rev. D **40**, 1569 (1989).
- [35] G. Barenboim, J. Bernabeu, J. Prades and M. Raidal, Phys. Rev. D **55**, 4213 (1997) [arXiv:hep-ph/9611347].
- [36] T. G. Rizzo, Phys. Rev. D **58**, 114014 (1998) [arXiv:hep-ph/9802401].
- [37] J. Erler, arXiv:hep-ph/0005084.
- [38] F. James and M. Roos, Comput. Phys. Commun. **10**, 343 (1975).
- [39] C. Amsler *et al.* [Particle Data Group], Phys. Lett. B **667**, 1 (2008).
- [40] [ALEPH Collaboration and DELPHI Collaboration and L3 Collaboration and], Phys. Rept. **427**, 257 (2006) [arXiv:hep-ex/0509008].
- [41] P. Vilain *et al.* [CHARM-II Collaboration], Phys. Lett. B **364**, 121 (1995).
- [42] P. L. Anthony *et al.* [SLAC E158 Collaboration], Phys. Rev. Lett. **95**, 081601 (2005) [arXiv:hep-ex/0504049].
- [43] C. S. Wood, S. C. Bennett, D. Cho, B. P. Masterson, J. L. Roberts, C. E. Tanner and C. E. Wieman, Science **275**, 1759 (1997).

- [44] J. Guena, M. Lintz and M. A. Bouchiat, arXiv:physics/0412017.
- [45] P. A. Vetter, D. M. Meekhof, P. K. Majumder, S. K. Lamoreaux and E. N. Fortson, Phys. Rev. Lett. **74**, 2658 (1995).
- [46] N. H. Edwards, S. J. Phipp, P. E. G. Baird, and S. Nakayama, Phys. Rev. Lett. **74**, 2654 (1995).
- [47] R. D. Young, R. D. Carlini, A. W. Thomas and J. Roche, Phys. Rev. Lett. **99**, 122003 (2007) [arXiv:0704.2618 [hep-ph]].
- [48] V. Khachatryan *et al.* [CMS Collaboration], [arXiv:1012.5945 [hep-ex]].
- [49] S. Chatrchyan *et al.* [CMS Collaboration], JHEP **1105**, 093 (2011) [arXiv:1103.0981 [hep-ex]].
- [50] T. Aaltonen *et al.* [CDF Collaboration], Phys. Rev. **D83**, 031102 (2011). [arXiv:1012.5145 [hep-ex]].
- [51] T. Aaltonen *et al.* [CDF Collaboration], Phys. Rev. Lett. **103**, 041801 (2009). [arXiv:0902.3276 [hep-ex]].
- [52] V. M. Abazov *et al.* [D0 Collaboration], Phys. Lett. B **695**, 88 (2011) [arXiv:1008.2023 [hep-ex]].
- [53] T. Aaltonen *et al.* [CDF Collaboration], Phys. Rev. D **84**, 072004 (2011) [arXiv:1107.5063 [hep-ex]].
- [54] G. Aad *et al.* [ATLAS Collaboration], Phys. Lett. B **705**, 28 (2011) [arXiv:1108.1316 [hep-ex]].
- [55] G. Aad *et al.* [ATLAS Collaboration], Phys. Rev. Lett. **107**, 272002 (2011) [arXiv:1108.1582 [hep-ex]].
- [56] [CMS Collaboration], CMS-PAS-EXO-11-092(2012).
- [57] G. Aad *et al.* [ATLAS Collaboration], ATL-PHYS-PUB-2009-063. ATL-COM-PHYS-2009-222. (2009)
- [58] G. Aad *et al.* [The ATLAS Collaboration], [arXiv:0901.0512 [hep-ex]].

- [59] V. M. Abazov *et al.* [D0 Collaboration], Phys. Lett. **B695**, 88-94 (2011). [arXiv:1008.2023 [hep-ex]].
- [60] T. Aaltonen *et al.* [CDF Collaboration], Phys. Rev. Lett. **100**, 231801 (2008). [arXiv:0709.0705 [hep-ex]].
- [61] T. Aaltonen *et al.* [CDF Collaboration], Phys. Rev. **D77**, 051102 (2008). [arXiv:0710.5335 [hep-ex]].
- [62] M. S. Carena, A. Daleo, B. A. Dobrescu, T. M. P. Tait, Phys. Rev. **D70**, 093009 (2004). [hep-ph/0408098].
- [63] E. Accomando, A. Belyaev, L. Fedeli, S. F. King, C. Shepherd-Themistocleous, [arXiv:1010.6058 [hep-ph]].
- [64] E. Salvioni, G. Villadoro, F. Zwirner, JHEP **0911**, 068 (2009). [arXiv:0909.1320 [hep-ph]].
- [65] C. W. Bauer, Z. Ligeti, M. Schmaltz, J. Thaler, D. G. E. Walker, Phys. Lett. **B690**, 280-288 (2010). [arXiv:0909.5213 [hep-ph]].
- [66] M. Schmaltz, C. Spethmann, [arXiv:1011.5918 [hep-ph]].
- [67] K. R. Lynch, E. H. Simmons, M. Narain, S. Mrenna, Phys. Rev. **D63**, 035006 (2001). [hep-ph/0007286].
- [68] P. M. Nadolsky, H. -L. Lai, Q. -H. Cao, J. Huston, J. Pumplin, D. Stump, W. -K. Tung and C. -P. Yuan, Phys. Rev. D **78**, 013004 (2008) [arXiv:0802.0007 [hep-ph]].
- [69] T. Aaltonen *et al.* [CDF Collaboration], Phys. Rev. D **79**, 112002 (2009).
- [70] S. Chatrchyan *et al.* [CMS Collaboration], $\hat{\Lambda} \hat{\Lambda}$ Phys. Lett. B **704**, 123 (2011) $\hat{\Lambda} \hat{\Lambda}$ [arXiv:1107.4771 [hep-ex]]. $\hat{\Lambda} \hat{\Lambda}$
- [71] S. Gopalakrishna, T. Han, I. Lewis, Z. -g. Si and Y. -F. Zhou, Phys. Rev. D **82**, 115020 (2010).
- [72] T. Aaltonen *et al.* [CDF Collaboration], Phys. Rev. D **83**, 112003 (2011)
- [73] V. M. Abazov *et al.* [D0 Collaboration], arXiv:1107.4995 [hep-ex].

- [74] J. Pumplin, D. R. Stump, J. Huston, H. L. Lai, P. M. Nadolsky and W. K. Tung, JHEP **0207**, 012 (2002) [hep-ph/0201195].
- [75] M. Cacciari, G. P. Salam and G. Soyez, Eur. Phys. J. C **72**, 1896 (2012).
- [76] ATLAS Collaboration, JINST **3**, S08003 (2008).
- [77] CMS Collaboration, J. Phys. G G **34**, 995 (2007).
- [78] W. Bernreuther and Z. -G. Si, Nucl. Phys. B **837**, 90 (2010).
- [79] J. H. Kühn and G. Rodrigo, Phys. Rev. Lett. **81**, 49 (1998); J. H. Kuhn and G. Rodrigo, Phys. Rev. D **59**, 054017 (1999).
- [80] D. Krohn, T. Liu, J. Shelton and L. T. Wang, arXiv:1105.3743 [hep-ph].
- [81] A. Falkowski, G. Perez and M. Schmaltz, arXiv:1110.3796 [hep-ph].
- [82] S. Jung, H. Murayama, A. Pierce, and J. D. Wells, Phys. Rev. **D81**, 015004 (2010).
- [83] K. Cheung, W. Y. Keung and T. C. Yuan, Phys. Lett. B **682**, 287 (2009);
- [84] P. Ferrario and G. Rodrigo, Phys. Rev. D **80** (2009) 051701;
- [85] P. H. Frampton, J. Shu and K. Wang, Phys. Lett. B **683**, 294 (2010);
- [86] Q. H. Cao, D. McKeen, J. L. Rosner, G. Shaughnessy and C. E. M. Wagner, Phys. Rev. D **81**, 114004 (2010) [arXiv:1003.3461 [hep-ph]].
- [87] B. Xiao, Y. -k. Wang, S. -h. Zhu, Phys. Rev. **D82**, 034026 (2010). [arXiv:1006.2510 [hep-ph]].
- [88] K. Yan, J. Wang, D. Y. Shao and C. S. Li, arXiv:1110.6684 [hep-ph].
- [89] A. Djouadi, G. Moreau, F. Richard, R. K. Singh, Phys. Rev. **D82**, 071702 (2010).
- [90] A. Djouadi, G. Moreau, F. Richard, Phys. Lett. **B701**, 458-464 (2011).

- [91] E. L. Berger, Q. H. Cao, C. R. Chen, C. S. Li and H. Zhang, Phys. Rev. Lett. **106** (2011) 201801
- [92] S. Chatrchyan *et al.* [CMS Collaboration], JHEP **1108** (2011) 005
- [93] G. Mahlon and S. J. Parke, Phys. Rev. D **53**, 4886 (1996)
- [94] E. L. Berger, Q. H. Cao, C. R. Chen and H. Zhang, Phys. Rev. D **83**, 114026 (2011)
- [95] O. Antunano, J. H. Kuhn and G. Rodrigo, Phys. Rev. D **77**, 014003 (2008) [arXiv:0709.1652 [hep-ph]].
- [96] J. M. Campbell and R. K. Ellis, Phys. Rev. D **60** (1999) 113006.
- [97] G. Aad *et al.* [ATLAS Collaboration], arXiv:1103.1391 [hep-ex].
- [98] V. M. Abazov *et al.* [D0 Collaboration], Phys. Lett. B **699**, 145 (2011) [arXiv:1101.0806 [hep-ex]].
- [99] Zack Sullivan, Phys. Rev. D **66**, 075011 (2002) [arXiv:hep-ph/0207290].
- [100] V. M. Abazov *et al.* [D0 Collaboration], arXiv:1011.6278 [hep-ex].
- [101] K. Cheung, W. Y. Keung and T. C. Yuan, Phys. Lett. B **682**, 287 (2009) [arXiv:0908.2589 [hep-ph]].
- [102] V. Barger, W. -Y. Keung, C. -T. Yu, Phys. Rev. **D81**, 113009 (2010). [arXiv:1002.1048 [hep-ph]].
- [103] K. Cheung and T. C. Yuan, Phys. Rev. D **83**, 074006 (2011) [arXiv:1101.1445 [hep-ph]].
- [104] V. Barger, W. -Y. Keung, C. -T. Yu, Phys. Lett. **B698**, 243-250 (2011). [arXiv:1102.0279 [hep-ph]]
- [105] M. I. Gresham, I. W. Kim and K. M. Zurek, arXiv:1102.0018 [hep-ph].
- [106] T. Aaltonen *et al.* [CDF Collaboration], Phys. Rev. Lett. **102**, 222003 (2009) [arXiv:0903.2850 [hep-ex]].

- [107] J. Alwall, M. Herquet, F. Maltoni, O. Mattelaer and T. Stelzer, arXiv:1106.0522 [hep-ph].
- [108] Zack Sullivan, Phys. Rev. D **66**, 075011 (2002) [arXiv:hep-ph/0207290].
- [109] K. Cheung, W. Y. Keung and T. C. Yuan, Phys. Lett. B **682**, 287 (2009) [arXiv:0908.2589 [hep-ph]].
- [110] V. Barger, W. -Y. Keung, C. -T. Yu, Phys. Rev. **D81**, 113009 (2010). [arXiv:1002.1048 [hep-ph]].
- [111] K. Cheung and T. C. Yuan, Phys. Rev. D **83**, 074006 (2011) [arXiv:1101.1445 [hep-ph]].
- [112] V. Barger, W. -Y. Keung, C. -T. Yu, Phys. Lett. **B698**, 243-250 (2011). [arXiv:1102.0279 [hep-ph]]
- [113] M. I. Gresham, I. W. Kim and K. M. Zurek, arXiv:1102.0018 [hep-ph].
- [114] T. Aaltonen *et al.* [CDF Collaboration], Phys. Rev. Lett. **102**, 222003 (2009) [arXiv:0903.2850 [hep-ex]].
- [115] G. Cowan, "Statistical data analysis," Oxford, UK: Clarendon (1998).
- [116] G. Cowan, K. Cranmer, E. Gross and O. Vitells, Eur. Phys. J. C **71**, 1554 (2011) [arXiv:1007.1727 [physics.data-an]].
- [117] Adam Bourdarios, *et al.* [ATLAS Collaboration], ATL-PHYS-PUB-2009-063 (2009).